Computational Studies on C−H Activation Reactions at Iridum, Rhodium and Ruthenium

Amalia I. Poblador-Bahamonde

Submitted for the degree of

Doctor of Philosophy

Heriot-Watt University

School of Engineering and Physical Sciences

December 2009

Abstract

Density Functional Theory (DFT) calculations have been carried out to study the factors that affect the cyclometallation reactions of the model system [Ir(η-Cp)(dmba−H)(κ^2-RCO_2)]$^+$ (R= CH_3, CF_3, CCl_3, OH and Ph), as well as the triflate analogue. The limiting step is, in all cases, the dissociation of one arm of the chelating base and in most cases a κ^1-intermediate was located. The transition state for the subsequent C−H activation exhibits short M···C−H and O···H interactions which combine to allow an easy hydrogen transfer. The combination of these two factors leads to a new term *Ambiphilic Metal Ligand Activation* (AMLA) to describe these C−H activation processes.

The above study was extended to [M(ring)(dmba−H)(κ^2-OAc)] systems, (where M(ring) = {Rh(η-Cp)}$^+$, {Ru(η-C_6H_6)}$^+$ and {Ru(η-Cp)}). Cationic systems have very similar activation energies ($\Delta E^{\ddagger}$), although small variations in the overall energy were computed. These effects were rationalized in terms of the strengths of the M−C and M−O bonds formed and broken in the reaction. The neutral systems gave a lower $\Delta E^{\ddagger}$ although the products were less stable. In addition, the substitution of the dmba−H ligand for related imine or amide substrates shows that these species also readily undergo facile cyclometallation.

Finally, the intermolecular C−H activation of benzene by [Ir(η-Cp)(PH_3)(κ^2-OAc)]$^+$ and the incorporation of this step into a catalytic cycle for the hydroarylation of ethene was assessed. The rate-limiting step is associated with the alkene insertion step ($\Delta E^{\ddagger}$ = 16.7 kcal/mol), while the C−H activation is slightly more accessible. Therefore, this model appears to be a promising target for catalysis.

To my parents, Leonor and Cándido

To my beloved sister Leonor

Acknowledgments

I would first like to express my sincere gratitude to my supervisor Prof. Stuart Macgregor for all his support, encouragement and patience during all these years. I would also like to thank Dr. David Davies and Youcef Boutadla at the University of Leicester for all their research and interesting feedback.

Special thanks are for Julien. His support, discussions and inherent ability to make me smile have helped me to be the person that I am today.

I would also like to thank my parents, my sister and other members of my family for all the support throughout these years. I would like to thank you for my education and your example day after day.

A great deal of thanks goes the previous and current members of the CICG for their help, discussions, friendship and enjoyable atmosphere during my PhD. A special mention goes to Dave, because it has been an honour to be at your left hand-side all this years and be gifted with your friendship.

I would also like to thank the cheerful spirit to my friends, those in Spain and the new ones I got to know in Scotland. Particular mention goes to Camino who turned out to be a box full of surprises.

ACADEMIC REGISTRY
Research Thesis Submission

Name*:*	Amalia I. Poblador Bahamonde		
School/PGI:	Engineering and Physical Sciences		
Version: *(i.e. First, Resubmission, Final)*	First	Degree Sought (Award **and** Subject area)	PhD in Chemistry

Declaration

In accordance with the appropriate regulations I hereby submit my thesis and I declare that:

1) the thesis embodies the results of my own work and has been composed by myself
2) where appropriate, I have made acknowledgement of the work of others and have made reference to work carried out in collaboration with other persons
3) the thesis is the correct version of the thesis for submission and is the same version as any electronic versions submitted*.
4) my thesis for the award referred to, deposited in the Heriot-Watt University Library, should be made available for loan or photocopying and be available via the Institutional Repository, subject to such conditions as the Librarian may require
5) I understand that as a student of the University I am required to abide by the Regulations of the University and to conform to its discipline.

* *Please note that it is the responsibility of the candidate to ensure that the correct version of the thesis is submitted.*

Signature of Candidate*:*		Date:	

Submission

Submitted By *(name in capitals):*	Amalia I. Poblador-Bahamonde
Signature of Individual Submitting:	
Date Submitted:	

For Completion in Academic Registry

Received in the Academic Registry by *(name in capitals):*			
Method of Submission *(Handed in to Academic Registry; posted through internal/external mail):*			
*E-thesis Submitted (**mandatory for final theses from January 2009)***			
Signature:		Date:	

Please note this form should bound into the submitted thesis.

Updated February 2008, November 2008, February 2009

Chapter 1: Introduction

Chapter 2: Cyclometallation of *N,N*-dimethylbenzylamine with $[IrCl_2Cp^*]_2$: the role of the chelating base

List of Publications

1. A. B. Chaplin, A. I. Poblador-Bahamonde, H. A. Sparkes, J. A. K. Howard, S. A. Macgregor and A. S. Weller, *Chem. Commun.*, 2009, 244-246.

2. Y. Boutadla, D. L. Davies, S. A. Macgregor and A. I. Poblador-Bahamonde, *Dalton Trans.*, 2009, 5820-5831.

3. Y. Boutadla, D. L. Davies, S. A. Macgregor and A. I. Poblador-Bahamonde, *Dalton Trans.*, 2009, 5887-5893.

1. Introduction

C−H activation is an extremely important process, both for its fundamental scientific interest and for its potential for producing functionalised hydrocarbons.[1] Transition metal catalysed C−H activation followed by C−C bond formation is very efficient in terms of atom economy, and is therefore an extremely desirable transformation from the Green Chemistry point of view. In order to increase the effectiveness of this chemical synthesis many investigations have been directed towards catalytic C−H bond activation, mainly intramolecular[2], as intermolecular functionalization still remains challenging.[3-5] Determining the precise nature of a C−H activation step experimentally can be especially difficult due to the fact that the dividing line between the various mechanistic possibilities can be unclear.

Computational chemistry is ideally suited to provide insight into such mechanistic issues. Recently, improvements in methodology[6] and computer power have greatly widened the range of systems that can be studied and the nature of the problems that can be assessed.

This introduction will highlight the powerful synergy that the combination of experimental and computational study provides towards the understanding of the mechanisms of C−H activation[7] and the incorporation of this step into catalytic cycles. Unless otherwise stated, all the computational work cited in this introduction has been carried out using density functional theory (DFT).[6]

1.1. Development of C−H activation

Historically, the mechanisms describing C−H activation by organometallic complexes were considered to be: (I) oxidative addition (OA), (II) σ-bond metathesis (SBM) and; (III) electrophilic activation (EA). These three categories were classified depending on the nature of the metal centre, therefore electron-rich low-valence metals usually promote oxidative addition, early electrophilic transition metals undergo σ-bond metathesis and electron deficient late transition metals react through electrophilic activation. However, more recently the distinction depending on the metal centre involved is more blurred and a number of alternative processes have been described.

One of the first reported studies with a transition metal system capable of intermolecular oxidative addition of a single C−H bond activation was made by Bergman *et. al.*[8] and involved the photolysis of [Ir(η-Cp*)(PMe_3)(H_2)] in hydrocarbon solvents. As shown in Figure 1.1, the reaction proceeds via H_2 loss to form a very reactive Ir^I 16 electron metal intermediate. The C−H activation via an oxidative addition of the alkane proceeds via a 3-centered transition state which leads to an Ir^{III} hydrido-alkyl complex in a high yield at room temperature.

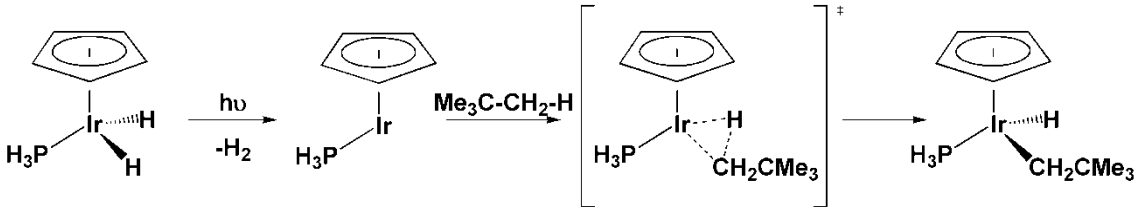

Figure 1.1 – C−H activation upon photolysis of [Ir(η-Cp*)(PMe_3)(H_2)].

Later, Watson and Parshall[9] reported in 1985 the first example of a σ-bond metathesis. The interchange observed is between [$Cp^*_2MCH_3$] (M = Y and Lu) and ^{13}C-labeled methane. The mechanism that they proposed followed a concerted 4-centered transition state, as shown in Figure 1.2.

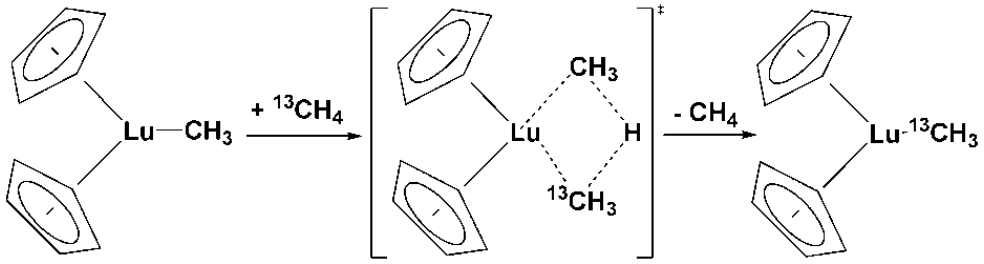

Figure 1.2 – Methyl exchange reaction of $Cp^*_2LuCH_3$ with $^{13}CH_4$ via a σ-bond metathesis mechanism.[9]

After these examples, Bergman[10] reported an Ir^{III} complex [Ir(η-Cp*)(PMe_3)(CH_3)(OTf)] (where OTf = OSO_2CF_3) which was able to promote facile C−H and Si−H bond activation. Their proposed mechanism is shown in Figure 1.3. The first step would be the ionization of [Ir(η-Cp*)(PMe_3)(CH_3)(OTf)] by elimination of OTf^- followed by C−H activation. However, in this case both σ-bond metathesis and oxidative addition were considered as in the latter case it was not clear whether an Ir(V) intermediate would be accessible.

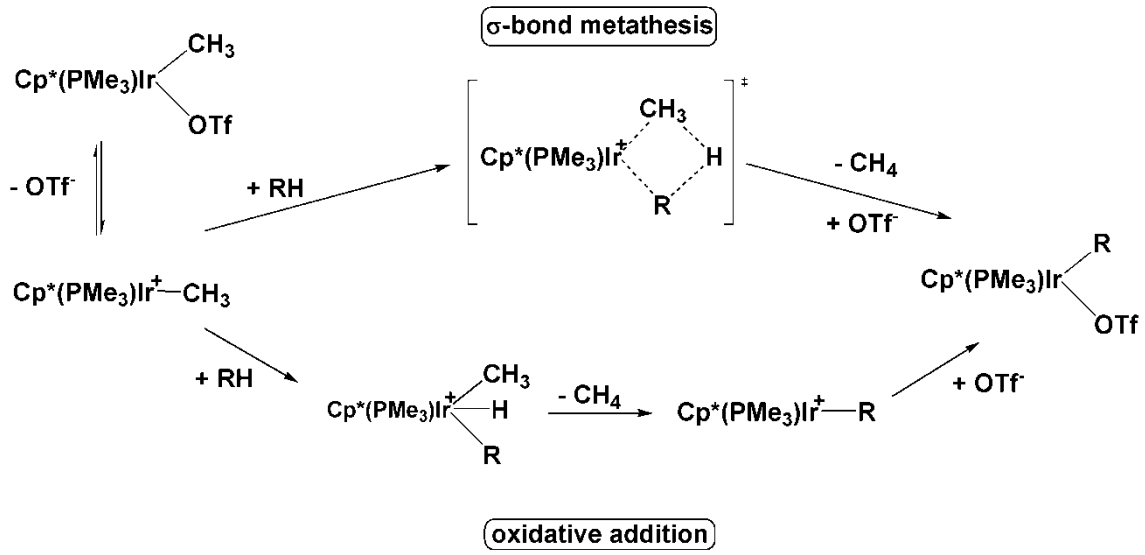

Figure 1.3 – Proposed mechanisms for C−H activation at $[Ir(\eta\text{-}Cp^*)(PMe_3)(CH_3)]^+$.[10]

Computational studies have provided more insight into such mechanistic issues. Calculations carried out by Strout *et. al.*[11] on the model complex $[Ir(\eta\text{-}Cp)(PH_3)(CH_3)]^+$ reacting with methane showed that the oxidative addition mechanism is the lower energy pathway. The activation energy required is only 11.5 kcal/mol and involves the initial formation of an agostic complex which was found to be 1 kcal/mol more stable that the separated reactants. All attempts to locate a σ-bond metathesis mechanism failed. Also, calculations on an analogous complex, $[Ir(\eta\text{-}Cp^*)(PMe_3)(CH_3)]^+$, by Niu and Hall[12] confirms the oxidative addition process to be the lower energy pathway. Experimentally, σ-bond metathesis leads to the same outcome as oxidative addition followed by reductive elimination thus, these two pathways are difficult to discern.

Computational methods have also been used to understand the factors that make σ-bond metathesis favourable. Ziegler *et. al.*[13] investigated the ability of $[Cp_2Sc{-}H]$ and $[Cp_2Sc{-}CH_3]$ to undergo σ-bond metathesis with the C−H bonds of methane, ethene and ethyne. The electronic barrier computed for the methyl exchange with $[Cp_2ScCH_3]$ complex is 10.8 kcal/mol, which correlates with the experimental process with Lu described above (11.7 kcal/mol). Lower barriers were computed for ethene (9.3 kcal/mol) and ethyne (3.4 kcal/mol). They therefore concluded that σ-bond metathesis is favoured as the {Sc···R···H···R'} core exhibits greater s character and lesser p character at the carbon atom included due to the directionality of the σ-bond being formed.

The most commonly observed examples of C−H bond activation by electrophilic activation occur with Pd(II), Rh(III) and Au(III). The most detailed experimental study of electrophilic activation appeared in 1985 by Ryabov *et. al.*[14] They reported a detailed mechanistic and kinetic study of activation of *N*,*N*-dimethylbenzylamine (dmba−H) by palladium acetate in chloroform solution, to give the cyclopalladated acetate-bridged dimer, $[Pd(OAc)(dmba)]_2$, as a final product (see Figure 1.4). Interestingly, this reaction occurs at room temperature. Based on H/D kinetic isotope effects and large negative entropy, Ryabov, suggested a highly ordered transition state similar to a Wheland intermediate. In this transition state, the approach of the metal towards the aryl group leads to the delocalization of a positive charge around the ring. A second effect is a stabilization of this transition state due to an interaction of the leaving hydrogen with the acetate. The electrophilic nature of the reaction was supported by a comparison of the rate of the cyclopalladation step for a series of *para*-substituted amines. Thus, electron-withdrawing substituents result in higher rates of reaction.

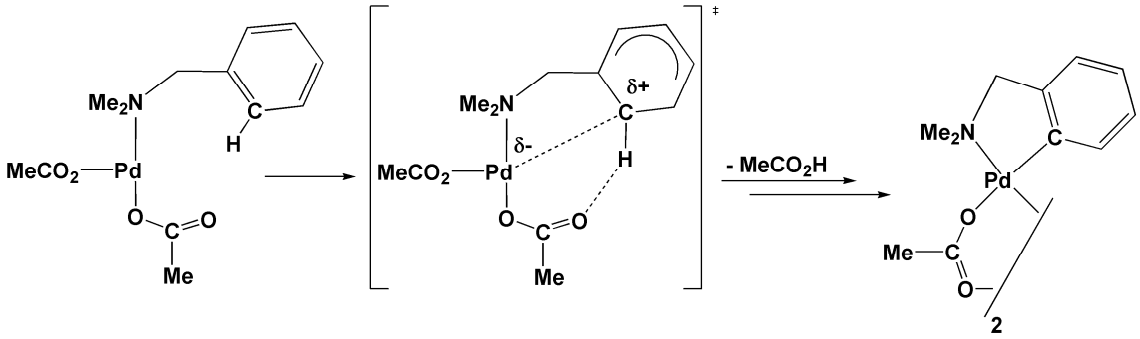

Figure 1.4 – Mechanism of cyclopalladation of dmba-H by $Pd(OAc)_2$.[12]

More recently, computational studies have provided some insight into this electrophilic activation mechanism and these will be described in detail in Section 1.2.

The above examples have described the classic C−H activation mechanisms. Now the focus will move to cases where the mechanistic choice is more ambiguous. Lin, Lau and Eisenstein[5] studied the C−H activation of methane by $[M(\eta\text{-Tp})(PH_3)(CH_3)]$ (M = Fe, Ru and Os; Tp = hydridotris(3,5-dimethylpyrazolyl)borate). As seen in Figure 1.5, the computed activation barriers increase depending on the nature of the metal centre, following the trend Os < Ru < Fe. When M = Os a typical two step mechanism via an Os^{IV} oxidative addition intermediate was computed. In the Fe system reaction occurs by a one step process in which the transition state features a very short Fe···H distance

(1.53 Å). Finally, the Ru system exhibits intermediate behaviour, as a very shallow Ru^{IV} intermediate was located. A structural study of each of the transition states concluded that the Fe system undergoes reaction via a transition state formed under oxidative addition. Therefore, transition states which feature short M···H contacts have been called by Lin as 'oxidatively-added transition state' (OATS).[15]

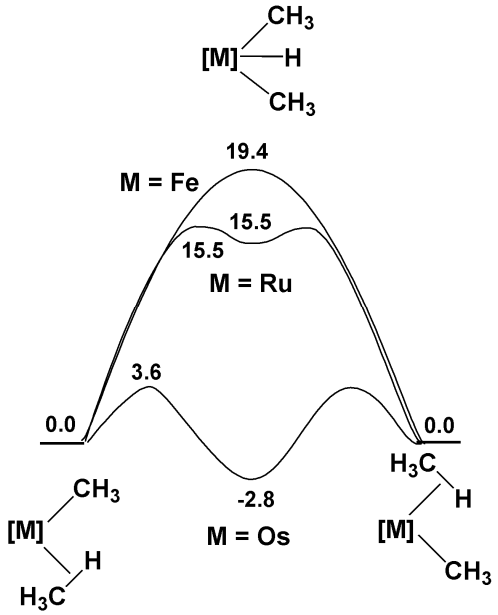

Figure 1.5 – Computed C−H activation energy profiles (kcal/mol) for species ($[M(\eta\text{-Tp})(PH_3)]$[16] where (M = Fe, Ru and Os; Tp = hydridotris(3,5-dimethylpyrazolyl)borate).[5]

Similar ideas emerged from the work of Goddard and Periana.[17] As part of a detailed computational study of the hydroarylation of ethene by benzene catalysed by the $[Ir(acac)Ph(H_2O)]$ complex, they considered C−H activation in the model intermediate $[Ir(acac')(\eta^2\text{-}C_6H_6)C_2H_4Ph]$ (see Figure 1.6). The transition state structure exhibits a seven coordinate Ir^V species and a short Ir−H bond (1.58 Å). In this case, the mechanism was named 'oxidative hydrogen migration' (OHM). Their suggestion is that by reducing the electron density in the Ir^{III} centre by electron donating ligands, the following C−H activation can change from an oxidative addition to an oxidative hydrogen migration mechanism.

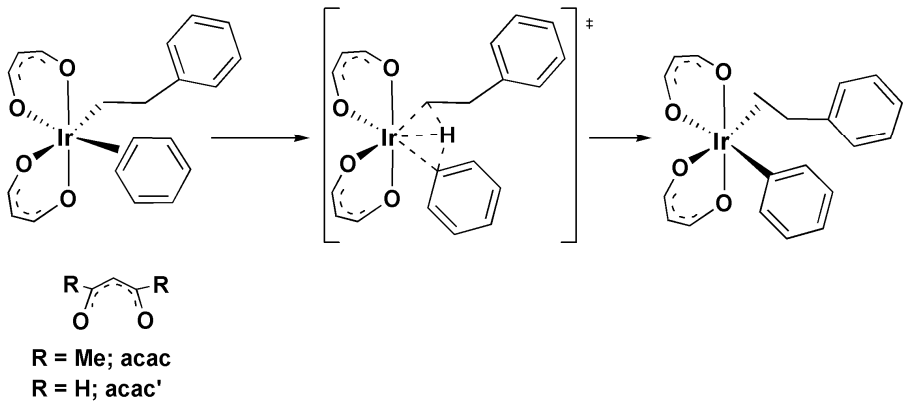

Figure 1. 6 – Mechanism of C−H activation in $[Ir(acac')(\eta^2\text{-}C_6H_6)C_2H_4Ph]$.[17]

The importance of the steric hindrance was observed by Bergman *et. al.*[18] in the computational study of C−H activation of methane by $[CpRe(CO)_2]$ and $[TpRe(CO)_2]$ (where Cp = C_5H_5 and Tp = tris(1-pyrazolyl)borate). Their results suggest that the seven coordinate product $[TpRe(CO)_2(H)(Me)]$ is not favorable as it suffers from closer intramolecular contacts, while the $[CpRe(CO)_2(H)(Me)]$ ligand affords a less crowded coordination sphere promotes an exothermic C−H activation via an oxidative addition intermediate.

Changes in the metal environment can be also generated by a prior coordination of a H−R ligand which acts as a two electron donor to the metal centre via a H−R σ bond. A detailed study by Perutz and Sabo-Etienne[19] based on the experimental observation of reactant and product σ-complexes lead to the proposal of σ-complex-assisted metathesis (σ-CAM). This idea allows σ-bond metathesis to be adapted for C−H activation of σ-complexes at late transition metals. Figure 1.7 shows the mechanism that describes dynamic rearrangement of σ-complexes. To date, this process has only been observed experimentally for silanes and boranes, however in principle this can be extended to hydrocarbon substrates.

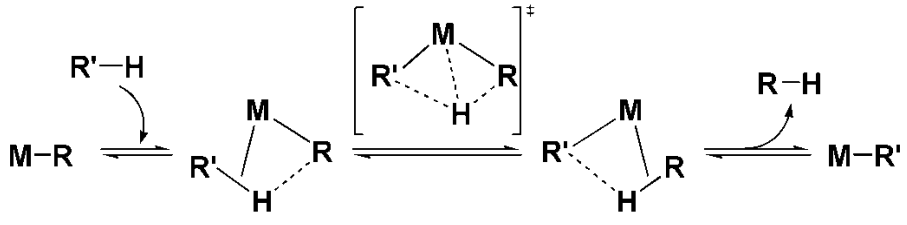

Figure 1.7 – σ-Complex-assisted metathesis. [19]

As described above, several of the groups active in the field have proposed a number of mechanistic interpretations of the mechanisms of C−H activation, mainly based on the geometry computed for the transition state. Hall[20] also described this mechanistic spectrum by an analysis of the reaction coordinate middle point using Bader's atoms in molecules (AIM) approach, which describes the bond critical points (BCP) and ring critical points (RCP) present in the system. Through this study, it was proposed that the mechanisms described above can be differentiated by variations in the position and number of BCP and RCP, and suggested the assignments depicted in Figure 1.8.

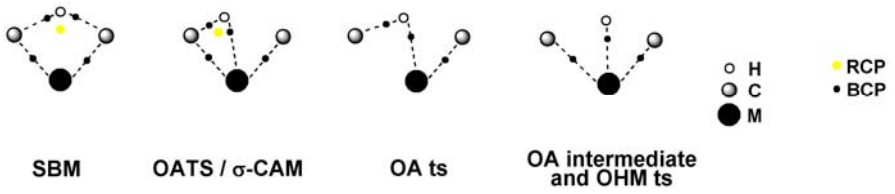

Figure 1.8 – Spectrum of mechanisms for C−H activation assigned via AIM analysis.[20]

1.2. C−H activation assisted by carboxylate or carbonate bases

Species that promote C−H activation that include carboxylates or carbonate in their structure have been studied broadly. One of the most common is palladium acetate, $[Pd(OAc)_2]$, where the acetate is thought to play an active role in the C−H activation step. Therefore, a number of computational studies oriented towards understanding the detailed mechanism involved in the C−H activation step have appeared in recent years and these will be the focus of this section.

The first computational study was carried out by Sakaki[21] and compared the C−H activation of benzene and methane by $[M(\eta^2\text{-}O_2CH)_2]$ (M = Pd and Pt). Both reaction profiles computed with $[Pd(\eta^2\text{-}O_2CH)_2]$ are depicted in Figure 1.9. In the case of benzene, from a van der Waals complex at -2.3 kcal/mol, a partial dissociation of one oxygen lead to an η^2-benzene intermediate that features a short H···O contact. These interactions lead to an extra stabilization of 9.8 kcal/mol in the η^2-benzene intermediate and the following C−H cleavage requires an activation energy of 16.1 kcal/mol. Interestingly, methane intermediates are different and feature a weaker C−H···M σ-interaction which leads to a much higher intermediate. The following proton transfer is the rate limiting step of the process with an overall energy barrier of 20.2 kcal/mol. Additional studies with $[M(PH_3)_2]$ (M = Pd and Pt) showed that C−H activation goes

through an oxidative addition mechanism with high energy barriers (for $Pd(PH_3)_2$: $\Delta E^{\ddagger}(CH_4)$ = 34.0 kcal/mol and $\Delta E^{\ddagger}(C_6H_6)$ = 22.7 kcal/mol). Overall these processes are much more difficult than for [$Pd(\eta^2\text{-}O_2CH)_2$] since the free oxygen of the η^1-O_2CH ligand facilitates a less constrained 6-membered transition state. A comparison between the energies of the final products also highlights the high strength of the O−H bond versus the M−H bond ($Pd(PH_3)_2$: $\Delta E(CH_4)$ = 31.5 kcal/mol and $\Delta E(C_6H_6)$ = 22.1 kcal/mol).

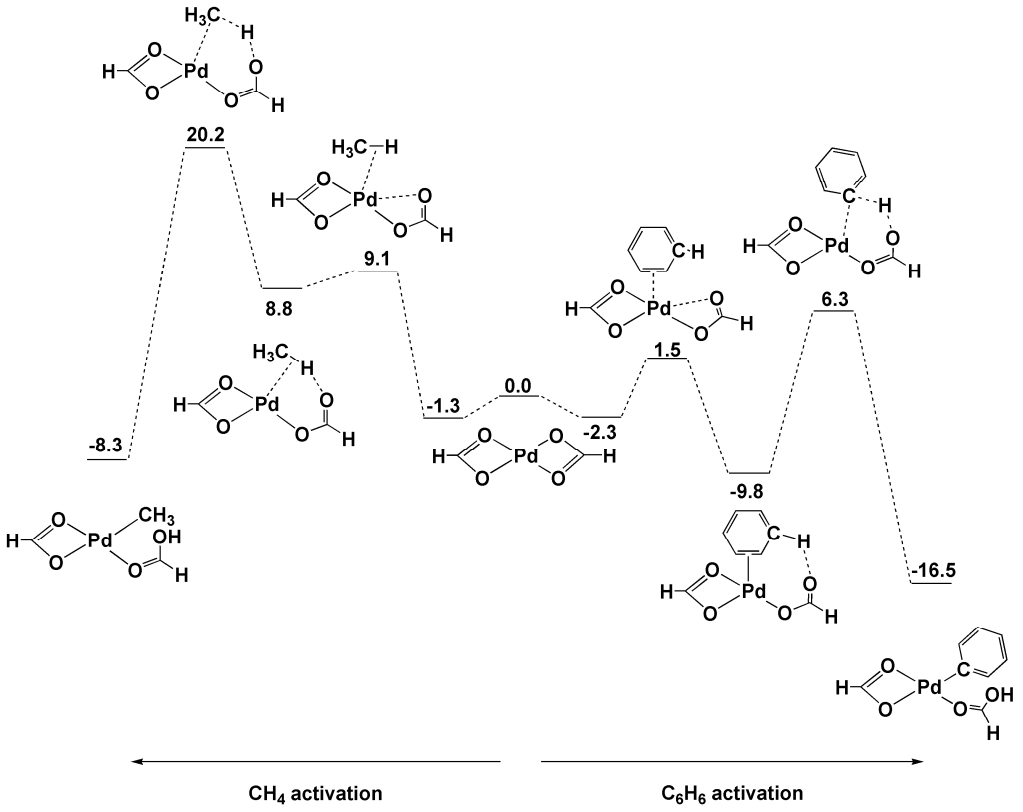

Figure 1.9 – C−H bond activation of benzene and methane by [$Pd(\eta^2\text{-}O_2CH)_2$].[21]

Acetate assisted C−H activation is also an important mechanism in cyclometallation reactions. Macgregor *et al.*[22] computed the mechanism of cyclometallation of dimethylbenzylamine (dmba−H) by [$Pd(OAc)_2$] studied experimentally by Ryabov and co-workers[14] (see Section 1.1). The C−H activation step was modelled via three possible transition states, a 6-membered acetate-assisted process, where the proton is transferred to the outer oxygen of acetate, a 4-membered process via a transfer to the inner oxygen and oxidative addition, all of which are shown in Figure 1.10. The C−H cleavage via an acetate-assisted 6-membered transition state was the most favourable, with an energy barrier of 11.1 kcal/mol. The other two processes were shown to have

very high computed barriers of 34.3 kcal/mol and 25.7 kcal/mol for the 4-membered and oxidative addition mechanisms, respectively. The 4-membered transition state exhibits a geometry that resembles a σ-bond metathesis, although in this case a strongly polarised M−O bond helps the hydrogen transfer. This process is therefore similar to a 1,2-addition and this type of reaction will be discussed in more detail in Section 1.3.

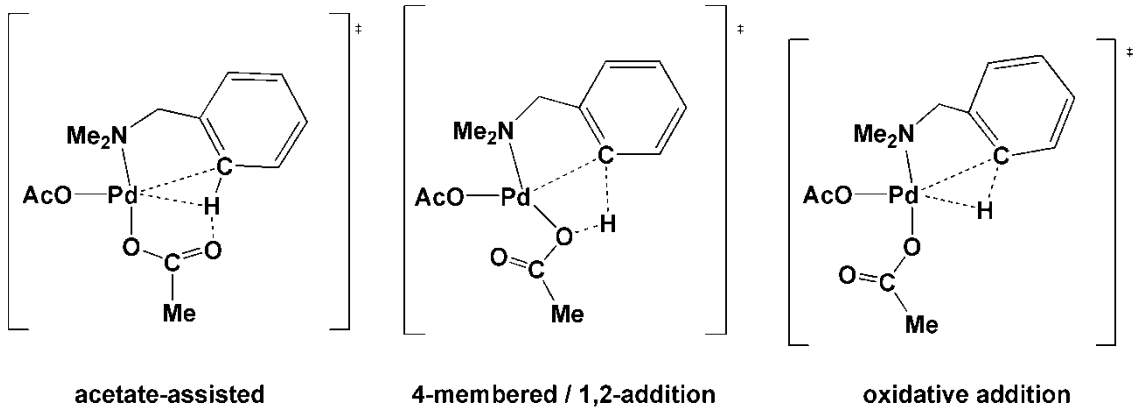

Figure 1.10 – Suggested transition states for the C−H activation of dmba-H by $[Pd(OAc)_2]$.[22]

The details of the cyclometallation reaction via a 6-membered transition state are shown in Figure 1.11. In contrast to the mechanism proposed by Ryabov, the reaction proceeds via an C−H agostic intermediate **2a** rather than the generally assumed Wheland structure proposed by Ryabov[14] (see Figure 1.4). The first step is initiated from [Pd(κ^2-OAc)(κ^1-OAc)(dmba−H)] by the displacement of one arm of the κ^2-acetate by the approach of the ortho C−H bond, which leads to an agostic intermediate **2a**. The second step describes a H−transfer via a 6-membered transition state, which involves the C−H bond of the aryl moiety, the metal and the free oxygen arm of the acetate ligand. In **2a** the agostic C−H bond exhibits enhanced acidity and this facilitates a hydrogen bonding interaction with the displaced arm of the acetate (C−H···O=C = 2.04 Å) which helps to stabilize the intermediate. Therefore, **2a** is ideally set up for the following proton transfer which occurs via a minimal activation barrier. Overall, it is the formation of the agostic intermediate that is the rate determining step and the key stage of the process.

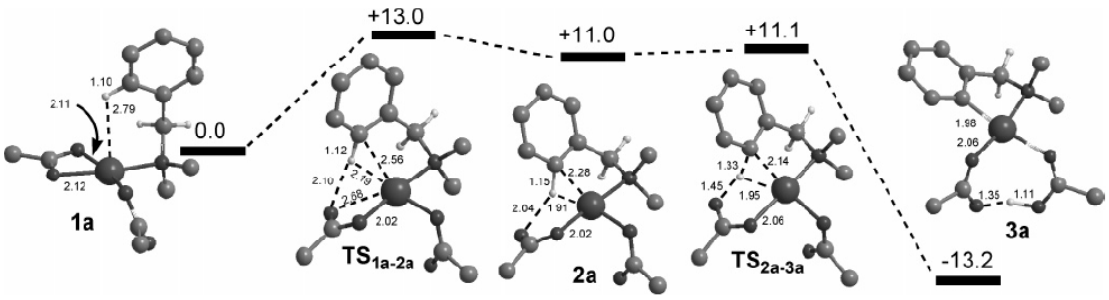

Figure 1.11 - Computed reaction profile (kcal/mol) and key distances (Å) for the cyclometallation of dmba-H by $Pd(OAc)_2$ via a 6-membered C−H activation transition state. Methyl and non-participating phenyl hydrogens are omitted for clarity.[22]

A similar mechanism, also with $[Pd(OAc)_2]$, was reported by Lledós[23, 24] for the selective cyclopalladation of $R_3P{=}NCH_2Ar$ iminophosphoranes. A detailed assessment of the thermodynamic and kinetic stability between the endo and exo products was given. The energy profile found for the exo cyclometalation (Figure 1.12) exhibited exactly the same mechanism described above (Figure 1.11), with an agostic intermediate (**5**) again being located.

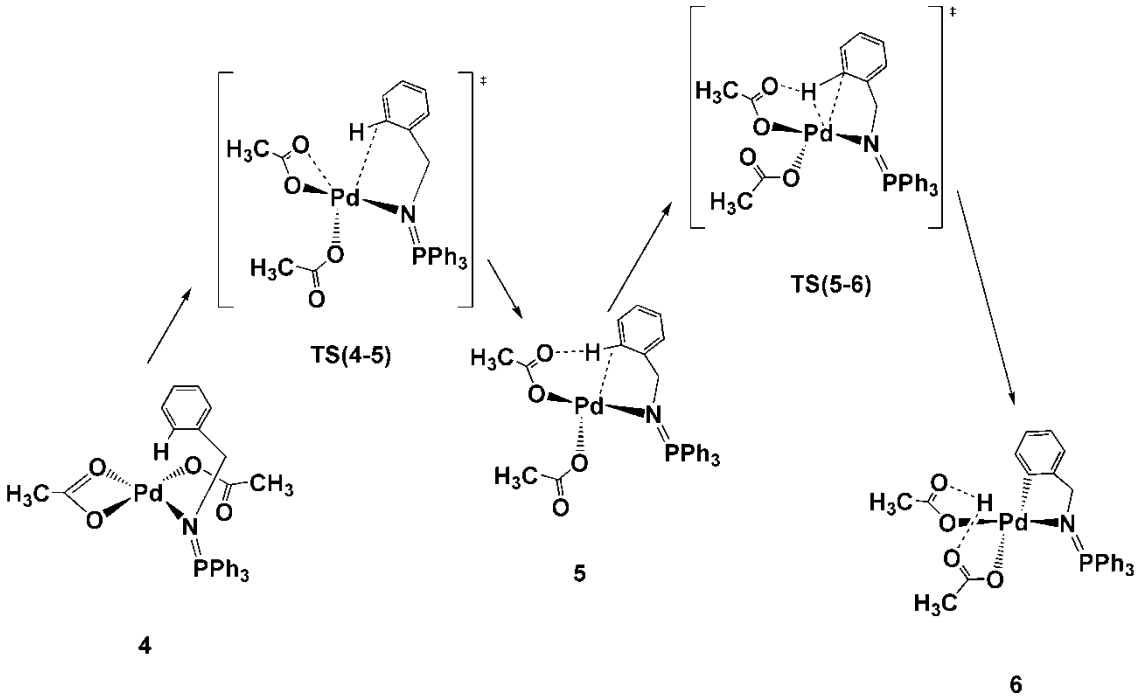

Figure 1.12 – Mechanism for the exo metalation of $Ph_3P{=}NCH_2Ph$ by $[Pd(OAc)_2]$.[23]

Experimental studies by Davies and co-workers[25] showed that dmba−H would react with $[IrCl_2Cp^*]_2$ in presence of sodium acetate under mild conditions to form [Ir(η-Cp*)(dmba)Cl] as the final cyclometallated product. This product was not observed

when another base such as triethylamine was used instead of acetate. The combination of sodium acetate and $[IrCl_2Cp^*]_2$ also results in the cyclometallation of imines and similar reactivity is seen with $[RhCl_2Cp^*]_2$ and $[RuCl_2(p\text{-cymene})]_2$.

Based on these experimental results, Macgregor *et al*[26] reported a computational study of this cyclometallation reaction focusing on the mechanism involved in the C−H activation step (Figure 1.13). The model system considered was $[Ir(\eta\text{-Cp})(\kappa^2\text{-OAc})(dmba{-}H)]^+$ (**7**). The lowest pathway involves a 6-membered transition state, **TS(7-9)**, with an activation barrier of 16.0 kcal/mol, similar to the value found with $[Pd(OAc)_2(dmba{-}H)]$. The 1,2 addition and oxidative addition pathways are higher in energy (**TS(8-10)** = 22.8 and **TS(8-11)**= 30.7 kcal/mol, respectively) and follow the same pattern as seen for the palladium system as a κ^2-κ^1 displacement (**8**) is required before the following C−H activation.

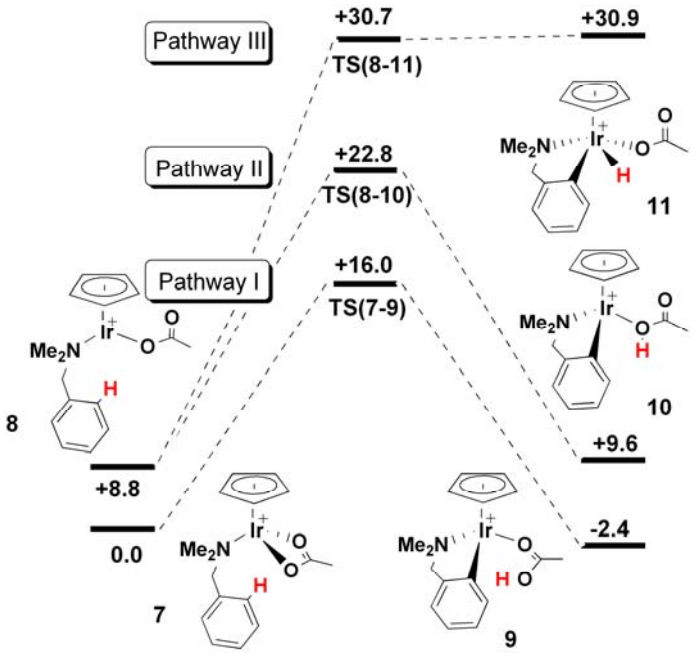

Figure 1.13 - Computed reaction profiles (kcal/mol) for C−H activation in $[Ir(\eta\text{-Cp})(dmba\text{-}H)(\kappa^2\text{-OAc})]^+$.[26]

A comparison between the key distances in the three C−H activation transition states is shown in Figure 1.14. The degree of availability of the acetate is the key in all three pathways. Along Pathway I, **TS(7-9)** exhibits short contacts between the hydrogen and the free arm of the acetate. Indeed, this transition state bears a resemblance to the κ^1-intermediate **2a** computed with $[Pd(OAc)_2]$ system. In Pathway II a rotation around the

Ir−O_1 bond permits the hydrogen to be transferred to the metal-bound oxygen, via **TS(8-10)**. For Pathway III, the free oxygen is twisted away from the hydrogen and the metal must become fully involved for the success of the C−H activation process (**TS(8-11)**). Further calculations with Cp* instead of Cp did not result on any significant change in the reaction energies.

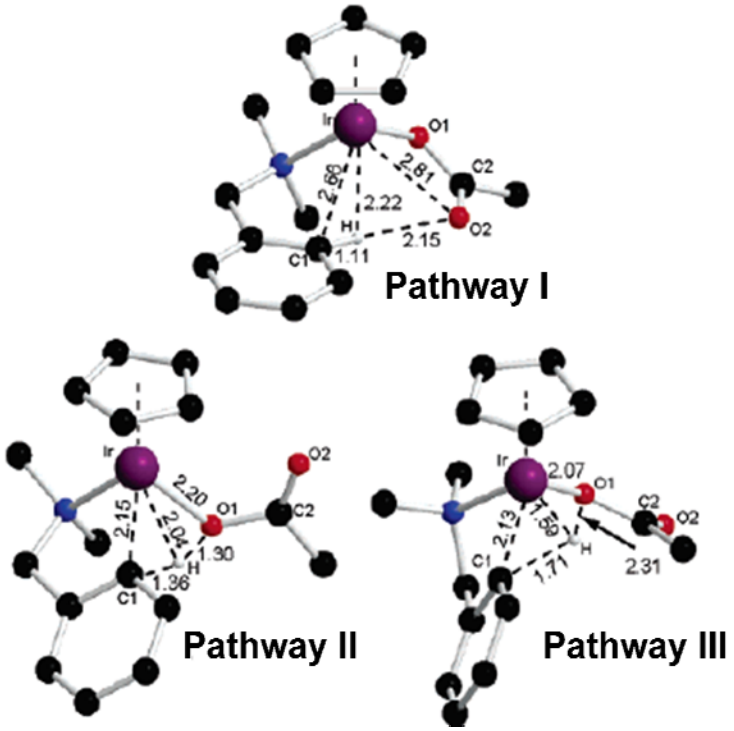

Figure 1.14 - Computed C−H activation transition states (Å) along Pathways I-III. Non participating H atoms are omitted for clarity.[26]

These studies on the $[Pd(OAc)_2(dmba\text{-}H)]$ and $[Ir(\eta\text{-}Cp)(dmba\text{-}H)(\kappa^2\text{-}OAc)]^+$ systems have highlighted the important roles played by both the metal and the acetate in the C−H activation process. For this reason the transition states have been described as displaying ambiphilic character. This behaviour is also apparent in comparing the C−H and N−H bond activation reactions of $[Ir(\eta\text{-}Cp)(NH{=}CH{-}NC_4H_4)(\kappa^2\text{-}OAc)]^+$ computed by Davies and Macgregor.[27] In the transition states, the more acidic nature of the N−H bond leads to a greater H-bonding interaction with acetate, but less metal involvement, while for C−H activation the metal is more prominent and the H-bonding contribution less significant. Overall, C−H activation was computed to be only 6.4 kcal/mol greater. This underlines the high potential of such ambiphilic character to facilitate easy bond activation processes.

Similar ambiphilic bounding character was observed by Goddard and Periana[28] in the intermolecular C−H activation of benzene and methane by [Ir(acac′)$_2$(X)] complexes (X = CH_3COO and OH). Again an acetate-assisted deprotonation via a 6-membered transition state was computed as the lowest energy process in both cases.

Maseras and Echavarren[29] have observed similar behaviour in intramolecular arylation promoted by [Pd(OAc)$_2$] (Figure 1.15). Interestingly, results were satisfactory only when an excess of K_2CO_3 is present in the reaction, whereas Et_3N or DBU (1,8-diazabycycloundec-7-ene) led to unchanged starting material.

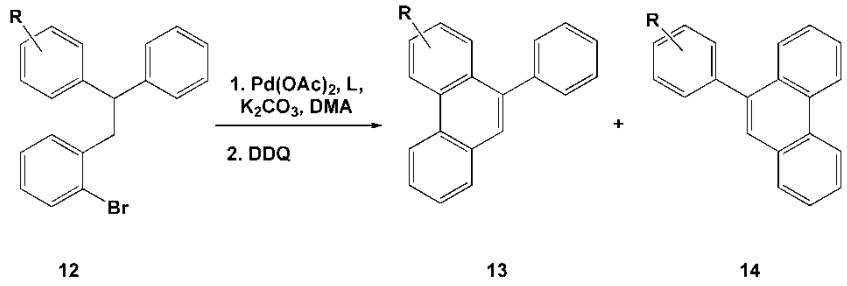

Figure 1.15 – Pd-catayzed intramolecular arylation.[29]

The computational study started from the model species **16** (see Figure 1.16) which can be viewed as being formed via C-Br oxidative addition of the substrate to give **15**, followed substitution of Br^- by an intramolecular base, HCO_3^-. The energy barrier for the C−H activation is as low as 23.5 kcal/mol, consistent with the experimental temperature of 100-135 ºC, and occurs via a 6-membered transition state. They named this process as 'proton abstraction mechanism' analogous to the acetate-assisted C−H bond activation, although in this process a bicarbonate instead of an acetate is bound to the metal.

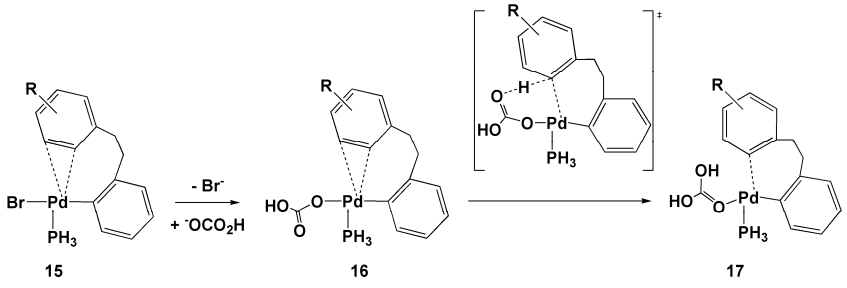

Figure 1.16 – Mechanism computed for the formation of a palladacycle via a 6-membered transition state using [Pd(PH$_3$)(κ^1-OCO$_2$H)(*o*-(CH$_2$)$_2$-C$_6$H$_4$R)Ph)] (R = H) as model system.[29]

Echavarren and Maseras[30] reported a more wide ranging study of the mechanism a year later. In this case, special attention was paid to the substituents on the aromatic ring to probe their directing effect. Using [Pd(PH_3)Br(*o*-((CH_2)$_2$-C_6H_4R)Ph)], **15**, as a model system, three possible pathways were considered (Figure 1.17). The highest energy barrier is computed for the unassisted path, where proton transfer occurs onto Br. This correlates with the dependence on the nature of the base observed experimentally. The activation barriers found for the two assisted pathways are 17.4 kcal/mol for the intermolecular assisted route and 23.5 kcal/mol for the intramolecular mechanism. However, changing the R group from CH_3 to CF_3 inverts this pattern (14.4 kcal/mol *vs.* 13.2 kcal/mol, for inter- *vs.* intra-molecular). Thus, both mechanisms can be operative and the preference for one over another may depend on the substrate.

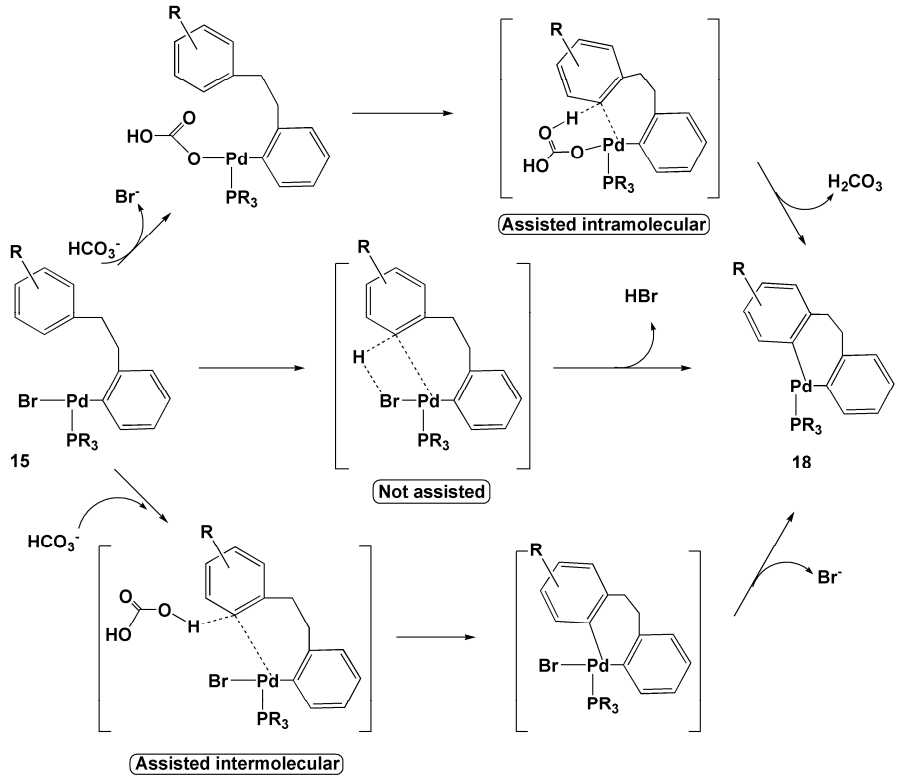

Figure 1.17 – Three possible mechanisms proposed for the formation of a palladacyle.[30]

Similar behaviour for the activation of sp^3 C−H bonds by [Pd(OAc)$_2$] was reported by Fagnou *et. al.*[31] The Pd-catalyzed alkylation reactions of aryl bromides and chlorides featuring *o*-ether substituents lead to the formation of dihydrobenzofurans in good yields (Figure 1.18). Greater reactivity was observed by the combination of a carbonate base, such as Cs_2CO_3, and a carboxylate base such as $^tBuCO_2H$. In addition, a

preferential reactivity of methyl groups over other secondary sp^3 C−H bonds at the same proximity is observed.

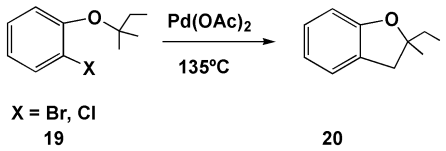

Figure 1.18 – Pd-catalyzed alkylation reaction of aryl bromides and chlorides to form benzofurans.[31]

In order to understand the parameters leading to high yield and selectivity this reaction was examined computationally. The three transition states corresponding to concerted cyclopalladation-deprotonation are shown in Figure 1.19. **TS-A** corresponds to the lowest energy pathway and describes the formation of the palladacycle via a 6-membered transition state by activation of a primary C−H bond. The reaction barrier at the secondary carbon was found to be higher by 5.5 kcal/mol and similarly, the reaction to the more remote CH_3 is also less favourable, possibly as it would lead to a 6-membered ring in the product. Their results directly correlate with the experimental observations.

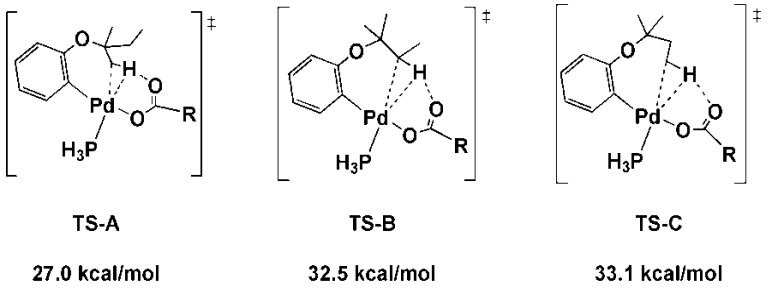

Figure 1.19 – Three possible C−H activation transition states accounting for site selectivity in the formation of palladacycles.[31]

Baudoin and Clot[32] also studied the C−H activation of sp^3 carbons for the synthesis of benzocyclobutanes as shown in Figure 1.20. The use of K_2CO_3 as a base and bulky phosphines as co-ligands was shown to be crucial for the reaction to proceed. Computational studies showed that a bulky phosphine is required for the formation of a κ^1-coordination of the base which reacts via a base-assisted transition state to form the palladacycle. The following C−C bond formation leads to the final benzocyclobutane.

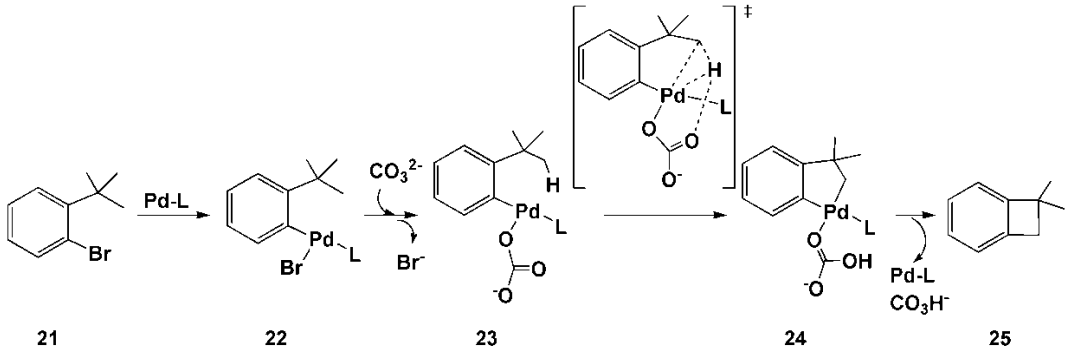

Figure 1.20 – Proposed base-assisted mechanism for the synthesis of benzocyclobutane by Pd-L (L = P^tBu_3) with K_2CO_3 as a base.[32]

1.3. C−H activation at M−X bonds (X = O and N): 1, 2 addition

Many of the reactions described above can be viewed as a proton transfer. Therefore, the idea that a more polarized accepting M−X bond could facilitate such reactions would be a logical suggestion. Thus, different groups have directed their efforts towards the study of the C−H activation via M−X bonds (where X = anionic N or O-based ligands) which could lead to the development of routes for hydrocarbon functionalization. Such processes have been described as 1,2 addition reactions.

The first examples for a 1,2-addition of C−H bonds to an M−X (X = O and N) single bond were described by Gunnoe and Cundari[33] and Periana and Goddard.[34] Gunnoe *et al.*[33] reported the C−H activation of d^6-benzene by [RuTp(PMe_3)$_2$(OH)] at 80 ºC. This results in a H/D exchange at the hydroxide ligand to form [RuTp(PMe_3)$_2$(OD)]. In addition, this system catalyses H/D exchange between H_2O and C_6D_6 at 100 ºC to produce C_6DH_5. Their proposed mechanism is shown in Figure 1.21 and involves initial ligand dissociation of PMe_3 from **26**, followed by benzene coordination to give the η^2-intermediate **28** (ΔG = +11.2 kcal/mol). The C−H activation step features a 4-membered transition state where the C−H bond adds across the Ru−OH bond to allow the proton transfer. This step requires an energy barrier of 17.6 kcal/mol relative to **28**.

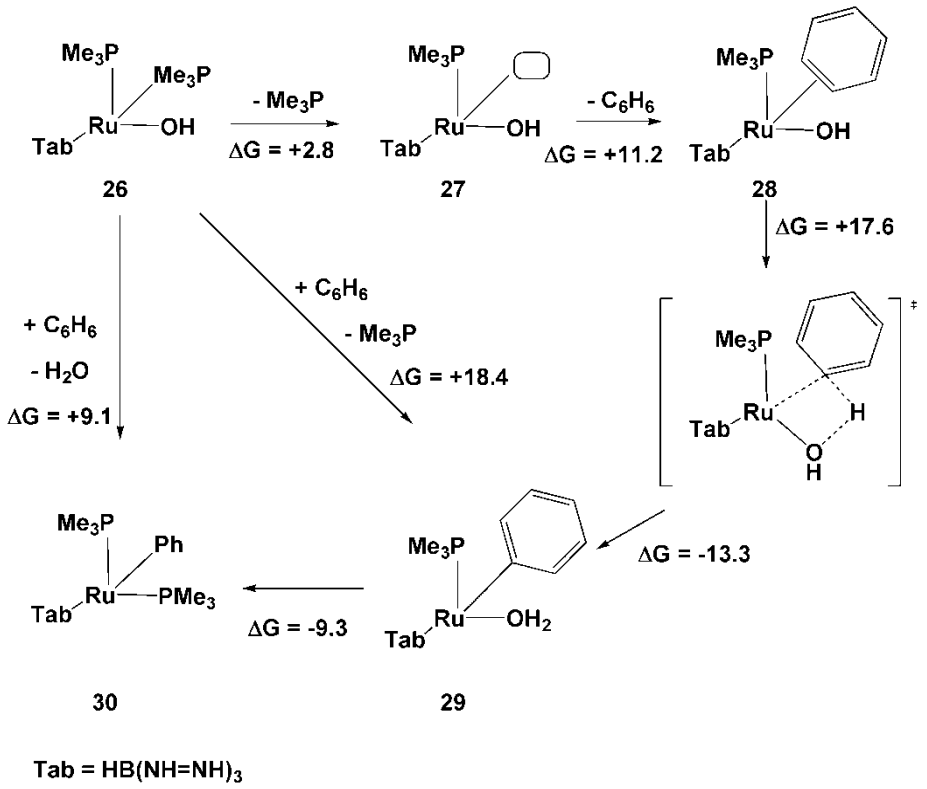

Figure 1.21 – Proposed mechanism for the C−H activation of C_6D_6 by $[Ru(Tab)(PMe_3)_2(OH)]$ (Tab = tris(azo)borate). Energies in kcal/mol.[33]

Gunnoe and Cundari[35] broadened their research to complexes of type $[RuTp(PMe_3)_2X]$ where X = OH, OPh, Me, Ph or NHPh and observed that systems with ligands, X, without a lone pair (X = Me and Ph) exhibit slower 1,2-addition than those with heteroatom-based ligands (X = OH, OPh and NHPh). Overall, they concluded that C−H activation mediated by the combination of a late transition metal centre in a low oxidation state and a heteroatom-based ligand will proceed by low energy barriers.

Similar C−H activation at an iridium-methoxo complex was reported by Periana and Goddard.[34] The reaction of benzene with $[Ir(acac)_2(OMe)L]$ (L = MeOH, pyridine) at 160 ºC for 10 minutes led to the formation of $[Ir(acac)_2(Py)Ph]$ in a 75% yield. Calculations on the C−H activation step located a 4-membered transition state and this was interpreted in terms of a σ-bond metathesis process. This structure, however, closely resembles the previously reported 1,2-addition transition state of Gunnoe and Cundari (see Figure 1.22).

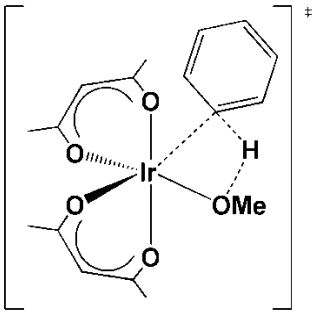

Figure 1.22 – Computed transition state for the C−H activation of benzene by $[Ir(acac)_2(OMe)]$.[34]

In addition, Goddard *et al.*[36] also carried out a mechanistic analysis of the above reaction on the basis of orbital changes and predicted reactivity. The orbital analysis of the transition state shows that the forming O−H bond is not based on the same orbital as the breaking O−Ir bond, as the orbital used by the oxygen is the lone pair. As the reaction evolves there is a charge reorganization, especially in the hydrogen which becomes more acidic in the transition state. Both features show that the mechanism is not a traditional σ-bond metathesis, instead they denote this mechanism to be an internal electrophilic substitution (IES).

Previously, the three main categories in promoting C−H activation were divided depending on the nature of the reacting metal. Nowadays, these categories have changed and expanded as the insight provided into mechanistic issues by computational techniques allowed a better understanding of the process. Indeed, the literature highlights several systems that can react via different mechanisms that are very close in energy.[37] Thus, computational studies need to consider all possible pathways and, if possible, seek agreement with experimental data to define the lowest energy route.

In recent years, the development of base-assisted C−H activation by carboxylate or carbonate bases has been broadly reported in the literature, aiming at the synthesis of new catalysts. Interestingly, a key feature of these systems is the ambiphilic character of the C−H activation transition state in which both the metal centre and the base are involved.

1.4. Catalytic C−H activation and functionalization

The real challenge in organometallic chemistry is the integration of the C−H activation processes described above into a full catalytic cycle. Indeed such a process would achieve the conversion of cheap and abundant hydrocarbons into valuable functionalized chemical compounds. In addition, on the basis of the understanding of the mechanism, computational chemistry also aims to develop new catalysts that operate at low temperatures with high yields.

The following will describe the implementation of C−H activation into successful catalytic cycles, first of all from a historical perspective, and then with some more recent developments.

1.4.1. Shilov Chemistry

Over 40 years ago, Shilov and co-workers[38] reported the remarkable reactivity of alkanes with $[PtCl_4]^{2-}$ and $[PtCl_6]^{2-}$ salts shown in Figure 1.23. This reaction was catalytic in Pt^{II} but required Pt^{IV} as an oxidant, and the oxidation step was shown to be the rate-limiting step of the process. The unprecedented transformation of an alkane to an alcohol had a great impact because it demonstrated that transition metal complexes in solution were capable of mediating such an important reaction.

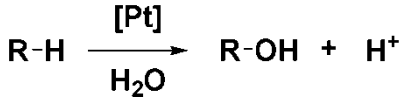

Figure 1.23 – General equation for the Shilov reaction.

Using model systems several groups have carried out computational mechanistic investigations in order to provide more insight into the mechanism, especially focussing on the C−H activation step (see Figure 1.24). Oxidative addition, σ-bond metathesis and electrophilic activation mechanisms have all been proposed, depending on the ligands present in the complex.

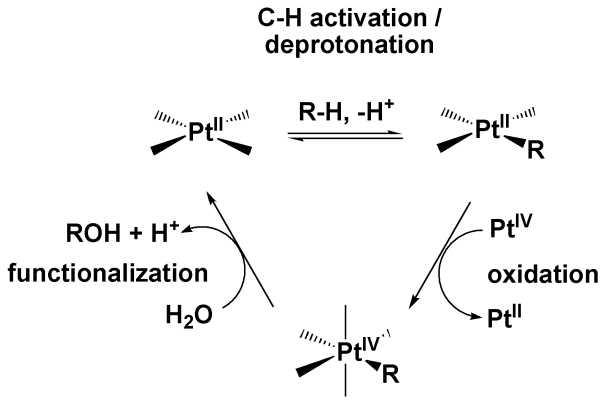

Figure 1.24 – General catalytic cycle for the 'Shilov system'.[38]

In 1996 Siegbahn and Crabtree[39] modelled the reaction of methane with *trans*-$[PtCl_2(H_2O)_2]$ in water. Their proposed mechanism starts with the substitution of a water ligand by methane followed by C−H activation via what they termed a σ-bond metathesis transition state, where the hydrogen is transferred to a *cis*-chloride (see Figure 1.25 (**I**)). The inclusion of a H-bonded water molecule was found to be important in order to obtain reasonable energy barriers. In addition, an oxidative addition/reductive elimination mechanism was also found to be competitive.

Periana *et. al.*[40] reported the conversion of methane to methanol by reaction with $[(NH_3)_2PtCl_2]$ and $[(bpym)PtCl_2]$ (bpym = η^2-(2,2′-bipyrimidyl)) as catalysts. Although in both cases the yields are relatively poor, the bpym system does provides better selectivity, although it still requires high temperatures (over 150 ºC). Computational studies by Goddard *et. al.*[41] on these systems showed they exhibited different behaviours. $[(NH_3)_2PtCl_2]$ undergoes oxidative addition (Figure 1.25 (**II**)) while $[(bpym)PtCl_2]$ promotes C−H activation via electrophilic activation (Figure 1.25 (**III**)).

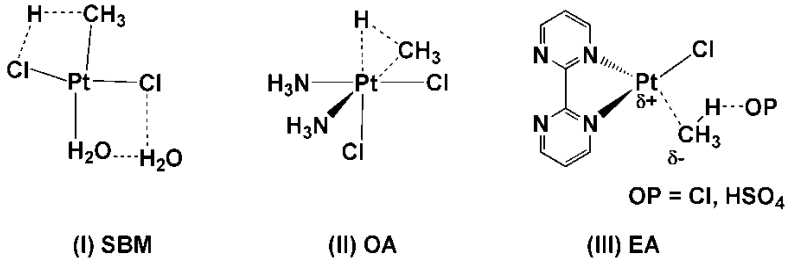

Figure 1.25 – Comparison between the three transition state computed for the C−H activation of methane by (I) $[PtCl_2(H_2O)_2]$ via an SBM, (II) $[(NH_3)_2PtCl_2]$ via OA and (III) $[bpymPtCl_2]$ by EA.[40]

The systems described above are only a small part of the overall research effort on Pt^{II}/Pt^{IV} systems. In general this work has shown that small changes in the catalyst (e.g.

via variation in the ligands) can lead to a specific behaviour that directly affects the mechanism involved in the C−H activation step.

1.4.2. The Murai reaction

The Murai[42] reaction is one of the most successful examples of catalytic functionalization of an aromatic C−H bond. It describes the functionalization of a C−H bond at the ortho position in aromatic ketones by a $[Ru(H)_2(CO)(PPh_3)_3]$ catalyst under reflux conditions in toluene solution, as shown in Figure 1.26. Other complexes such as $[Ru(CO)_2(PPh_3)_3]$ and $[Ru(CO)_3(PPh_3)_2]$ are also effective catalysts and a range of ketones and aldehydes are able to insert a variety of olefins. The scope of this reaction is therefore very broad.

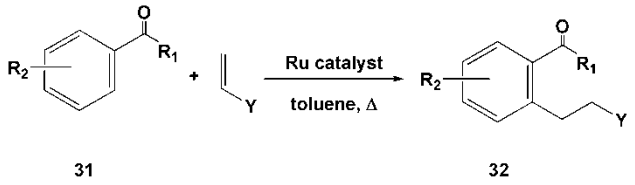

Figure 1.26 – General scheme for the Murai reaction.[42]

A detailed computational study by Morokuma and co-workers[43] investigated the mechanism of the entire catalytic cycle. The reaction starts by modelling of catalytically-active species $[Ru(CO)(PH_3)_2]$, **33**. The most favourable pathway is shown in Figure 1.27 and involves initial addition of benzaldehyde on to **33** to give $[Ru(O,\kappa^1\text{-}O{=}CHPh)(CO)(PH_3)_2]$, **34**, by the coordination of the oxygen to the metal centre. Complex **34** is more stable than the separated reactants by 25.9 kcal/mol. The C−H activation is a two-step oxidative addition process and passes through an agostic intermediate, **35**, in which one ortho-C−H bond is in close proximity to the metal centre. This first step requires an activation energy of only 3.3 kcal/mol. The following C−H cleavage has an activation energy of 2.8 kcal/mol, leading onto the formation of the cyclometallated $[Ru(O,C,\kappa^2\text{-}O{=}CPh)(H)(CO)(PH_3)_2]$ complex, **36**. **36** is 11 kcal/mol more stable than **34**. The subsequent ethene insertion reaction requires the substitution of the labile phosphine trans to the Ru−C bond to achieve the required cis geometry. Alkene insertion into the Ru−H bond then occurs with a barrier of 11 kcal/mol to give **38**. The high energy of complex **38** is a result of creating a new Ru−alkyl bond trans to the already existing Ru−aryl bond. Isomerisation then occurs to give the more stable *cis*-geometry (**39**, E = -35.5 kcal/mol) which allows coordination of PH_3 to the vacant

site (**40**, E = -55.1 kcal/mol). The subsequent C−C bond formation via a reductive elimination, has the highest activation energy computed ($\Delta E^{\ddagger}$ = 27.0 kcal/mol) and is therefore shown to be the rate-limiting step, in agreement with the experimental observations.

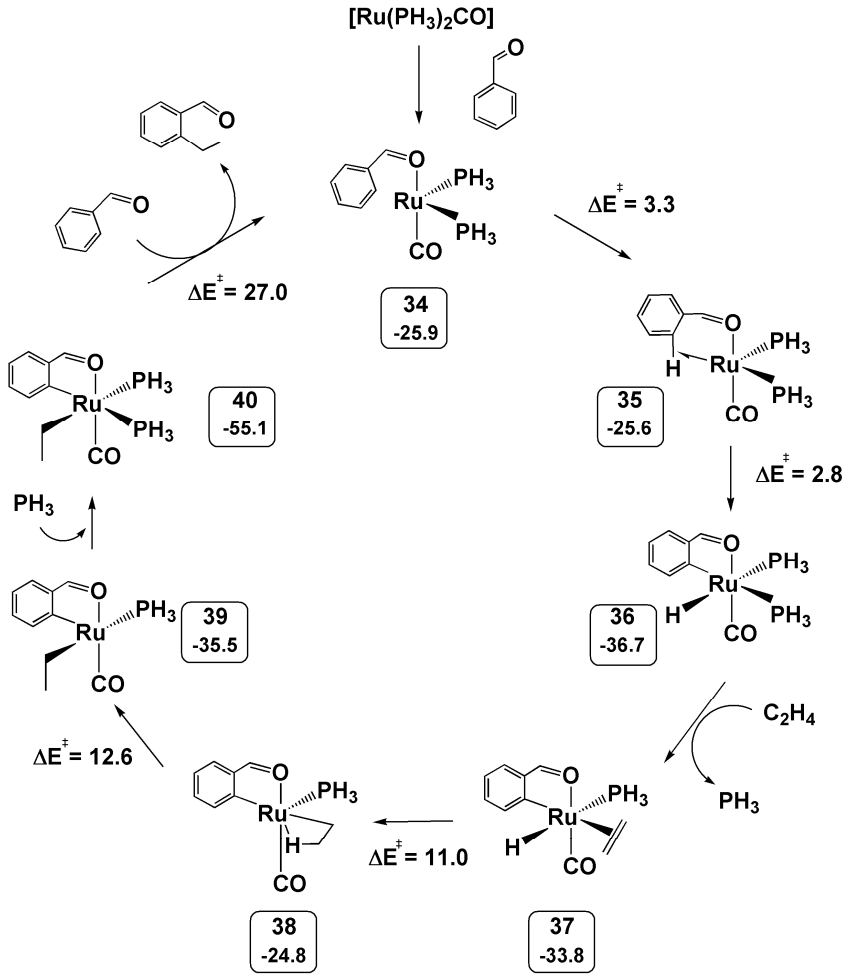

Figure 1.27 – Computed catalytic cycle for the insertion of ethene in the ortho C−H bond of benzaldehyde, catalysed by [Ru(CO)(PH_3)$_2$], **33**. Activation energies in kcal/mol.[43]

1.4.3. Alkane dehydrogenation

One of the most detailed computational studies of alkane dehydrogenation was carried out by Krogh-Jespersen and Goldman[44] on the reaction of a pincer dihydrido Ir^{III} complex, (PCP)Ir(H)$_2$ (PCP = η^3-$C_6H_3(CH_2PR_2)_2$-1,3 (R = ^{t}Bu, ^{i}Pr)) with various alkanes. Their focus was on the nature of the mechanism, which can be associative or dissociative, as shown in Figure 1.28. The dissociative process (**D**) proposes initial reductive elimination of H_2 to afford the three-coordinate 14-electron complex **42**, followed by oxidative C−H cleavage to give **44**. The associative process (**A**) would

involve initial hydrocarbon oxidative addition to form seven coordinate **43** which reductively eliminates H_2 to produce the 16–electron Ir(III) alkyl-hydride complex. The energy barrier for the associative process is much lower than the barrier computed for the dissociative process ($\Delta H^{\ddagger}_A$ = 15.0 kcal/mol *cf.* $\Delta H^{\ddagger}_D$ = 25.0 kcal/mol). However, the computed Gibbs free energies are swapped ($\Delta G^{\ddagger}_A$ = 28.3 kcal/mol *cf.* $\Delta G^{\ddagger}_D$ = 24.9 kcal/mol). Extrapolating the high temperatures, bulkier phosphines and alkenes used experimentally suggests that the dehydrogenation of alkanes is easier via a dissociative process.

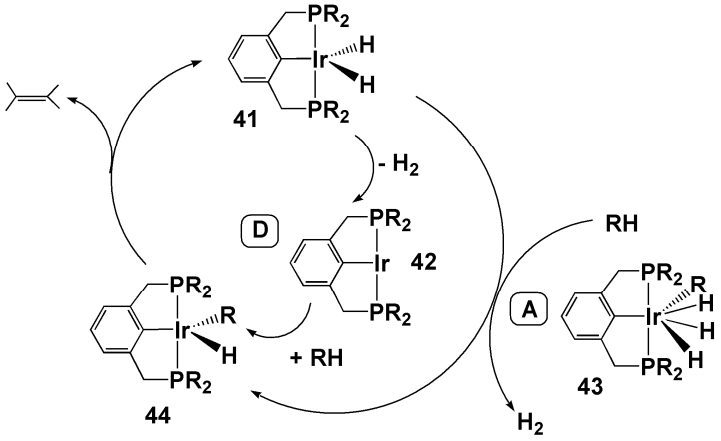

Figure 1.28 – Catalytic cycle for the alkane dehydrogenation with a (PCP)Ir(H)$_2$ catalyst via an associative (A) or dissociative (D) pathway.[44]

1.4.4. Borylation of alkanes

The borylation of alkanes follows the general scheme shown in Figure 1.29. It begins with the substitution of one ligand, L, in a precursor complex, **45**, by an alkane to generate **46**. C−H activation then occurs to generate σ-borane complex **47**, which then undergoes rotation to give **48**. C−B bond formation then gives the borylated product.

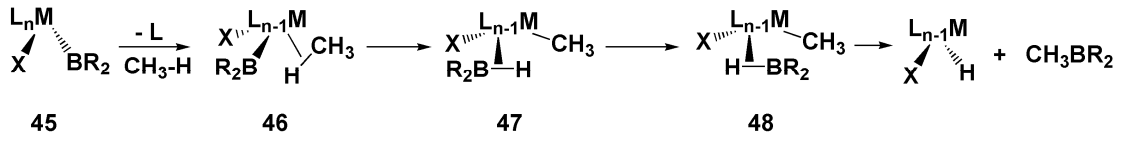

Figure 1.29 - General scheme for the borylation of alkanes.

The C−H activation step has been studied by Hartwig and Hall[45] for $CpM(CO)_{n+1}B(OCH_2)_2$, (M = Fe, n = 1; M = Mo, n = 2) and a σ-bond metathesis mechanism was computed. A local orbital analysis, also supported by a charge analysis, showed that the unoccupied boron p orbital plays an important role in the C−H

bond activation mechanism, as shown in Figure 1.30. The empty orbital of the boron accepts electron density from the metal centre which can then be used to attack the proton. This is also supported by the transfer of the electron pair from the R−H bond to the new M−C bond. Hall named this process boron-assisted σ-bond metathesis.

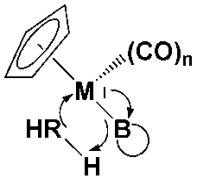

Figure 1.30 – Scheme for the transition state of the hydrogen transfer from the alkyl group to the boron.[45]

This work was followed by a combined experimental/computational study on rhodium boryl complexes, $[Cp^*Rh(H)_2(Bpin)_2]$ and $[Cp^*Rh(H)(Bpin)_3]$, with methane. These systems showed catalytic activity with C−H activation proceeding in a similar fashion to that described above.[3]

1.4.5. Hydroarylation of alkenes

In a series of papers, Periana and Goddard[16, 17, 46] studied in detail the mechanism of homogenous Ir^{III} catalyzed hydroarylation of alkenes with $[Ir(acac)_2(Ph)(H_2O)]$ as the catalyst.[47]

The computed mechanism for the hydroarylation of ethene was studied with the model catalyst $[Ir(acac')_2(Ph)(H_2O)]$ (**49**) and is shown in Figure 1.31.[17] Through the dissociation of the water ligand (ΔH = +11.9 kcal/mol) a 5-coordinated 16 electron species, $[Ir(acac)_2(Ph)]$, is located. This complex must then rearrange from a trans to a cis geometry in order to allow the coordination of ethene cis to the phenyl ligand to form $[Ir(acac)_2(Ph)(\eta^2\text{-}C_2H_4)]$ (**50**, ΔH = -9.4 kcal/mol). This isomerization requires an activation barrier of $\Delta H^{\ddagger}$ = 35.1 kcal/mol and $\Delta G^{\ddagger}$ = 26.1 kcal/mol, in good agreement with the free energy of activation determined experimentally (-28.7 kcal/mol). The catalytic cycle then starts from **50** with a migratory insertion process to form complex $[Ir(acac)_2(C_2H_4Ph)]$ (**51**) via a 4-membered transition state with an activation energy of $\Delta H^{\ddagger}$ = 27.0 kcal/mol. Complex **51** features an agostic interaction with one ortho C−H bond of the phenyl group. The rotation of this ligand away from the metal to give **52** (15.7 kcal/mol) creates a vacant site that allows the coordination of a benzene molecule to give **53** (4.6 kcal/mol). The final C−H activation step proceeds via an oxygen

hydrogen migration transition state to give **54** with an activation energy of 12.0 kcal/mol. To complete the catalytic cycle, complex **54** dissociates ethyl benzene (uphill by 2.9 kcal/mol) and coordinates a new ethene molecule (ΔH = -19.2 kcal/mol). The limiting step of the process is the alkene insertion ($\Delta H^{\ddagger}$ = 27.0 kcal/mol).

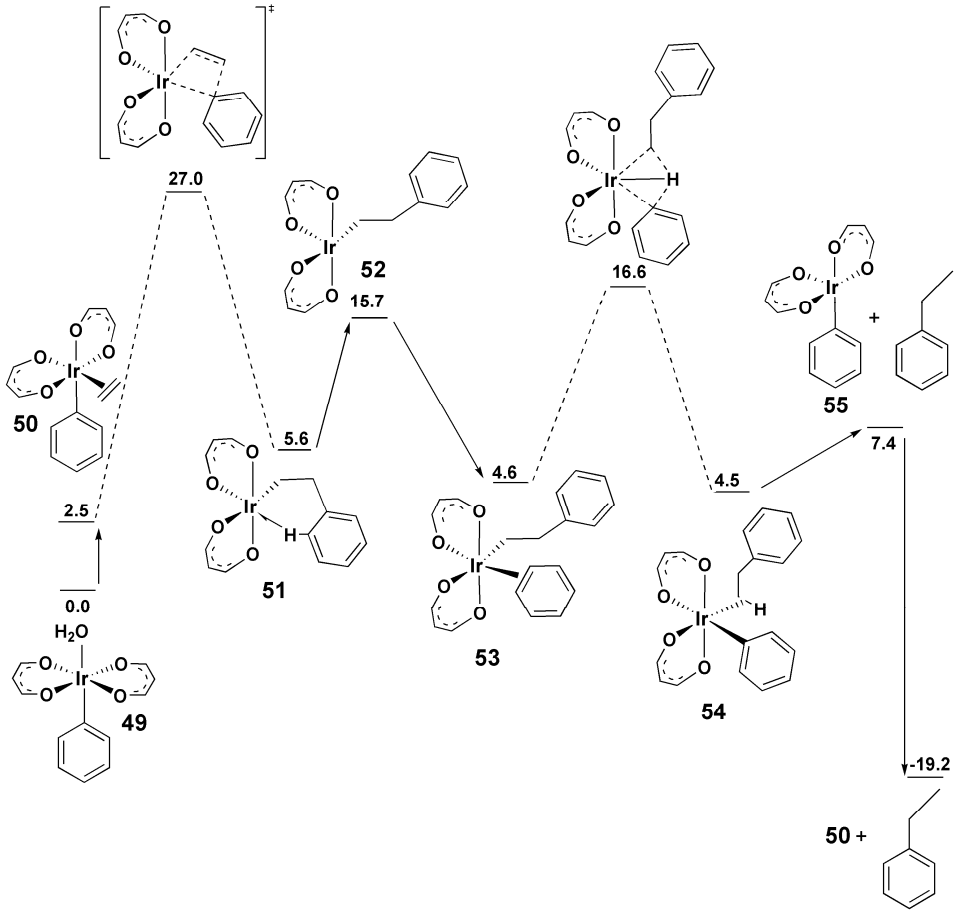

Figure 1.31 – Computed energy profile for the hydroarylation of ethene catalyzed by [Ir(acac′)$_2$(Ph)(H_2O)] (**49**, acac′ = $H_3C_3O_2$) . Energies (kcal/mol) are reported relative to free ethene and **49**.[17]

The authors also studied possible side reactions from structure **51**. β-H elimination and inhibition of the catalyst by binding a second molecule of ethene were assessed. β-H transfer to form [Ir(acac)$_2$(C_2H_3Ph)(H)] was found to be more favorable than the benzene coordination (Figure 1.32). However, the activation energy required for elimination of styrene is slightly higher than that computed for the insertion of ethene ($\Delta H_{elimination}$ = 28.5 kcal/mol *cf.* $\Delta H_{insertion}$ = 27.0 kcal/mol). Thus, the β-H transfer step is facile, but reversible.

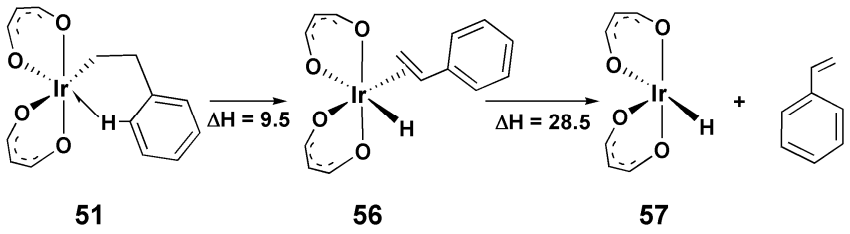

Figure 1.32 – Computed reaction for the β−H elimination from [Ir(acac′)(C_2H_3Ph)], **51**.[17]

The addition of an ethene molecule to **52** is also significantly more favorable than the formation of **53** (Figure 1.33). The ethene complex **58** can follow two pathways, double insertion to form **59** or C−H activation which leads to a vinyl complex and ethylbenzene. The barriers associated with these process make them competitive with ethane insertion (**58** → **59**, $\Delta E^{\ddagger}$ = 17.2 kcal/mol; **58** → **60**, $\Delta E^{\ddagger}$ = 15.2 kcal/mol). The relative rates of formation of **59** and **60** should therefore be proportional to the ratio of the ethene to benzene concentrations.

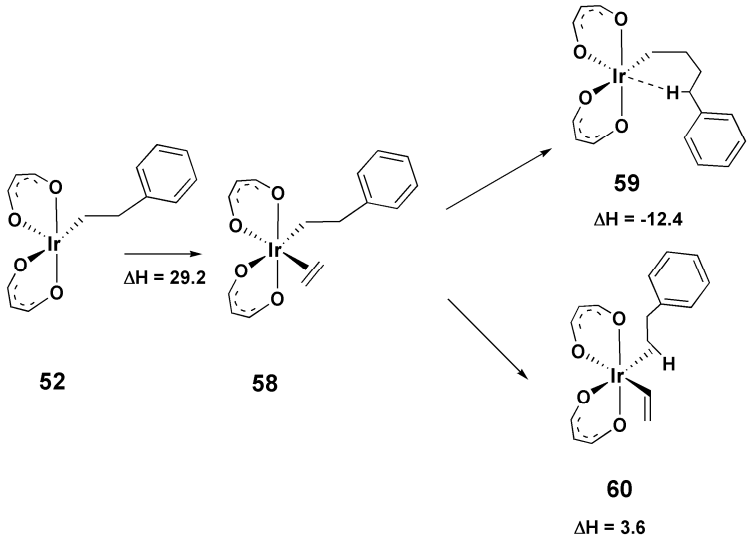

Figure 1.33 - Computed sides reactions of [Ir(acac′)(C_2H_4Ph)], **52**, with ethene.[17]

Another system which catalyzes the hydroarylation of alkenes is the [RuTp(CO)(NCMe)(Ph)] catalyst reported by Gunnoe and co-workers.[48] The system shows moderate selectivity for ethylbenzene over isopropylbenzene with a 1.6:1.0 ratio. In order to understand the mechanism, Goddard[49] carried out a computational study of the full catalytic cycle of this system (Figure 1.34). Alkene insertion (**62→63**) is again the limiting step of the process and requires an activation energy of 21.1 kcal/mol. The following C−H activation step (**65→66**) features a transition state via an oxidative hydrogen migration and requires an activation barrier of 18.0 kcal/mol. The

regeneration of the catalyst **62** is exothermic, as is the overall reaction (ΔH = -18.0 kcal/mol).

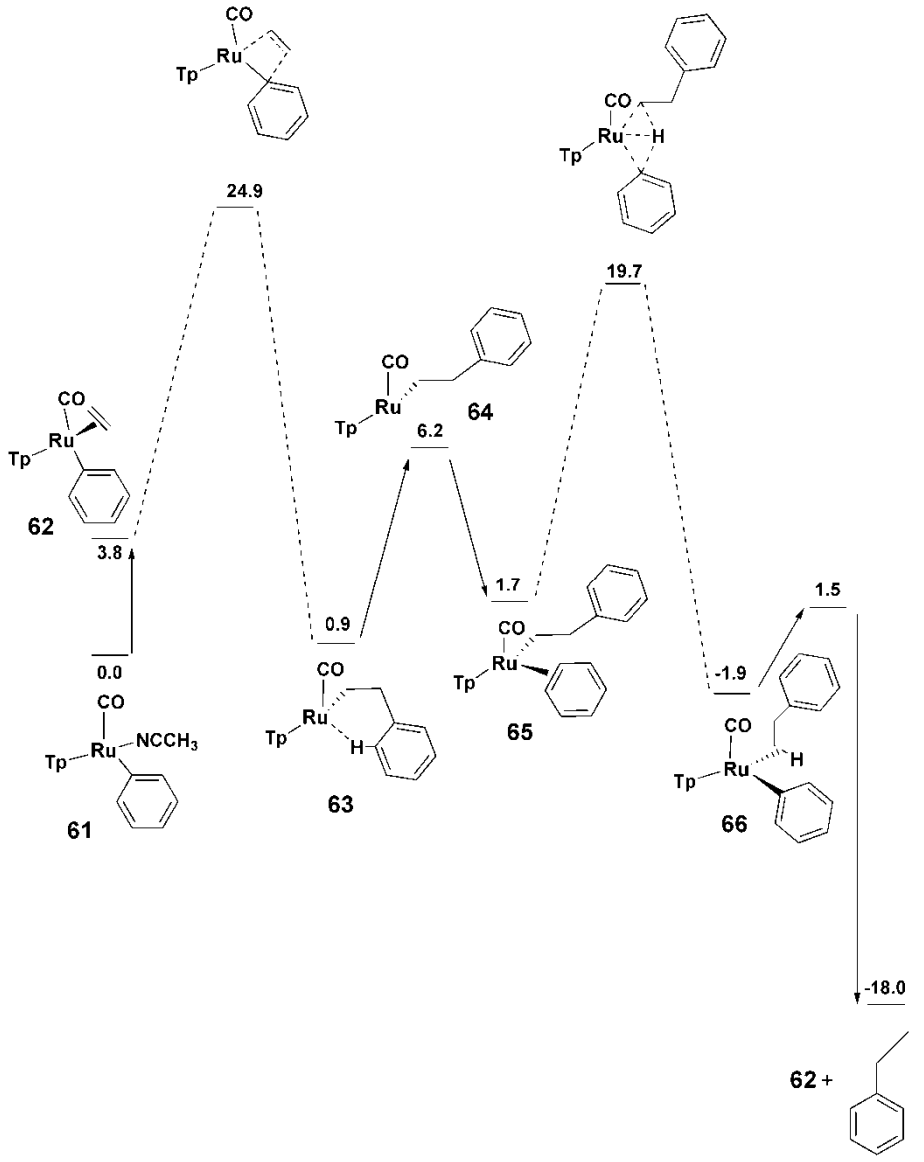

Figure 1.34 - Computed energy profile (ΔH) for the hydroarylation of ethene catalyzed by [RuTp(CO)(NCMe)(Ph)]. Energies (kcal/mol) reported relative to ethylene and the acetonitrile complex.[48]

Recently, Gunnoe and Cundari[50] reported a detailed study focused on the nature of the *para*-C−H activation step of [RuTp(CO)(Me)(C_6H_5X)] and [RuTp(PMe_3)(Me)(C_6H_5X)] (X = CN, H, NH_2, NO_2, Br, Cl, F or OCH_3). Their approach was based on the transition state geometries and a computational Hammett analysis. Structural observations lead to longer Ru−H bond distances for electron donating substituents. The Gibbs free energy of activation for C−H bond cleavage allows the calculation of the rate constants and the construction of Hammett plots (Figure 1.35). The positive δ values of 2.6 (L = CO) and

3.2 (L = PMe_3) are larger than those found in typical reactions that undergo σ-bond metathesis.

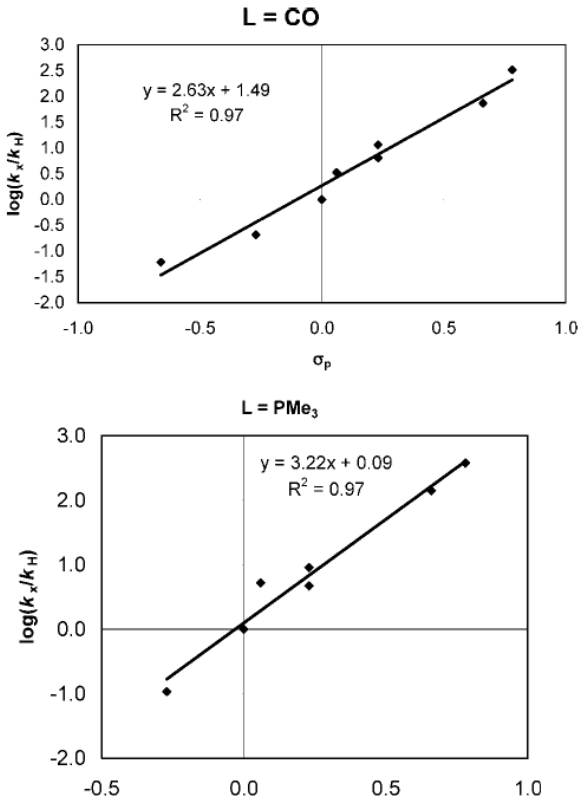

Figure 1.35 – Hammett plots calculated for the *para*-C−H activation step of [RuTp(CO)(C_6H_5X)] and [RuTp(PMe_3)(Me)(C_6H_5X)] systems (X = CN, H, NH_2, NO_2, Br, Cl, F or OCH_3).[50]

As Figure 1.36 shows, their description of the C−H activation step is a Ru-mediated process, where the metal center coordinates the C−H bond and activates it toward an intramolecular proton transfer, analogous to a C−H activation via 1,2-addition across Ru−X (X = OH or NHPh).

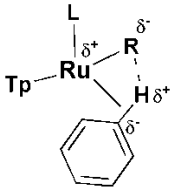

Figure 1.36 – Model for C−H activation in [RuTp(PMe_3)(Me)(C_6H_5X)] systems.[50]

Overall, the mechanism for catalytic hydroarylation in this ruthenium species is very similar to that of the Ir(acac′)$_2$ systems. The ruthenium system follows a lower energy pathway in all steps except for the C−H activation. The rate determining step is in both

cases the alkene insertion and is 3.7 kcal/mol lower in the ruthenium species (Ru: ΔE = 21.1 kcal/mol; Ir: ΔE = 24.8 kcal/mol) and correlates with the rate enhancement of 200 at 90 ºC observed experimentally. Moreover, the C−H activation is higher in energy for ruthenium systems. Goddard has therefore suggested that the opposing trends in these two key points of the catalytic cycle may involve a balancing act.

Therefore, a detailed mechanistic analysis by Periana and Goddard[4] has been carried out to investigate the generality of this trend. They elected to study Rh, Pd, Os and Pt with the $\{(acac')_2\}$ ligand set and also Rh and Os with the {Tp(CO)} ligand set. Figure 1.37 shows a correlation between the computed ΔH of the C−H activation and the alkene insertion step. This extended previous observations where the two steps are inversely correlated complicating the optimization of the catalytic process. The C−H activation step proceeds via an oxidative hydrogen migration transition state in all cases except for the two Os^{II} compounds where an Os^{IV} oxidative addition intermediate was located.

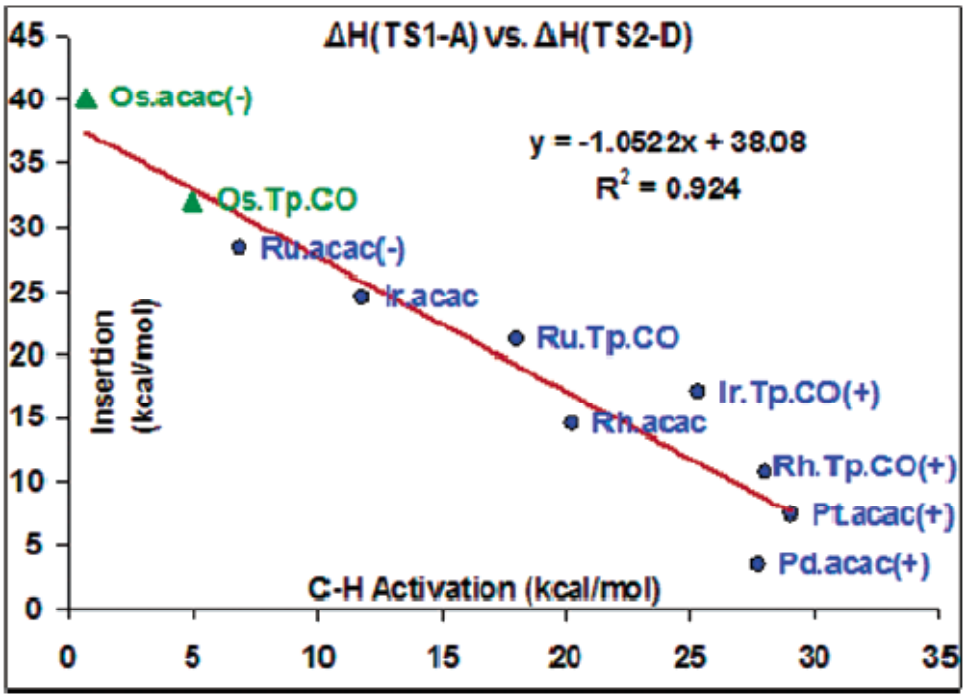

Figure 1.37 – The correlation of the activation energy for insertion versus the activation energy for C−H activation. The linear trend fits the points with a correlation of $R^2 = 0.924$.[4]

1.4.6. Arene functionalization via a base-assisted mechanism

All the systems described so far perform C−H activation via oxidative hydrogen migration or oxidative addition transition states. As described in previous sections, catalysts able to promote C−H activation via an inter- or intra-molecular base have been a promising alternative that could be incorporated into schemes for the functionalisation of arenes. However, almost all the computational studies on systems that achieve catalytic conversion have been focused on understanding the details of the C−H activation step and no studies of the overall catalytic cycle have been performed. In this context, the contributions of Echavarren and Maseras,[30] Fagnou[31] and Baudoin and Clot[32] in the area of Pd-catalysed organic synthesis have been discussed in Section 1.2.

However, one particularly important development was the catalytic intermolecular arylation reaction of electron-deficient benzenes, reported by Fagnou in 2006.[51] Figure 1.38 shows the reaction of 4-bromotoluene with pentafluorobenzene in the presence of K_2CO_3 with [$Pd(OAc)_2$] leading to a 98% yield of the cross-coupled arylation product.

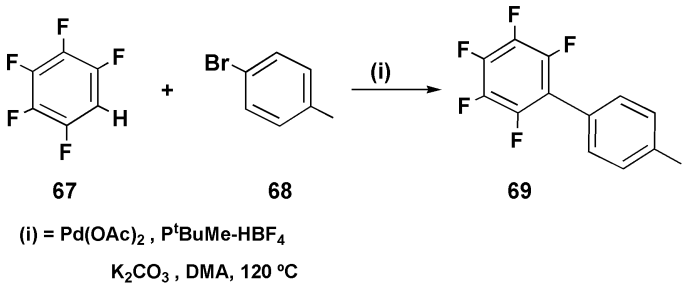

Figure 1.38 – Reaction scheme for the catalytic intermolecular arylation of pentafluorobenzene by $Pd(OAc)_2$.[51]

Experimentally, they showed that more electron deficient arenes react preferentially, which is a complete reversal in reactivity in comparison with classical electrophilic aromatic mechanism. Several mechanisms were explored for C−H activation: oxidative addition of the arene C−H bond to the palladium centre and electrophilic aromatic substitution could not be located as well as both inter- or intra-molecular acetates-assisted processes. The lowest energy pathway showed that the reaction was computed by an exchange of the bromide ligand with the bicarbonate base at the metal centre which facilitates C−H activation via an base-assisted transition state shown in Figure 1.39.

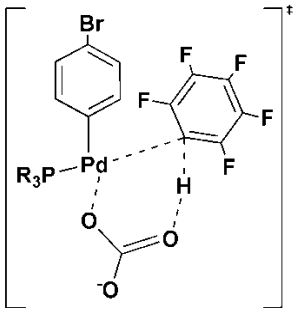

Figure 1.39 – Transition state computed for the C−H activation step of the arylation reaction of pentafluorobenzene by $Pd(OAc)_2$.[51]

1.5. Summary and overall aims

Great progress has been seen over the last decade focusing especially on gaining insight into the processes by which C−H bonds are activated by transition metals complexes. The increasingly common use of computational techniques in collaboration with experimentalists has provided a deeper understanding, in particular in the field of C−H activation. Thus, more in-depth mechanistic studies have highlighted subtleties in previously generalised processes, leading to a large catalogue of mechanistic possibilities. This powerful synergy has facilitated the synthesis of new catalysts where C−H activation can be exploited. Heteroatom-assisted C−H activation is especially important as the ambiphilic character observed between the metal, the inter- or intra-molecular base and the C−H bond to be activated leads to an easier C−H activation step and, as a consequence, milder reaction conditions.

This thesis will describe the results of DFT calculations on C−H activation reactions at Ir, Rh and Ru metal centres. In Chapter 2, the importance of the intramolecular base in the cyclometallation reactions of dmba−H with $[IrCl_2Cp^*]_2$ will be assessed. In Chapter 3, the focus will be on the effect of varying the metal centre and the substrate on the cyclometallation reaction. Chapter 4 will describe the intermolecular C−H activation reaction of benzene and the assessment of a new catalyst for alkene hydroarylation. The work in this thesis has been carried out in collaboration with experimental studies undertaken at the University of Leicester.

1.6. References

1. R. G. Bergman, *Nature*, 2007, **446**, 391-393; R. H. Crabtree, *J. Chem. Soc.-Dalton Trans.*, 2001, 2951-2951; Y. Guari, S. Sabo-Etienne and B. Chaudret, *Eur. J. Inorg. Chem.*, 1999, 1047-1055.
2. R. B. Bedford, *Chem. Commun.*, 2003, 1787-1796; J. C. Lewis, R. G. Bergman and J. A. Ellman, *Accounts Chem. Res.*, 2008, **41**, 1013-1025.
3. J. F. Hartwig, K. S. Cook, M. Hapke, C. D. Incarvito, Y. B. Fan, C. E. Webster and M. B. Hall, *J. Am. Chem. Soc.*, 2005, **127**, 2538-2552.
4. J. Oxgaard, R. A. Periana and W. A. Goddard, *J. Am. Chem. Soc.*, 2004, **126**, 11658-11665.
5. W. H. Lam, G. C. Jia, Z. Y. Lin, C. P. Lau and O. Eisenstein, *Chem.-Eur. J.*, 2003, **9**, 2775-2782.
6. W. Koch and M. C. Holthausen, *A Chemist's Guide to Density Functional Theory*, 2001, **Wiley-VCH**.
7. A. Dedieu, *Chem. Rev.*, 2000, **100**, 543-600; S. Q. Niu and M. B. Hall, *Chem. Rev.*, 2000, **100**, 353-405; Y. Boutadla, D. L. Davies, S. A. Macgregor and A. I. Poblador-Bahamonde, *Dalton Trans.*, 2009, 5820-5831.
8. A. H. Janowicz and R. G. Bergman, *J. Am. Chem. Soc.*, 1982, **104**, 352-354; J. K. Hoyano and W. A. G. Graham, *J. Am. Chem. Soc.*, 1982, **104**, 3723-3725.
9. P. L. Watson and G. W. Parshall, *Acc. Chem. Res.*, 1985, **18**, 51-56.
10. P. Burger and R. G. Bergman, *J. Am. Chem. Soc.*, 1993, **115**, 10462-10463.
11. D. L. Strout, S. Zaric, S. Niu and M. B. Hall, *J. Am. Chem. Soc.*, 1996, **118**, 6068-6069.
12. S. Q. Niu and M. B. Hall, *J. Am. Chem. Soc.*, 1998, **120**, 6169-6170.
13. T. Ziegler, E. Folga and A. Berces, *J. Am. Chem. Soc.*, 1993, **115**, 636-646.
14. A. D. Ryabov, I. K. Sakodinskaya and A. K. Yatsimirsky, *J. Chem. Soc.-Dalton Trans.*, 1985, 2629-2638.
15. Z. Lin, *Coord. Chem. Rev.*, 2007, **251**, 2280-2291.
16. G. Bhalla, J. Oxgaard, W. A. Goddard and R. A. Periana, *Organometallics*, 2005, **24**, 5499-5502.
17. J. Oxgaard, R. P. Muller, W. A. Goddard and R. A. Periana, *J. Am. Chem. Soc.*, 2004, **126**, 352-363.

18. R. G. Bergman, T. R. Cundari, A. M. Gillespie, T. B. Gunnoe, W. D. Harman, T. R. Klinckman, M. D. Temple and D. P. White, *Organometallics*, 2003, **22**, 2331-2337.
19. R. N. Perutz and S. Sabo-Etienne, *Angew. Chem.-Int. Edit.*, 2007, **46**, 2578-2592.
20. B. A. Vastine and M. B. Hall, *J. Am. Chem. Soc.*, 2007, **129**, 12068-12069.
21. B. Biswas, M. Sugimoto and S. Sakaki, *Organometallics*, 2000, **19**, 3895-3908.
22. D. L. Davies, S. M. A. Donald and S. A. Macgregor, *J. Am. Chem. Soc.*, 2005, **127**, 13754-13755.
23. R. Bielsa, R. Navarro, E. P. Urriolabeitia and A. Lledos, *Inorg. Chem.*, 2007, **46**, 10133-10142.
24. D. Aguilar, R. Bielsa, M. Contel, A. Lledos, R. Navarro, T. Soler and E. P. Urriolabeitia, *Organometallics*, 2008, **27**, 2929-2936.
25. D. L. Davies, O. Al-Duaij, J. Fawcett, M. Giardiello, S. T. Hilton and D. R. Russell, *Dalton Trans.*, 2003, 4132-4138.
26. D. L. Davies, S. M. A. Donald, O. Al-Duaij, S. A. Macgregor and M. Poelleth, *J. Am. Chem. Soc.*, 2006, **128**, 4210-4211.
27. D. L. Davies, S. M. A. Donald, O. Al-Duaij, J. Fawcett, C. Little and S. A. Macgregor, *Organometallics*, 2006, **25**, 5976-5978.
28. D. H. Ess, S. M. Bischof, J. Oxgaard, R. A. Periana and W. A. Goddard, *Organometallics*, 2008, **27**, 6440-6445.
29. D. Garcia-Cuadrado, A. A. C. Braga, F. Maseras and A. M. Echavarren, *J. Am. Chem. Soc.*, 2006, **128**, 1066-1067.
30. D. Garcia-Cuadrado, P. de Mendoza, A. A. C. Braga, F. Maseras and A. M. Echavarren, *J. Am. Chem. Soc.*, 2007, **129**, 6880-6886.
31. M. Lafrance, S. I. Gorelsky and K. Fagnou, *J. Am. Chem. Soc.*, 2007, **129**, 14570.
32. M. Chaumontet, R. Piccardi, N. Audic, J. Hitce, J. L. Peglion, E. Clot and O. Baudoin, *J. Am. Chem. Soc.*, 2008, **130**, 15157-15166.
33. Y. Feng, M. Lail, K. A. Barakat, T. R. Cundari, T. B. Gunnoe and J. L. Petersen, *J. Am. Chem. Soc.*, 2005, **127**, 14174-14175.
34. W. J. Tenn, K. J. H. Young, G. Bhalla, J. Oxgaard, W. A. Goddard and R. A. Periana, *J. Am. Chem. Soc.*, 2005, **127**, 14172-14173.

35. Y. Feng, M. Lail, N. A. Foley, T. B. Gunnoe, K. A. Barakat, T. R. Cundari and J. L. Petersen, *J. Am. Chem. Soc.*, 2006, **128**, 7982-7994.
36. J. Oxgaard, W. J. Tenn, R. J. Nielsen, R. A. Periana and W. A. Goddard, *Organometallics*, 2007, **26**, 1565-1567.
37. Y. Fan and M. B. Hall, *J. Chem. Soc.-Dalton Trans.*, 2002, 713-718.
38. K. I. Goldberg and A. S. Goldman, *ACS Symposium Series 885*, 2004.
39. P. E. M. Siegbahn and R. H. Crabtree, *J. Am. Chem. Soc.*, 1996, **118**, 4442-4450.
40. R. A. Periana, D. J. Taube, S. Gamble, H. Taube, T. Satoh and H. Fujii, *Science*, 1998, **280**, 560-564.
41. J. Kua, X. Xu, R. A. Periana and W. A. Goddard, *Organometallics*, 2002, **21**, 511-525.
42. S. Murai, F. Kakiuchi, S. Sekine, Y. Tanaka, A. Kamatani, M. Sonoda and N. Chatani, *Nature*, 1993, **366**, 529-531.
43. T. Matsubara, N. Koga, D. G. Musaev and K. Morokuma, *Organometallics*, 2000, **19**, 2318-2329.
44. K. Krogh-Jespersen, M. Czerw, M. Kanzelberger and A. S. Goldman, *J. Chem. Inf. Comput. Sci.*, 2001, **41**, 56-63.
45. C. E. Webster, Y. B. Fan, M. B. Hall, D. Kunz and J. F. Hartwig, *J. Am. Chem. Soc.*, 2003, **125**, 858-859.
46. G. Bhalla, X. Y. Liu, J. Oxgaard, W. A. Goddard and R. A. Periana, *J. Am. Chem. Soc.*, 2005, **127**, 11372-11389.
47. R. A. Periana, X. Y. Liu and G. Bhalla, *Chem. Commun.*, 2002, 3000-3001.
48. M. Lail, B. N. Arrowood and T. B. Gunnoe, *J. Am. Chem. Soc.*, 2003, **125**, 7506-7507.
49. J. Oxgaard and W. A. Goddard, *J. Am. Chem. Soc.*, 2004, **126**, 442-443.
50. N. J. DeYonker, N. A. Foley, T. R. Cundari, T. B. Gunnoe and J. L. Petersen, *Organometallics*, 2007, **26**, 6604-6611.
51. M. Lafrance, C. N. Rowley, T. K. Woo and K. Fagnou, *J. Am. Chem. Soc.*, 2006, **128**, 8754-8756.

2. Cyclometallation of *N,N*-dimethylbenzylamine with $[IrCl_2Cp^*]_2$: the role of the chelating base

2.1. Introduction

As described in Chapter 1, Ryabov *et al.*[1] reported the cyclometallation reaction of N,N−dimethylbenzylamine (dmba−H) by $[Pd(OAc)_2]$ in chloroform solution which led to the cyclopalladated acetate-bridged dimer, $[Pd(OAc)(dmba)]_2$, as a final product. He suggested a highly ordered transition state similar to a Wheland intermediate. However, computational studies of this cyclometallation reaction carried out by Macgregor *et al.*[2] showed that the reaction proceeds via a C−H agostic intermediate. Thus, the cyclometallation reaction involves a two step process, in which C−H activation occurs via a 6-membered acetate-assisted transition state. The key feature of the process was an intermediate in which the the *ortho*−C-H bond exhibited an agostic interaction with the metal centre and hydrogen bonding with the displaced acetate. Both effects facilitate the C−H activation step.

More recently experimental studies by Davies and co-workers[3] showed that the use of sodium acetate in promoting the cyclometallation of dmba−H with $[IrCl_2Cp^*]_2$ is crucial to achieve C−H activation at room-temperature (Figure 2.1). Indeed, when another simple base such as triethylamine was used instead of acetate, the cyclometallation was not observed.

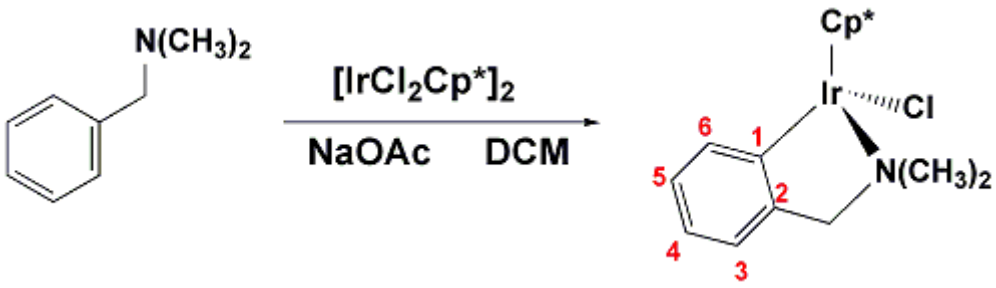

Figure 2.1 – Room temperature cyclometallation of dmba-H by $[IrCl_2Cp^*]_2$ in dichloromethane in the presence of sodium acetate

Their proposed mechanism is shown in Figure 2.2. The first step described was the dimer opening, either by acetate to form **A**, or by adding the amine to form **B**. The substitution of a chloride ligand in either **A** (by dmba−H) or **B** (by acetate) leads to the formation of **C**. From complex **C** a vacant site is needed in order for C−H activation to

occur and is this achieved by dissociation either of chloride or acetate. C−H activation was then proposed to proceed by one of two mechanisms: (I) oxidative addition (via $\mathbf{D_1}$) or (II) electrophilic activation via a Wheland intermediate (via $\mathbf{D_2}$), similar to that proposed by Ryabov in the palladium system. The final cyclometallated product **E** was obtained by loss of HOAc. Thus, their suggestion is that the acetate may help to facilitate the breaking up of the dimer and the exchange of the chloride ligand. In addition, it has the potential to act as an intramolecular base in the C−H activation step.

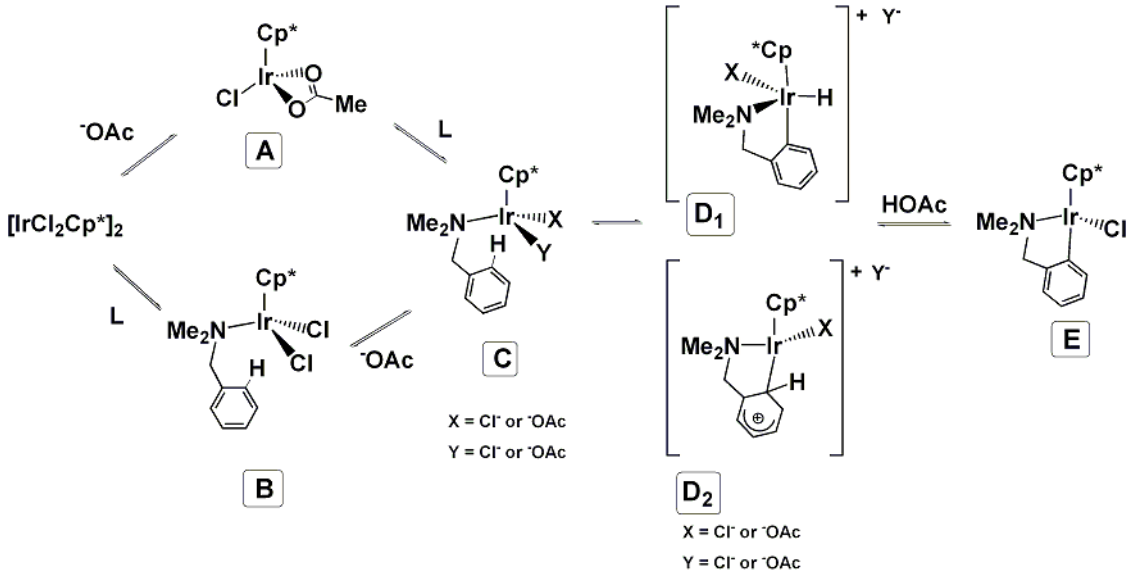

Figure 2.2 – Proposed mechanism by Davies *et al.*[3] for the cyclometallation of a dmba-H ligand by $[IrCl_2Cp^*]_2$ in the presence of sodium acetate

The mechanistic study of this room temperature reaction was carried out by Macgregor *et al.,*[4] and it focused on the mechanism of the cyclometallation. In this case the active species, related to **C** in Figure 2.2, was considered to be $[Ir(\eta\text{-Cp})(dmba{-}H)(\kappa^2\text{-}RCO_2)]^+$ **F** (see Figure 2.3). For this study, four main mechanisms were considered. Firstly, an oxidative addition mechanism (OA) via $\mathbf{TS(F\text{-}G)_1}$. Secondly, an electrophilic activation mechanism (EA) through a Wheland type structure, $\mathbf{TS(F\text{-}G)_2}$, as proposed by Ryabov. Thirdly, a 6-membered transition state via an agostic C−H interaction, $\mathbf{TS(C\text{-}D)_3}$, has been also considered. Finally, a 4-membered transition state similar to a 1,2-addition, refers to $\mathbf{TS(F\text{-}G)_4}$.

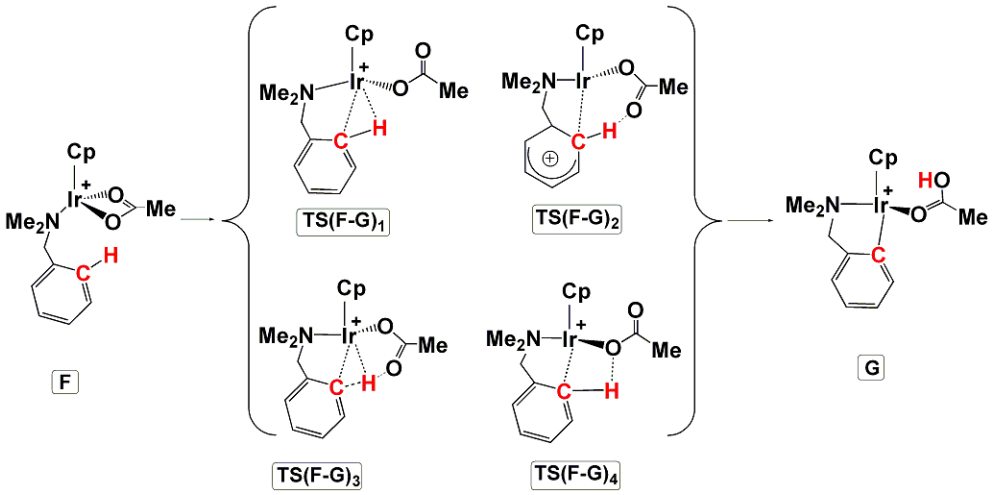

Figure 2.3 - Proposed transition states for the cyclometallation reaction from **C** to **D** proposed by Macgregor *et al.*[4]

The lowest energy pathway proceeds via a single 6-membered transition state, which corresponds to **TS(F-G)$_3$** ($\Delta E^{\ddagger}$ = 16 kcal/mol) proposed above. The transition state **TS(F-G)$_2$** could not be located. The degree of availability of the acetate is the key in all three pathways. The transfer of the proton to the outer oxygen proceeds via **TS(F-G)$_3$**, while **TS(F-G)$_4$** describes a rotation around the Ir–O_2 bond which means that the hydrogen must be transferred to the inner oxygen. For the oxidative addition transition state **TS(F-G)$_1$**, the free oxygen is twisted away from the hydrogen and the metal must become fully involved for the success of the cyclometallation process. Further calculations with Cp* instead of Cp did not result in any significant change in the reaction energies.

Overall, computational chemistry has provided insight into the nature of the transition state in the C–H activation step in the cyclometallation reaction of dmba–H by [$Pd(OAc)_2$] where the key intermediate is an agostic species in which the acetate plays a dual role, both stabilising the agostic complex and acting as an intramolecular base. The same behaviour was now observed with [Ir(η-Cp)(dmba–H)(κ^2-OAc)]$^+$ in which the co-ligand κ^2-OAc provides both strong basic character and a geometrically convenient route via arm dissociation for intramolecular H transfer. Therefore, the role of the acetate is crucial in promoting facile cyclometallation. This chapter will extend this work through the use of density functional theory (DFT) calculations to study the effects of varying the chelating base on the cyclometallation reaction. The basic model employed in these calculations is shown in Figure 2.4 where R = Me, Ph, CF_3, CCl_3 and OH. Additionally, triflate analogues were also computed.

2.1.1. Computational approach

The structures of the $[Ir(\eta\text{-}Cp)(dmba{-}H)(\kappa^2\text{-}RCO_2)]^+$ complexes were adapted from $[Ir(\eta\text{-}Cp)(dmba{-}H)(\kappa^2\text{-}OAc)]^+$ computed in previous studies by substituting the methyl group by the appropriate substituent, R. In order to locate the C−H activation transition state, a scan which involved the approach of the C−H bond towards the metal was computed. Contrary to what was expected, this led instead to the dissociation of one arm of the chelating base and the location of a κ^1-intermediate, as shown schematically in Figure 2.4. Attempts to find the following hydrogen transfer via a 6-membered transition state from this intermediate proved difficult. Therefore, this second step was modelled from the final cyclometallated product by a scan based on shortening the Ir-C···HO distance. After locating the C−H activation transition state IRC calculations, followed by geometry optimizations, were run and confirmed the presence of the same κ^1-intermediate. Several scans designed to locate a single transition state analogous to that computed in previous studies were run, but proved unsuccessful.

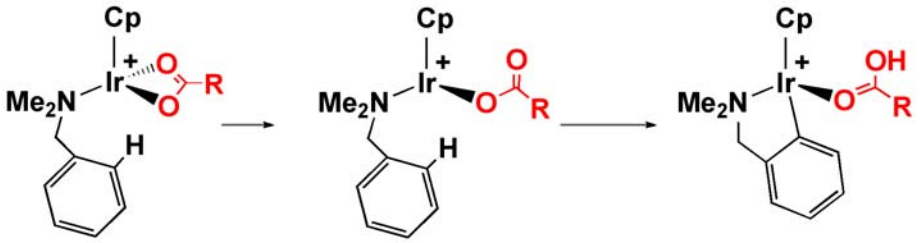

Figure 2.4 – General reaction scheme for the cyclometallation of $[Ir(\eta\text{-}Cp)(dmba\text{-}H)(\kappa^2\text{-}RCO_2)]^+$ (**1_R**) where R = Me, Ph, CF_3, CCl_3 and OH.

The location of a κ^1-intermediate with the new RCO_2^- bases indicates that these systems react in a two step process. The first step involves κ^2–κ^1 displacement of the chelating base while the second defines the C-H activation. The overall process follows the same pattern than the mechanism of cyclometallation by $[Pd(OAc)_2]$.[2]

Due to this unexpected behaviour, the reaction profile of the cyclometallation reaction of $[Ir(\eta\text{-}Cp)(dmba{-}H)(\kappa^2\text{-}OAc)]^+$ was reassessed following the new scan approach.

2.2. Reassessment of the cyclometallation reaction of [Ir(η-Cp)(dmba−H)(κ²-OAc)]⁺ ($\mathbf{1_{Me}}$)

All three possible pathways described in the previous studies on [Ir(η-Cp)(dmba−H)(κ²-OAc)]⁺ ($\mathbf{1_{Me}}$) were reassessed. In all cases the conformation of $\mathbf{1_{Me}}$ was the same as that found before.[4] The identification of all main features along the three mechanisms will be described in turn below.

2.2.1. Cyclometallation via a 6-membered C−H activation transition state

The first step of the process is described in Figure 2.5. It involves the dissociation of one arm of the acetate (Ir−O_1) and rotation around the Ir−O_2 bond. The transition state $\mathbf{TS(1\text{-}2)_{Me}}$ shows an increase in the Ir···O_1 distance from 2.17 Å in $\mathbf{1_{Me}}$ to 2.77 Å in $\mathbf{TS(1\text{-}2)_{Me}}$ and further to 3.17 Å in $\mathbf{2_{Me}}$. An approach of the C_1−H_1 bond towards the metal was also computed ($\mathbf{1_{Me}}$: Ir···C_1 = 3.63 Å, Ir···H_1 = 3.41 Å; $\mathbf{TS(1\text{-}2)_{Me}}$: Ir···$C_1$ = 3.07 Å, Ir···H_1 = 2.65 Å). The structure of $\mathbf{2_{Me}}$ shows that one arm of the acetate is fully dissociated (Ir···O_1 = 3.17 Å) and that H_1 lies closer to the oxygen bound to the metal, rather than to the free oxygen of acetate (H_1···O_2 = 2.27 Å *cf.* H_1···O_1 = 3.16 Å). The rotation around Ir−O_2 is quantified by the X−Ir−O_2−C_2 torsion angle, where X = the Cp ring centroid. This angle decreases from 122.2º in $\mathbf{1_{Me}}$ to 82.1º in $\mathbf{TS(1\text{-}2)_{Me}}$ and then to 35.2º in $\mathbf{2_{Me}}$. In addition, a shortening of the Ir−O_2 bond from 2.17 Å in $\mathbf{1_{Me}}$ to 2.07 Å in $\mathbf{2_{Me}}$ is computed. Energetically, the dissociation of one arm of the acetate proceeds via a small barrier of 13.4 kcal/mol and $\mathbf{2_{Me}}$ is less stable than $\mathbf{1_{Me}}$ by 8.6 kcal/mol.

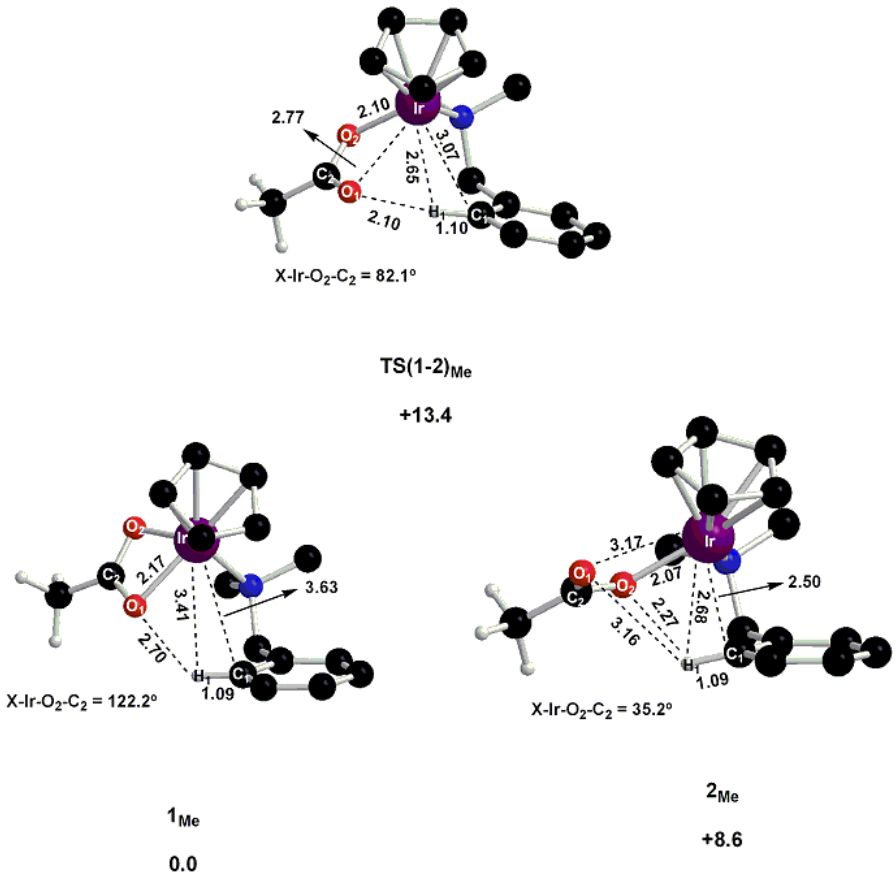

Figure 2.5 - Computed stationary points (kcal/mol, distances in ångstroms) for κ^2–κ^1 displacement of acetate in $\mathbf{1_{Me}}$. Non-participating hydrogens are omitted for clarity.

As shown in Figure 2.6, the C-H activation step involves the deprotonation of the C_1–H_1 bond by the free arm of the acetate and the formation of the cyclometallated product. This hydrogen transfer proceeds via **TS(2-3)$_{Me}$** and is associated with a barrier of only 0.9 kcal/mol. In **TS(2-3)$_{Me}$** there is a minimal elongation of the C_1-H_1 bond to 1.12 Å, however both the $O_1\cdots H_1$ and $Ir\cdots H_1$ distances decrease by 1.0 Å and 0.43 Å, respectively. Therefore, the major movement involves rotation around the Ir–O_2 bond such that O_1 approaches the aryl group. Indeed, several energy profiles for the rotation back and forth around the Ir–O_2 bond were computed, and indicated that hydrogen transfer readily occurs whenever O_1 lies close to the C_1–H_1 bond. Proton transfer results in an elongation of the Ir–O_2 bond, from 2.07 Å in $\mathbf{2_{Me}}$ to 2.20 Å in the cyclometallated product, $\mathbf{3_{Me}}$, which also features a new Ir–C bond with a computed distance of 2.06 Å. The C-H activation step is exothermic (by 14.1 kcal/mol) as is the overall cyclometallation reaction (by 5.5 kcal/mol).

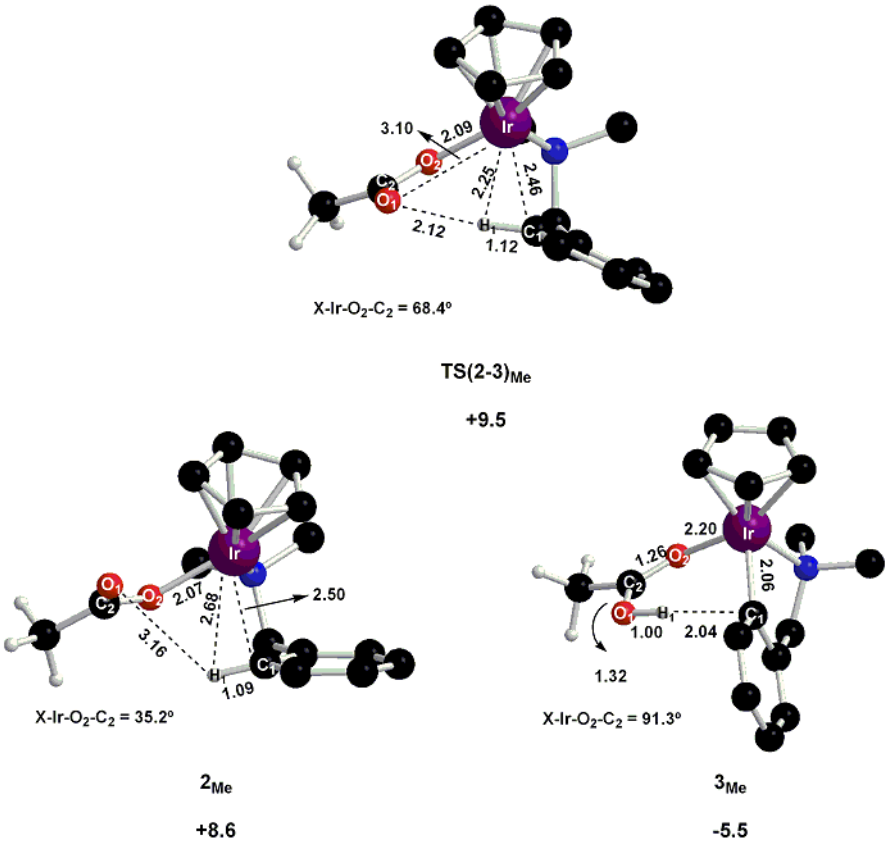

Figure 2.6 - Computed stationary points (kcal/mol, distances in ångstroms) for C-H activation in $\mathbf{2}_{\mathbf{Me}}$ via a 6-membered transition state. Non-participating hydrogens are omitted for clarity.

The full two step profile is shown in Figure 2.7. The limiting step of the process is associated with **TS(1-2)$_{\mathbf{Me}}$** which was located at 13.4 kcal/mol. As observed in the computational studies of the [Pd(OAc)$_2$]/dmba-H system, in the C−H activation step the metal and the acetate combine to promote a facile hydrogen transfer.

Figure 2.7 also emphasizes the changes in the hybridisation state that occur at the O atoms as the reaction evolves. This accounts for the shortening of the Ir−O_2 bond from $\mathbf{1}_{\mathbf{Me}}$ (2.17 Å) to $\mathbf{2}_{\mathbf{Me}}$ (2.07 Å) as O_2 takes on more formal anionic character. In contrast, in $\mathbf{3}_{\mathbf{Me}}$ O_2 takes on sp^2-hybridised carbonyl character and this is consistent with the increase in the Ir−O_2 distance to 2.20 Å in that species.

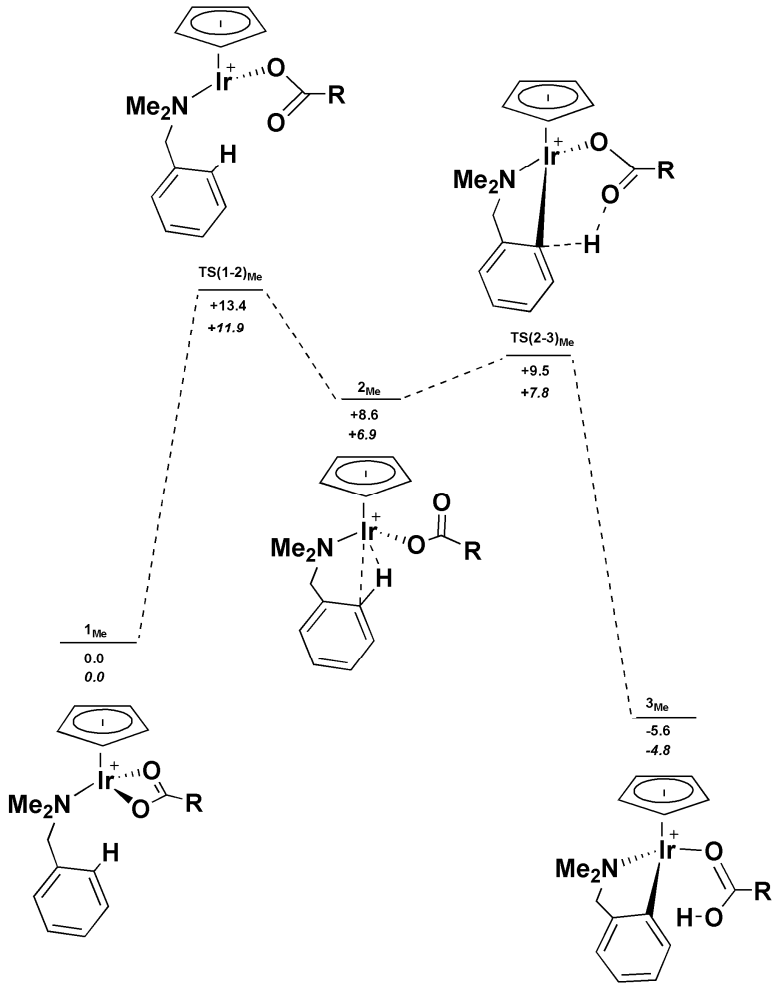

Figure 2.7 - Computed reaction profile (kcal/mol) for cyclometallation of $\mathbf{1_{Me}}$ via a 6-membered C-H activation transition state. Energies corrected for solvation (dichloromethane, PCM method) are shown in italics.

The effect of solvation by dichloromethane was assessed using standard PCM solvent calculations and the results are shown in italics in Figure 2.7. A slight stabilization of all stationary points along the profile was computed, except for the product $\mathbf{3_{Me}}$. The κ^2–κ^1 displacement barrier decreases to 11.9 kcal/mol, while that for C-H activation remains the same (0.9 kcal/mol). The final product $\mathbf{3_{Me}}$ is slightly destabilized, however, the overall process remains exothermic (E = -4.8 kcal/mol).

2.2.2. Cyclometallation via a 4-membered C−H activation transition state

Attempts to locate a 4-membered C−H activation transition state were initiated from $\mathbf{2_{Me}}$ by a scan shortening the $O_2\cdots H$ distance. This allowed the location of $\mathbf{TS(2'\text{-}4)_{Me}}$ in which H_1 is transferred to O_2, the oxygen bound to the metal. IRC calculations, followed by geometry optimization, did show that $\mathbf{TS(2'\text{-}4)_{Me}}$ leads to a cyclometalated species, $\mathbf{4_{Me}}$ but, surprisingly, did not link back to intermediate $\mathbf{2_{Me}}$. Instead a slightly different intermediate $\mathbf{2'_{Me}}$ was located which is only 0.2 kcal/mol less stable than $\mathbf{2_{Me}}$. Details of this process are given in Figure 2.8.

Intermediates $\mathbf{2_{Me}}$ and $\mathbf{2'_{Me}}$ have very similar geometries, with the major difference being due to rotation around $Ir\cdots O_2$ bond ($X{-}Ir{-}O_2{-}C_2$ angle = 35.2º in $\mathbf{2_{Me}}$ *cf.* 6.4º in $\mathbf{2'_{Me}}$). Although no transition state for this rotation was located, such a process would be expected to be facile. $\mathbf{TS(2'\text{-}4)_{Me}}$ exhibits a far greater elongation of the C_1-H_1 bond than was seen in the 6-membered transition state $\mathbf{TS(2\text{-}3)_{Me}}$. H_1 now lies approximately between the O_2 and C_1 atoms, with distances of 1.27 Å and 1.38 Å respectively. Product $\mathbf{4_{Me}}$ presents a $Ir{-}C_1$ bond with a distance of 2.05 Å and an Ir-O_2 distance of 2.32 Å, significantly longer than in $\mathbf{3_{Me}}$. This greater elongation is due to the lower electron donating ability of the hydroxyl group in $\mathbf{4_{Me}}$ in comparison with the carbonyl oxygen in $\mathbf{3_{Me}}$. Overall, relative to $\mathbf{2'_{Me}}$ the C-H activation step via a four membered transition state has an activation barrier of 11.0 kcal/mol and is endothermic by 0.2 kcal/mol.

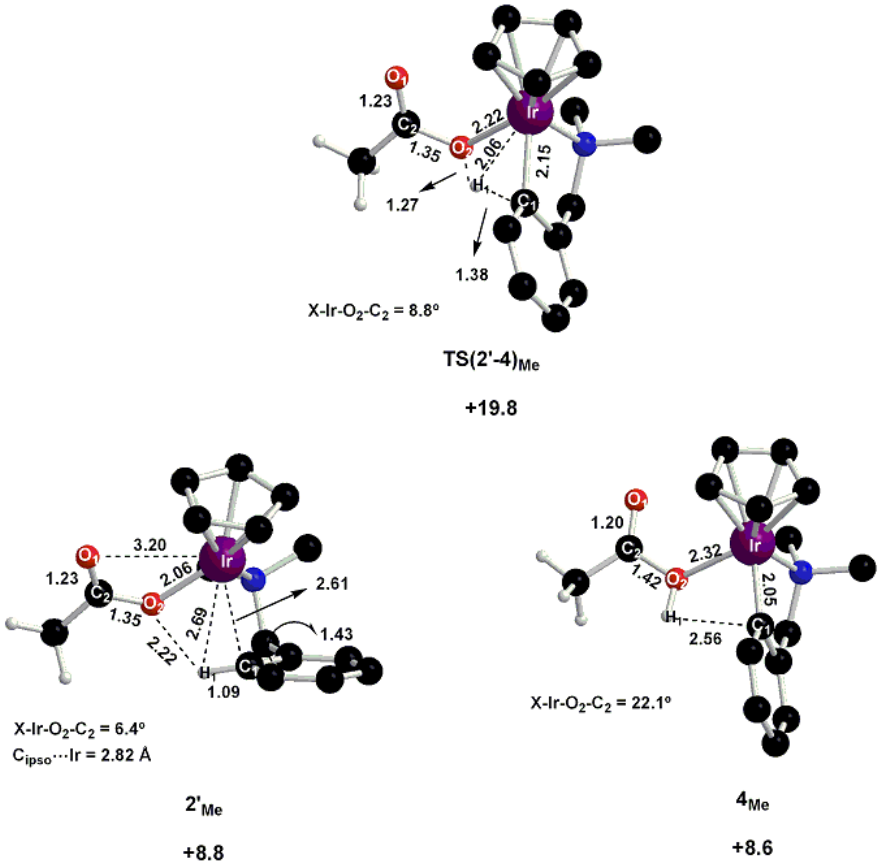

Figure 2.8 - Computed stationary points (kcal/mol, distances in ångstroms) for C-H activation of $\mathbf{2'_{Me}}$ via a 4-membered transition state. Non-participating hydrogens are omitted for clarity.

The full profile for cyclometallation via a 4-membered C−H activation transition state is shown in Figure 2.9. The limiting step is now associated with the C−H cleavage and the overall energy barrier is +19.8 kcal/mol. In this case C-H activation requires an activation energy of 11 kcal/mol, considerably higher than the minimal activation energy required for the same step via a 6-membered transition state (0.9 kcal/mol). Therefore, the 4-membered mechanism is much less favourable than the 6-membered mechanism. Moreover, the product formed is not stable from the thermodynamic point of view, although it would probably easily rearrange to the more stable product, $\mathbf{3_{Me}}$.

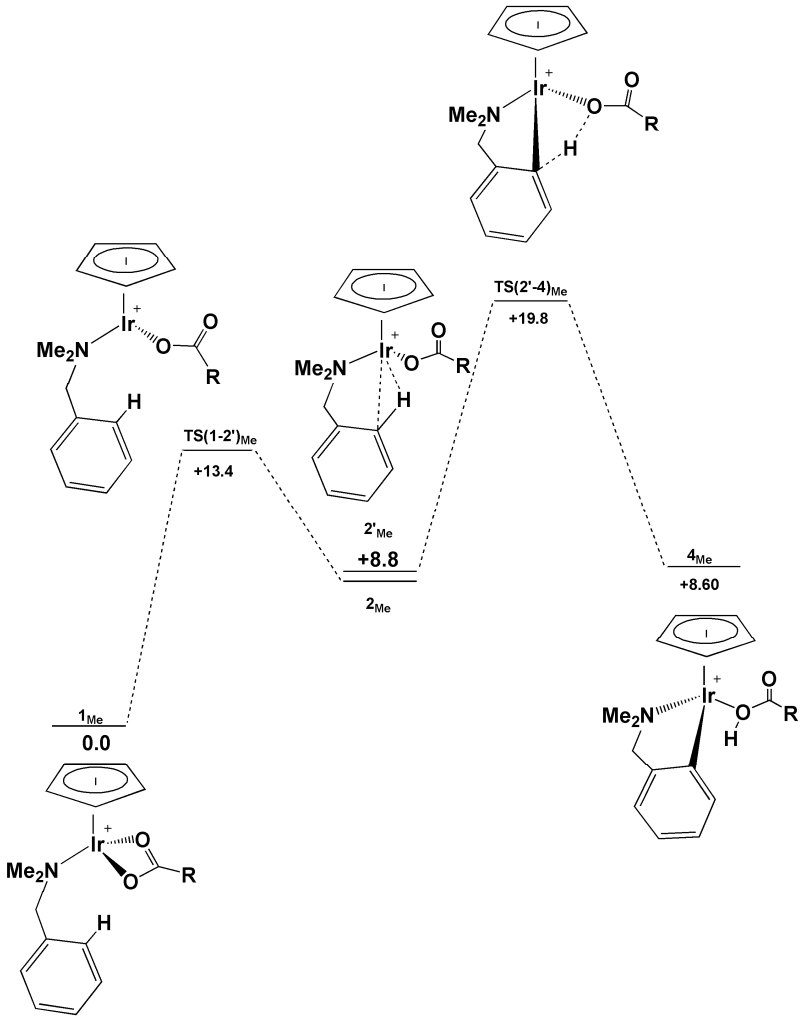

Figure 2.9 - Computed reaction profile (kcal/mol) for cyclometallation of $\mathbf{1_{Me}}$ via a 4-membered C-H activation transition state.

2.2.3. Cyclometallation via an oxidative addition C−H activation transition state

Oxidative addition from $\mathbf{2_{Me}}$ involves the transfer of a hydrogen to the metal and several attempts to characterize a reaction profile on this basis were made. However, any transition state optimizations always converged on $\mathbf{TS(2'\text{-}4)_{Me}}$ that was described in the previous section. Moreover, the potential product, $[Ir(\eta\text{-}Cp)(H)(dmba)(\kappa^1\text{-}OAc)]^+$ in which the hydride is cis to OAc ($\mathbf{\textit{c}\text{-}5a_{Me}}$) and which had been located before,[4] could not be found here. This is due to a different orientation of the dmba moiety, as discussed in Section 2.3 below. Instead a new species in which the hydride is trans to OAc ($\mathbf{\textit{t}\text{-}5_{Me}}$) was found and a transition state for the oxidative addition process, $\mathbf{TS(2''\text{-}\textit{t}\text{-}5)_{Me}}$, was then characterised from a scan based on shortening the distance between the aryl carbon and the hydride ligand.

The computed geometries and energies are shown in Figure 2.10. IRC calculations on the transition state **TS(2′′-*t*-5)$_{Me}$**, confirmed that it led to product ***t*-5$_{Me}$**, however, as in the 4-membered process, the presence of a new intermediate, **2′′$_{Me}$** was also revealed. **2′′$_{Me}$** is 4.5 kcal/mol higher in energy than **2$_{Me}$** and this energy difference is due to a rotation around the C_{benzyl}–C_{ipso} bond of the aryl moiety. This leads to the loss of interactions of the C_1–H_1 bond with both the metal centre and O_2. A scan probing rotation about the C_{benzyl}–C_{ipso} bond suggested a low barrier would be associated with this process, although no attempt to locate a transition state was made. **TS(2′′-*t*-5)$_{Me}$** presents very short, product-like Ir···H_1 and Ir···C_1 distances of 1.59 Å and 2.12 Å respectively. **TS(2′′-*t*-5)$_{Me}$** is therefore a very late transition state and the major change in forming ***t*-5$_{Me}$** is an opening of the C_3–Ir–H_2 angle by 17.2º. In addition, there is an increase in the Ir-O_2 bond in ***t*-5$_{Me}$**, possibly due to the high trans influence of the hydride ligand. Overall, C-H activation via oxidative addition from **2′′$_{Me}$** has an activation barrier of 9.9 kcal/mol and is endothermic by 9.7 kcal/mol.

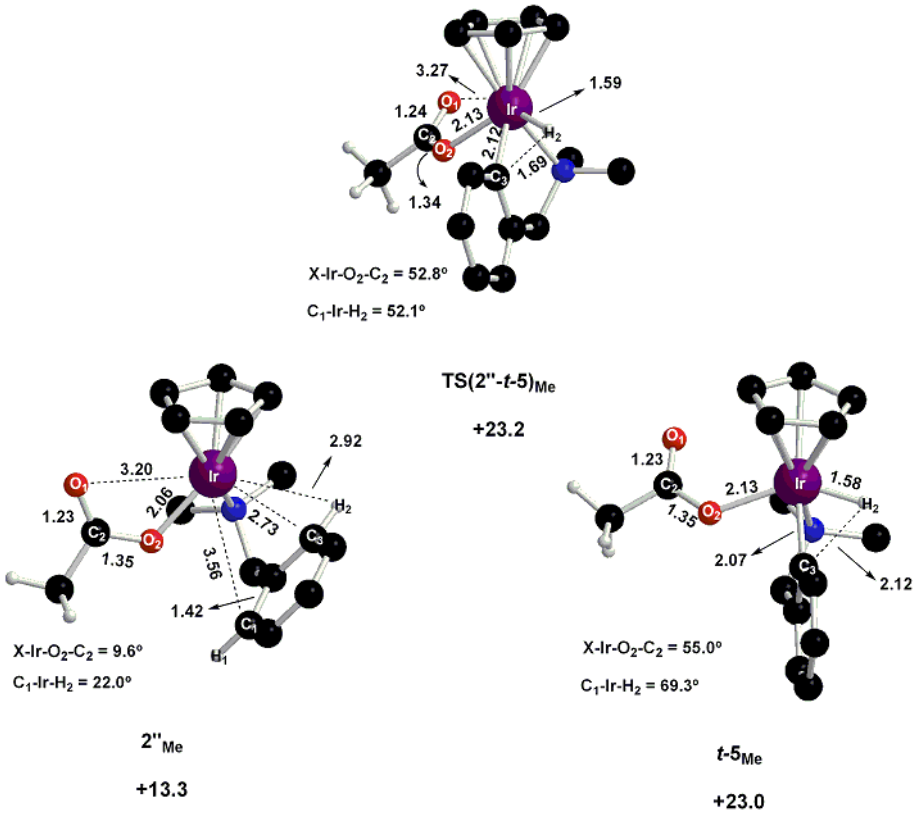

Figure 2.10 - Computed stationary points (kcal/mol, distances in ångstroms) for the C-H activation of **2′′$_{Me}$** via an oxidative addition transition state. Non-participating hydrogens are omitted for clarity.

The complete profile for cyclometallation via an oxidative addition C−H activation transition state is shown in Figure 2.11. Overall this process requires an activation energy of +23.3 kcal/mol and, as in the 4-membered pathway, C−H cleavage is the limiting step. Thus, the oxidative addition has the highest energy barrier for all the mechanisms studied, and is highly endothermic.

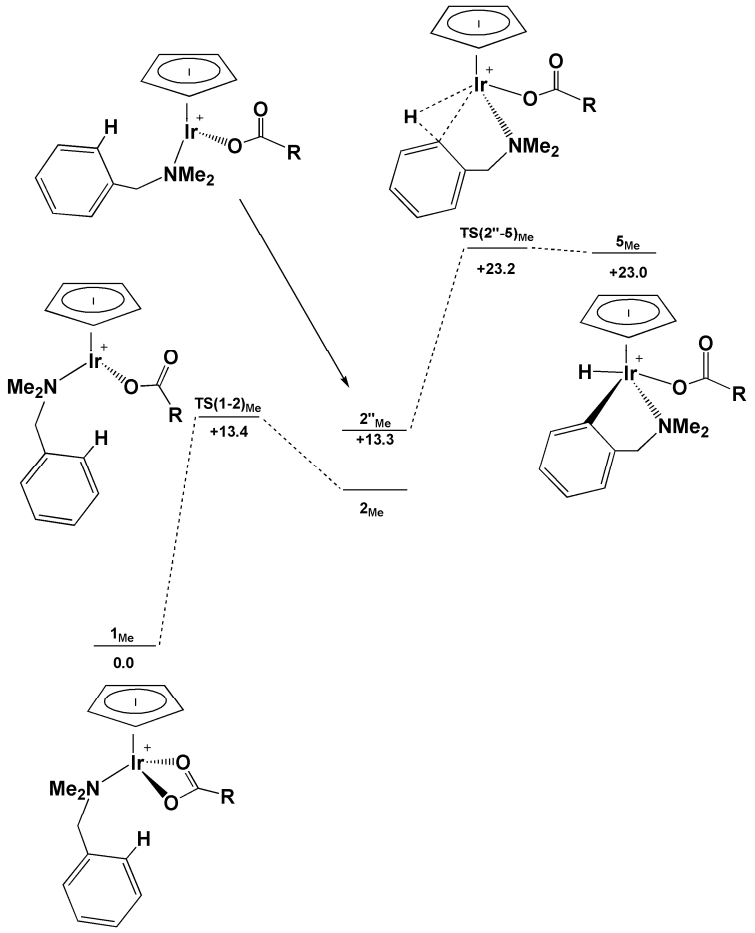

Figure 2.11 - Computed reaction profile (kcal/mol) for cyclometallation of $\mathbf{1_{Me}}$ via an oxidative addition C-H activation transition state.

2.2.4. Comparison with previous studies

A different behaviour has been computed for the cyclometallation reaction of [Ir(η-Cp)(dmba−H)(κ^2-OAc)]$^+$ during this project. In previous studies, C−H activation via 6-membered transition state was characterised as a one step process.[4] However, the reassessment of it here shows a two step process, with both a lower energy barrier and a more stable product. In addition, differences in the profiles for C-H activation via 4-membered and oxidative addition transition states have been computed. These

differences can be understood by comparing the structures located here with those from previous studies.

Figure 2.12 compares the two computed energy profiles for cyclometallation of $\mathbf{1_{Me}}$ involving 6-membered C-H activation transition states. In addition, the rate-limiting transition states in each case are shown, $\mathbf{TS(1\text{-}3a)_{Me}}$ ($\Delta E^{\ddagger}$ = +16.0 kcal/mol), computed previously and the new transition state, $\mathbf{TS(1\text{-}2)_{Me}}$ ($\Delta E^{\ddagger}$ = +13.4 kcal/mol), described here. The key difference is the orientation of the dmba-H ligand due to rotations around the Ir−N bond and the C_{benzyl}−C_{ipso} bond. In $\mathbf{TS(1\text{-}3a)_{Me}}$ both the aryl moiety and the acetate are in an almost co-planar arrangement and the structure features short contacts between H_1 and both Ir (2.22 Å) and O_1 (2.15 Å). As a result this leads directly to C-H activation. In contrast, in $\mathbf{TS(1\text{-}2)_{Me}}$ the different angle of approach of the dmba−H ligand leads only to displacement of one arm of the acetate ($H_1\cdots O_1$ = 2.10 Å) without a close interaction with the metal centre (H1⋯Ir = 2.65 Å). Therefore in this case a second step in which C-H activation occurs is unavoidable. It seems that C-H activation requires the transferring hydrogen to interact with both the free oxygen of the acetate and the metal centre. This highlights the ambiphilic character of the C-H activation process in these systems. Indeed, the C-H activation transition state $\mathbf{TS(1\text{-}3)_{Me}}$ computed here does feature short contacts from H_1 to both Ir (2.25 Å) and O_1 (2.12 Å). Work described in the following sections with different chelating bases will confirm the importance of this ambiphilic behaviour.

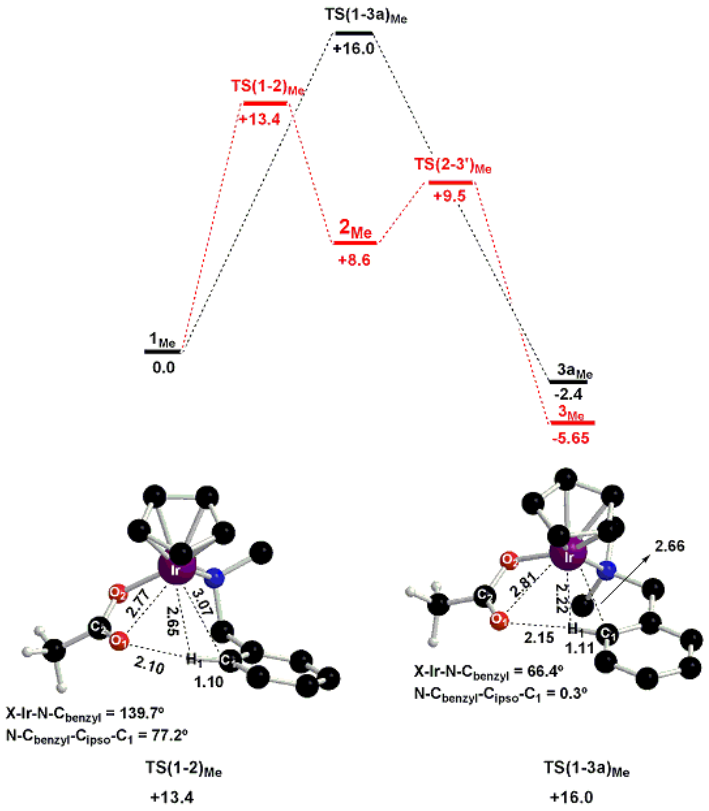

Figure 2.12 - Computed reaction profiles (kcal/mol) for cyclometallation of $\mathbf{1_{Me}}$ involving 6-membered C-H activation transition states, computed here (in red) and previously[4] (in black). Geometries for the two rate-limiting transitions states $\mathbf{TS(1\text{-}2)_{Me}}$ and $\mathbf{TS(1\text{-}3a)_{Me}}$ (distances in ångstroms) are also shown.

The comparison of the 4-membered pathways computed here and previously is shown in Figure 2.13. The first step is common to both processes and involves κ^1-κ^2 displacement of acetate to give $\mathbf{2_{Me}}$ which would then rearrange to $\mathbf{2'_{Me}}$. The variation appears in the C-H activation step where the energy barrier computed here is lower by 3 kcal/mol. A comparison of the transition states, $\mathbf{TS(2'\text{-}4)_{Me}}$ and $\mathbf{TS(2'\text{-}4a)_{Me}}$ shows that this is due to similar geometrical effects as those seen along the 6-membered pathway. Indeed, the final product $\mathbf{4_{Me}}$ has a similar orientation of the aryl and dmba ligands as those described for $\mathbf{3_{Me}}$.

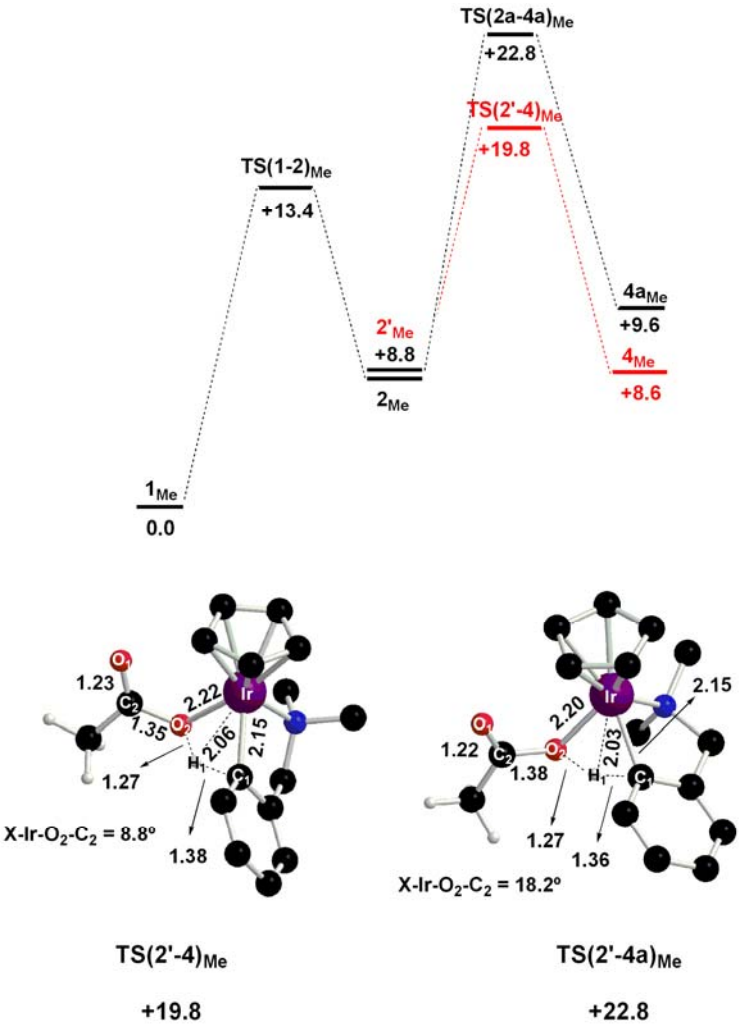

Figure 2.13 - Computed reaction profiles (kcal/mol) for cyclometallation of $\mathbf{1_{Me}}$ involving 4-membered C-H activation transition states, computed here (in red) and previously[4] (in black). Geometries for the two rate-limiting transitions states $\mathbf{TS(2'\text{-}4)_{Me}}$ and $\mathbf{TS(2'\text{-}4a)_{Me}}$ (distances in ångstroms) are also shown.

The new cyclometallation involving oxidative addition is compared with that computed before in Figure 2.14. The transition state computed here is 7.5 kcal/mol more stable than that seen previously. In this case, the major change arises from the formation of a trans geometry in the product where before a cis geometry was computed. In addition, subtle changes in the dmba ligand can also be seen in both the transition states and the alternative products.

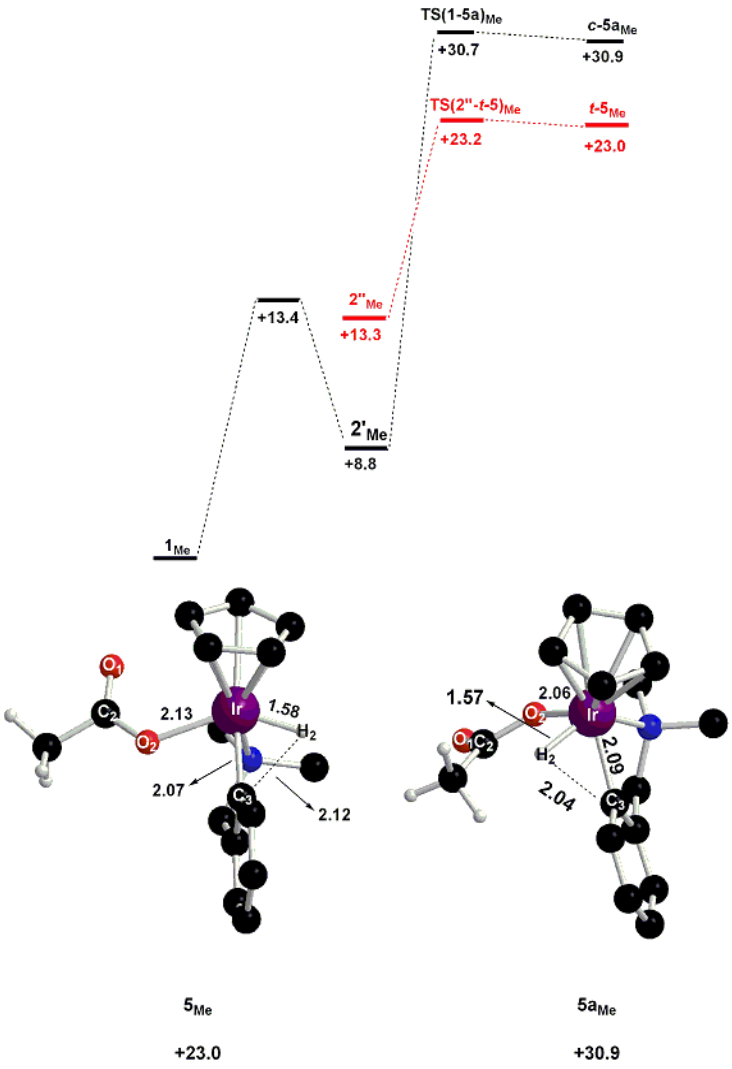

Figure 2. 14 - Computed reaction profiles (kcal/mol) for cyclometallation of $\mathbf{1_{Me}}$ involving oxidative addition C-H activation transition states, computed here (in red) and previously[4] (in black). Geometries for the two rate-limiting transitions states $\mathbf{TS(2''\text{-}5)_{Me}}$ and $\mathbf{TS(2a\text{-}5a)_{Me}}$ (distances in ångstroms) are also shown.

2.2.5. Summary

The results described above show that a new conformation of the dmba−H ligand has led to a stabilization of all the stationary points along the three computed cyclometallation pathways. Pathway I, via a 6-membered C-H activation transition state, is still the lowest energy route. However it now appears as a two step process, in which the first step involves a κ^2-κ^1 displacement of the chelating base to produce a new κ^1-intermediate $\mathbf{2_{Me}}$. In the second step C−H activation occurs with an activation energy of less than 1 kcal/mol. A key feature is the ambiphilic character of this process in which the reacting C-H bond interacts with both the metal and the free oxygen of the acetate to facilitate bond cleavage with a very small energy barrier. Alternative pathways based on C-H activation via 4-membered or oxidative addition transition states proved significantly higher in energy. These three profiles are compared in Figure 2.15.

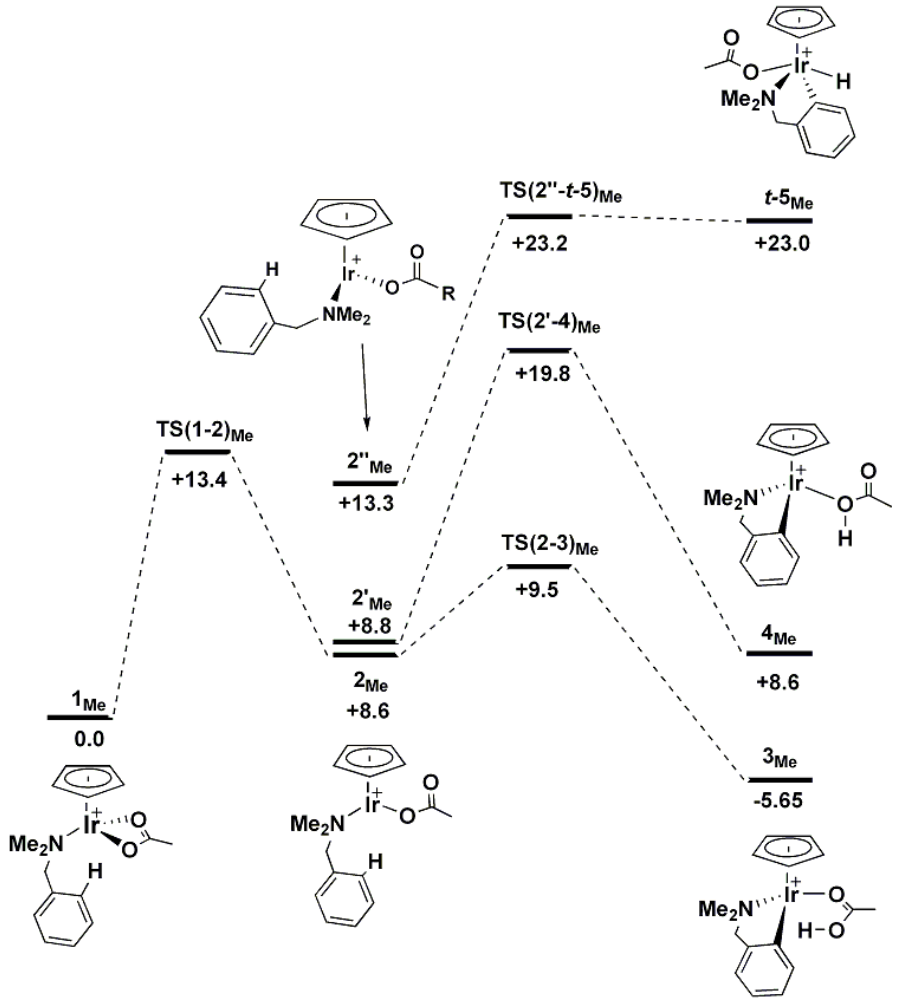

Figure 2.15 - Computed reaction profiles (kcal/mol) for cyclometallation of $\mathbf{1}_{Me}$ via 6-membered, 4-membered and oxidative addition C–H activation transition states.

2.3. C−H activation of [Ir(η-Cp)(dmba−H)(κ^2-RCO$_2$)]$^+$: Variation of the chelating base

In this section the effects of changing acetate to other chelating bases on the cyclometallation reactions of [Ir(η-Cp)(dmba−H)(κ^2-RCO$_2$)]$^+$ complexes (**1$_R$**, where R = Ph, CF_3, CCl_3 and OH) will be discussed. This range of bases has been chosen to monitor how varying both the coordination ability and the proton accepting ability of the base affects the cyclometallation process.

Overall these bases react in a similar way to that already described for the acetate system, however, for each base subtle variation in behaviour was seen. The key geometrical parameters and energies for all stationary points will be described in each case. However, only the main six atoms directly participating in the C−H activation will be highlighted, as these positions enclose the greatest variation in geometry of the overall structure. In each case, the reactant **1$_R$** is very similar and so will not be described. As before, the pathway involving 6-membered C-H activation transition states proved the most accessible, although the alternative 4-membered and oxidative addition pathways will also be discussed.

2.3.1. Cyclometallation of 1$_R$ via 6-membered C-H activation transition states

These cyclometallation reaction profiles fell into two distinct groups which will be discussed separately below. With the benzoate or trichloroacetate systems a two step process is computed, similar to that seen with acetate. In both cases, the limiting step is the arm displacement from the metal while the C-H cleavage involves a barrier of no more than 1.3 kcal/mol. Key geometrical parameters and energies for **TS(1-2)$_R$**, **2$_R$**, **TS(2-3)$_R$** and **3$_R$** (R = Ph, CCl_3) are described in Figure 2.16, where the equivalent results found with acetate are also included for comparison.

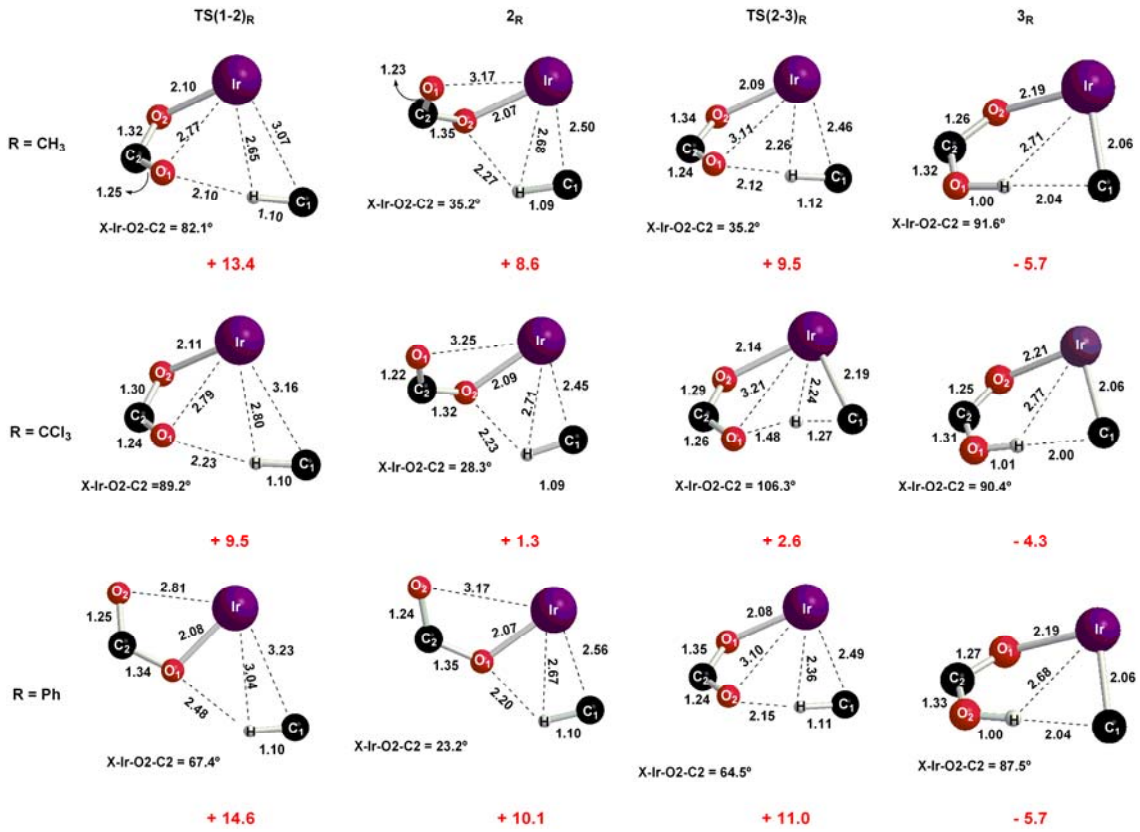

Figure 2.16 - Computed geometrical parameters (Å, degrees) for cyclometallation of $\mathbf{1_R}$ (R = Me, CCl_3, Ph) via a 6-membered C-H activation transiton state, highlighting the six atoms directly involved. Energies (kcal/mol) are quoted relative to $\mathbf{1_R}$ in each case, in red.

Of the two species the trichloroacetate system is closer to the behaviour seen with acetate. The κ^2–κ^1 displacement occurs by a similar approach of the aryl moiety towards the metal, followed by the dissociation of the Ir–O_1 bond and rotation around the Ir–O_2 bond. The intermediate $\mathbf{2_{CCl3}}$ has a similar geometry to $\mathbf{2_{Me}}$, as H_1 lies closer to the oxygen directly bound to the metal. $\mathbf{TS(2\text{-}3)_{CCl3}}$ presents a later transition state geometry than $\mathbf{TS(2\text{-}3)_{Me}}$, with a longer $H_1\cdots C_1$ distance (1.27 Å) and a shorter $C_1\cdots$Ir distance (2.19 Å). Consistent with this, the following hydrogen transfer does have a slightly higher barrier, although it is still small at 1.3 kcal/mol. The overall cyclometallation process is exothermic by 4.3 kcal/mol.

For the benzoate analogue an unexpected result was obtained. The approach of the aryl moiety towards the metal led to the dissociation of the Ir–O_2 bond and not, as seen before, the Ir–O_1 bond. All attempts to compute the dissociation of the Ir–O_1 bond led instead to the 6-membered C–H activation transition state. The movement of the benzoate moiety is therefore better quantified by the X–Ir–O_1–C_2 torsion, which

decreases from 67.4º in **TS(1-2)$_{Ph}$** to 23.2º in **2$_{Ph}$**. Apart from the orientation of the carboxylate groups, the geometries of **2$_{Ph}$** and **2$_{Me}$** are very similar. To access **TS(2-3)$_{Ph}$** therefore requires significant rotation around the Ir−O_1 bond. However, as described for acetate this rotation is very easy and overall C-H bond cleavage occurs with a low energy barrier of 0.9 kcal/mol. Cyclometallation is exothermic by 5.7 kcal/mol.

The comparison of the acetate system with the trifluoroacetate and bicarbonate, analogues is shown in Figure 2.17. Even though related intermediates to **2$_{Me}$** were computed in both cases, and the following C-H activation transition states were characterised, the inclusion of the zero-point energy corrections caused the enthalpies of these transition states to fall below those of the intermediates. Thus, the low energy barriers computed for the C−H cleavage step with the other bases now disappear and it can be considered that the transition states involved, **TS(1-3)$_{CF3}$** and **TS(1-3)$_{OH}$** lead directly to the cyclometallation products (see Figure 2.17). The limiting step is therefore still associated with the κ^2–κ^1 displacement of the chelating base. Both transition states present earlier geometries than **TS(1-2)$_{Me}$** with increased Ir···C_1, Ir···H_1 and H_1···O_1 distances. Both processes are exothermic, by 5.9 kcal/mol when R = OH and 4.3 kcal/mol when R = CF_3.

For all the systems, **1$_R$**, considered the effect of dichloromethane solvent (the solvent used experimentally in parallel synthetic studies, see section 2.4) was assessed via PCM calculations. These showed a similar trend to that seen with the acetate system with, in each case, a slight stabilization of the rate-limiting transition states, **TS(2-3)$_R$**, by *ca*. 1 kcal/mol as well as a reduction in reaction exothemicity of around 1.5 kcal/mol.

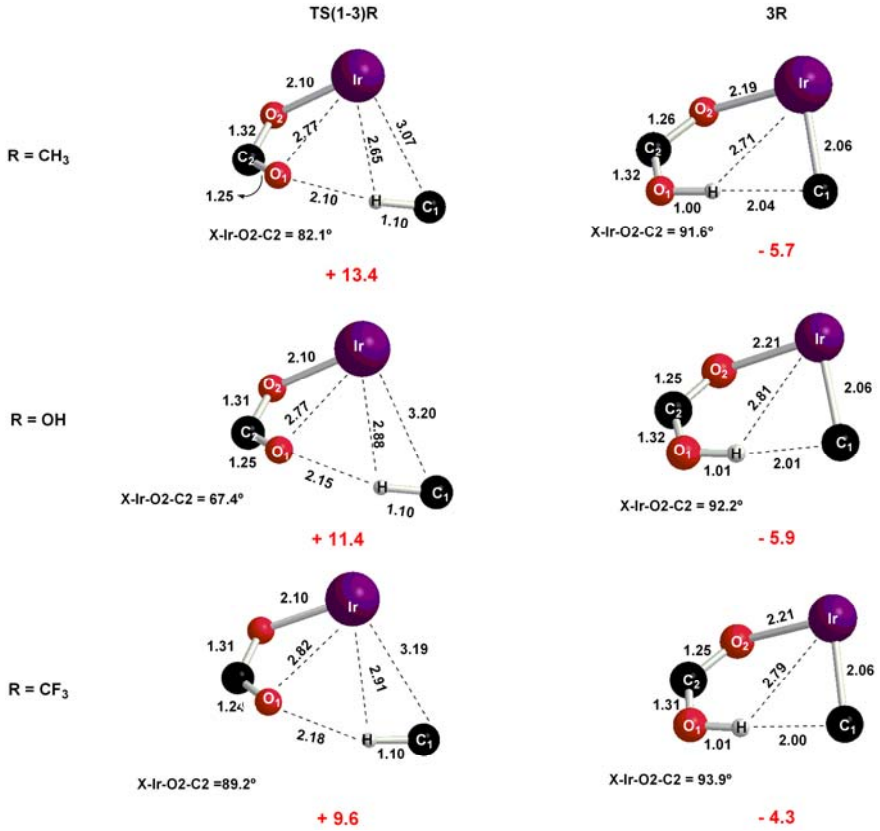

Figure 2.17 - Computed geometrical parameters (Å, degrees) for cyclometallation of $\mathbf{1_R}$ (R = Me, OH, CF_3) via a 6-membered C-H activation transiton state, highlighting the six atoms directly involved. Energies (kcal/mol) are quoted relative to $\mathbf{1_R}$ in each case, in red.

All the computed energies for cyclometallation of the $\mathbf{1_R}$ species via a 6-membered process are brought together in Table 2.1. Also included in Table 2.1 are the $-pK_a$ values[5] associated with the free chelating bases. These will be used as a measure of the proton accepting ability of these bases and is most negative for the strongest base, acetate. Similarly, the strongest bases would be expected to have the greatest metal coordination ability.

RCO_2^-	$TS(1\text{-}2)_R$	2_R	$TS(2\text{-}3)_R$	3_R	$-pK_a$
$CH_3CO_2^-$	13.4	8.6	9.5	- 5.7	- 4.76
$PhCO_2^-$	14.6	10.1	11.0	- 5.7	- 4.31
$OHCO_2^-$	11.4	---	---	- 5.9	- 3.83
$CCl_3CO_2^-$	9.5	1.3	2.6	- 4.3	- 0.65
$CF_3CO_2^-$	9.6	---	---	-4.3	+ 0.23

Table 2.1 – Computed energies (kcal/mol) for cyclometallation of $\mathbf{1_R}$ via a 6-membered C-H activation transition state relative to the appropriate reactant set to zero in each case. $-pK_a$ values are also indicated.[5]

The data in Table 2.1 show that, in general, there is an approximate correlation between the coordinating ability of the chelating base and the ease of κ^2–κ^1 displacement. Thus the barriers via $\mathbf{TS(1\text{-}2)_R}$ are highest for the strongest bases (acetate and benzoate) and lowest with weakest bases (trichloroacetate and trifluoroacetate). This trend is also reflected in the relative energy of the intermediates, $\mathbf{2_R}$, which is much lower in energy for trichloroacetate than for benzoate or acetate.

The correlation between the barrier to C-H bond cleavage via $\mathbf{TS(2\text{-}3)_R}$ and the proton accepting ability of the base is less obvious. Indeed, in the three cases where a distinct barrier was computed this was minimal (< 1.5 kcal/mol). As this step can be thought of as an intramolecular proton transfer it is surprising that so little variation is seen despite a variation of over 5 orders of magnitude in the $-pK_a$ values of the base. To acquire a better understanding of this behaviour, the C_2–O_1 distances and the charge associated with the free oxygen in the κ^1–intermediates ($\mathbf{2_{Me}}$, $\mathbf{2_{Ph}}$ and $\mathbf{2_{CCl3}}$) were computed and compared with the same parameters for the free bases. The results are summarized in Figure 2.18 and show that the C_2–O_1 bond distances are slightly shorter in the intermediates $\mathbf{2_R}$ than for the free bases, indicating greater carbonyl character. The free anions carry significant negative charge on the two oxygen atoms O_A which follows the trend $q(O_A)_{Me} > q(O_A)_{Ph} >> q(O_A)_{CCl3}$, with an overall range of 0.12. This is consistent with the $-pK_a$ values which indicate acetate is the strongest base. In the intermediates $\mathbf{2_R}$ a reduced negative charge is associated with the free oxygen and, although the trend is similar to before, the range in charge is reduced from 0.12 to only 0.05. This indicates that the R group has a much less significant effect on the basicity of the accepting oxygen atom in the κ^1-intermediates than in the free anions. This now

explains why, although the stronger bases do have a lower barrier to C-H activation ($\Delta E^{\ddagger}$ = + 0.9 kcal/mol for both acetate and benzoate whereas $\Delta E^{\ddagger}$ = + 1.3 kcal/mol for trichoroacetate) this effect is very small.

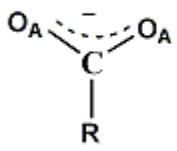

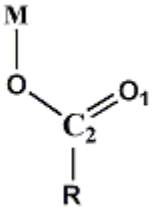

	$C - O_A$	$q (O_A)$	$C - O_1$	$q (O_1)$
R = Me	1.27	- 0.76	1.23	- 0.61
R = Ph	1.27	- 0.73	1.24	- 0.62
R = CCl_3	1.24	- 0.64	1.22	- 0.57

Figure 2.18 - Computed C-O distances (Å) and natural atomic charges on oxygen for intermediates 2_{Me}, 2_{Ph} and 2_{CCl3} via a 6-membered C-H activation transition state and for the equivalent free anions.

In contrast to the weak trend noted above for the barriers to C-H activation, the energy associated with this step (**$2_R \rightarrow 3_R$**) does correlate more strongly with the -pK_a values of the chelating base. Thus ΔE(**$2_R \rightarrow 3_R$**) = -14.3 kcal/mol for acetate and -15.8 kcal/mol for benzoate, while it is only -5.6 kcal/mol for trichloroacetate. Thus, a more favourable C−H bond cleavage step is associated with less accessible κ^1-κ^2 displacement (**$1_R \rightarrow 2_R$**), and *vice versa*. This explains why these cyclometallation reactions all show similar reaction exothermicities (ΔE = - 5.1 kcal/mol ± 0.8 kcal/mol), despite the wide range of bases studied.

2.3.2. Cyclometallation of 1_R via 4-membered C-H activation transition states

Cyclometallation via a 4-membered C−H activation process followed the same two step reaction defined for the acetate species. In all cases, the limiting step was C-H cleavage and so this process will be discussed in detail in the following. The initial displacement of one arm of the chelating base via **$TS(1\text{-}2)_R$**, is the same as that seen already in the 6-membered pathways.

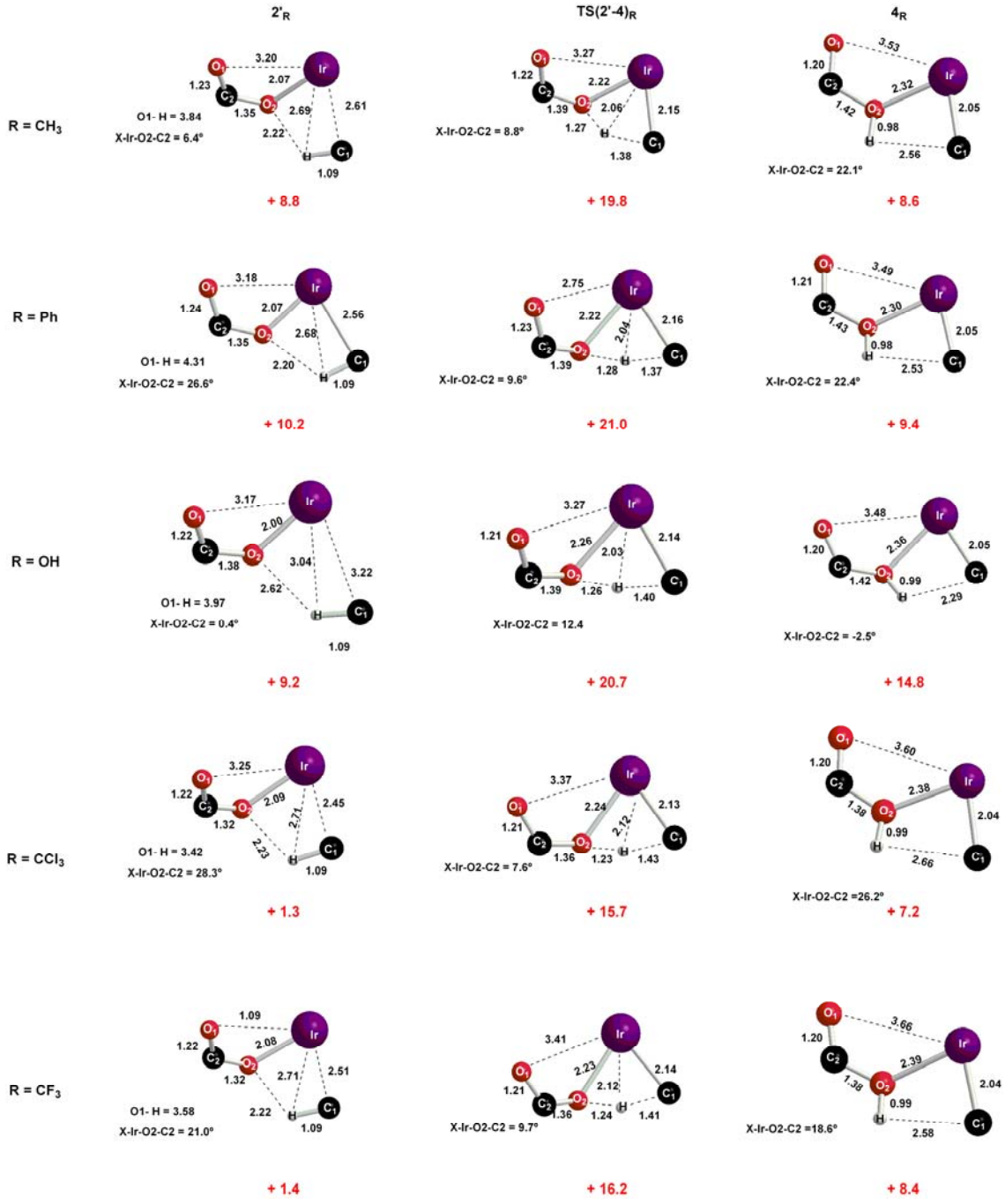

Figure 2.19 - Computed geometrical parameters (Å, degrees) for cyclometallation of $\mathbf{1_R}$ (R = Me, Ph, OH, CCl_3 and CF_3) via a 4-membered C-H activation transition state, highlighting the six atoms directly involved. Energies (kcal/mol) are quoted relative to the appropriate reactant in each case, in red. In the case of R = CCl_3 the only intermediate located is $\mathbf{2_{CCl3}}$, see text.

In most cases an intermediate, $\mathbf{2'_R}$, analogous to $\mathbf{2'_{Me}}$ has been computed. The exception is when R = CCl_3, where the only structure located was $\mathbf{2_{CCl3}}$, the same intermediate as found along the 6-membered pathway. In the cases where both $\mathbf{2'_R}$ and $\mathbf{2_R}$ were located, they were shown to be very close in energy. C-H bond cleavage then occurs via a 4-membered transition state in which the transferring hydrogen, H_1, always

lies closer to O_2 than to C_1. In general the geometries of the transition states are very similar, although those with the stronger bases (R = Me, Ph) exhibit a slightly earlier structure with shorter $C_1\cdots H_1$ distances and longer $H_1\cdots O_1$ distances. This trend was seen previously in the 6-membered C-H activation transition states, although the effect of varying the base is again very small. The final products $\mathbf{4_R}$ have similar Ir−C_1 distances in all cases and a longer Ir−O_2 distance for weaker bases. It is worth noting that the elongation of the Ir−O_2 bond upon proton transfer, seen above with $\mathbf{4_{Me}}$, is even more pronounced with weaker bases.

The computed energies of C−H activation of $[Ir(\eta\text{-Cp})(dmba{-}H)(\kappa^2\text{-}RCO_2)]^+$ complexes via a 4-membered pathway are shown in Table 2.2. As with the intermediates $\mathbf{2_R}$, the $\mathbf{2'_R}$ species are more accessible for the weaker bases. A weak correlation between the proton accepting ability of the base and the barrier to C−H cleavage step is also computed, with the largest values being found when R = CF_3 and CCl_3 (*ca*. 14.5 kcal/mol *cf. ca*. 10.8 kcal/mol when R = Me, Ph or OH). Similarly the C-H activation step is only exothermic for the strongest bases (R = Me: $\Delta E(\mathbf{2'_R \rightarrow 4_R}) = -0.2$ kcal/mol; R = Ph: $\Delta E(\mathbf{2'_R \rightarrow 4_R}) = -0.8$ kcal/mol). With weaker bases this process is endothermic.

RCO_2^-	$2'_R$	$TS(2'\text{-}4)_R$	4_R	$-pK_a$
$CH_3CO_2^-$	8.8	19.8	+ 8.6	- 4.76
$PhCO_2^-$	10.2	21.0	+ 9.4	- 4.31
$OHCO_2^-$	9.2	20.7	+ 14.8	- 3.83
$CCl_3CO_2^-$	1.3	15.7	+ 7.2	- 0.65
$CF_3CO_2^-$	1.4	16.2	+ 8.4	+ 0.23

Table 2.2 - Computed energies (kcal/mol) for cyclometallation of $\mathbf{1_R}$ via a 4-membered C-H activation transition state, relative to the appropriate reactant set to zero in each case. $-pK_a$ values are also indicated.[5]

2.3.3. Cyclometallation of 1_R via oxidative addition C-H activation transition states.

Cyclometallation of $\mathbf{1_R}$ via an oxidative addition process also followed the same two-step pattern defined for the acetate analogue and so the focus will again be on the rate-limiting C-H activation step. Key geometrical parameters and energies for the

stationary points involved are given in Figure 2.20. In each case a product in which hydride was trans to the base was characterised (***t*-5$_R$**) and this involves the C_3-H_2 bond and not the C_1-H_1 bond seen in the previous sections. The C_3 and H_2 centres are therefore highlighted in Figure 2.20.

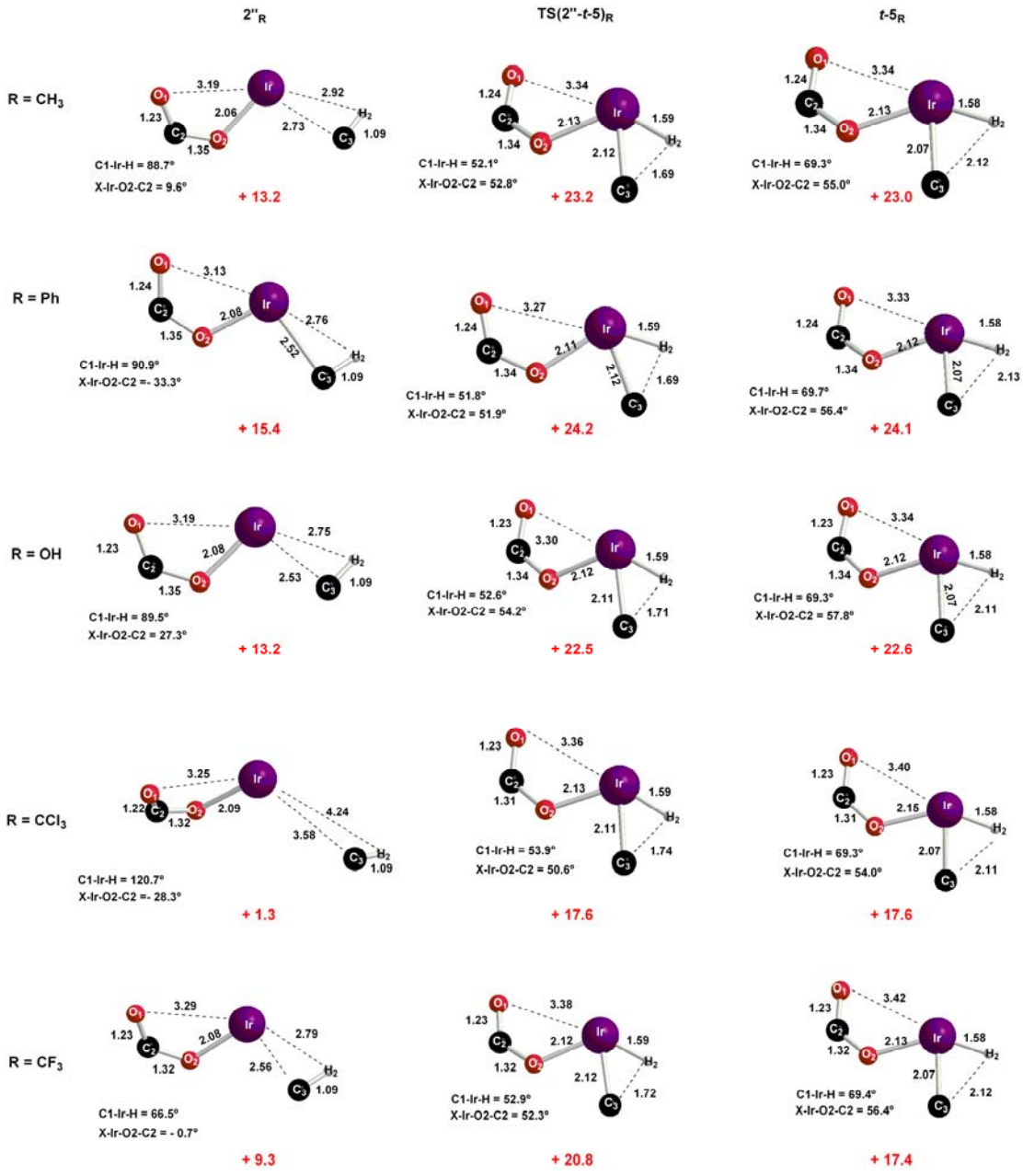

Figure 2.20 - Computed geometrical parameters (Å, degrees) for cyclometallation of **1$_R$** (R = Me, Ph, OH, CCl_3 and CF_3) via oxidative addition C-H activation transition state, highlighting the six atoms directly involved. Energies (kcal/mol) are quoted relative to the appropriate reactant in each case, in red. In the case of R = CCl_3 the only intermediate located is **2$_{CCl3}$**, see text.

For R = Ph, OH and CF_3 the precursor to oxidative addition was shown to be species $\mathbf{2''_R}$ analogous to $\mathbf{2''_{Me}}$ described previously. When R = CCl_3 $\mathbf{2_{CCl3}}$ was again the only intermediate located. The oxidative addition transition states $\mathbf{TS(2''\text{-}\textit{t}\text{-}5)_R}$ are all very similar and show late geometries with almost fully formed $H_2\cdots$Ir and $C_3\cdots$Ir bonds. In addition, the geometries of the products, $\mathbf{\textit{t}\text{-}5_R}$, are also almost identical. These observations suggest that the nature of the base does not significantly affect the oxidative addition step and this is supported by the computed energetics of this process (see Table 2.3). Thus no correlation between the activation barrier and the base strength is seen and in each case oxidative addition is significantly endothermic. The much higher barrier and greater endothermicity when R = CCl_3 is due to the greater stability of the intermediate $\mathbf{2_{CCl3}}$ in that case.

$\mathbf{RCO_2^-}$	$\mathbf{2''_R}$	$\mathbf{TS(2''\text{-}\textit{t}\text{-}5)_R}$	$\mathbf{\textit{t}\text{-}5_R}$	$\mathbf{-\textit{pK}_a}$
$\mathbf{CH_3CO_2^-}$	13.2	23.2	+ 23.0	- 4.76
$\mathbf{PhCO_2^-}$	15.5	24.2	+ 24.1	- 4.31
$\mathbf{OHCO_2^-}$	13.2	22.5	+ 22.6	- 3.83
$\mathbf{CCl_3CO_2^-}$	1.3	17.6	+ 17.9	- 0.65
$\mathbf{CF_3CO_2^-}$	9.3	20.8	+ 17.4	+ 0.23

Table 2. 3 - Computed energies (kcal/mol) for cyclometallation of $\mathbf{1_R}$ via oxidative addition C-H activation transition state, relative to the appropriate reactant set to zero in each case. -pK_a values are also indicated.[5]

2.3.4. Summary

The cyclometallation reactions of $[Ir(\eta\text{-Cp})(dmba{-}H)(\kappa^2\text{-}RCO_2)]^+$ species ($\mathbf{1_R}$, where R = Ph, CF_3, CCl_3, and OH) have been computed via a 6-membered, 4-membered and oxidative addition C-H activation transition states. In all cases, the lowest energy pathway is the 6-membered process. In this case the limiting step is the κ^2-κ^1 displacement of the base and when a C-H cleavage process was characterized the barrier was no more than 1.3 kcal/mol. Generally, weak bases enhance reactivity through easier base displacement and this follows the trend R = $CF_3 \approx CCl_3 < OH < CH_3 < Ph$. Only a weak correlation between the barrier to C−H cleavage and carboxylate basicity is computed. Overall, the cyclometallation reaction is exothermic in all cases and shows a minimal variation regardless of the intramolecular base involved.

The C−H cleavage becomes the limiting step of the process when activation occurs via a 4-membered transition state. A weak correlation between the nature of the base and the energetics of C−H cleavage is found and this step is only exothermic for strong bases. Cyclometallation via this route is always endothermic, although the product $\mathbf{4_R}$ would probably easily rearrange to $\mathbf{3_R}$.

The oxidative addition pathway shows that the nature of the base does not significantly affect the energies of this process. In all cases cyclometalation is strongly endothermic.

2.3.5. Cyclometallation of [Ir(η-Cp)(dmba−H)(κ²-CF₃SO₃)]⁺, 1OTf

The results reported above show that the limiting step of the C−H activation process is the κ^2-κ^1 displacement. In addition, the ambiphilic nature of the C-H activation, in which both the metal centre and the free arm of the base are involved, means that a strong base may not be required to break the C-H bond. These two effects allow us to target a very weak base, triflate ($-pK_a$ = +14.9) which, due to its poor coordinating ability towards the metal, would be expected to lower the energy barrier for the κ^2-κ^1 displacement.

The following will present the details of the cyclometallation of [Ir(η-Cp)(dmba−H)(κ^2-CF_3SO_3)]$^+$, $\mathbf{1_{OTf}}$, via a 6-membered C-H activation transition state. The analogous 4-membered and oxidative addition pathways were also computed, however, these proved to be much higher in energy.

The first step of the process is described in Figure 2.21. It involves the dissociation of one arm of the triflate by an elongation of the Ir−O_1 bond from 2.24 Å in $\mathbf{1_{OTf}}$ to 3.57 Å in $\mathbf{2_{OTf}}$, and the rotation around the Ir−O_2 bond, in this case quantified by the X−Ir−O_2−S angle which reduces from 104.5º in $\mathbf{1_{OTf}}$ to 37.8º in $\mathbf{2_{OTf}}$. These changes are all very similar to those seen with the acetate system. Intermediate $\mathbf{2_{OTf}}$ resembles $\mathbf{2_{Me}}$, $\mathbf{2_{Ph}}$ and $\mathbf{2_{CCl3}}$, in having a shorter contact between H_1 and O_2 (2.25 Å) than to O_1 (2.44 Å). However, in this case the κ^1-intermediate $\mathbf{2_{OTf}}$ is 3 kcal/mol more stable than the κ^2-reactant $\mathbf{1_{OTf}}$.

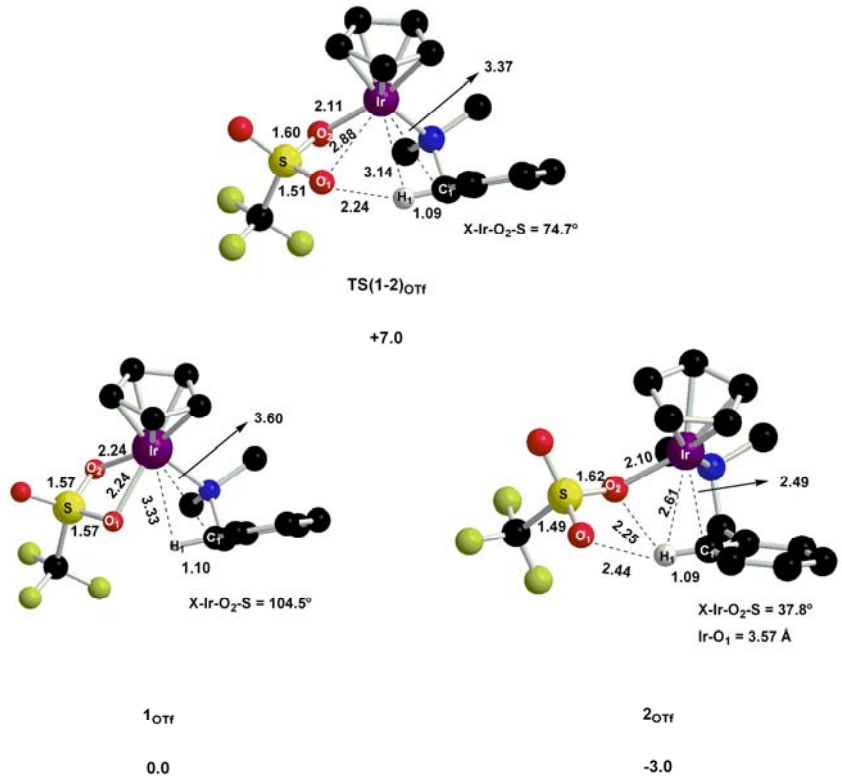

Figure 2.21 - Computed stationary points (kcal/mol, distances in ångstroms) for κ^2–κ^1 displacement of triflate in $\mathbf{1}_{\mathbf{OTf}}$. Non-participating hydrogens are omitted for clarity.

Figure 2.22 shows the C−H cleavage step. In contrast with all the bases studied thus far, the hydrogen transfer does not require significant rotation around the Ir−O_2 bond. This is due to the tetrahedral geometry around S in the triflate ligand. Energetically, C−H cleavage requires the highest activation energy so far ($\Delta E^{\ddagger}$ = +3.8 kcal/mol), which also correlates with the low basicity of trifate. In addition, $\mathbf{TS(2\text{-}3)_{OTf}}$ exhibits the latest transition state geometry, in which the $C_1\cdots H_1$ distance has lengthened by over 0.2 Å to 1.32 Å and the $O_1\cdots H_1$ distance is only 1.35 Å. The C-H activation step is exothermic by 4.3 kcal/mol.

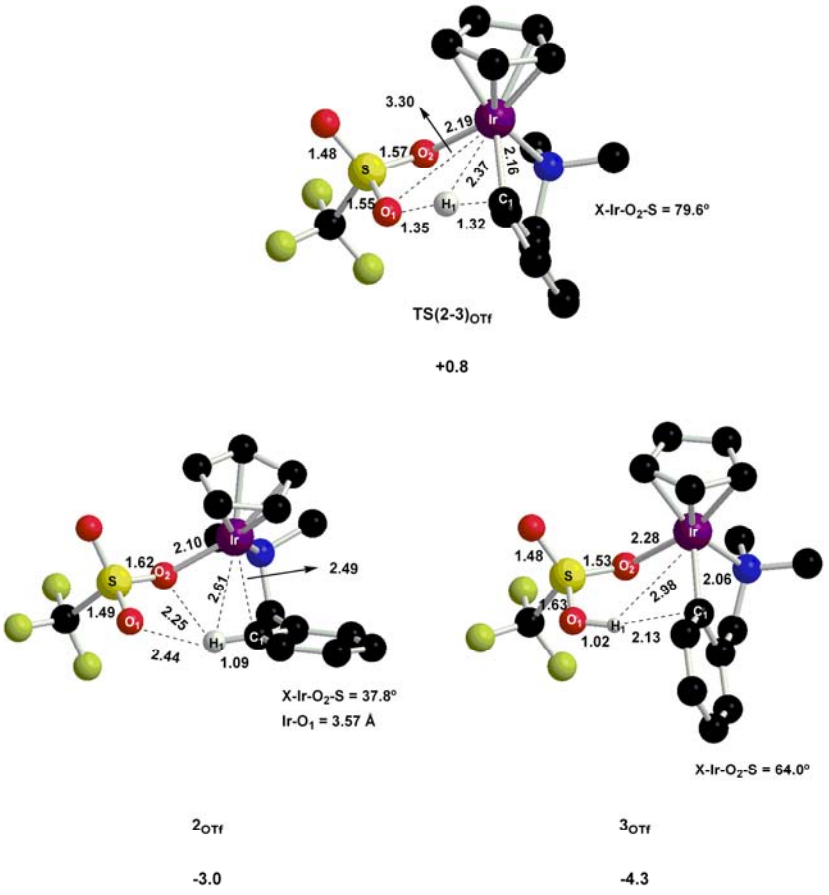

Figure 2.22 - Computed stationary points (kcal/mol, distances in ångstroms) for C-H activation of $\mathbf{2_{OTf}}$ via a 6-membered transition state. Non-participating hydrogens are omitted for clarity.

A complete profile for cyclometallation of $\mathbf{1_{OTf}}$ is shown in Figure 2.23. The overall reaction remains as a two step process in which the limiting step of the process is still the κ^2-κ^1 displacement of the base. This step only requires an activation energy of +7.0 kcal/mol, the lowest energy barrier computed for all the range of bases studied so far. The following C-H activation requires a relatively high barrier of +3.8 kcal/mol. In contrast to what was seen with the carboxylate systems, the κ^1-intermediate $\mathbf{2_{OTf}}$ is now more stable than the κ^2-reactant $\mathbf{1_{OTf}}$. Therefore in this case, $\mathbf{2_{OTf}}$ would be expected to be the dominant species present and the overall cyclometallation process would require an energy barrier of only +3.8 kcal/mol. This suggests that this triflate system would be the most reactive species of the systems considered so far. These relative sizes of the energies barriers for κ^2-κ^1 displacement and C-H activation have a direct correlation with the coordination ability and the basicity, respectively, of the triflate ligand.

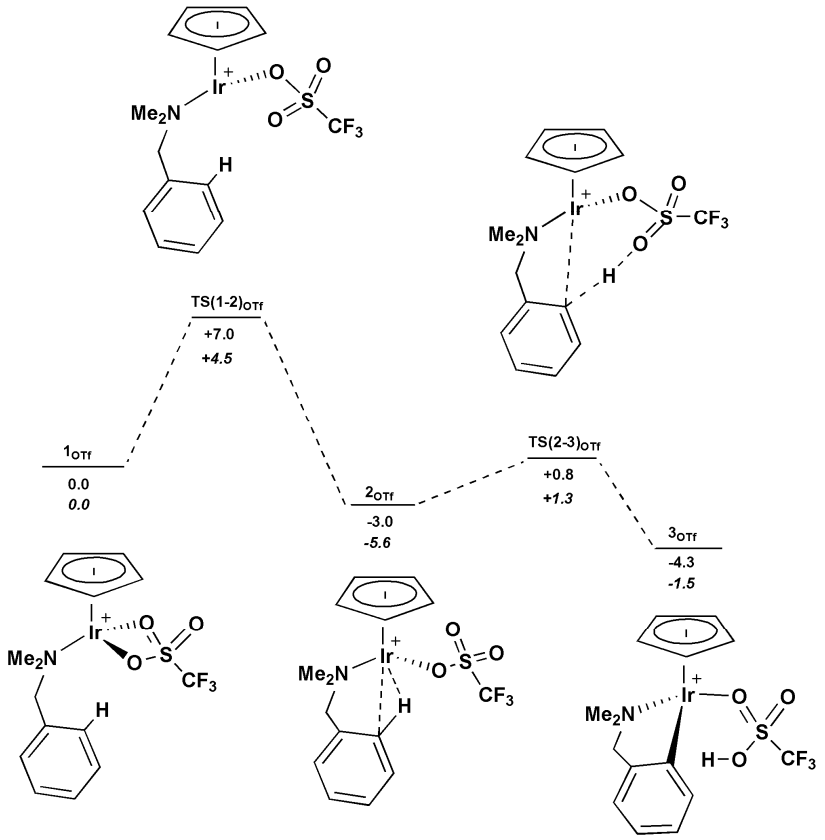

Figure 2.23 - Computed reaction profile (kcal/mol) for cyclometallation of $\mathbf{1_{OTf}}$ via a 6-membered C-H activation transition state.

Energies for all the stationary points incorporating a PCM correction (dichloromethane) are shown in italics in Figure 2.23. Both $\mathbf{TS(1\text{-}2)_{OTf}}$ and $\mathbf{2_{OTf}}$ are stabilized by about 2.5 kcal/mol. In contrast $\mathbf{TS(2\text{-}3)_{OTf}}$ and $\mathbf{3_{OTf}}$ are destabilised, by 0.5 kcal/mol and 2.8 kcal/mol respectively. Therefore solvent corrections significantly increase the barrier to C−H cleavage to +6.9 kcal/mol. However, as this step is rate-limiting in this case (as $\mathbf{2_{OTf}}$ is more stable than $\mathbf{1_{OTf}}$) this triflate system still presents the lowest computed barrier to cyclometallation so far.

The PCM calculation shows cyclometallation of $\mathbf{2_{OTf}}$, is endothermic by 4.1 kcal/mol, however, this system remains a promising target for experiment as the barrier of C−H activation is still small and this endothermicity should be overcome by the displacement of the CF_3SO_3H by Cl^- in the final step of the cyclometallation reaction. The following section will therefore describe the experimental investigations[6] of these cyclometallation reactions and compare the findings to the computational results.

2.4. Combining experimental and computational studies

Experimentally, the cyclometallation reaction of dmba-H by $[IrCp^*Cl_2]_2$ in the presence of the relevant sodium carboxylate, sodium triflate and sodium bicarbonate were carried out at room temperature. The mixture of the three reactants in dichloromethane was stirred for 18 hours, after which time the amount of product was determined by ^1H NMR spectroscopy. Table 2.4 summarizes the experimental yield obtained for these cyclometallation reactions.

intramolecular base	% yield $[IrCp^*(dmba)Cl]^+$
$CH_3CO_2^-$	65%
$PhCO_2^-$	29%
$OHCO_2^-$	---
$CCl_3CO_2^-$	28%
$CF_3CO_2^-$	55%
$CF_3SO_3^-$	50%*

Table 2.4 – Experimental yields of $[IrCp^*(dmba)Cl]^+$ obtained in the cyclometallation of dmba-H by $[IrCpCl_2]_2$ in the presence of a chelating base in dichloromethane at 18 hours at room temperature. * yield obtained after 4 days.

The highest yield is for the acetate (65%) then trifluoroacetate (55%), with benzoate (29%) and trichloroacetate (28%) approximately the same. A 50% yield for the triflate system was obtained but only after 4 days, very little conversion being achieved after 18 hours. Finally, the bicarbonate gives no product and this is thought to be due to the poor solubility of sodium bicarbonate in CD_2Cl_2.

Computationally, weaker bases are predicted to enhance the cyclometallation process due to lower energy barriers, the triflate being the most promising. However, the overall rate of formation of the cyclometallated products does not follow a simple correlation with the activation barriers computed for this process in the $[Ir(\eta\text{-}Cp)(dmba{-}H)(\kappa^2\text{-}RCO_2)]^+$ species, $\mathbf{1_R}$, and $[Ir(\eta\text{-}Cp)(dmba{-}H)(\kappa^1\text{-}CF_3SO_3)]^+$, $\mathbf{2_{OTf}}$. Indeed, $\mathbf{1_{Me}}$, which has the highest computed barrier for cyclometallation ($\Delta E^{\ddagger}$ = +11.9 kcal/mol, solvent-corrected), is the most efficient experimentally, while $\mathbf{1_{Ph}}$, which has a similar computed barrier, is much less effective. In addition, $\mathbf{2_{OTf}}$ ($\Delta E^{\ddagger}$ = +6.9 kcal/mol) is very slow and only reaches a reasonable yield after 4 days. With $\mathbf{2_{CCl3}}$ and $\mathbf{2_{CF3}}$,

which present very similar computed energies ($\Delta E^{\ddagger}$ = +9.5 kcal/mol and $\Delta E^{\ddagger}$ = +9.6 kcal/mol, respectively) very different experimental outcomes are seen (28% and 55% yields respectively). Therefore, it can be concluded that the rate determining step does not occur during the cyclometallation reactions of $\mathbf{1_R}$ and $\mathbf{2_{OTf}}$ and that the additional steps that are involved in the overall reaction starting from the $[IrCp^*Cl_2]_2$ dimer need to be considered.

The proposed mechanism for the reaction of dmba−H with $[Ir(\eta\text{-}Cp^*)Cl_2]_2$ in the presence of sodium acetate requires two processes, the dimer opening and the subsequent cyclometallation, the latter being the process considered so far (see Figure 2.2). In order to assess dimer opening, we computed the energies of the complexes from the dimer to the cyclometallation precursor, $\mathbf{1_R}$. Hence, $[Ir(\eta\text{-}Cp)Cl_2(\kappa^1\text{-}RCO_2)]^-$ and $[Ir(\eta\text{-}Cp)Cl(\kappa^2\text{-}RCO_2)]$ (and their triflate analogues) were computed to represent the likely initial species formed upon dimer opening.

Figure 2.24 shows the energies of all these species after correction for dichloromethane solvent via PCM calculations. The graphic is divided in three sections. Firstly, the formation of $[Ir(\eta\text{-}Cp)Cl_2(\kappa^1\text{-}RCO_2)]^-$ by addition of the base. This process is downhill in all cases and in general is more favourable for stronger bases. The second step is the displacement of one chloride ligand and the formation of $[Ir(\eta\text{-}Cp)Cl(\kappa^2\text{-}RCO_2)]$ featuring a κ^2-chelating base. In this case, the process is only downhill with strong bases (R = Me, Ph, OH). This correlates with the higher coordination ability of stronger bases toward the metal. Finally, substitution of chloride by dmba−H forms the intermediates $\mathbf{1_R}$ and this process is uphill in all cases. An equivalent sequence of events occurs for the triflate analogue.

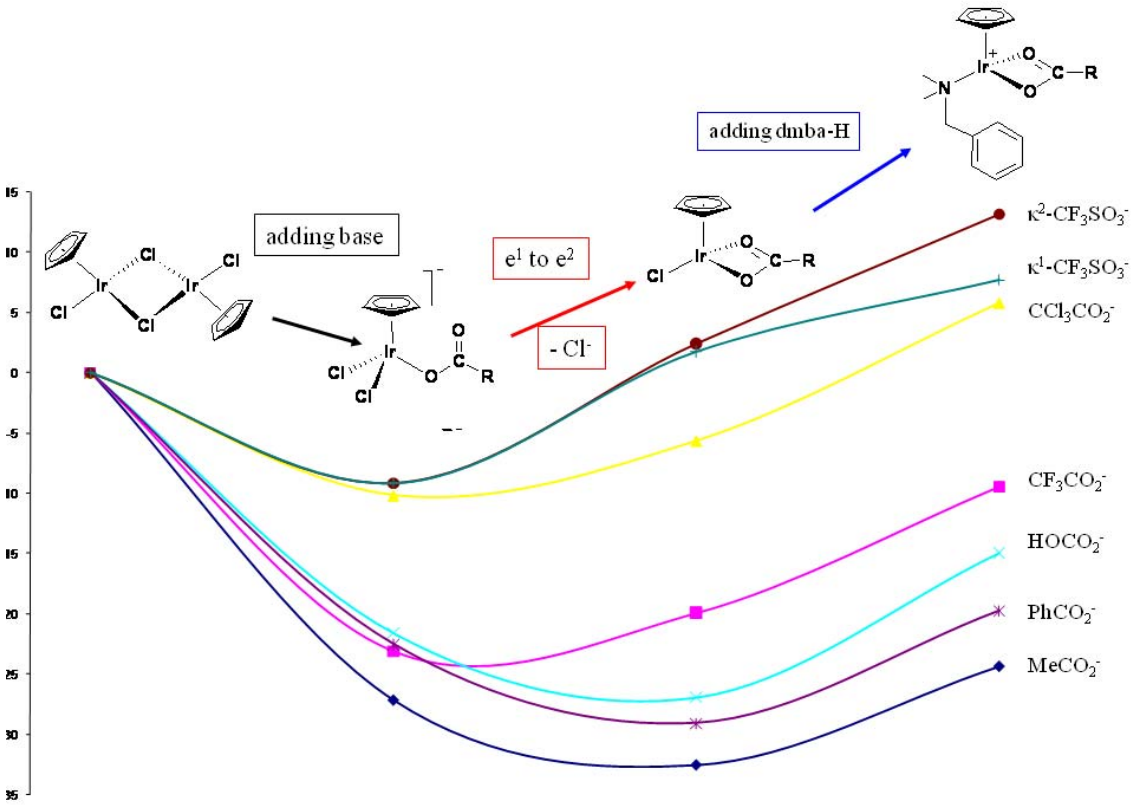

Figure 2.24 – Computed solvent energies (kcal/mol) for the key intermediates in the formation of κ^2-intermediate $\mathbf{2_R}$ by dimer opening computed for dichloromethane by PCM method. In the case of the triflate analogue, κ^1-intermediate $\mathbf{2_{OTf}}$ was also considered.

Overall, stronger bases appear to favour the opening of the dimer and a clear difference between the computational values for the acetate and triflate emerges. Figure 2.25 compares the overall process for these two systems, from opening the dimer to the final cyclometallation products. For the acetate system, formation of $\mathbf{1_{Me}}$ from [Ir(η-Cp)Cl(κ^2-OAc)] is slightly uphill, but it is followed by cyclometallation and displacement of HOAc by Cl^- both of which are exothermic processes which lead to a favourable overall reaction. In contrast, the formation of $\mathbf{2_{OTf}}$ and its cyclometallation are both significantly endothermic and although the final displacement of CF_3SO_3H by Cl^- is exothermic, the overall reaction remains approximately thermo-neutral. Therefore, the results are now consistent with the experimental yields in that a much more efficient reaction is computed with acetate rather than with triflate.

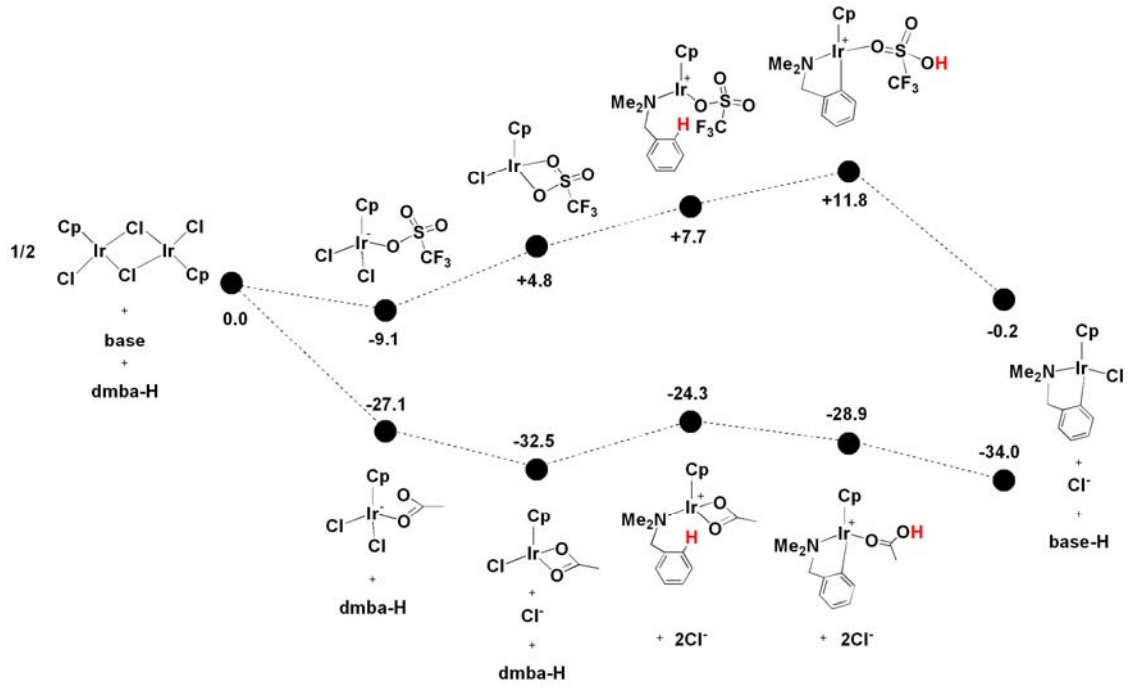

Figure 2.25 - Computed energies profile (kcal/mol) for key intermediates in the cyclometallation reaction of dmba-H by $[IrCpCl_2]_2$ in the presence of acetate or triflate as intramolecular bases. All energies include the solvation correction for dichloromethane by the PCM method.

2.5. Conclusions

DFT calculations have been employed to provide insight into the role played by the base in the cyclometallation reactions of dmba−H with $[IrCpCl_2]_2$. Starting from the model intermediate $[Ir(\eta\text{-}Cp)(dmba{-}H)(\kappa^2\text{-}RCO_2)]^+$ the cyclometalation via 6-membered, 4-membered and oxidative addition C-H activation transition states were assessed. In all cases, the 6-membered mechanism is the most accessible pathway in which κ^2- κ^1 displacement of the base is the rate limiting step and cyclometallation is an exothermic process. When the C−H activation occurs via 4-membered or oxidative addition mechanisms the C−H cleavage becomes the limiting step of the process. These processes have much higher activation barriers and are significantly endothermic.

Generally, weak bases enhance reactivity through an easier κ^2- κ^1 displacement of the base and the activation energy for this step follows the trend R = $CF_3 \approx CCl_3 <$ OH < $CH_3 <$ Ph. The analogous triflate system was also computed and in this case the κ^1-intermediate was found to be more stable than its κ^2-isomer. Cyclometallation was predicted to occur with a barrier of less than 7 kcal/mol and so this system was identified as a promising target for experiment studies.

Parallel synthetic studies confirm the ability of a range of chelating bases to effect cyclometallation of dmba-H with $[Ir(\eta\text{-}Cp^*)Cl_2]_2$. However, no simple correlation between the computed energy barriers and the experimental reactivity was seen. This suggests that the cyclometallation step is not rate determining in the overall reaction. Instead PCM calculations suggest that dimer opening controls the reactivity, this being much more favorable when acetate is employed rather than triflate. This is consistent with the experimentally observed yields.

A key feature computed in the cyclometallation reactions of $\mathbf{1_R}$ is the ambiphilic nature of the C−H activation step. The ambiphilic character of this process is defined by the interactions between the reacting C−H bond with both the metal and the free oxygen of the chelating base. These interactions combine to facilitate bond cleavage with a very small energy barrier. In the acetate model less metal involvement in the C−H activation transition state is computed, while with triflate shorter metal contacts are required due to its poor basicity. In addition, the fact that such a weak base promotes C−H activation through a low energy barrier highlights how powerful a tool is produced when these two features are brought together.

This synergy allows us to identify this behaviour as an *ambiphilic metal ligand assisted* C−H activation mechanism (AMLA). Throughout this chapter, the cyclometallation reaction of $\mathbf{1_R}$ followed an AMLA mechanism where the C−H activation step proceeds via a 6-memebered transition state. In the same way, proton transfer onto the inner oxygen also requires interaction with both the base and the metal, although in this case the lower availability of the base requires more metal involvement. This process involves four centres and so can be described as an AMLA-4 mechanism. Thus, depending on the number of atoms involved in the C-H activation transition state an AMLA-4 or AMLA-6 mechanism is defined.

2.6. References

1. A. D. Ryabov, I. K. Sakodinskaya and A. K. Yatsimirsky, *J. Chem. Soc.-Dalton Trans.*, 1985, 2629-2638.
2. D. L. Davies, S. M. A. Donald and S. A. Macgregor, *J. Am. Chem. Soc.*, 2005, **127**, 13754-13755.
3. D. L. Davies, O. Al-Duaij, J. Fawcett, M. Giardiello, S. T. Hilton and D. R. Russell, *Dalton Trans.*, 2003, 4132-4138.
4. D. L. Davies, S. M. A. Donald, O. Al-Duaij, S. A. Macgregor and M. Poelleth, *J. Am. Chem. Soc.*, 2006, **128**, 4210-4211.
5. J. F. J. Dippy, S.R.C.Hughes and A.Rozanki, *J. Chem. Soc.*, 1959, 2492.
6. Y. Boutadla, *Leicester University*, PhD Thesis, **unpublished results**.

3. Factors affecting cyclometallation: metal, substrate and overall charge of the complex

3.1. Introduction

The role of the chelating base in the cyclometallation reactions of dmba−H with $[IrCl_2Cp^*]_2$ was assessed in Chapter 2 and a combination of experimental observations by Davies *et al.*[1] and calculations has allowed a better understanding of the mechanism. Continuing this research and in order to explore the generality of this cyclometallation reaction, Davies *et al.*[1] also tested this process with $[RhCl_2Cp^*]_2$ and $[RuCl_2(p\text{-cymene})]_2$ with both dmba-H and a number of related imines (ArCH=NR) as substrates. The results showed that the iridium system reacts with all substrates while the rhodium and ruthenium systems only react with the imines. Therefore, in this chapter the effect of how changes in the metal and the substrate can affect the cyclometallation reaction will be assessed. In addition, the effect of the overall charge of the metal complex will also be assessed by considering a number of neutral complexes.

In changing the metal centre the $\{Ir(\eta\text{-Cp})\}^{2+}$ fragment will be substituted by the $\{Rh(\eta\text{-Cp})\}^{2+}$ and $\{Ru(\eta\text{-}C_6H_6)\}^{2+}$ fragments, maintaining overall cationic systems. To achieve neutral species, two different approaches have been followed: (I) the variation of the metal fragment from $\{Ir(\eta\text{-Cp})\}^{2+}$ to $\{Ru(\eta\text{-Cp})\}^{+}$ and (II) a change of the base from the mono-ionic acetate ($^-$OAc) to the di-ionic base carbonate (CO_3^{2-}).

3.2. Cationic metal complexes: cyclometallation reaction of $[Rh(\eta\text{-Cp})(dmba{-}H)(\kappa^2\text{-OAc})]^+$ ($\mathbf{1_{Rh+}}$) and $[Ru(\eta\text{-}C_6H_6)(dmba{-}H)(\kappa^2\text{-OAc})]^+$ ($\mathbf{1_{Ru+}}$)

In Chapter 2 the cyclometallation reaction of dmba−H with $[IrCl_2Cp^*]_2$ in the presence of acetate was assessed by the model $[Ir(\eta\text{-Cp})(dmba{-}H)(\kappa^2\text{-OAc})]^+$. As experimental observations showed no cyclometallated product when dmba−H was reacted in the same conditions with $[RhCl_2Cp^*]_2$ and $[RuCl_2(p\text{-cymene})]_2$ systems, our approach will be to compute analogous systems to $\mathbf{1_{Me}}$ such $[Rh(\eta\text{-Cp})(dmba{-}H)(\kappa^2\text{-OAc})]^+$ ($\mathbf{1_{Rh+}}$) and $[Ru(\eta\text{-}C_6H_6)(dmba{-}H)(\kappa^2\text{-OAc})]^+$ ($\mathbf{1_{Ru+}}$) in order to assess these differences in reactivity. This series of studies will also highlight the role of the metal centre on the C-H activation processes and the overall cyclometallation reaction.

Previously, the cyclometallation reaction of $\mathbf{1_{Me}}$ was described by a κ^2-κ^1 displacement of acetate followed by C−H cleavage, where two transition states were located. The construction of reaction profiles for $\mathbf{1_{Rh+}}$ and $\mathbf{1_{Ru+}}$ was built up from the re-optimization of the transition states $\mathbf{TS(1\text{-}2)_{Me}}$ and $\mathbf{TS(2\text{-}3)_{Me}}$ where the $\{Ir(\eta\text{-}Cp)\}^{2+}$ fragment was substituted by $\{Rh(\eta\text{-}Cp)\}^{2+}$ and $\{Ru(\eta\text{-}C_6H_6)\}^{2+}$. Characterization of these transition states by IRC calculations followed by geometry optimizations led to the new reactant, intermediate and product geometries. In both cases transition states corresponding to κ^2-κ^1 displacement and C−H activation, as well as a κ^1-intermediate, similar to those computed in $\mathbf{1_{Me}}$ system, were characterized. However, the inclusion of the zero-point energy correction caused the enthalpies of the second C−H activation transition state to fall below that of the κ^1-intermediates. Similar behaviour was previously observed in Chapter 2 for the $\mathbf{1_{CF3}}$ and $\mathbf{1_{OH}}$ systems. Therefore, the cyclometallation processes in $\mathbf{1_{Rh+}}$ and $\mathbf{1_{Ru+}}$ will be described as one step reaction proceeding via $\mathbf{TS(1\text{-}3)_{Rh+}}$ and $\mathbf{TS(1\text{-}3)_{Ru+}}$ which lead directly to the final cyclometallated products. Only the AMLA-6 mechanism was computed as it was previously shown to be the lowest energy pathway.

3.2.1. Structural changes in the cyclometallation of 1_{Rh+} and 1_{Ru+}

The computed geometries for the reactants $\mathbf{1_{Rh+}}$ and $\mathbf{1_{Ru+}}$ are very similar to that of $\mathbf{1_{Me}}$, with only small variations in the M···H_1, M···C_1 and O_1···H_1 distances being computed. Indeed, M···H_1 varies from 3.39 to 3.50 Å, M···C_1 from 3.60 to 3.72 Å and O_1···H_1 from 2.51 to 2.70 Å. In addition, geometries of the final products $\mathbf{3_{Me}}$, $\mathbf{3_{Rh+}}$ and $\mathbf{3_{Ru+}}$ exhibit only minimal changes.

Figure 3.1 shows the overall reaction profile for the cyclometallation reaction of $\mathbf{1_{Rh+}}$. The transition state, $\mathbf{TS(1\text{-}3)_{Rh+}}$, describes the dissociation of one arm of the acetate with an increase in the Rh−O_1 distance from 2.15 Å in $\mathbf{1_{Rh+}}$ to 2.72 Å in $\mathbf{TS(1\text{-}3)_{Rh+}}$, and the approach of the aryl moiety towards the metal ($\mathbf{TS(1\text{-}3)_{Rh+}}$: Rh···$C_1$ = 2.92 Å; Rh···H_1 = 2.58 Å). The combination of these changes leads to a close H_1···O_1 contact of 2.08 Å in $\mathbf{TS(1\text{-}3)_{Rh+}}$. The process requires an activation energy of 12.4 kcal/mol and the cyclometallation is exothermic by 2.5 kcal/mol.

Analogous behaviour has been computed for the cyclometallation reaction of $\mathbf{1}_{Ru+}$ described in Figure 3.2. In this case, the activation energy is 12.9 kcal/mol and the process is almost thermoneutral (ΔE_{Ru+} = -0.5 kcal/mol).

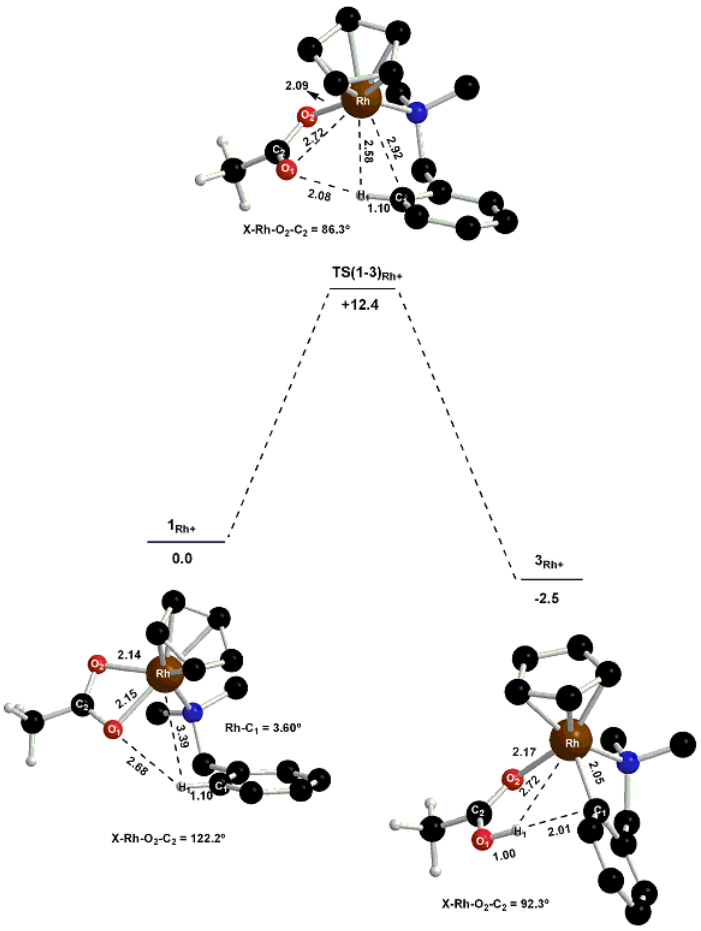

Figure 3.1 - Computed energy profile (kcal/mol, distances in ångstroms) for the cyclometallation reaction $\mathbf{1}_{Rh+}$. Non-participating hydrogens are omitted for clarity.

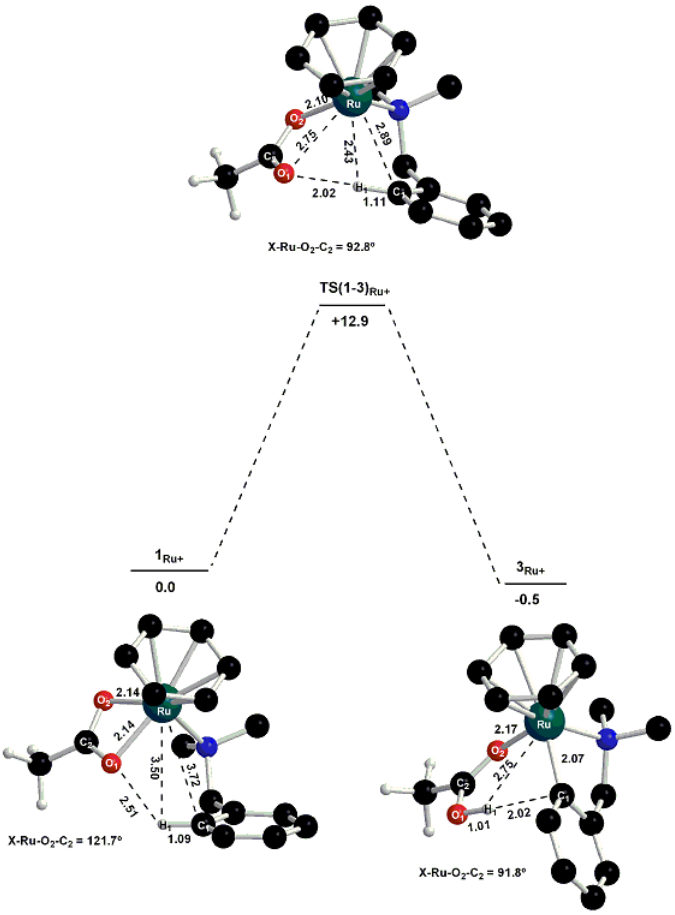

Figure 3.2 - Computed reaction profile (kcal/mol, distances in ångstroms) for the cyclometallation reaction of $\mathbf{1}_{\mathbf{Ru+}}$. Non-participating hydrogens are omitted for clarity.

The major difference computed between these processes and the iridium system can be seen in the structures for the three computed transition states shown in Figure 3.3, $\mathbf{TS(2\text{-}3)_{Me}}$, $\mathbf{TS(1\text{-}3)_{Rh+}}$ and $\mathbf{TS(1\text{-}3)_{Ru+}}$. Variations in the distances between the metal and the $C_1{-}H_1$ bond are seen and follow the trend Ru < Rh < Ir. The same trend can also be seen in the $O_1\cdots H_1$ contacts. Thus when more metal involvement is computed a stronger interaction between H_1 and the free oxygen of the acetate is also observed. The combination of these two interactions will help the proton transfer. Despite these changes there is not in a significant difference in the activation energy required for the cyclometallation reaction ($\Delta E^{\ddagger}_{Ir}$ = 13.4 kcal/mol, $\Delta E^{\ddagger}_{Rh+}$ = 12.4 kcal/mol and $\Delta E^{\ddagger}_{Ru+}$ = 12.9 kcal/mol). The reasons for these results are explored in the following section.

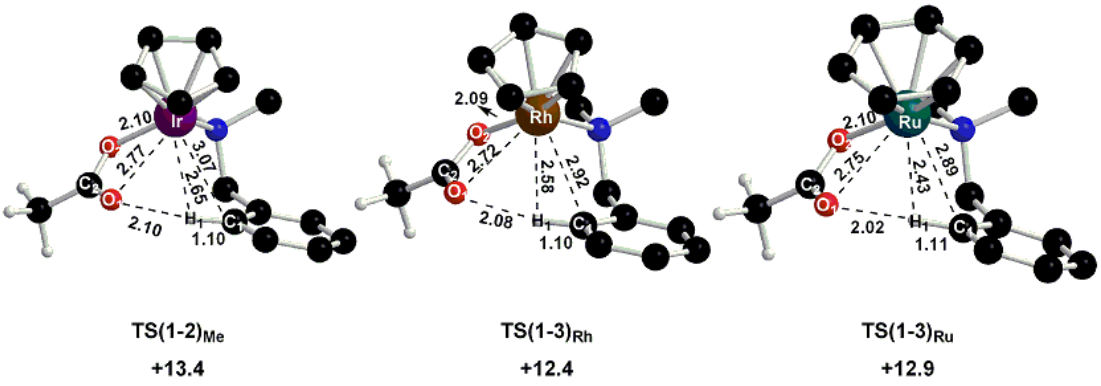

Figure 3.3 - Computed stationary points (kcal/mol, distances in ångstroms) of **TS(1-2)$_{Me}$**, **TS(1-3)$_{Rh+}$** and **TS(1-3)$_{Ru+}$**. Non-participating hydrogens are omitted for clarity

3.2.2. Trends in the energetics of the cyclometallation reaction of 1$_{Me}$, 1$_{Rh+}$ and 1$_{Ru+}$

The activation barriers required for the cyclometallation of **1$_{Me}$**, **1$_{Rh+}$** and **1$_{Ru+}$** ($\Delta E^{\ddagger}$) and the overall energy change of the process ($-\Delta E$) are shown in Table 3.1. Despite the change of metal centre, the activation barriers are very similar although the relative stabilities of the final cyclometallated products are different, with ΔE following the trend Ir > Rh > Ru.

	$\Delta E^{\ddagger}$ (kcal/mol)	**ΔE (kcal/mol)**
1$_{Me}$	13.4	-5.6
1$_{Rh+}$	12.4	-2.5
1$_{Ru+}$	12.9	-0.5

Table 3.1 – Summary of the activation barriers $\Delta E^{\ddagger}$ (kcal/mol) for the C-H activation of **1$_{Me}$**, **1$_{Rh+}$** and **1$_{Ru+}$** and the overall energy of the process (ΔE).

In order to understand ΔE a closer look at the cyclometallation reaction shown in Figure 3.4 is required. This process involves both the making and breaking of bonds, with the M−O and C−H bonds being broken and the O−H and M−C being formed.

Figure 3.4 – General cyclometallation reaction for $[M(ring)(dmba\text{-}H)(\kappa^2\text{-}OAc)]^+$ to form $[M(ring)(dmba)(\kappa^1\text{-}HOAc)]^+$ (M = Ir, Rh; ring = Cp and M = Ru; ring = C_6H_6)

Therefore, the trends in ΔE can be approximated by the following equation, where D = dissociation energy:

$$\Delta E \approx -(D_{M-C} + D_{O-H}) + (D_{M-O} + D_{C-H}) \quad \textbf{(Equation 1)}$$

A reasonable assumption would be that the C−H and O−H bonds remain constant as the changes in the overall structure along the process do not interfere in its strength. Thus, **Equation 1** would now be described as:

$$\Delta E \approx -(D_{M-C}) + (D_{M-O}) \quad \textbf{(Equation 2)}$$

The dissociation of M−O bond (D_{M-O}) will be assessed by computation of $[M(\eta\text{-}Cp)(NMe_3)(\kappa^2\text{-}OAc)]^+$ (M = Ir, Rh) and $[Ru(\eta\text{-}C_6H_6)(NMe_3)(\kappa^2\text{-}OAc)]^+$ in which the dmba−H ligand has been replaced by NMe_3. These systems model the cyclometalation reactants, but allow the energy associated with a simple $\kappa^2\text{-}\kappa^1$ displacement to be computed in the absence of any extra interactions with the aryl ring of the dmba−H moiety, as shown in Figure 3.5. The energies computed for this process are $\Delta E(\kappa^2\text{-}\kappa^1)_{Ir}$ = 10.8 kcal/mol, $\Delta E(\kappa^2\text{-}\kappa^1)_{Rh+}$ = 13.7 kcal/mol and $\Delta E(\kappa^2\text{-}\kappa^1)_{Ru+}$ = 16.0 kcal/mol. Thus, the lowest energy is computed for iridium and the highest for ruthenium, following the trend Ir < Rh < Ru.

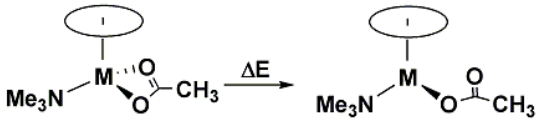

Figure 3.5 – General reaction for the $\kappa^2\text{-}\kappa^1$ displacement of $[M(\eta\text{-}Cp)(NMe_3)(\kappa^2\text{-}OAc)]^+$ (M = Ir, Rh) and $[Ru(\eta\text{-}C_6H_6)(NMe_3)(\kappa^2\text{-}OAc)]^+$.

To assess the dissociation of the M−C bonds (D_{M-C}) in the products the homolysis of the M−Ph bond in $[M(\eta\text{-}Cp)(C_6H_5)(NMe_3)(HOAc)]^+$ (M = Ir, Rh) and $[Ru(\eta\text{-}C_6H_6)(C_6H_5)(NMe_3)(HOAc)]^+$ complexes will be calculated, as shown in Figure 3.6.

This approach is chosen over M-C bond homolysis in the cyclometallated products as it avoids the problem of forming a bi-radical in the latter, as well as removing any extra intramolecular interactions that might occur. The results indicate that the strongest M−C bond is when M = iridium (ΔE = -62.8 kcal/mol), while the values for rhodium (ΔE = -53.4 kcal/mol) and ruthenium (ΔE_{Ru-C} = -54.8 kcal/mol) are rather similar.

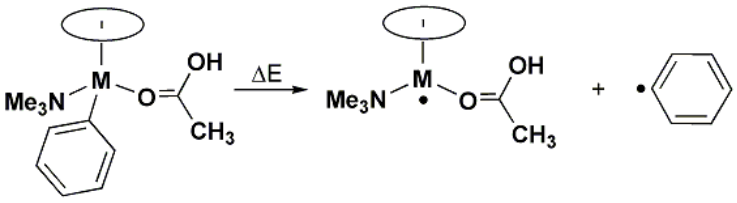

Figure 3.6 – General reaction for the homolysis of a M−C bond in $[M(\eta\text{-}Cp)(C_6H_5)(NMe_3)(HOAc)]^+$ (M = Ir, Rh) and $[Ru(\eta\text{-}C_6H_6)(C_6H_5)(NMe_3)(HOAc)]^+$ complexes.

Combining these two measures of the M−C and M−O bond strengths allows the overall trend in ΔE for the cyclometallation reaction to be assessed (ΔE_{theo}, see Table 3.2). This shows this process to be most favorable for iridium, followed by rhodium and then ruthenium. As shown in Table 3.2, a weaker M−O bond in the reactant and stronger M−C bond in the final product combine to make the reaction with $\mathbf{1_{Me}}$ most favorable, although the calculated proportional difference is much higher.

$\mathbf{1_R}$	D(M−O)	D(M−C)	ΔE_{theo}	ΔE
$\mathbf{1_{Me}}$	10.8	-62.8	-52.0	-5.6
$\mathbf{1_{Rh+}}$	13.7	-53.4	-39.7	-2.5
$\mathbf{1_{Ru+}}$	16.0	-54.8	-38.8	-0.5

Table 3. 2 - Summary of the energies for the dissociation of the M-O bond (D_{M-O}) and M-C bond (D_{M-C}), theoretical energies and calculated energies (kcal/mol) for the cyclometallation of $\mathbf{1_{Rh+}}$, $\mathbf{1_{Ru+}}$ and $\mathbf{1_{Me}}$.

It is worth noticing that the energy barrier computed for the three systems ($\Delta E^{\ddagger}$) could also be related to D_{M-O} since the major change associated with this process is the dissociation of one of the M−O bonds. However, a comparison between $\Delta E^{\ddagger}$ and D_{M-O} shows that the two trends do not agree (see Table 3.3).

$\mathbf{1_R}$	D(M−O)	$\Delta E^{\ddagger}$
$\mathbf{1_{Me}}$	10.8	13.4
$\mathbf{1_{Rh+}}$	13.7	12.4
$\mathbf{1_{Ru+}}$	16.0	12.9

Table 3. 3 - Summary of the energies for the dissociation of the M-O bond (D_{M-O}) and for the energy (kcal/mol) of the C-H activation transition state of $\mathbf{1_{Rh+}}$, $\mathbf{1_{Ru+}}$ and $\mathbf{1_{Me}}$.

However, in the previous section it was noted that the transition states located exhibit a different degree of interaction between the approaching C−H bond and both the metal centre and the free arm of the base. Indeed, the strongest contacts were computed for ruthenium and the weakest for iridium. Therefore, the different degree of stabilization will tend to affect the energy associated with a simple κ^2-κ^1 displacement. Thus, in the ruthenium system a harder κ^2-κ^1 displacement occurs with a strong stabilization in the transition state, while for iridium, the κ^2-κ^1 displacement is easier but less transition state stabilization is computed. Overall, the combination of these two effects would balance each other out and results in the similarity of the energy barriers computed for these processes.

Experimental results showed no reactivity for rhodium and ruthenium system with amines. However, the cyclometallation reactions computed here show a very similar behaviour. In Chapter 2, the assessment of the dimer opening allowed us to highlight the importance of acetate in that process. Therefore, the consideration of this step here appears to be logical. However, the modelling by PCM solvent calculations (dichloromethane) of each of the structures assumed for the dimer opening shown in Figure 3.7 results in very similar behaviour independent of the metal fragment used. In all cases, the formation of $[M(ring)Cl_2(\kappa^1\text{-}OAc)]^-$ and $[M(ring)Cl(\kappa^2\text{-}OAc)]$ species is highly exothermic (by between 31.6 and 34.5 kcal/mol) and the following formation of the reactant $\mathbf{1_{Rh+}}$ and $\mathbf{1_{Ru+}}$ is slightly uphill by approximately 9 kcal/mol.

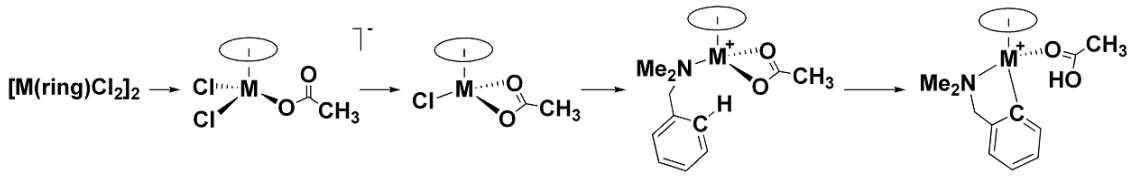

Figure 3.7 – Computed reaction for the dimer opening of [M(η-Cp)Cl_2] (M = Ir, Rh) and [Ru(η-C_6H_6)Cl_2] species.

The overall profile computed for the cyclometallation reactions of dmba−H by [RhCpCl_2]$_2$ and [Ru(C_6H_6)Cl_2]$_2$ result in similar behaviour to that computed with [IrCpCl_2]$_2$. It is therefore not clear why these systems exhibit such different reactivities experimentally.

3.3. Neutral metal complexes: cyclometallation reactions of [Ru(η-Cp)(dmba−H)(κ^2-OAc)] ($\mathbf{1_{Ru}}$) and [Ru(η-Cp)(dmba−H)(κ^2-CF_3SO_3)] ($\mathbf{4_{OTf}}$)

In order to assess the role of the overall charge of the metal complex on the cyclometallation reaction the {Ir(η-Cp)}$^{2+}$ fragment in $\mathbf{1_{Me}}$ was substituted by a {Ru(η-Cp)}$^{+}$ fragment to give the neutral system [Ru(η-Cp)(dmba−H)(κ^2-OAc)], $\mathbf{1_{Ru}}$. Previous studies on cationic systems showed that weaker bases lowered the overall energy barrier to reaction. Therefore, in order to assess how a weak base will affect the process in a neutral system, the [Ru(η-Cp)(dmba−H)(κ^2-CF_3SO_3)] complex, $\mathbf{4_{OTf}}$, was also computed.

3.3.1. Cyclometallation of [Ru(η-Cp)(dmba−H)(κ^2-OAc)], 1_{Ru}

The first step of the process is shown in Figure 3.8. The main difference in the geometry computed for the reactant $\mathbf{1_{Ru}}$ and the cationic analogues, $\mathbf{1_{Me}}$ and $\mathbf{1_{Ru+}}$ computed previously are the very long Ru−O bonds (2.23 Å). Also, the aryl moiety is closer to both the metal and oxygen O_1 of the acetate. The first step is again the κ^2-κ^1 displacement of one arm of the acetate and the transition state, $\mathbf{TS(1\text{-}2a)_{Ru}}$, features a very similar geometry to $\mathbf{TS(1\text{-}2)_{Me}}$ with a dissociation of one arm of the acetate and an approach of the aryl moiety toward the metal. However, the interactions of the aryl C_1-H_1 bond with the metal and O_1 are the longest computed so far. Moreover, in contrast to the cationic systems, $\mathbf{TS(1\text{-}2a)_{Ru}}$ leads to a new intermediate $\mathbf{2a_{Ru}}$ which is characterized by even weaker interaction between the aryl ring and the metal centre ($\mathbf{TS(1\text{-}2a)_{Ru}}$**:** Ru···$C_1$ = 3.25 Å, Ru···H_1 = 2.72 Å *cf.* $\mathbf{2a_{Ru}}$**:** Ru···C_1 = 3.43 Å, Ru···H_1 = 2.93 Å). Thus the aryl moiety initially moves toward the metal centre, but then moves

away again. This backward movement of the aryl moiety also interrupts the $O_1\cdots H_1$ contact which lengthens from 2.12 Å in **TS(1-2a)$_{Ru}$** to 2.68 Å in **2a$_{Ru}$**. Energetically, this step proceeds via a small barrier of 8.2 kcal/mol and **2a$_{Ru}$** is less stable than **1$_{Ru}$** by only 6.4 kcal/mol.

To account for the low barrier associated with κ^2-κ^1 displacement, the calculation of the D_{M-O} energy was carried out in an analogous way to that for cationic systems by the computation of the [Ru(η-Cp)(NMe$_3$)(κ^2-OAc)] model system. In this case, D_{M-O} = 8.5 kcal/mol, very similar to $\Delta E^{\ddagger}$ = 8.2 kcal/mol. Hence in this case the activation energy is well modelled by a simple κ^2-κ^1 displacement. This also correlates with the weaker interaction of the aryl ring with the ruthenium and the longer contact between the hydrogen and the free oxygen in **TS(1-2a)$_{Ru}$**. Thus, this transition state is not significantly stabilized by these extra interactions.

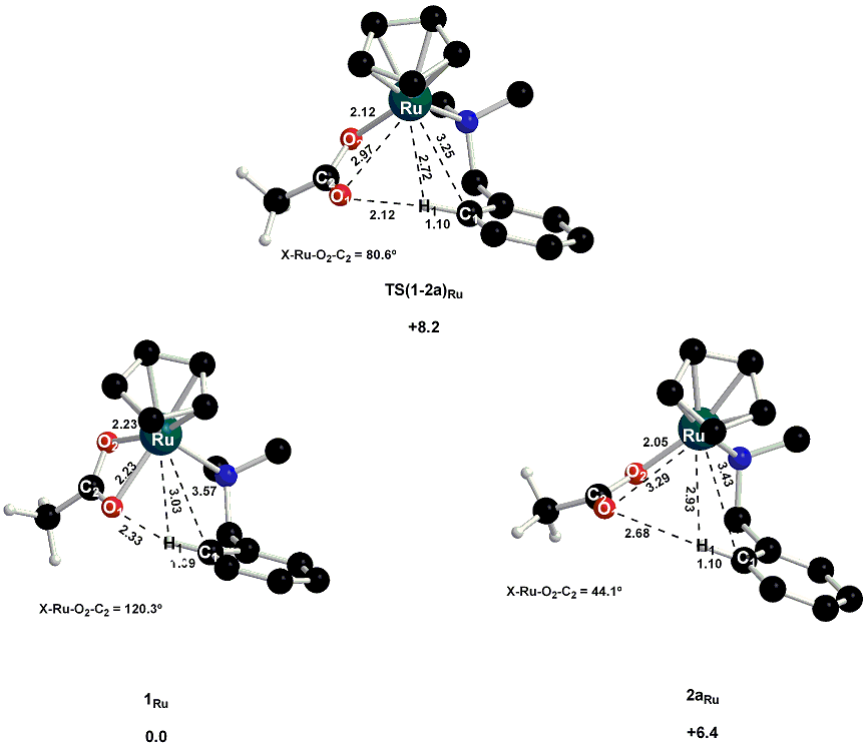

Figure 3.8 - Computed stationary points (kcal/mol, distances in ångstroms) for the κ^2-κ^1 displacement of acetate in **1$_{Ru}$**. Non-participating hydrogens are omitted for clarity.

Further differences computed with the neutral systems were also seen in the location of a new transition state, **TS(2a-2b)$_{Ru}$** (see Figure 3.9). This step involves the isomerisation of the non-agostic species, **2a$_{Ru}$**, to an agostic intermediate, **2b$_{Ru}$**. The

main features are the approach of the C_1–H_1 bond towards the metal by shortening the Ru···C_1 and Ru···H_1 distances by 1.01 Å and 0.99 Å, respectively, and the elongation of the C_1–H_1 bond from 1.10 Å in **2a$_{Ru}$** to 1.15 Å in **2b$_{Ru}$**. In addition, a dramatic shortening in the H_1···O_1 distance from 2.68 Å in **2a$_{Ru}$** to 2.10 Å in **2b$_{Ru}$** is also computed. The activation barrier of the process is only 1.3 kcal/mol and the new intermediate **2b$_{Ru}$** is only 0.3 kcal/mol less stable than **2a$_{Ru}$**. The geometry of **2b$_{Ru}$** means that it is ideally set up for the following hydrogen transfer.

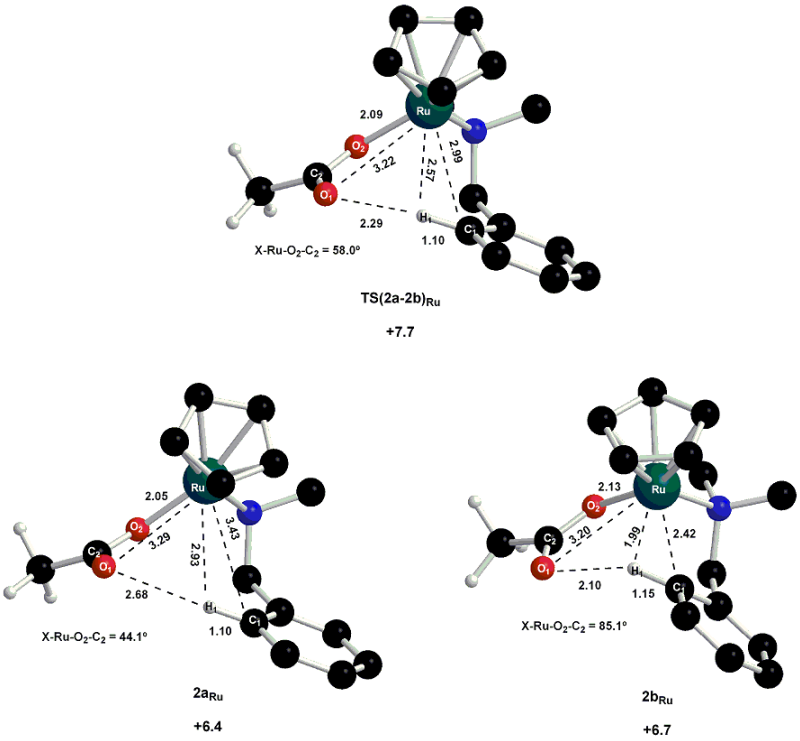

Figure 3.9 - Computed stationary points (kcal/mol, distances in ångstroms) for the formation of the agostic intermediate **2b$_{Ru}$**. Non-participating hydrogens are omitted for clarity.

The C–H activation step proceeds via an AMLA-6 mechanism (Figure 3.10). The hydrogen transfer proceeds via **TS(2b-3)$_{Ru}$** and is associated with an energy barrier of 2.1 kcal/mol, 1.2 kcal/mol higher than that computed for **1$_{Me}$**. **TS(2b-3)$_{Ru}$** shows the greatest amount of metal and ligand involvement computed for a C-H activation step so far, with very short Ru···H_1 and Ru···C_1 distances (2.06 Å and 2.15 Å, respectively). It also involves a significant elongation in the C_1–H_1 bond distance from 1.15 Å in **2b$_{Ru}$** to 1.44 Å in **TS(2b-3)$_{Ru}$**, which leads to the shortening in the O_1···H_1 distance to 1.32 Å.

It is worth noticing that C-H activation step is only slightly exothermic by 0.2 kcal/mol, while the analogous processes in cationic systems have always been much more

exothermic. An attempt to account for this was made through relating ΔE to $D_{M–O}$ and $D_{M–C}$ computed in [Ru(η-Cp)(NMe_3)(κ^2-OAc)] and [Ru(η-Cp)(C_6H_5)(NMe_3)(HOAc)] respectively. Although a good correlation between D_{M-O} and $\Delta E^{‡}$ had previously been found, a very strong Ru-Ph bond dissociation energy was computed in [Ru(η-Cp)(C_6H_5)(NMe_3)(HOAc)] (-65.2 kcal/mol). This suggests that cyclometalation should be far more favourable than the computed value (ΔE = +6.5 kcal/mol). One possible reason for this discrepancy might be the short H1···O1 interaction of 2.33 Å seen in the reactant, while, in addition, the product shows a short Ru···H_1 contact of 2.22 Å. Overall this different behaviour may invalidate the approach that relates ΔE to simple differences in $D_{M–O}$ and $D_{M–C}$.

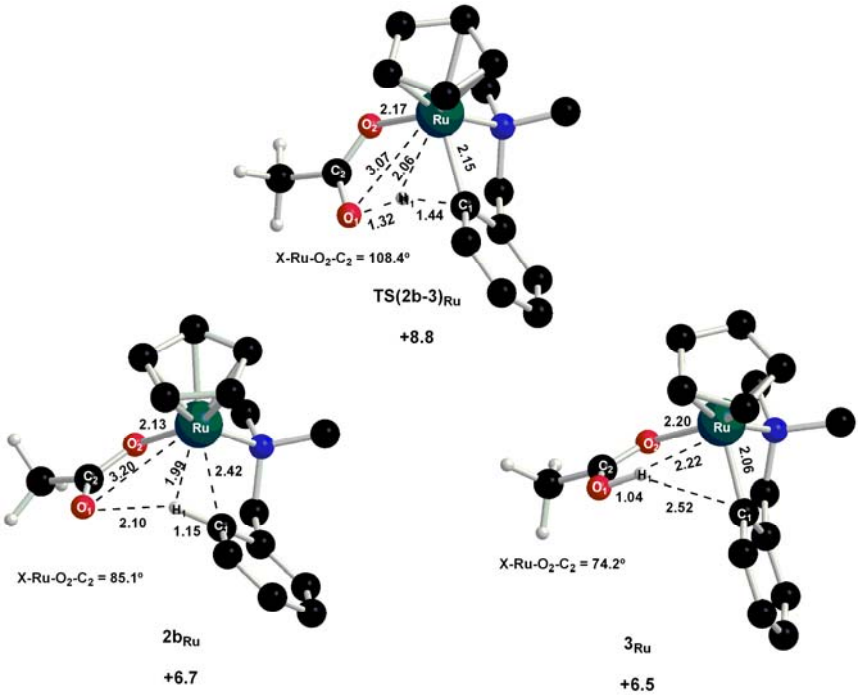

Figure 3.10 - Computed stationary points (kcal/mol, distances in ångstroms) for the C-H activation of $\mathbf{1_{Ru}}$ via an AMLA-6 mechanism. Non-participating hydrogens are omitted for clarity.

The full three step profile for the cyclometallation reaction of $\mathbf{1_{Ru}}$ is shown in Figure 3.11. This process has the lowest overall barrier computed so far ($\Delta E^{‡}$ = 8.8 kcal/mol), although it is the least favourable thermodynamically (ΔE = +6.5 kcal/mol). The first step of the process describes a simple κ^2-κ^1 displacement and almost no interaction is computed in the transition state between the aryl moiety with either the metal or the acetate base. Interestingly, even though a very different transition state for the C−H

activation step is formed, with the strongest metal involvement computed so far for an AMLA-6 mechanism, the barrier for this process was still only 2.1 kcal/mol.

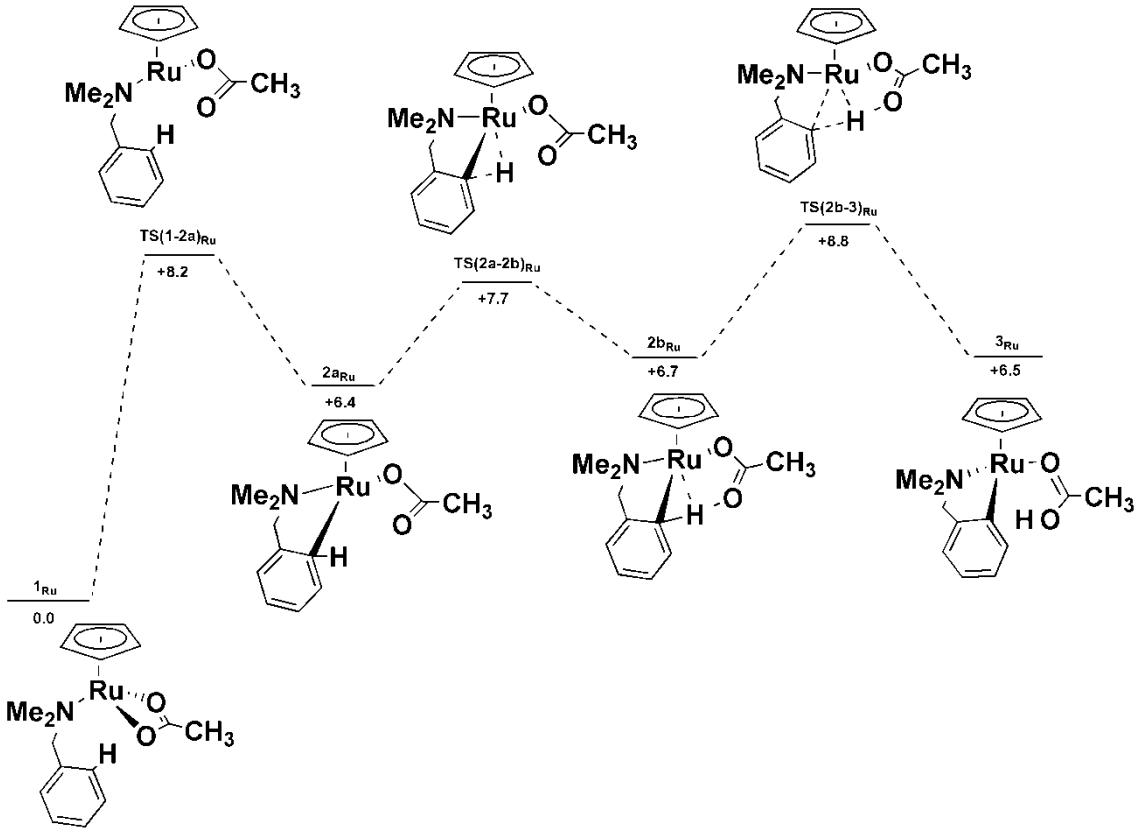

Figure 3.11 - Computed stationary points (kcal/mol, distances in ångstroms) of the cyclometallation reaction of $\mathbf{1_{Ru}}$ via an AMLA-6 mechanism.

3.3.2. Cyclometallation of [Ru(η-Cp)(dmba−H)(κ²- CF_3SO_3)], 4_{OTf}

The full profile for the cyclometallation of $\mathbf{4_{OTf}}$ is shown in Figure 3.12. Comparison of the geometry of reactant $\mathbf{4_{OTf}}$ with $\mathbf{1_{OTf}}$ shows even longer M−O bond distances (2.32 Å and 2.34 Å) and a very short $H_1\cdots O_1$ contact (2.28 Å). The first step, characterized by $\mathbf{TS(4\text{-}5)_{OTf}}$, is very easy ($\Delta E^{\ddagger}$ = 3.3 kcal/mol) and in fact is even easier than the κ^2-κ^1 displacement previously computed for the cationic triflate analogue, $\mathbf{1_{OTf}}$ (7.0 kcal/mol see Chapter 2, Figure 2.21). As before, the κ^1-intermediate ($\mathbf{5_{OTf}}$) is more stable than the κ^2-reactant ($\mathbf{4_{OTf}}$). Now, the structure of $\mathbf{5_{OTf}}$ exhibits longer aryl-metal interactions and shorter $H_1\cdots O_1$ contacts (2.21 Å) than the analogous κ^1-intermediate $\mathbf{2_{OTf}}$. In addition, a small elongation of the $M{-}O_2$ bond is also seen (2.18 Å *cf.* 2.10 Å).

Unexpectedly, the C−H activation step from $\mathbf{5_{OTf}}$ features an oxidative addition transition state, $\mathbf{TS(5\text{-}6)_{OTf}}$, and this requires an energy barrier of 6.9 kcal/mol. Any attempt to locate an AMLA-6 transition state failed. In addition, several optimizations targetting the final cyclometallated product where the proton is transferred to the free oxygen of the triflate were attempted and also proved unsuccessful. $\mathbf{TS(5\text{-}6)_{OTf}}$ is a very late transition state as it presents very short, product-like Ru−H_1 and Ru−C_1 distances of 1.58 Å and 2.11 Å respectively.

The final product $\mathbf{6_{OTf}}$ is higher in energy than the transition state when the zero-point energy is included. This suggests that the C−H activation step (and therefore the overall cyclometallation reaction) cannot be considered as occurring as once the zero-point energy is taken into account no product minimum would exist. However, computationally, it is interesting that the only mechanism that could be characterised for C-H activation in this case was oxidative addition.

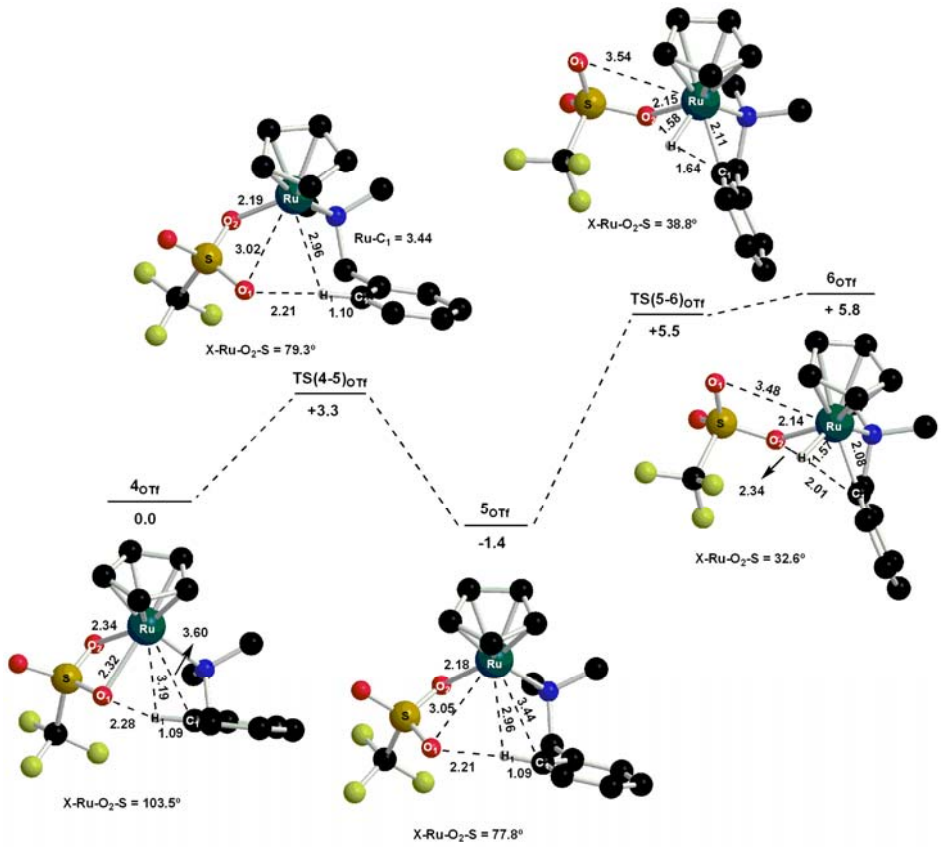

Figure 3.12 - Computed stationary points (kcal/mol, distances in ångstroms) for the cyclometallation reaction of $\mathbf{4_{OTf}}$. Non-participating hydrogens are omitted for clarity.

3.4. Neutral metal complexes: cyclometallation reaction of [Ir(η-Cp)(dmba−H)(κ^2-CO_3)] ($\mathbf{1}_{CO3}$)

Figure 3.13 shows the reaction profile for the cyclometallation reaction of $\mathbf{1}_{CO3}$. A close look at the geometry of the reactant, $\mathbf{1}_{CO3}$, shows that this species exhibits much shorter M−O distances (2.08 Å) compared to $\mathbf{1}_{Me}$ (2.17 Å). The first step of the cyclometallation proceeds through $\mathbf{TS(1\text{-}2)}_{CO3}$ and involves the κ^2-κ^1 displacement of the carbonate base. Interestingly, this dissociation leads to a significant shortening of the Ir···O_2 bond to 1.84 Å and an extreme elongation of the O_2−C_2 bond to 2.22 Å. Also, the geometry describes an opening of the O_3−C_2−O_1 angle from 125.7º in $\mathbf{1}_{CO3}$ to 160.9º in $\mathbf{TS(1\text{-}2)}_{CO3}$. This step is associated with a very high energy barrier of 28.6 kcal/mol, and the κ^1-intermediate is very unstable at 21.1 kcal/mol. This result is not so surprising as CO_3^{2-} is an extremely strong base (*-pKa* = -10.3) that should bind strongly to the metal centre. Moreover, the κ^2- κ^1 displacement involves the displacement of an anionic arm of the carbonate, whereas with carboxylate bases the displaced arm is formally a neutral carbonyl group.

The geometry of the carbonate in $\mathbf{TS(1\text{-}2)}_{CO3}$ and, to a lesser extent, the κ^1-intermediate exhibits a near-linear {CO_2} moiety and a very long O_2−C_2 bond. In addition, the very short Ir−O_2 bond suggests that a very strong interaction is present, possibly through π-donation. Therefore the carbonate could be described as a combination of {CO_2 +O^{2-}} rather than a normal CO_3^{2-} ligand. In order to support this idea, NBO charges were computed and these are shown in italics in Figure 3.13. For the reactant an average charge of -0.67 was computed for O_1 and O_2, the oxygens bound directly to the metal, while a charge of -0.60 was computed for O_3. In $\mathbf{TS(1\text{-}2)}_{CO3}$ O_2 become slightly more negative (-0.69) while O_1 and O_3 are less negative (average charge = -0.55). Comparison with free CO_2 shows a charge of -0.35 on each oxygen. Therefore the changes in charge distribution in going from $\mathbf{1}_{CO3}$ to $\mathbf{TS(1\text{-}2)}_{CO3}$ do suggest an increase in "CO_2" character in the {O_1-C_2-O_3} moiety. These odd features can also be explained by the instability of the zwitterions in the gas phase or in a non-polar solvent. The elongation of the C−O bonds is a consequence of the unfavourable charge separation. Therefore, in reality such a process would be result in very strong H bonding to solvent.

The following C−H cleavage via an AMLA-6 transition state requires an extremely high activation energy of 11.4 kcal/mol, by far the highest barrier for C-H activation computed so far. Compared to **TS(2-3)$_{Me}$**, the geometry of **TS(2-3)$_{CO3}$** features more metal involvement, with a short Ir···C_1 distance of 2.42 Å and longer C_1−H_1 and O_1···H_1 interactions (1.18 Å and 1.61 Å, respectively). However, transition states with more metal involvement have not previously been associated with such a large increase in the activation barrier. Moreover, greater metal involvement usually occurs when a weaker base such as triflate is employed, but in this case carbonate is a very strong base. One explanation may be that this reflects the elongation of the Ir−O_2 bond in **TS(2-3)$_{CO3}$**, from 1.89 Å in **2$_{CO3}$** to 2.01 Å, as well as the shortening of the C_2−O_2 bond to 1.43 Å. This suggests a reorganization of the base from {CO_2 + O^{2-}} back to CO_3^{2-} is required in order to facilitate the proton transfer. This will also interrupts the strong interaction of the O_2 atom with the metal centre and may account for the surprisingly large activation barrier for C-H activation.

Despite the unusual behaviour computed along the reaction profile described above, the overall cyclometallation reaction is an exothermic process with ΔE = -5.2 kcal/mol, a very similar value to that computed for **1$_{Me}$** (ΔE = -5.6 kcal/mol). Thus the strong M-O bond broken in **1$_{CO3}$** is compensated by a strong O-H bond in the product and the cyclometallation reaction energy remains favourable.

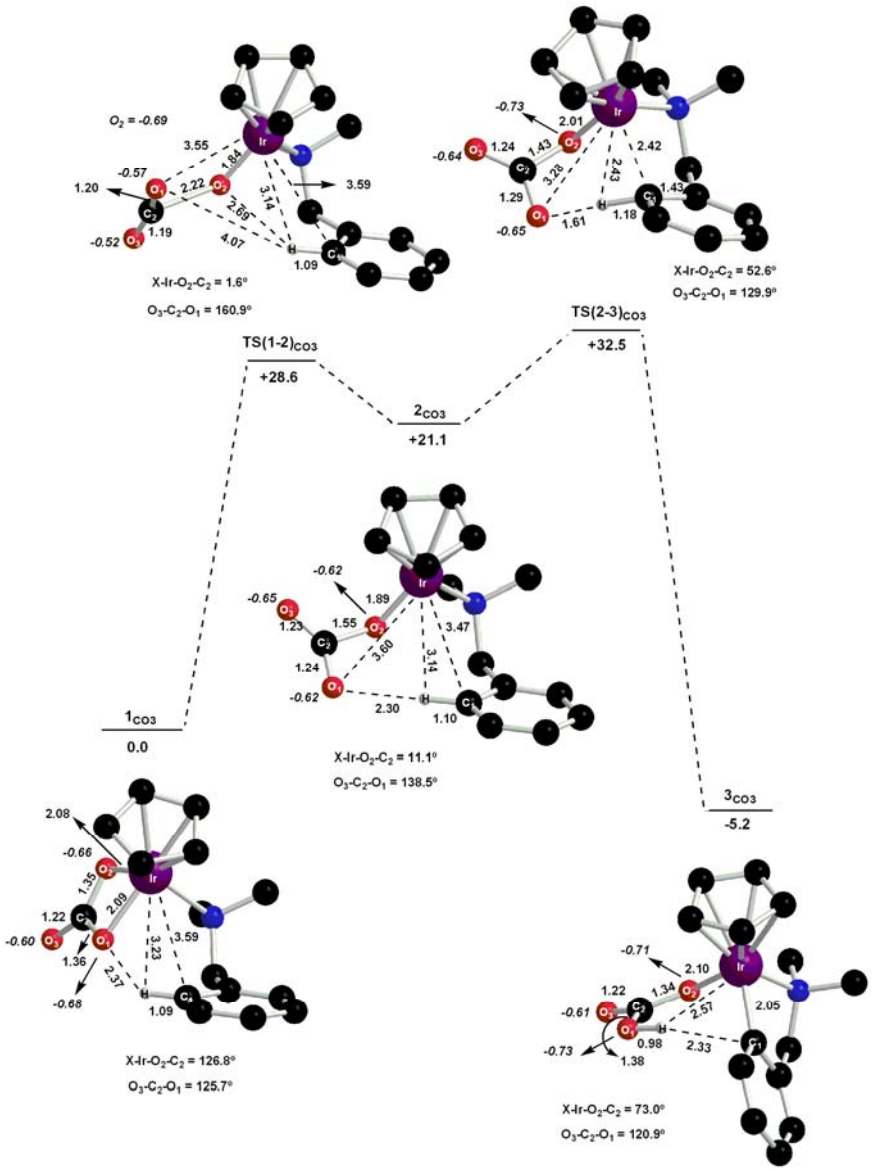

Figure 3.13 - Computed stationary points (kcal/mol, distances in ångstroms) for the cyclometallation reaction of $\mathbf{1}_{CO3}$. Non-participating hydrogens are omitted for clarity. NBO charges in italics.

3.5. Cyclometallation of [Ir(η-Cp)(ligand)(κ^2-OAc)]$^+$ (ligand = imine and amide)

Recently, Jones *et al.*[2] investigated the reactivity and scope of a series of *meta*- and *para*-substituted imine substrates of the type $(C_6H_4X)CH{=}NR$ using the methodology developed by the Davies group.[1] In this study they were able to isolate the monomers [Rh(η-Cp*)(OAc)Cl] and [Rh(η-Cp*)$(OAc)_2$] and so were able to focus on the C−H activation mechanism by UV-vis and NMR spectroscopy at room temperature. A kinetic isotopic effect was evaluated by comparing the reaction of a mixture of phenylimine-d_0 and partially deuterated phenylimine-d_5 with $[IrCl_2Cp^*]_2$ and NaOAc in methanol. This study gave a large isotopic effect of >5, and such a large isotopic effect

suggests the rate-determining step is associated with the C−H cleavage of the imine at the metal centre. Interestingly, this result differs with the interpretation gives in Chapter 2. There the computed energy profiles for the cyclometallation of [Ir(η-Cp)(dmba-H)(κ^2-RCO_2)] species showed no correlation with the rate of reaction found experimentally, suggesting that C-H activation was not the limiting step of the process. Therefore, in order to assess the role of the substrate in the cyclometallation reaction the energy profiles for various systems of the type [Ir(η-Cp)(ligand)(κ^2-OAc)]$^+$ were computed, where ligand = *trans*-methylbenzylimine (mbi−H), *trans*-phenylbenzylimine (pbi−H) and *N*,*N*-dimethylbenzylamide (dmbad−H).

3.5.1. Cyclometallation of [Ir(η-Cp)(mbi−H)(κ^2-OAc)]$^+$ (1_{NMe})

Figure 3.14 shows the computed profile for the cyclometallation reaction of [Ir(η-Cp)(mbi−H)(κ^2-OAc)]$^+$ (**1_{NMe}**). A comparison between the reactant geometries of **1_{Me}** and **1_{NMe}** showed that **1_{NMe}** exhibits closer interactions between the activating C_1−H_1 bond and both the metal and O_1 of the acetate (Ir···C_1 = 2.68 Å, Ir···H_1 = 2.73 Å and O_1···H_1 = 2.28 Å). In this case, this may be due to the orientation of the aryl moiety in **1_{NMe}** which is constrained due to the delocalization in the imine ligand which does not allow a free rotation around the N=C bond. A scan based on shortening the O_1···H_1 distance led to the location of **TS(1-3)$_{NMe}$** which unexpectedly linked directly to the final cyclometallated product, **3_{NMe}**. **TS(1-3)$_{NMe}$** features the usual dissociation of the Ir−O_1 bond (2.84 Å) and the approach of the aryl moiety towards the metal. However, in addition, it also shows short Ir···H_1 and O_1···H_1 contacts (2.19 Å and 2.02 Å, respectively). Therefore this transition state incorporates both κ^2-κ^1-displacement and the classic features of an AMLA-6 C-H activation process and this explains why cyclometalation occurs in a single step. The activation energy associated with this process is 14.5 kcal/mol and the final cyclometallated product **3_{NMe}** is more stable than **1_{NMe}** by 6.7 kcal/mol.

Support for this idea can be found by comparing the geometry of **TS(1-3)$_{NMe}$** with those of **TS(1-2)$_{Me}$**, where C-H activation does not occur and **TS(1-3a)$_{Me}$** computed in previous studies, where C-H activation occurs in one step[3] (see Figure 3.15). The orientation of the aryl moiety in each case will be quantified by the X−Ir−N−C_b torsion angle (θ) and the N−C_b−C_{ipso}−C_1 torsion angle (ϕ) (X = Cp centroid). In **TS(1-3)$_{NMe}$**

both angles, θ and ϕ, are closer to those in **TS(1-3a)$_{Me}$** than in **TS(1-2)$_{Me}$**, (**TS(1-3)$_{NMe}$:** θ = 81.8º; ϕ = 24.2º *cf.* **TS(1-3a)$_{Me}$:** θ = 66.4º; ϕ = 0.3º and **TS(1-2)$_{Me}$:** θ = 139.7º; ϕ = 77.2º). Thus in this case, the constrained geometry of the substrate conditions this reaction to be a single step process.

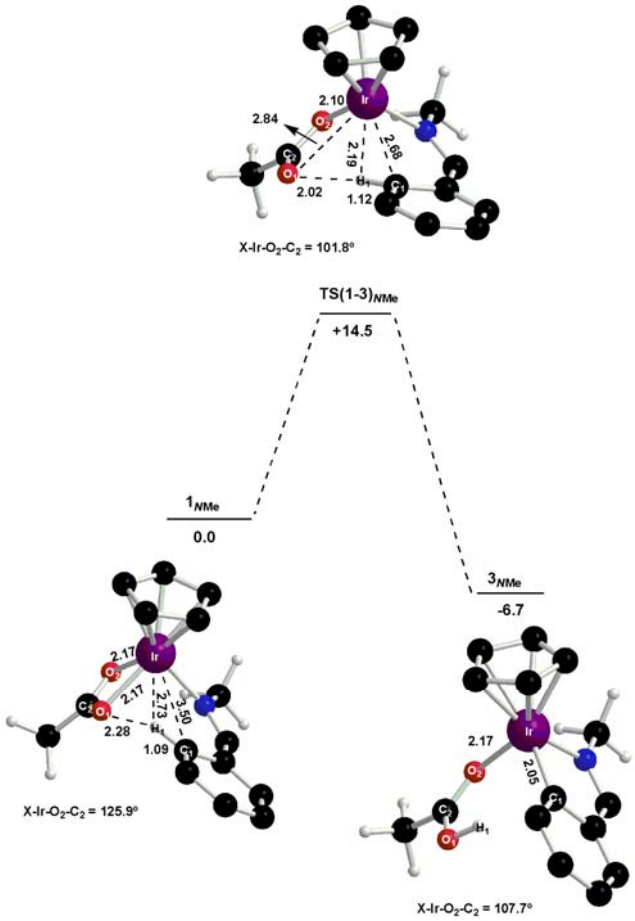

Figure 3.14 - Computed profile (kcal/mol, distances in ångstroms) for the cyclometallation reaction of **1$_{NMe}$** via an AMLA-6 mechanism. Non-participating hydrogens are omitted for clarity.

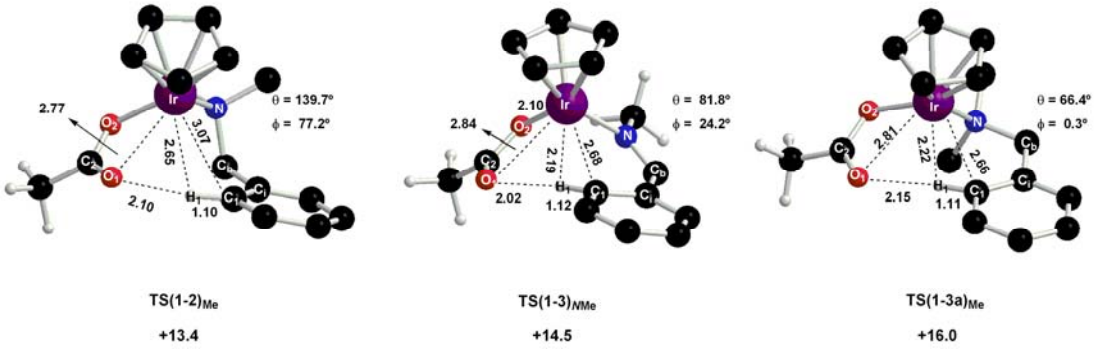

Figure 3.15 - Geometries for the three rate-limiting transitions states **TS(1-2)$_{Me}$**, **TS(1-3)$_{NMe}$** and **TS(1-3a)$_{Me}$** (distances in ångstroms, angles in degrees).

The experimental observation of a high kinetic isotopic effect (>5) in the C−H activation of imine substrates by Jones *et al.*[2] implies that the C−H activation is involved in the limiting step of the process. Therefore the transition state should feature a significant elongation of the C_1−H_1 bond. Figure 3.14 shows that C-H activation is involved in the rate-limiting step for the reaction of the imine substrate, unlike all the previous reactions of the $[Ir(\eta\text{-Cp})(dmba\text{-H})(\kappa^2\text{-}RCO_2)]^+$ species. However, the transition state involved, **TS(1-3)$_{NMe}$**, exhibits only a small elongation of the C_1-H_1 bond. Experimentally, the reactivity studies were carried out in methanol as solvent, and one possible reason for the discrepancy with our calculation might be that methanol might interact directly via hydrogen bonding with the free oxygen of the acetate in the transition state. This would make the oxygen less basic and previously this has been shown to result in later transition state geometries with elongated C_1−H_1 bonds. A transition state was therefore located in which methanol exhibits this hydrogen bonding interaction (see Figure 3.16). However, unfortunately no significant increase in the C_1−H_1 bond was computed.

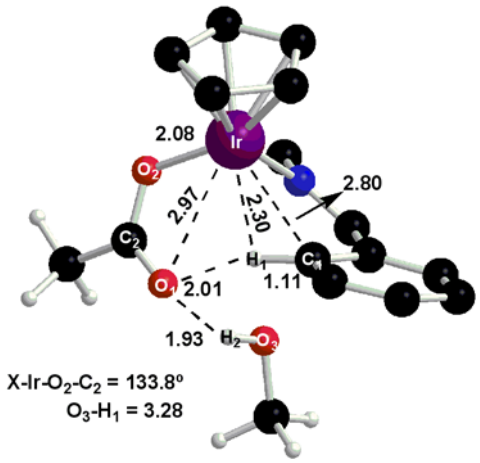

Figure 3.16 – Computed stationary point for **TS(1-3)$_{NMe}$** when an additional MeOH molecule interacting with O_1 (distances in ångstroms).

3.5.2. Cyclometallation of $[Ir(\eta\text{-Cp})(pbi{-}H)(\kappa^2\text{-OAc})]^+$ (1_{NPh})

In order to evaluate the steric and electronic effects of a different substituent on the nitrogen atom, the methyl group of the imine was substituted by a phenyl group. The full profile of the cyclometallation reaction of **1$_{NPh}$** is shown in Figure 3.17. The process follows exactly the same pattern as **1$_{NMe}$**, indeed the key distances are almost equivalent to those computed with the methyl analogue. Again, a one step process is computed and

the activation energy required is only 0.3 kcal/mol higher than before. The exothermicity of this process is -6.2 kcal/mol, 0.5 kcal/mol less than that computed for $\mathbf{1}_{\mathbf{NMe}}$. Therefore the implication is that the effect of the imine substituent is negligible.

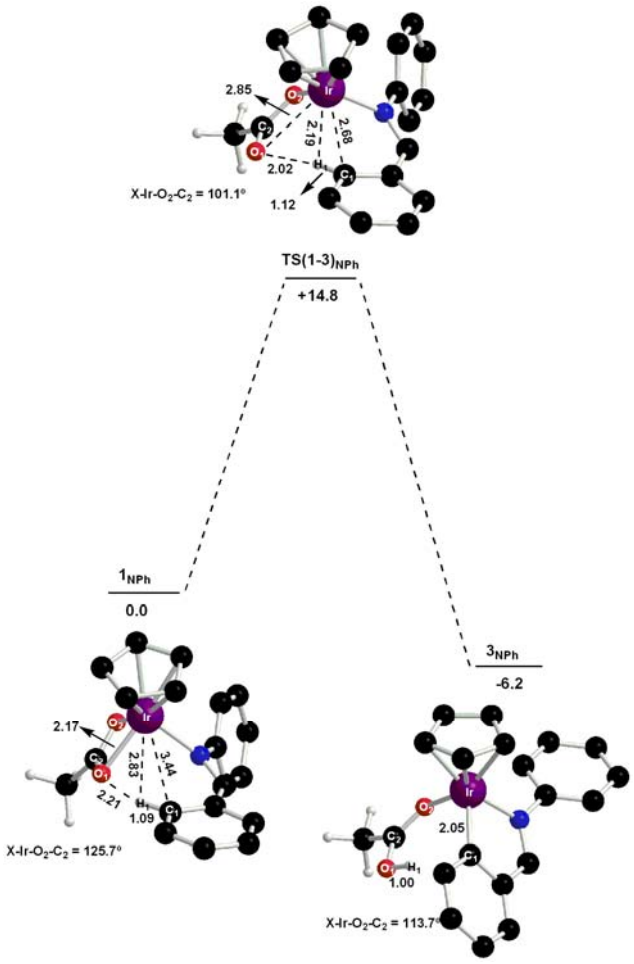

Figure 3.17 - Computed profile (kcal/mol, distances in ångstroms) for the cyclometallation reaction of $\mathbf{1}_{\mathbf{NPh}}$ via an AMLA-6 mechanism. Non-participating hydrogens are omitted for clarity.

3.5.3. Cyclometallation of [Ir(η-Cp)(dmbad−H)(κ²-OAc)]⁺ (1_{NCO})

Figure 3.18 shows the reaction profile for the cyclometallation reaction of $\mathbf{1}_{\mathbf{NCO}}$. The geometry of this reactant shows a similar conformation of the aryl moiety to that described by imines, due to delocalisation between the aryl and carbonyl groups. This explains why this system undergoes cyclometalation in a single step via $\mathbf{TS(1\text{-}3)}_{\mathbf{NCO}}$, which is very similar to $\mathbf{TS(1\text{-}3)}_{\mathbf{NMe}}$ and $\mathbf{TS(1\text{-}3)}_{\mathbf{NPh}}$. Energetically, the formation of the

cyclometallated product is exothermic (ΔE = -6.9 kcal/mol) and requires an activation energy of 16 kcal/mol.

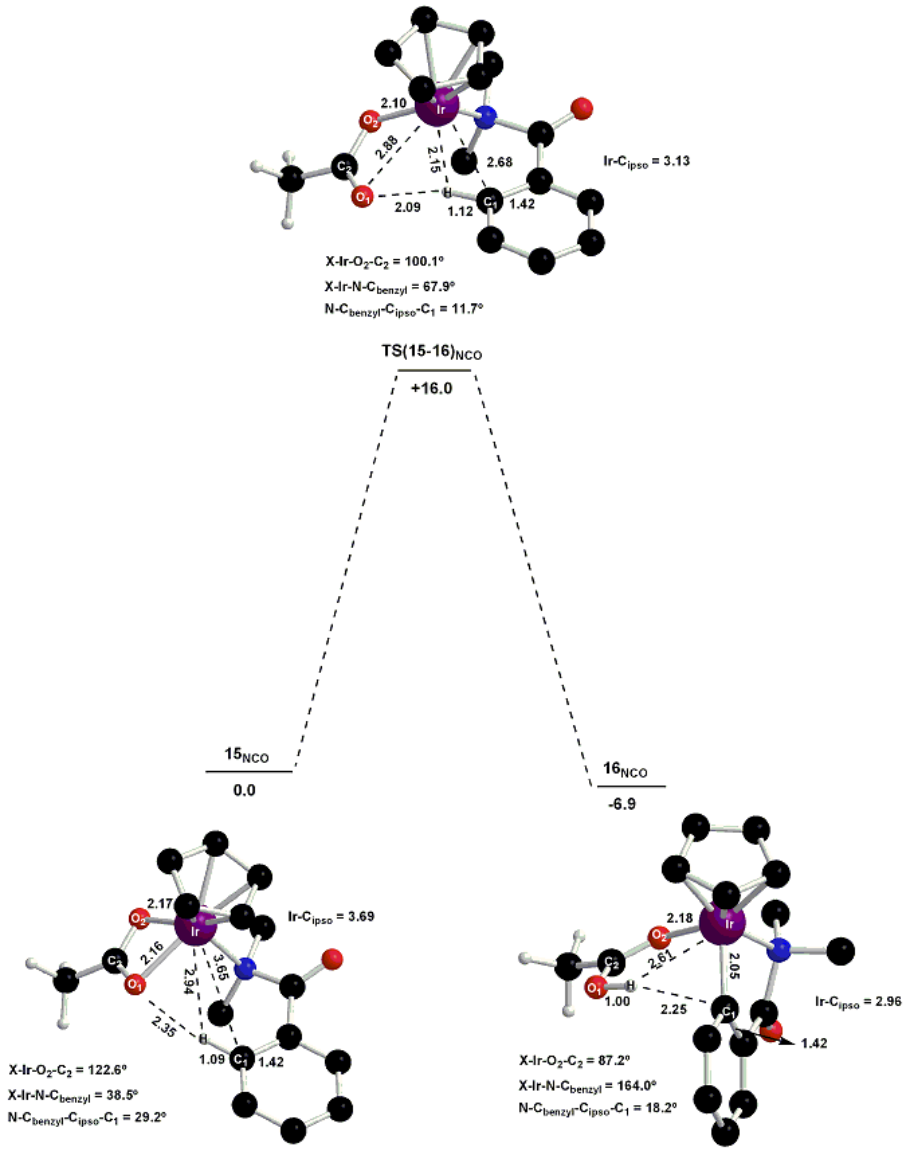

Figure 3.18 - Computed profiles (kcal/mol, distances in ångstroms) for the cyclometallation reaction of $\mathbf{1_{NCO}}$ via an AMLA-6 mechanism. Non-participating hydrogens are omitted for clarity.

3.6. Summary

The cyclometallation reactions of dmba-H in a range of cationic and neutral systems have been assessed. In addition, the cyclometalation of related imine and amide substrates at a cationic Ir centre have also been computed.

The cationic systems $[Rh(\eta\text{-}Cp)(dmba{-}H)(\kappa^2\text{-}OAc)]^+$ ($\mathbf{1_{Rh+}}$) and $[Ru(\eta\text{-}C_6H_6)(dmba{-}H)(\kappa^2\text{-}OAc)]^+$ ($\mathbf{1_{Ru+}}$) comparison with $\mathbf{1_{Me}}$ showed very similar activation barriers for cyclometallation. This was shown to be due to the competing effects of the M-O_1 bond strength (Ir < Rh < Ru) and the degree of stabilisation in the transition state arising from the M$\cdots$$H_1$-$C_1$ and $H_1\cdots O_1$ interaction (Ru > Rh > Ir). The overall energy of these cyclometallation process is more favourable for Ir > Rh > Ru and this could be related to trends in the strengths of the M−O and M-C bonds broken and formed in the reaction. Overall, changing the metal centre in these cationic complexes does not result in a significant different in the cyclometallation reaction. Moreover, calculations on the energies of the dimer opening confirm these similarities in behaviour.

For the neutral systems, $\mathbf{1_{Ru}}$ and $\mathbf{1_{OTf}}$, lower κ^2-κ^1 displacements and overall energy barriers are computed. In this case, however, these reactions are endothermic. The C−H activation transition states in these systems require more metal involvement than in the cationic systems. Indeed, the cyclometallation reaction of $\mathbf{1_{Ru}}$ requires an extra isomerisation step to access an agostic intermediate in order to facilitate the proton transfer to the free oxygen. The combination of a weak base and an overall neutral complex as in $\mathbf{4_{OTf}}$ requires such a high metal involvement that the only possible mechanism which could be located was oxidative addition.

In another neutral system, $\mathbf{1_{CO3}}$, the κ^2-κ^1 displacement entailed an extremely high activation barrier due to the dissociation an anionic carbonate arm. Unexpectedly a high barrier to C−H activation was also computed, despite carbonate being a very strong base. This is explained by a very strong Ir-O_2 interaction in the κ^1 intermediate.

With imine and amide substrates one step cyclometallation processes were characterised. This is due to the delocalization in these ligands that restricted the geometry in the transition state.

3.7. References

1. D. L. Davies, O. Al-Duaij, J. Fawcett, M. Giardiello, S. T. Hilton and D. R. Russell, *Dalton Trans.*, 2003, 4132-4138.
2. L. Li, W. W. Brennessel and W. D. Jones, *Organometallics*, 2009, **28**, 3492-3500.
3. D. L. Davies, S. M. A. Donald, O. Al-Duaij, S. A. Macgregor and M. Poelleth, *J. Am. Chem. Soc.*, 2006, **128**, 4210-4211.

4. Intermolecular C−H activation of benzene and catalytic alkene hydroarylation

4.1. Introduction

As described in Chapter 1, catalytic hydroarylation of alkenes has been widely studied by a combination of experimental and computational techniques.[1] Indeed, an inverse relationship between the barriers for C−H activation and the subsequent alkene insertion has been pointed out, suggesting that optimization of systems for catalysis may be problematic. Two systems that have been shown experimentally to promote intermolecular C−H activation are $[Ir(\eta\text{-}Cp^*)(PMe_3)(CH_3)]^+$ and $[Ir(acac)_2(OMe)(pyridine)]$. Computational studies have shown that these two systems react through different mechanisms. The first system, $[Ir(\eta\text{-}Cp^*)(PMe_3)(CH_3)]^+$, was studied by Hall[2] who focused on the C−H activation of methane. Hall concluded that this process occurred with transfer of a proton from methane to the methyl ligand via an oxidative addition/reductive elimination mechanism. The second system, $[Ir(acac)_2(OMe)(\ pyridine)]$, was studied by Goddard and Periana[3] who modelled C−H activation of benzene. In this case the proton is transferred to the oxygen of the methoxy ligand via what they called an internal electrophilic substitution (IES). This process could also be considered as analogous to the AMLA-4 mechanism discussed in Chapter 2.

Chapters 2 and 3 have highlighted the intramolecular C−H activation reaction of the $[Ir(\eta\text{-}Cp)(dmba{-}H)(\kappa^2\text{-}OAc)]^+$, $\mathbf{1_{Me}}$, and related systems. This chapter will consider adapting $\mathbf{1_{Me}}$ to a system that will allow us to model the intermolecular C−H activation of benzene. One related species known experimentally is $[Ir(\eta\text{-}Cp^*)(PMe_3)(\kappa^2\text{-}OAc)][PF_6]$ which has been synthesised by Maitlis and coworkers.[4] This cationic Ir(III) complex has many of the key features that promote C−H activation in $\mathbf{1_{Me}}$. Our calculations will therefore consider the intermolecular C−H activation of benzene at a model of this species, $[Ir(\eta\text{-}Cp)(PH_3)(\kappa^2\text{-}OAc)]^+$, $\mathbf{7_{OAc}}$. This will be compared with the equivalent reactions of benzene with $[Ir(\eta\text{-}Cp)(PH_3)(CH_3)]^+$ ($\mathbf{7_{Me}}$) and $[Ir(\eta\text{-}Cp)(PH_3)(OMe)]^+$ ($\mathbf{7_{OMe}}$). All three systems are cationic Ir(III) species and so will allow us to assess how the nature of the accepting ligand affects the C−H activation process. Additionally, changes in the metal centre and co-ligands of $\mathbf{7_{OAc}}$ will be also described.

The last part of this chapter will describe the use of $\mathbf{7_{OAc}}$ as a catalyst for a highly desirable C−H activation and functionalization process via reaction with ethene. This reaction involves the insertion of ethene into a C-H bond of benzene to give ethylbenzene was a hydroarylation product. The full catalytic cycle associated with this process will be assessed.

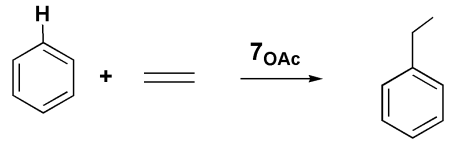

Figure 4.1 – Hydroarylation of ethene by $\mathbf{7_{OAc}}$.

The following chapter will be divided in two main sections: (I) C−H activation of benzene at $[Ir(\eta\text{-}Cp)(PH_3)(\kappa^2\text{-}OAc)]^+$ ($\mathbf{7_{OAc}}$) and related compounds and (II) the incorporation of C−H activation into a catalytic cycle for the hydroarylation of ethene.

4.2. C−H activation of benzene

The intermolecular C−H activation of benzene will be assessed at the model complex $[Ir(\eta\text{-}Cp)(PH_3)(\kappa^2\text{-}OAc)]^+$ ($\mathbf{7_{OAc}}$). This process was computed via AMLA-6, AMLA-4 and oxidative addition mechanisms. However, the AMLA-4 and oxidative addition pathways were shown to be much higher in energy, therefore, only the AMLA-6 path will be described in detail below.

The relative energy for each profile has been calculated by taking the sum of the energies of both reactants, benzene and the metal complex, computed separately. The following diagrams showing the reactions profiles will also include the Gibbs free energy in italics. This is important here as an intermolecular process is taking place and so the entropy of the system must also be considered.

4.2.1. C−H activation of benzene by $[Ir(\eta\text{-}Cp)(PH_3)(\kappa^2\text{-}OAc)]^+$ (7_{OAc})

The first step of the process is described in Figure 4.2. It involves the dissociation of one arm of the acetate and the approach of the benzene ring towards the metal which leads to the formation of a η^2-C=C benzene complex, $\mathbf{8_{OAc}}$. Reactant $\mathbf{7_{OAc}}$ exhibits a $Ir{-}O_1$ bond with a distance of 2.17 Å, the same distance computed in $\mathbf{1_{Me}}$. The transition state $\mathbf{TS(7\text{-}8)_{OAc}}$ shows a weak η^2-C−H interaction between the $C_1{-}H_1$ bond and the metal centre and a very long $H_1\cdots O_1$ interaction of 2.42 Å. Intermediate $\mathbf{8_{OAc}}$

shows a fully dissociated Ir···O_1 bond (3.15 Å) and short contacts between benzene and iridium (C_1···Ir = 2.57 Å and C_2···Ir = 2.46 Å). Additionally, a short H_1···O_1 contact with a distance of 2.55 Å is computed. The activation energy required is 15.9 kcal/mol and the step is endothermic by 10.6 kcal/mol.

A comparison of this process with the first step computed for $\mathbf{1_{Me}}$ highlights a number of differences. Comparing the κ^2- κ^1 displacement transition states, $\mathbf{TS(8\text{-}9)_{OAc}}$ and $\mathbf{TS(1\text{-}2)_{Me}}$, shows longer Ir···$H_1$ and H_1···O_1 contacts in the former and this is consistent with the slightly higher activation barrier computed with benzene ($\Delta E^{\ddagger}$ = 15.9 kcal/mol *cf.* 13.4 kcal/mol). Although $\mathbf{8_{OAc}}$ shows a very similar η^2-C=C interaction to that seen in $\mathbf{2_{Me}}$ a different degree of rotation about the Ir-O_2 bond is seen (X-Ir-O_2-C_2 = 58.8° *cf.* 35.2° in $\mathbf{2_{Me}}$). This means the shortest H_1···O contact involves the outer oxygen, O_1, and not the inner oxygen, O_2, as was seen in $\mathbf{2_{Me}}$.

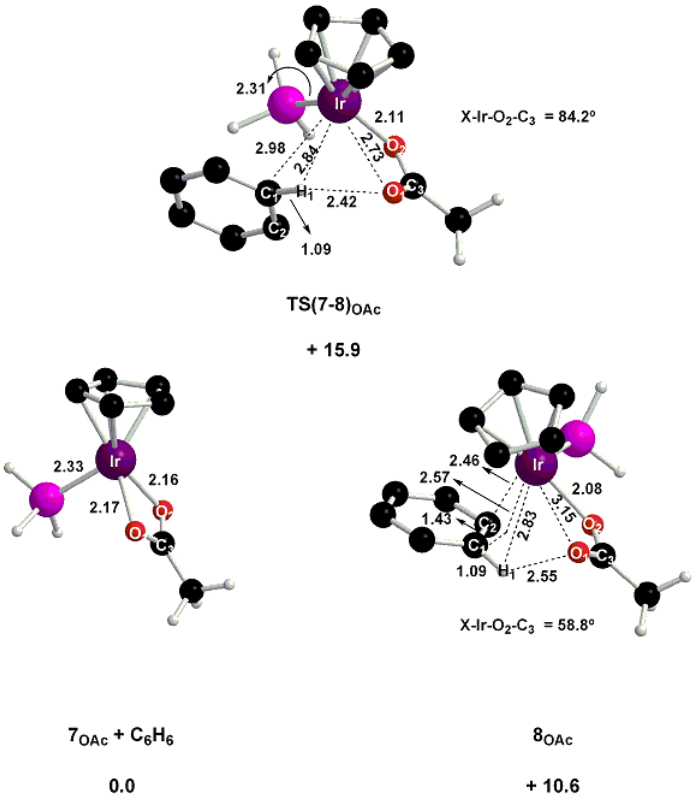

Figure 4.2 – Computed stationary points (kcal/mol, distances in ångstroms) for the initial step of the C−H activation of C_6H_6 by $\mathbf{7_{OAc}}$. Non-participating hydrogens are omitted for clarity.

The second step in the intermolecular C−H activation reaction is shown in Figure 4.3 and involves the deprotonation of the benzene C_1−H_1 bond by the free arm of the

acetate and the formation of an iridium−phenyl bond. The transition state **TS(8-9)$_{OAc}$**, exhibits short contacts between Ir and both C_1 and H_1 (Ir···C_1 = 2.26 Å and Ir···H_1 = 2.22 Å), elongation of the C_1-H_1 distance to 1.24 Å and a very short H_1···O_1 distance of 1.49 Å. This step is exothermic by 7.6 kcal/mol and the overall C−H activation reaction leads to **9$_{OAc}$** which is only 2 kcal/mol less stable than **7$_{OAc}$**. A comparison between **TS(8-9)$_{OAc}$** and the intramolecular C−H activation transition state, **TS(2-3)$_{Me}$**, and shows that the transition state for the intramolecular process is much earlier, in terms of both a longer Ir···C_1 distance (2.46 Å), a shorter C_1-H_1 bond (1.10 A) and a much longer H_1···O_1 interaction (2.10 Å). Interestingly, the Ir···H_1 distance is not so affected (2.25 Å). Despite these different structures, the C−H activation of benzene is still associated with a small barrier of only 2.6 kcal/mol.

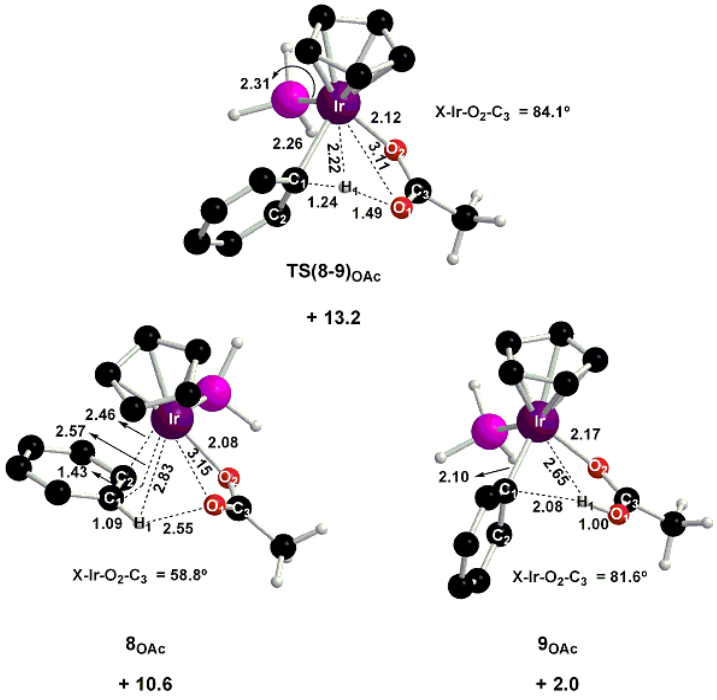

Figure 4.3 - Computed stationary points (kcal/mol, distances in ångstroms) for the second step of the C−H activation of C_6H_6 by **7$_{OAc}$**. Non-participating hydrogens are omitted for clarity.

The full two step profile is shown in Figure 4.4. The limiting step of the process is still associated with the displacement of one arm of the acetate via **TS(7-8)$_{OAc}$**, which is located at 15.9 kcal/mol. The ambiphilic character present in the transition state **TS(8-9)$_{OAc}$** allows hydrogen transfer to occur with a low activation energy of 2.6 kcal/mol. The overall process is endothermic by 2.0 kcal/mol.

The role of entropy in this associative process where a benzene molecule is added to $\mathbf{7_{OAc}}$ means that the Gibbs free energies (in italics in Figure 4.4) of all stationary points from $\mathbf{TS(7\text{-}8)_{OAc}}$ onwards are approximately 11 kcal/mol higher than the previously computed energies. Therefore, the limiting step now requires a free energy of activation, $\Delta G^{\ddagger}$, of 26.9 kcal/mol while ΔG for the overall process is endergonic by 13.6 kcal/mol.

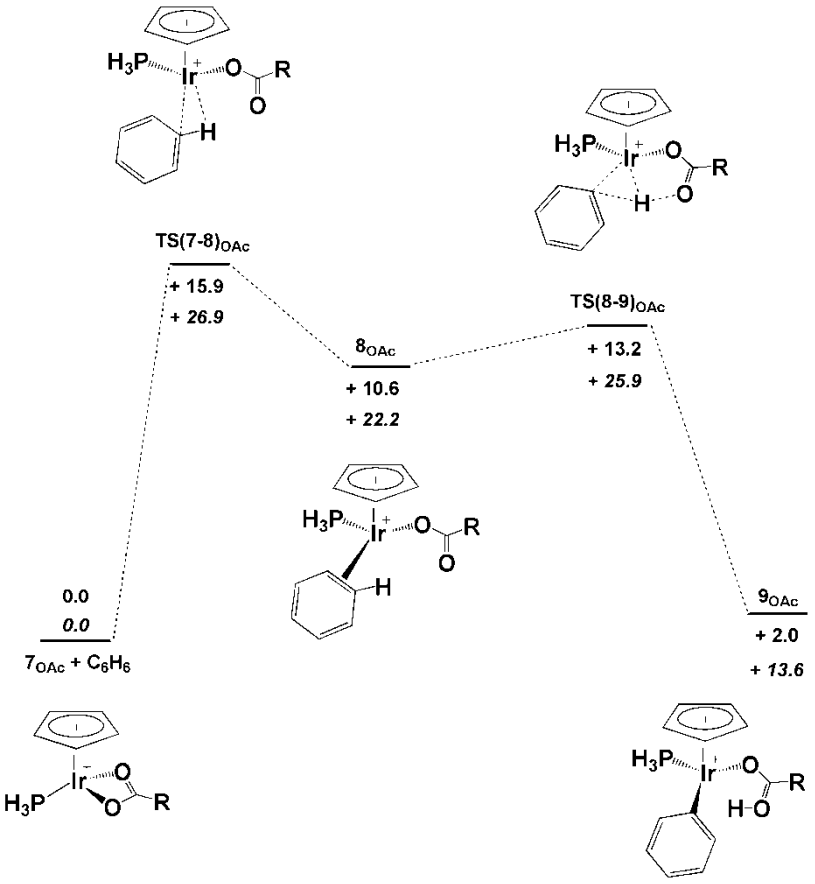

Figure 4.4 - Computed profile (kcal/mol) for the C−H activation of C_6H_6 by $\mathbf{7_{OAc}}$ via an AMLA-6 mechanism. Gibbs free energies are shown in italics.

4.2.2. C−H activation of benzene by $[Ir(\eta\text{-}Cp)(PH_3)(CH_3)]^+$ (7_{Me})

Figure 4.5 shows the full profile for the C−H activation of benzene by $[Ir(\eta\text{-}Cp)(PH_3)(CH_3)]^+$ ($\mathbf{7_{Me}}$). The first step is a barrierless coordination of the benzene molecule which leads to an η^2-benzene complex, $\mathbf{7'_{Me}}$ (E = -11.3 kcal/mol). The following step proceeds via $\mathbf{TS(7'\text{-}8)_{Me}}$, and describes the C−H activation of benzene in $\mathbf{7'_{Me}}$ to give an Ir^V hydride intermediate, $\mathbf{8_{Me}}$. $\mathbf{TS(7'\text{-}8)_{Me}}$ exhibits a product-like geometry, as short Ir−C_2 and Ir−H_1 contacts are computed (2.18 Å and 1.60 Å,

respectively). In $\mathbf{8_{Me}}$ the hydride ligand, H_1, is almost equidistant between C_1 and C_2 ($H_1\cdots C_2$ = 2.24 Å and $H_1\cdots C_1$ = 2.16 Å). This oxidative addition step requires an activation energy of 12.5 kcal/mol and intermediate $\mathbf{8_{Me}}$ is less stable than $\mathbf{7'_{Me}}$ by 10.7 kcal/mol. A comparison with the intramolecular oxidative addition transition state, $\mathbf{TS(2''\text{-}\textit{t}\text{-}5)_{Me}}$, showed similar behaviour.

The transfer of H_1 onto C_1 of the methyl ligand involves the reductive elimination transition state, $\mathbf{TS(8\text{-}9)_{Me}}$. The main movement involves the shortening of the $H_1\cdots C_1$ distance from 2.16 Å in $\mathbf{8_{Me}}$ to 1.53 Å in $\mathbf{TS(8\text{-}9)_{Me}}$, an elongation of the Ir-C_1 distance by 0.08 Å, while very little change was computed for the Ir−C_2 and Ir−H_1 distances. The final product, $[Ir(\eta\text{-}Cp)(PH_3)Ph(CH_4)]^+$, $\mathbf{9_{Me}}$, is a σ-complex of methane with an elongated $H_1\cdots C_1$ distance of 1.15 Å. Reductive elimination requires an activation energy of 3.1 kcal/mol and $\mathbf{9_{Me}}$ is more stable than $\mathbf{8_{Me}}$ by 3.8 kcal/mol.

The overall profile shows that the limiting step of the process corresponds to the reductive elimination transition state, $\mathbf{TS(8\text{-}9)_{Me}}$ and it requires an activation energy of 13.8 kcal/mol relative to $\mathbf{7'_{Me}}$. The inclusion of entropy in the calculations maintains $\mathbf{TS(8\text{-}9)_{Me}}$ as the limiting transition state although $\Delta G^{\ddagger}$ increases to 15.3 kcal/mol. Entropy does not affect the energy change for C-H activation relative to $\mathbf{7'_{Me}}$ (ΔE = +6.9 and ΔG = + 6.7 kcal/mol).

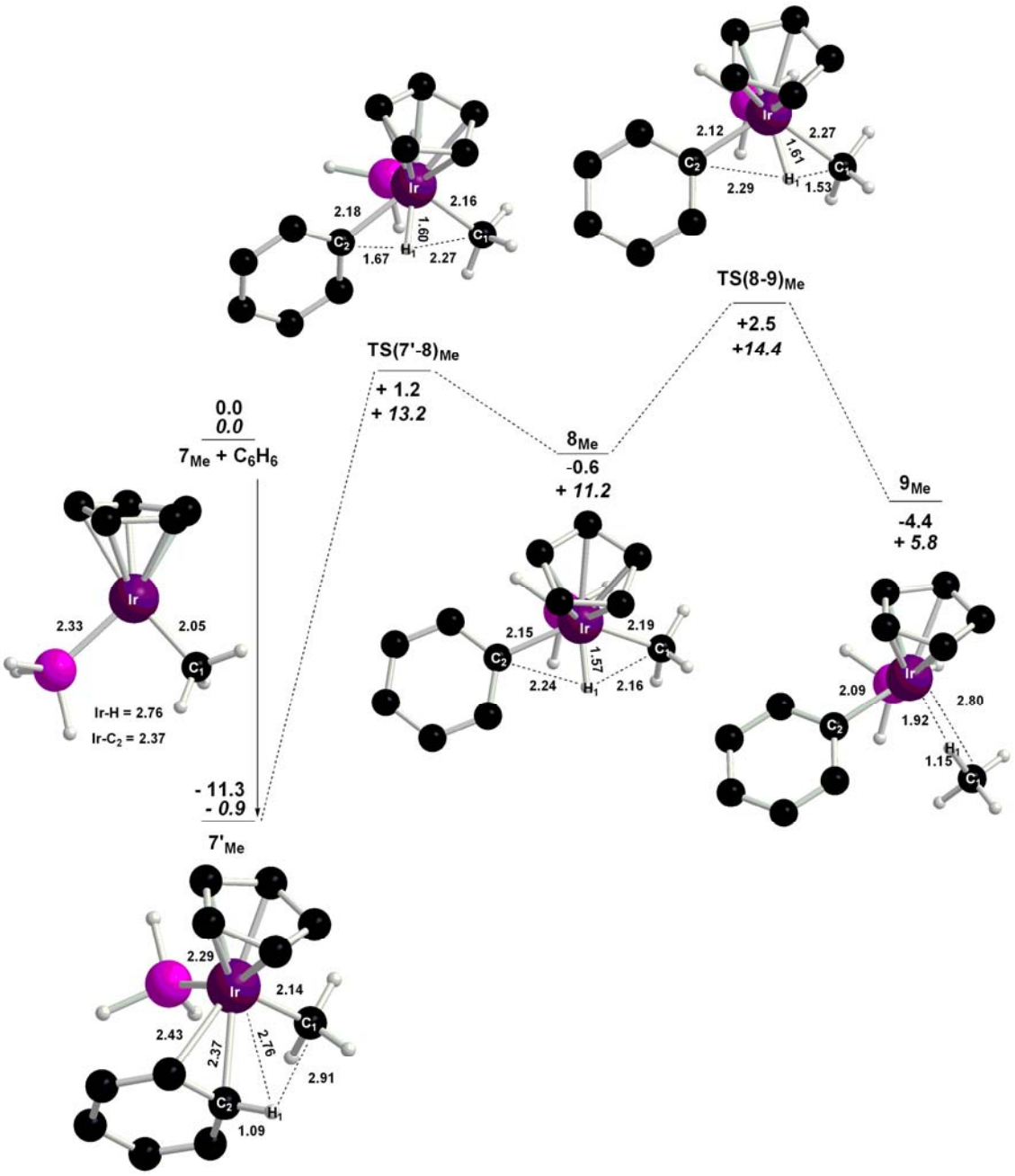

Figure 4.5 - Computed stationary points (kcal/mol, distances in ångstroms) of the C−H activation of C_6H_6 by $\mathbf{7_{Me}}$. Non-participating hydrogens are omitted for clarity.

4.2.3. C−H activation of benzene by [Ir(η-Cp)(PH$_3$)(OCH$_3$)]$^+$(7_{OMe})

The full profile of the C−H activation of benzene by $[Ir(\eta\text{-}Cp)(PH_3)(OCH_3)]^+$, $\mathbf{7_{OMe}}$, is shown in Figure 4.7. In contrast with the previous two systems, an η^2-benzene complex has not been located. This can be explained by the specific geometry computed for the methoxy ligand in $\mathbf{7_{OMe}}$, which depicts a very short Ir−O_1 bond of 1.92 Å and an O_1−Ir−P angle of 82.8º. Indeed, these characteristics are well known to reflect

enhanced π-donation from a p orbital of the oxygen to a vacant d-orbital of the Ir^{III} centre (see Figure 4.6). Calculations carried out on the model system $[Ir(PH_3)_2(H)_2(OH)]$ by Riehl *et al.*[5] showed the most stable geometry exhibited a distorted trigonal bipyramidal structure with α = 70.4°. Our complex $[Ir(\eta\text{-}Cp)(PH_3)(OCH_3)]^+$ can be considered to be analogous to this, where the Cp ligand occupies in a facial position of the trigonal pyramidal and the phosphine is in the other axial position. This leaves the methoxy ligand in an equatorial position where it can bind to the Ir centre in a similar fashion to that described for the OH ligand in $[Ir(PH_3)_2(H)_2(OH)]$. This extra electron donation stabilizes the 16 electron complex and therefore the addition of benzene is disfavoured.

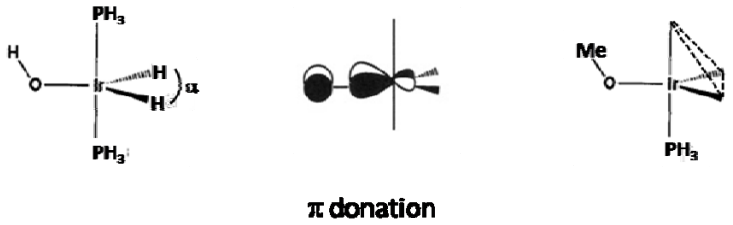

Figure 4.6 – Geometry approximation for $\mathbf{7_{OMe}}$ to a distorted trigonal bipyramid.

The stability of the 16 electron species $\mathbf{7_{OMe}}$ means that the addition and C−H activation of benzene must occur in one step and this is achieved via $\mathbf{TS(7\text{-}9)_{OMe}}$ with an activation energy of 15.6 kcal/mol. This transition state exhibits a short Ir···H_1 contact and Ir−C_1 bond (2.10 Å and 2.23 Å respectively) and leads to the product $\mathbf{9_{OMe}}$ (ΔE = -4.1 kcal/mol). As the reaction evolves an elongation of the Ir−O_1 bond is computed, from 1.92 Å in $\mathbf{7_{OMe}}$ to 2.14 Å in $\mathbf{TS(7\text{-}9)_{OMe}}$ and further to 2.22 Å in $\mathbf{9_{OMe}}$. This elongation reflects the breaking of the O→Ir π-donation as the system evolves from a 16 electron methoxy complex to an 18 electron methanol complex. C−H activation by $\mathbf{7_{OMe}}$ can be described as an AMLA-4 process, indeed the transition state closely resembles $\mathbf{TS(2'\text{-}4)_{Me}}$ computed in Chapter 2. In that case, an elongation of the Ir−O_1 bond was also seen in the C−H activation transition state (2.22 Å in $\mathbf{TS(2'\text{-}4)_{Me}}$ *cf.* 2.06 Å in $\mathbf{2'_{Me}}$), although this effect is less strong than in $\mathbf{TS(7\text{-}9)_{OMe}}$.

The inclusion of the entropy is reflected in a higher values for the Gibbs free energies along the energy profile, by approximately 12 kcal/mol. Thus, $\Delta G^{\ddagger}$ = +27.5 kcal/mol and the overall reaction becomes endergonic by 7.3 kcal/mol.

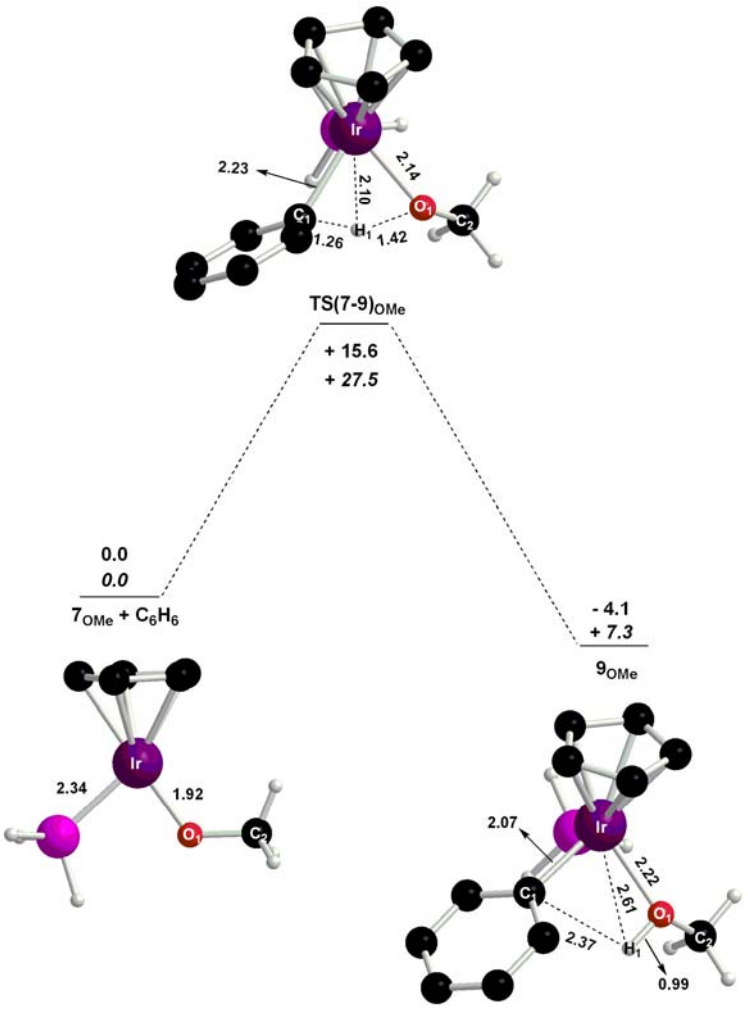

Figure 4.7 - Computed stationary points (kcal/mol, distances in ångstroms) of the C−H activation of C_6H_6 by $\mathbf{7_{OMe}}$. Non-participating hydrogens are omitted for clarity.

4.2.4. Comparison between 7_{OAc}, 7_{Me} and 7_{OMe}

The C−H activation of benzene has been computed with three different complexes, $\mathbf{7_{OAc}}$, $\mathbf{7_{Me}}$ and $\mathbf{7_{OMe}}$, and each system exhibits a different mechanism. Thus, in $\mathbf{7_{OAc}}$ when a chelating base such as acetate is present in the complex, the rate limiting step is the κ^2- κ^1 displacement of acetate and the following C−H activation proceeds via an AMLA-6 mechanism. In $\mathbf{7_{OMe}}$ the methoxy ligand is also involved in the proton transfer, although, in this case, an AMLA-4 mechanism is computed which is also the rate-limiting step. Finally, in $\mathbf{7_{Me}}$ where the methyl ligand acts as the ultimate proton acceptor, much greater metal involvement is required and therefore an oxidative addition/reductive elimination process via an Ir^V intermediate, is computed. In this case the reductive elimination is the limiting step of the process.

Table 4.1 summarizes the computed energetics for the C−H activation processes, both in terms of the activation barriers ($\Delta E^{\ddagger}$, $\Delta G^{\ddagger}$) and the overall energy change (ΔE, ΔG). All three systems have accessible computed energy barriers for benzene activation and the most favourable appears to be $\mathbf{7_{Me}}$. However, the energies shown in Table 4.1 are computed relative to the separated reactants and the reaction with $\mathbf{7_{Me}}$ involves the initial formation of the η^2-benzene complex $\mathbf{7'_{Me}}$. The barrier from this species then increases to 13.8 kcal/mol, very similar to those computed for $\mathbf{7_{OMe}}$ and $\mathbf{7_{OAc}}$. Therefore, on this basis $\Delta E^{\ddagger}$ follows the trend $\mathbf{7_{Me}} < \mathbf{7_{OMe}} \approx \mathbf{7_{OAc}}$. All three reactions are also reasonably accessible being either slightly exothermic ($\mathbf{7_{Me}}$, $\mathbf{7_{OMe}}$) or slightly endothermic ($\mathbf{7_{OAc}}$). In terms of the computed values for $\Delta G^{\ddagger}$ the reaction with $\mathbf{7_{Me}}$ is clearly more favoured, mainly as the disfavourable entropy change associated with benzene addition is cancelled by the favourable enthalpy associated with the formation of $\mathbf{7'_{Me}}$. The associative nature of the intermolecular C−H activation means that all the ΔG values are less favourable than the ΔEs by approximately the same amount (*ca*. 11 kcal/mol).

	$\Delta E^{\ddagger}$	$\Delta G^{\ddagger}$	ΔE	ΔG
$\mathbf{7_{OAc}}$	+ 15.9	+ 26.9	+ 2.0	+ 13.6
$\mathbf{7_{Me}}$	+ 2.5	+ 14.4	- 4.4	+5.8
$\mathbf{7_{OMe}}$	+ 15.6	+ 27.5	-4.1	+ 7.3

Table 4. 1 – Computed energetics (kcal/mol) for the C−H activation of benzene at $\mathbf{7_{OAc}}$, $\mathbf{7_{Me}}$ and $\mathbf{7_{OMe}}$ complexes

$\mathbf{7_{OAc}}$, $\mathbf{7_{Me}}$ and $\mathbf{7_{OMe}}$ can all be considered as potentially useful species for catalysis. Analogues to $\mathbf{7_{Me}}$ are accessible via the precursor [IrCp*(PMe_3)(CH_3)(CF_3SO_3)] complex reported by Bergman and co-workers.[6] However, the synthesis of this species requires a number of synthetic steps and high temperatures. Moreover, it must then undergo dissociation of $CF_3SO_3^-$ to form the active $[IrCp^*(PMe_3)(CH_3)]^+$ complex. Moreover, while this complex has been shown to undergo C−H activation with several hydrocarbons and Si−H bond activation of silanes, it has not been able to promote catalysis. Therefore, even though $\mathbf{7_{Me}}$ is computed to have an accessible energy barrier for the C−H activation step, the use of similar species in catalysis appears to be problematic.

Complex $\mathbf{7_{OMe}}$ appears to be promising as the 16 electron species can be stabilized by the π-donation from oxygen, making the creation of an unsaturated metal centre more achievable. In addition, the following benzene activation occurs via a reasonable barrier and so such a system could be promising synthetic target for a catalyst.

Finally, with $\mathbf{7_{OAc}}$, the limiting step of the process is fundamentally different to $\mathbf{7_{Me}}$ and $\mathbf{7_{OMe}}$ as it does not involve the C−H activation step. Once the κ^2-κ^1 displacement has occurred C−H activation is very facile and requires an activation energy of only 2.6 kcal/mol. Therefore, this species has some very promising features that might help it to act as an efficient catalyst. Moreover the synthesis of closely related complexes has already been reported in the literature.[4]

4.3. Modifications of the main features of $[Ir(\eta\text{-}Cp)(PH_3)(\kappa^2\text{-}OAc)]^+$ ($\mathbf{7_{OAc}}$)

In the study of intramolecular C−H activation comparison of $[Ir(\eta\text{-}Cp)(dmba{-}H)(\kappa^2\text{-}base)]^+$ ($\mathbf{1_{Me}}$, base = acetate; $\mathbf{1_{OTf}}$, base = triflate) showed the triflate species to be promising as it lowers considerably the barrier associated with the limiting step of the process. In addition moving to a neutral species such as $[Ru(\eta\text{-}Cp)(dmba{-}H)(\kappa^2\text{-}OAc)]$ ($\mathbf{1_{Ru}}$), also provided a lower energy pathway, although in this case the products were less stable. Therefore, in order to assess how similar changes will affect the intermolecular process reactions profiles for C−H activation of benzene by $[Ir(\eta\text{-}Cp)(PH_3)(\kappa^2\text{-}CF_3SO_3)]^+$ ($\mathbf{7_{OTf}}$) and the neutral complex $[Ru(\eta\text{-}Cp)(PH_3)(\kappa^2\text{-}OAc)]$ ($\mathbf{7_{Ru}}$) will be computed. In addition, calculations will also be carried out on the full experimental system $[Ir(\eta\text{-}Cp^*)(PMe_3)(\kappa^2\text{-}OAc)]^+$ ($\mathbf{7^*_{Me}}$) that has been characterized by Maitlis and coworkers.[4]

4.3.1. C−H activation of benzene by $[Ir(\eta\text{-}Cp)(PH_3)(\kappa^2\text{-}CF_3SO_3)]^+$ (7_{OTf})

The full profile for the C−H activation of benzene by $[Ir(\eta\text{-}Cp)(PH_3)(\kappa^2\text{-}CF_3SO_3)]^+$ ($\mathbf{7_{OTf}}$) is shown in Figure 4.8. The reaction profile remains a two step process where the limiting step is still associated with the displacement of one arm of the chelating base. This is very similar to the energy profile computed for $\mathbf{1_{OTf}}$, although now only a slight stabilization of the κ^1-intermediate is computed ($\Delta E(\kappa^2\text{-}\kappa^1)$ = -0.3 kcal/mol for $\mathbf{7_{OTf}}$ and -3.0 kcal/mol for $\mathbf{1_{OTf}}$, see Section 2.3.5).

The C−H activation transition state **TS(8-9)$_{OTf}$** exhibits a lengthening of the $C_1\cdots H_1$ distance by over 0.2 Å to 1.34 Å and a very short $O_1\cdots H_1$ contact of only 1.32 Å, the lowest such distance computed so far. The interaction of the metal centre with the C_1−H_1 bond leads to a Ir−C_1 bond of 2.20 Å and an Ir$\cdots H_1$ interaction of 2.41 Å.

The introduction of triflate lowers the barrier for κ^2-κ^1 displacement ($\Delta E^{\ddagger}_{OTf}$ = 9.7 kcal/mol *cf.* $\Delta E^{\ddagger}_{OAc}$ = 15.9 kcal/mol) but increases the energy required to favour the C−H cleavage ($\Delta E^{\ddagger}_{OTf}$ = 8.1 kcal/mol *cf.* $\Delta E^{\ddagger}_{OAc}$ = 2.6 kcal/mol). This higher barrier is consistent with **TS(8-9)$_{OTf}$** being much later transition state than **TS(8-9)$_{OAc}$**, in particular in terms of shorter Ir−C_1 and a $O_1\cdots H_1$ distances. The trend towards a more difficult C−H activation step was also computed in the related intramolecular systems.

The inclusion of the entropy increases the both activation barriers and in fact **TS(8-9)$_{OTf}$** moves slightly above **TS(7-8)$_{OTf}$**, so swapping the limiting step of the process ($\Delta G^{\ddagger}$ = 20.9 kcal/mol). The κ^1-intermediate **8$_{OTf}$** is also now less accessible (ΔG = 11.0 kcal/mol) and the process becomes endergonic by +14.4 kcal/mol.

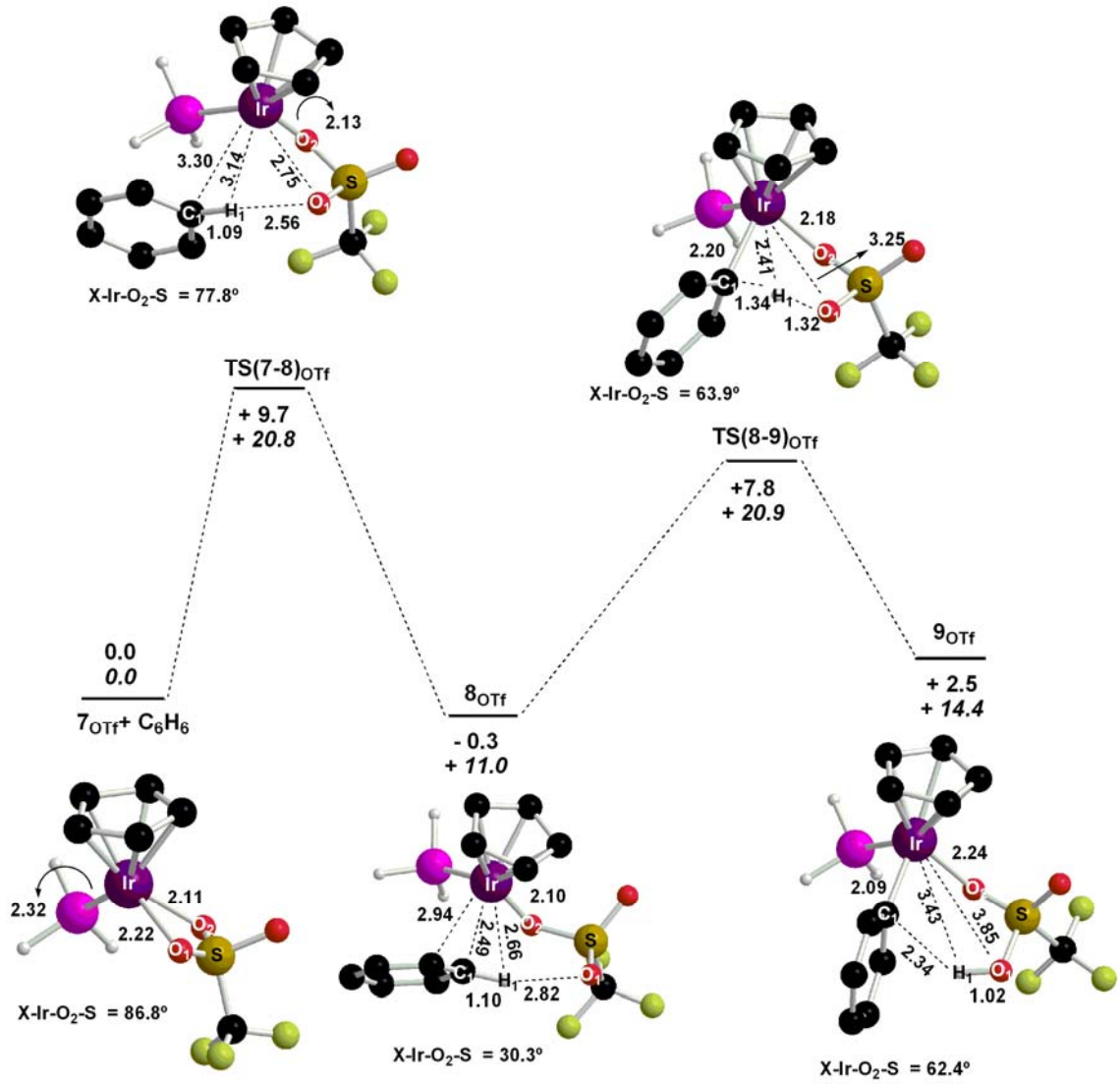

Figure 4.8 - Computed stationary points (kcal/mol, distances in ångstroms) of the C−H activation of C_6H_6 by $\mathbf{7_{OTf}}$. Non-participating hydrogens are omitted for clarity.

4.3.2. C−H activation of benzene by [Ru(η-Cp)(PH$_3$)(κ^2-OAc)] (7$_{Ru}$)

The full reaction profile for the C−H activation of benzene by [Ru(η-Cp)(PH_3)(κ^2-OAc)] ($\mathbf{7_{Ru}}$) is shown in Figure 4.9. Even though the same two step process is computed a change of behaviour from $\mathbf{7_{OAc}}$ is observed as now the rate determining step is associated with the C−H cleavage with a very high barrier of 21.0 kcal/mol. In addition, the κ^2-κ^1 displacement is the highest energy barrier computed so far, at 18.2 kcal/mol. This is surprising as in the intramolecular studies κ^2-κ^1 displacement was much easier for the neutral system. In the present case the reactant $\mathbf{7_{Ru}}$ does exhibit longer M−O bond distances compared to $\mathbf{7_{OAc}}$. However, in $\mathbf{TS(7\text{-}8)_{Ru}}$ the Ru···O_1

distance of 2.96 Å is the longest computed so far, while the interactions of H_1 with the metal and the free oxygen are relatively short (Ru···H_1 = 2.70 Å and C_1···H_1 = 2.31 Å).

In the κ^1-intermediate **8_{Ru}** an η^2-interaction with the benzene ring is evident, as seen in the longer C_1−C_3 bond (1.44 Å). The following **TS(8-9)$_{Ru}$** shows a later transition state geometry than **TS(8-9)$_{OAc}$**, in particular in terms of the Ru−C_1, C_1-H_1 and O_1···H_1 (2.22 Å, 1.40 Å and 1.33 Å respectively). A similar later transition state geometry was seen above for **TS(8-9)$_{OTf}$**, however, whereas in that case the Ir···H_1 distance was 2.41 Å, in **TS(8-9)$_{Ru}$** this shortens to 2.09 Å. The equivalent distance in **TS(8-9)$_{OAc}$** was 2.22 Å, suggesting that the degree of M···H_1 interaction in these intermolecular C−H activation processes is not the key factor in determining the activation energy.

Overall, intermolecular C−H activation of benzene at **7_{Ru}** looks very unfavourable, as it requires a higher energy barrier than that computed for **7_{OAc}** as well having a more unstable product. The inclusion of the entropy makes this situation worse with $\Delta G^{\ddagger}$ = +33.3 kcal/mol and the overall reaction being highly endergonic by 28.6 kcal/mol.

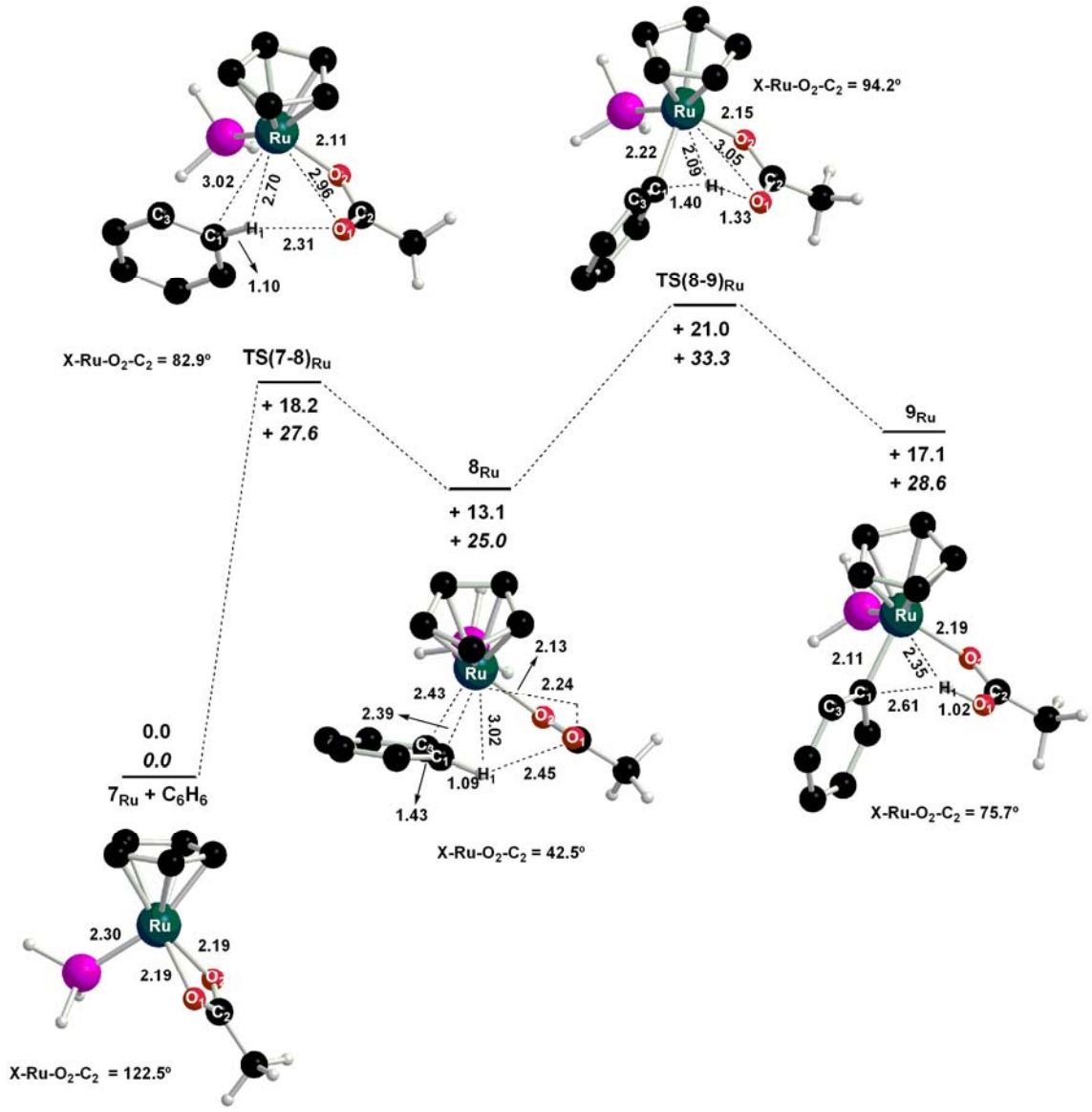

Figure 4.9 - Computed stationary points (kcal/mol, distances in ångstroms) of the C−H activation of C_6H_6 by $\mathbf{7_{Ru}}$. Non-participating hydrogens are omitted for clarity.

4.3.3. C−H activation of benzene by [Ir(η-Cp)(PMe$_3$)(κ^2-OAc)]$^+$ (7$^*_{OAc}$)*

Figure 4.10 shows the full profile of the C−H activation of benzene by [Ir(η-Cp*)(PMe$_3$)(κ^2-OAc)]$^+$ ($\mathbf{7^*_{OAc}}$). As for $\mathbf{7_{OAc}}$, the reaction remains a two step process, however now the C−H cleavage becomes the limiting step with an overall energy barrier of 23.9 kcal/mol.

The reactant geometry of $\mathbf{7^*_{OAc}}$ exhibits longer Ir−O bonds than those computed in $\mathbf{7_{OAc}}$ (2.21 Å in $\mathbf{7^*_{OAc}}$ and 2.17 Å in $\mathbf{7_{OAc}}$). The following κ^2-κ^1 displacement proceeds via $\mathbf{TS(7\text{-}8)^*_{OAc}}$ and shows a completely different behaviour as almost no interaction

between the metal and the free arm of the acetate with the benzene ring is seen. Indeed, the energy of κ^2-κ^1 displacement of $\mathbf{7^*_{OAc}}$ computed in the absence of benzene to give $[Ir(\eta\text{-}Cp^*)(PMe_3)(\kappa^1\text{-}OAc)]^+$ was 11.3 kcal/mol, very similar to $\Delta E^‡$. This suggests that benzene plays very little role in this process, possibly due to the high steric hindrance present in $\mathbf{7^*_{OAc}}$.

The following C−H activation transition state, $\mathbf{TS(8\text{-}9)^*_{OAc}}$, is rather similar to $\mathbf{TS(8\text{-}9)_{OAc}}$ computed with the small model, the major difference being a greater elongation of the $C_1\cdots H_1$ bond (1.33 Å) and a shorter $O_1\cdots H_1$ distance (1.40 Å). Despite this the activation energy required for the C−H cleavage is, interestingly, very high ($\Delta E^‡$ = 12.1 kcal/mol), compared with $\mathbf{7_{OAc}}$ ($\Delta E^‡$ = 2.6 kcal/mol). Again this may be due to the greater steric effects in the $\mathbf{7^*_{OAc}}$ system.

As usual, including entropy increases the Gibbs free energies. This affects the whole profile, however it has a relatively lower effect in the first step of the process. This can be explained by the lack of interaction between the arene ring and the metal complex in both $\mathbf{TS(7\text{-}8)^*_{OAc}}$ and $\mathbf{8^*_{OAc}}$. The overall free energy barrier to C−H activation is +36.8 kcal/mol and the process is very endergonic ($\Delta G^‡$ = 27.0 kcal/mol).

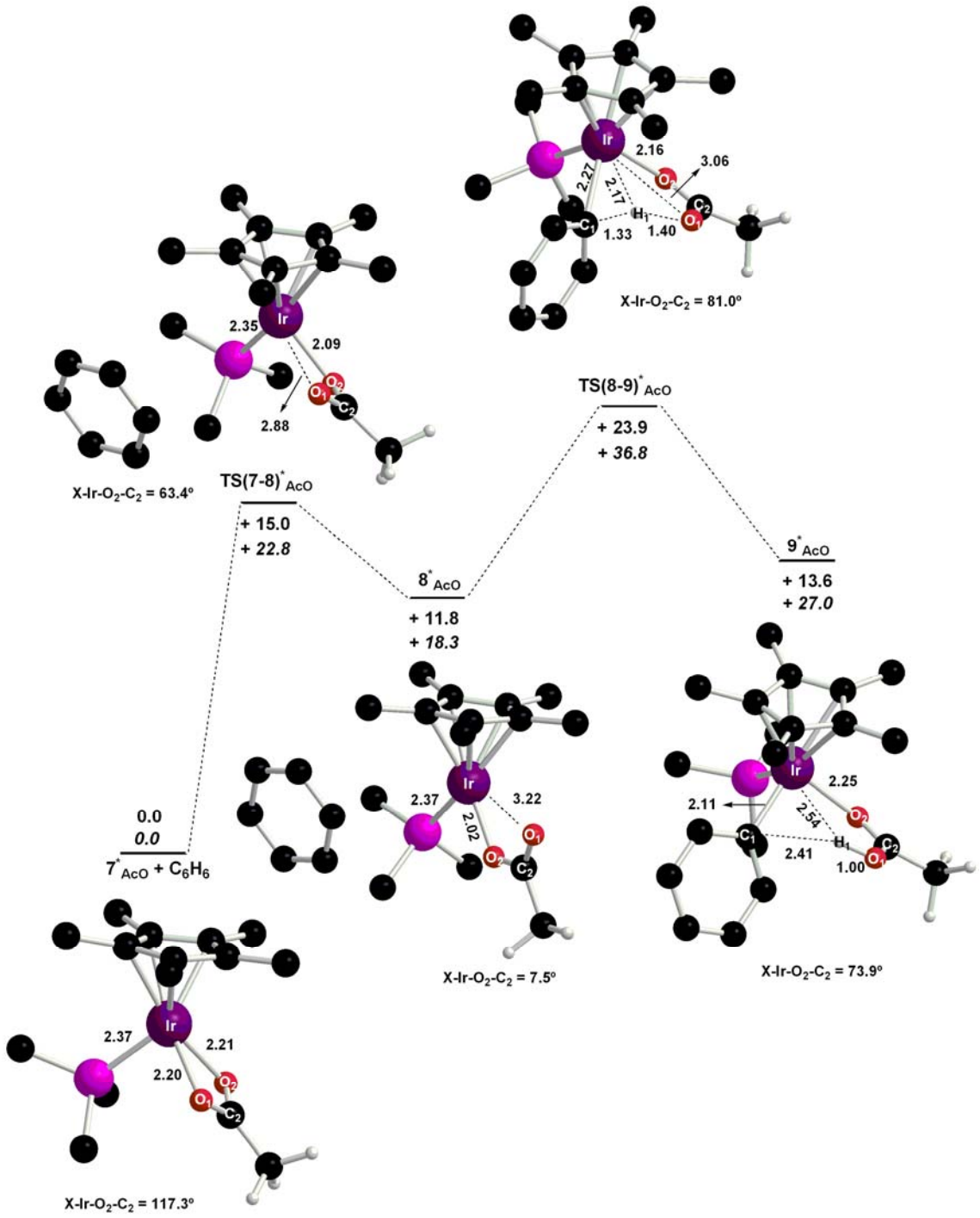

Figure 4.10 - Computed stationary points (kcal/mol, distances in ångstroms) of the C−H activation of C_6H_6 by 7^*_{OAc}. Non-participating hydrogens are omitted for clarity.

4.3.4. Summary

The C−H activation of benzene has been computed at $\mathbf{7_{OAc}}$ and the related species [Ir(η-Cp)(PH$_3$)(κ^2-CF$_3$SO$_3$)]$^+$ ($\mathbf{7_{OTf}}$), [Ru(η-Cp)(PH$_3$)(κ^2-OAc)] ($\mathbf{7_{Ru}}$) and [Ir(η-Cp*)(PMe$_3$)(κ^2-OAc)]$^+$ ($\mathbf{7^*_{OAc}}$) via an AMLA-6 mechanism. In all cases, a two step process is computed, with first a κ^2-κ^1 displacement of one arm of the chelating base followed by C−H cleavage. However, the energies of these processes are very different depending on the metal system involved (see Table 4.2).

	$\Delta E^{\ddagger}$	$\Delta G^{\ddagger}$	ΔE	ΔG
$\mathbf{7_{OAc}}$	+ 15.9	+ 26.9	+ 2.0	+ 13.6
$\mathbf{7_{OTf}}$	+ 9.7	+ 20.9	+ 2.5	+ 14.4
$\mathbf{7_{Ru}}$	+ 21.0	+ 33.3	+ 17.1	+ 28.6
$\mathbf{7^*_{OAc}}$	+ 23.9	+ 36.8	+ 13.6	+ 27.0

Table 4. 2 - Computed energetics (kcal/mol) for $\mathbf{7_{OAc}}$, $\mathbf{7_{OTf}}$, $\mathbf{7_{Ru}}$ and $\mathbf{7^*_{OAc}}$ complexes

Overall $\mathbf{7_{OAc}}$ and $\mathbf{7_{OTf}}$ appear to be the most promising systems for C−H activation of benzene. These species have the lowest energy barriers and their reactions are only slightly endothermic. In contrast $\mathbf{7_{Ru}}$ and $\mathbf{7^*_{OAc}}$ have very high energy barriers and are much more endothermic. This full model system reflects the high importance of steric effects in the intermolecular process. This behaviour is different to that computed in the intramolecular reaction, where the change from Cp to Cp* did not modify the overall energy profile.[7] The associative nature of the intermolecular C−H activation process results in higher barriers and more endergonic reactions when the Gibbs free energy is considered. In the following section one of the more promising candidates for catalysis, $\mathbf{7_{OAc}}$, will be assessed for its activity for alkene hydroarylation.

4.4. Catalytic hydroarylation of ethene by [Ir(η-Cp)(PH$_3$)(κ^2-OAc)]$^+$, $\mathbf{7_{OAc}}$.

Building on previous studies on the C−H activation of benzene by [Ir(η-Cp)(PH$_3$)(κ^2-OAc)]$^+$, $\mathbf{7_{OAc}}$, this section will describe the main features computed for the inclusion of this step into a catalytic cycle for alkene hydroarylation to form ethylbenzene. Figure 4.11 shows the general catalytic cycle for this process with $\mathbf{7_{OAc}}$. The reaction starts with the C−H activation of benzene by $\mathbf{7_{OAc}}$ which, as described in the previous section, requires an activation energy of 15.9 kcal/mol to form [Ir(η-Cp)(PH$_3$)(κ^1-HOAc)(Ph)]$^+$,

9$_{OAc}$. The subsequent substitution of acetic acid by ethene gives [Ir(η-Cp)(PH$_3$)(C$_2$H$_4$)(Ph)]$^+$, **10**. From here, alkene insertion into the Ir−Ph bond could occur to form [Ir(η-Cp)(PH$_3$)(C$_2$H$_4$Ph)]$^+$, **11**. Addition of acetic acid gives **12**, [Ir(η-Cp)(PH$_3$)(C$_2$H$_4$Ph)(κ^1-HOAc)]$^+$, and sets up the system for protonolysis to give [Ir(η-Cp)(PH$_3$)(C$_2$H$_5$Ph)(κ^1-OAc)]$^+$, **13**. Dissociation of ethylbenzene and binding of acetate in a κ^2 fashion regenerates the catalyst **7$_{OAc}$**.

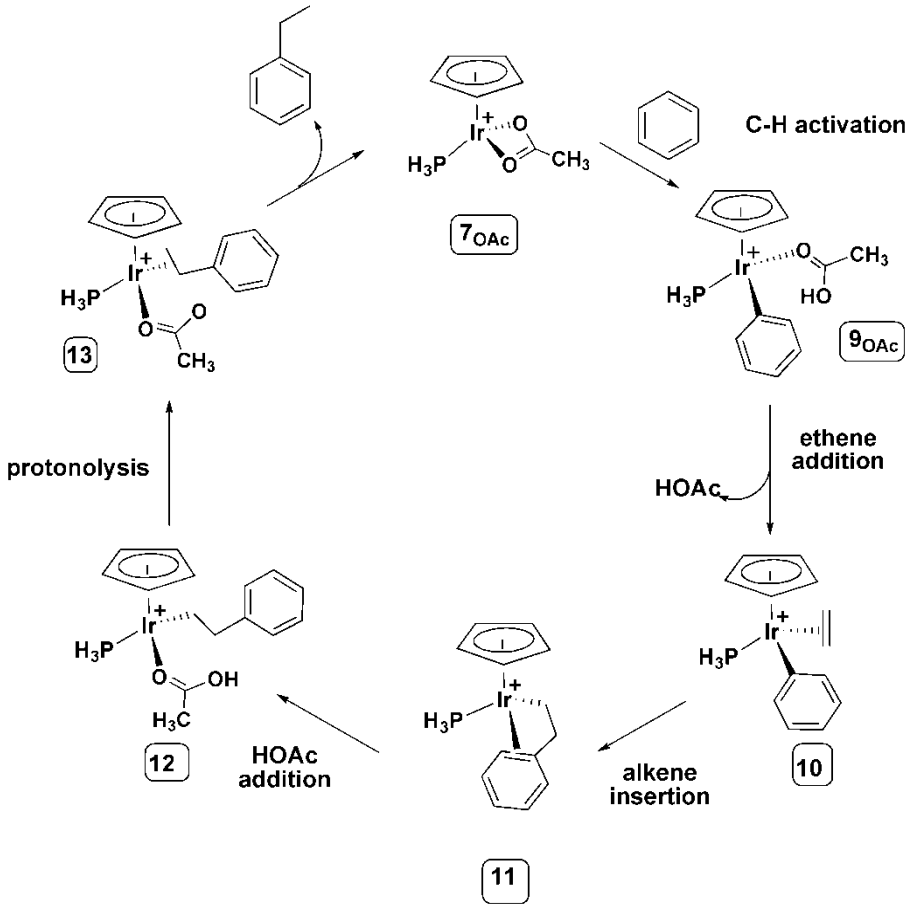

Figure 4.11 – General catalytic cycle for the hydroarylation of ethene by **7$_{OAc}$**.

4.4.1. Addition of ethene to 9$_{OAc}$ and the following migration insertion step

Figure 4.12 shows the energy associated with substitution of acetic acid by ethene in [Ir(η-Cp)(PH$_3$)(C$_6$H$_5$)(κ^1-HOAc)]$^+$ (**9$_{OAc}$**) to form [Ir(η-Cp)(PH$_3$)(C$_2$H$_4$)(Ph)]$^+$ (**10**) and this process was modelled by simply computing each of these species. This substitution step is exothermic by 3.7 kcal/mol and not significantly affected by the inclusion of entropy (ΔG = -3.1 kcal/mol).

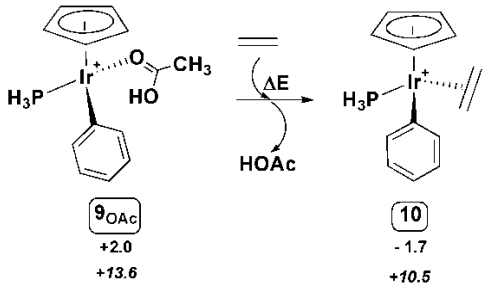

Figure 4.12 - Reaction for the substitution of acetic acid by ethene in $\mathbf{9_{OAc}}$. Energies (kcal/mol) and Gibbs free energies in italics.

The details for the ethene insertion in complex $[Ir(\eta\text{-}Cp)(PH_3)(C_2H_4)(Ph)]^+$ (**10**) are shown in Figure 4.13. From **10** a scan shortening the $C_1\cdots C_2$ distance allowed the location of the transition state, **TS(10-11)**, which exhibits a short $C_1\cdots C_2$ contact of 1.98 Å. As the reaction evolves, both the $Ir{-}C_1$ and $C_2{-}C_3$ bond distances elongate as the ligand is taking on more alkyl character. The final product **11** exhibits a $C_1{-}C_2$ single bond with a length of 1.52 Å and an η^2 interaction between the aryl ring and the metal centre via the $C_4{-}C_1$ bond which elongates slightly to 1.44 Å. The overall process requires an activation energy of 18.3 kcal/mol and the product **11** is more stable than the reactant alkene complex by 4.3 kcal/mol. Very similar values are computed for $\Delta G^{\ddagger}$ and ΔG.

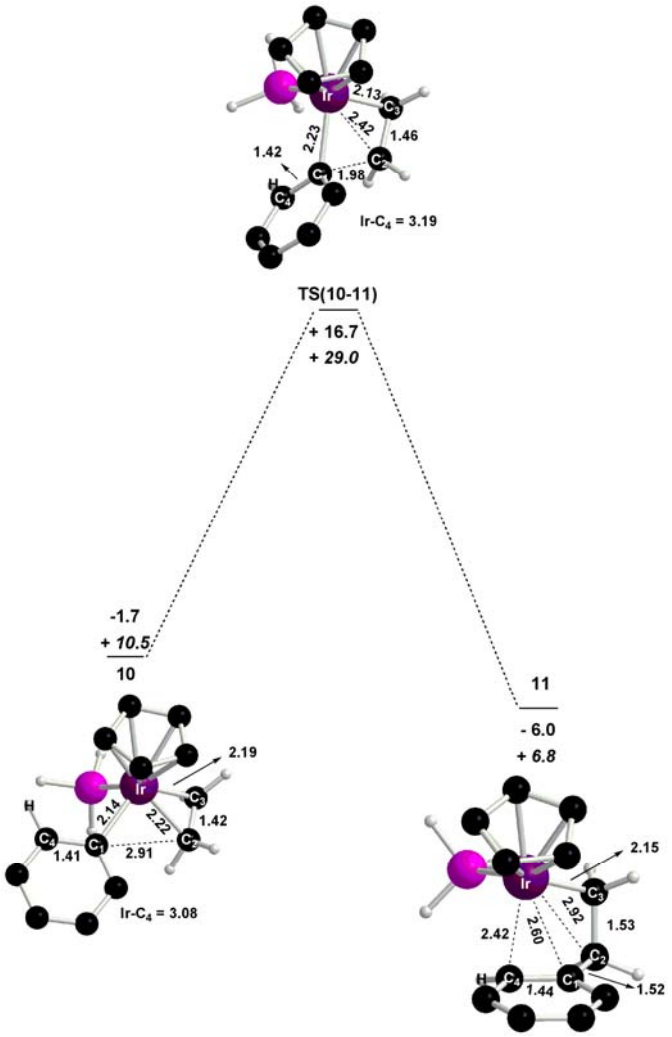

Figure 4.13 - Computed stationary points (kcal/mol, distances in ångstroms) for the insertion of ethene in **10**. Non-participating hydrogens are omitted for clarity. Gibbs free energies in italics.

4.4.2. Protonolysis of [Ir(η-Cp)(PH$_3$)(C$_2$H$_4$Ph)]$^+$ (11) by acetic acid: formation of ethylbenzene and regeneration of 7$_{OAc}$

The next step of the process will lead to the closing of the catalytic cycle. It initially involves the addition of acetic acid to [Ir(η-Cp)(PH$_3$)(C$_2$H$_4$Ph)]$^+$ **(11)** to form complex [Ir(η-Cp)(PH$_3$)(C$_2$H$_4$Ph)(κ^1-HOAc)]$^+$ (**12**). The following proton transfer from the acetic acid to the sp^3 alkyl carbon bound to the metal gives complex [Ir(η-Cp)(PH$_3$)(C$_2$H$_5$Ph)(κ^1-OAc)]$^+$ (**13**) which is a σ-complex of ethylbenzene. The final step involves the dissociation of ethylbenzene and the regeneration of the catalyst [Ir(η-Cp)(PH$_3$)(κ^2-OAc)]$^+$ (**7$_{OAc}$**).

The energies computed for the displacement of the η^2-aryl moiety in **11** by HOAc are shown in Figure 4.14.

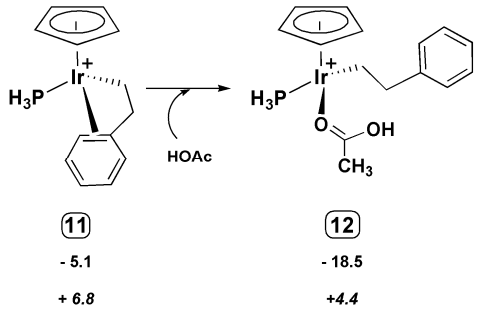

Figure 4.14 - Reaction for the displacement of the η^2-aryl moiety to form **12**. Energies (kcal/mol) and Gibbs free energies in italics.

The addition of acetic acid is highly exothermic and involves the displacement of the η^2-interaction between the aryl group and the metal centre and the formation of an Ir−O bond. The final product is 13.4 kcal/mol more stable than **11**. As this process is associative in nature the inclusion of the entropy is unfavourable and ΔG is only -2.4 kcal/mol.

Details of the energy profile computed for the protonolysis step are shown in Figure 4.15. The reaction occurs via **TS(12-13)** which describes the transfer of H_1 from the acetic acid to the alpha-carbon of the 2-phenylethyl ligand. This transition state exhibits a shortening in the $H_1\cdots C_1$ distance from 3.11 Å in **12** to 1.39 Å in **TS(12-13)**, and an elongation of the $H_1\cdots O_1$ distance to 1.43 Å. In addition, a very short $Ir\cdots H_1$ interaction is computed (1.97 Å). The final product **13** exhibits an interaction between the C_1−H_1 bond of ethylbenzene and the metal centre. Although this is very weak, it is enough to prevent the acetate ligand binding in an η^2-fashion to the metal ($Ir\cdots O_1$ = 3.13 Å). This step requires an energy barrier of 14.5 kcal/mol and the final product is 6.1 kcal/mol less stable than the reactant **12**. Although the overall process is endothermic the inclusion of the entropy is favourable along the reaction due to the partial dissociation of ethylbenzene. The Gibbs free energy change is therefore only +2.4 kcal/mol.

Interestingly, if this final proton transfer reaction is considered in the reverse direction it could be defined as a C−H activation of an alkyl C−H bond via an AMLA-6 mechanism. A comparison between **TS(12-13)** and **TS(8-9)$_{OAc}$** highlights how much

harder the C−H activation is for an alkyl group ($\Delta E^{\ddagger}$ = 8.4 kcal/mol) compared to an arene groups ($\Delta E^{\ddagger}$ = 2.6 kcal/mol). However, the overall ΔE of the process is similar in both cases.

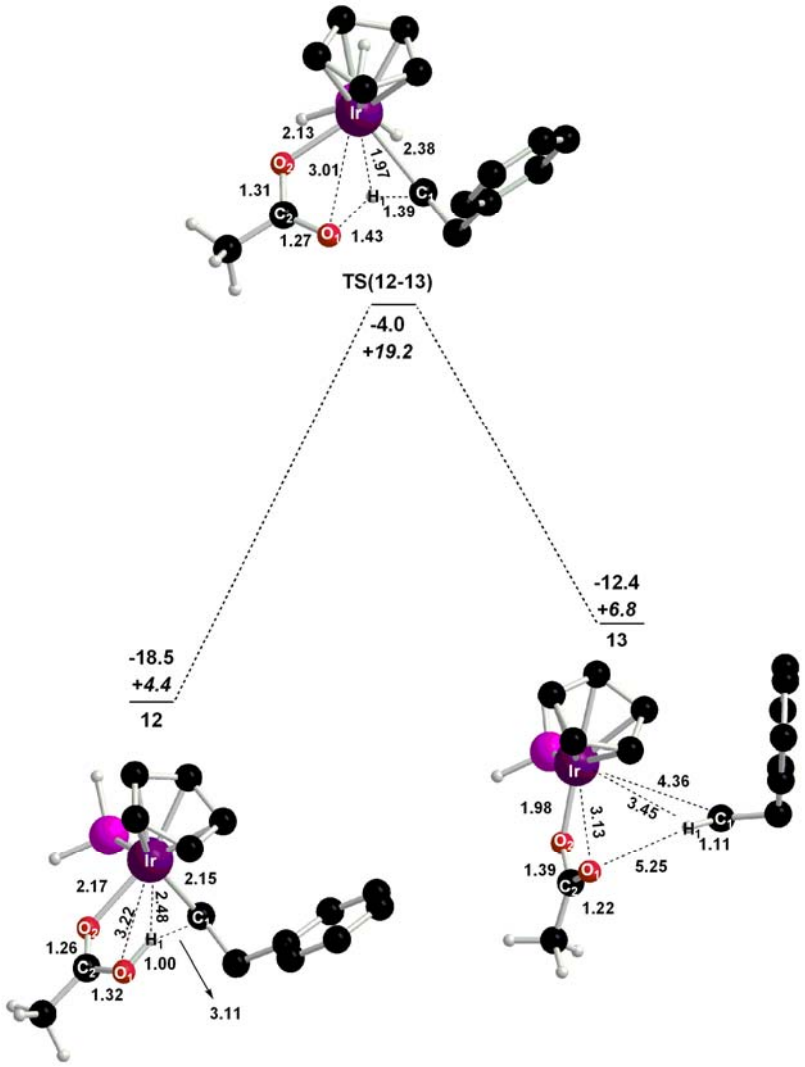

Figure 4.15 - Computed stationary points (kcal/mol, distances in ångstroms) for the protonolysis of **12**. Non-participating hydrogens are omitted for clarity.

Finally, the dissociation of ethylbenzene from **13** was computed by the modelling of ethylbenzene and $\mathbf{7_{OAc}}$ separately, leading to an exothermic reaction with ΔE = -10.0 kcal/mol. This reaction is dissociative, therefore entropy also favours the process and ΔG = -20.1 kcal/mol (see Figure 4.16).

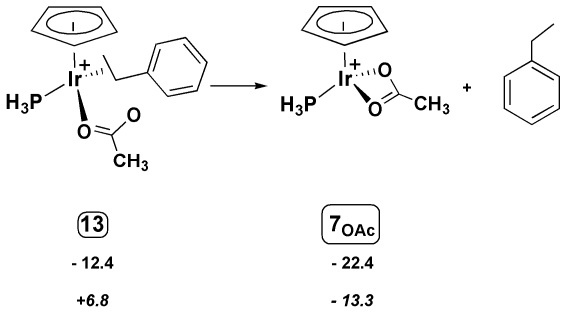

Figure 4.16 - Reaction for the dissociation of ethylbenzene from **13** and regeneration of $\mathbf{7_{OAc}}$. Energies (kcal/mol) and Gibbs free energies in italics.

The reaction profile from the addition of acetic acid to **11** and regeneration of the catalyst $\mathbf{7_{OAc}}$ and formation of ethylbenzene is shown in Figure 4.17. This process looks promising as the formation of complex **12** is very favourable and the subsequent protonolysis can occur with an accessible activation energy.

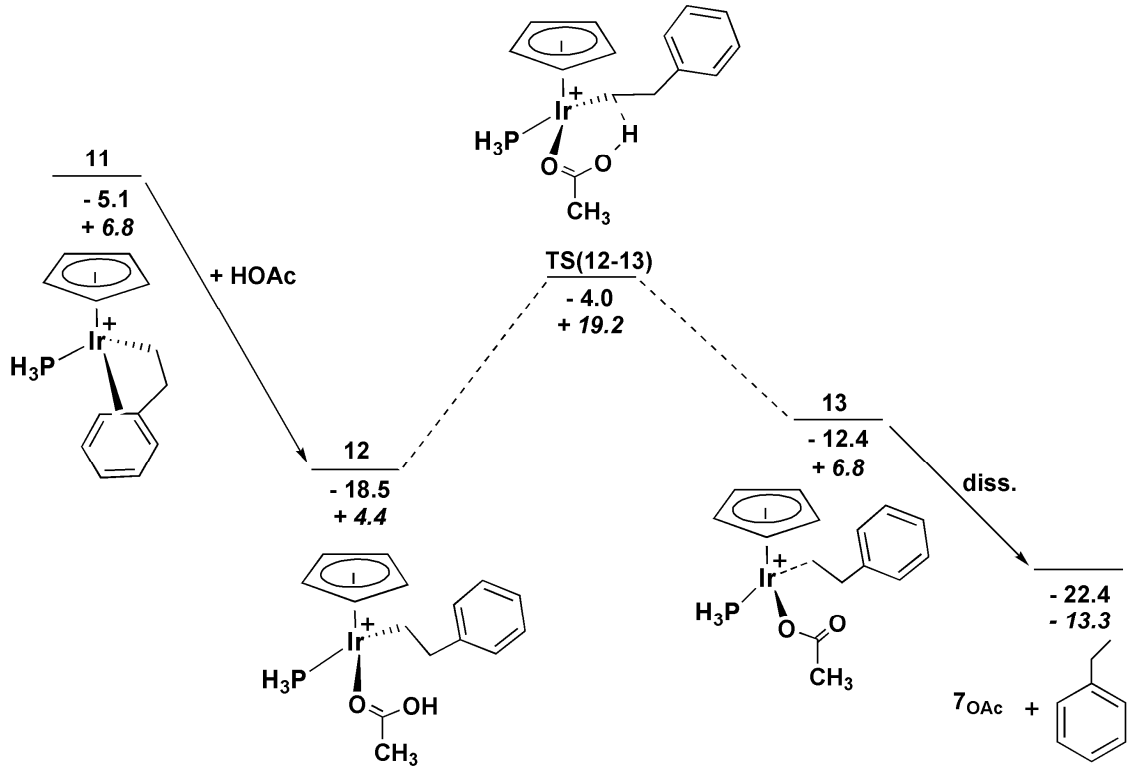

Figure 4.17 – Energy profile (kcal/mol) for addition of acetic acid to **11** and protonolysis to form $\mathbf{7_{OAc}}$ and ethylbenzene. Gibbs free energy in italics.

4.4.3. Side reactions

The closing of the catalytic cycle for alkene hydroarylation is one of the most intricate steps as additional side reactions can occur. Considering the possible experimental conditions of this process four possible side reactions were considered, as shown in Figure 4.18. The excess of ethene would lead to two different possibilities: (I) double insertion of ethene which would lead initially to **15** (and possibly to polymerization); and (II) protonolysis by ethene with loss of ethylbenzene and formation of the vinyl complex, **19**. In an excess of benzene **11** could also undergo protonolysis with formation of an Ir−phenyl complex, **23**, with release of ethylbenzene. Finally, the availability of β−hydrogens on the 2-phenylethyl ligand may result in β-H transfer to form complex **25** which could then dissociate styrene to form an Ir hydride complex. The following will describe each of these side reactions from **11** and their direct competition with the desirable protonolysis by acetic acid described in the previous section.

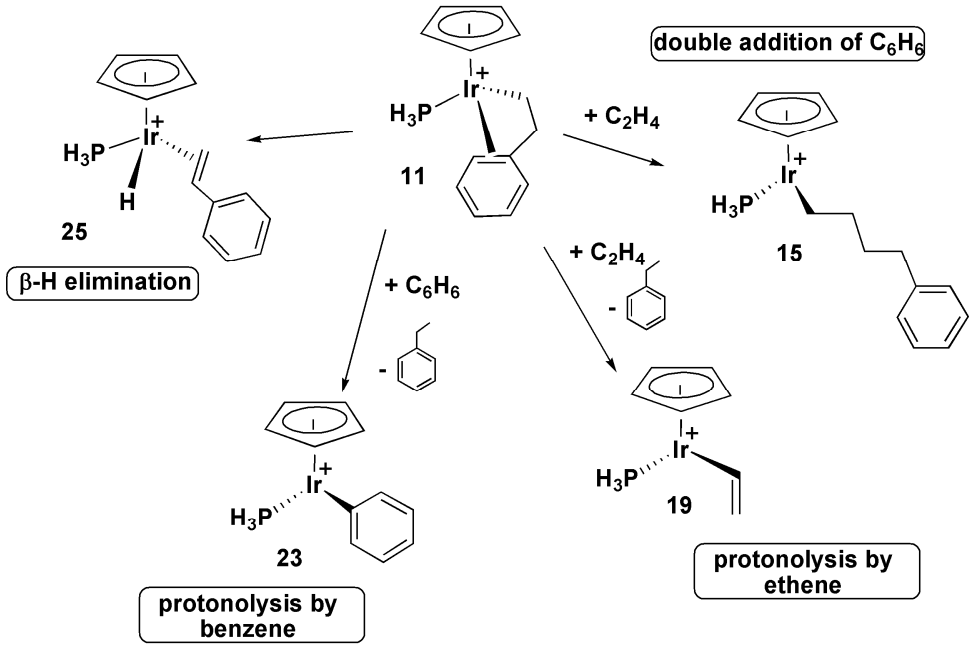

Figure 4.18 – Side reactions considered for intermediate **11**.

I. Double insertion of ethene

The computed profile for the insertion of an second ethene molecule is shown in Figure 4.19. From **11**, the addition of an extra ethene molecule is very exothermic (ΔE = -19.9 kcal/mol). However, the following insertion is less favourable as it requires a very high activation energy of +27.4 kcal/mol. The double insertion product, **15**, is also less stable than **14** by 4.1 kcal/mol. The inclusion of the entropy affects only the ethene addition step from **11** to **14** for which ΔG is only -8.1 kcal/mol.

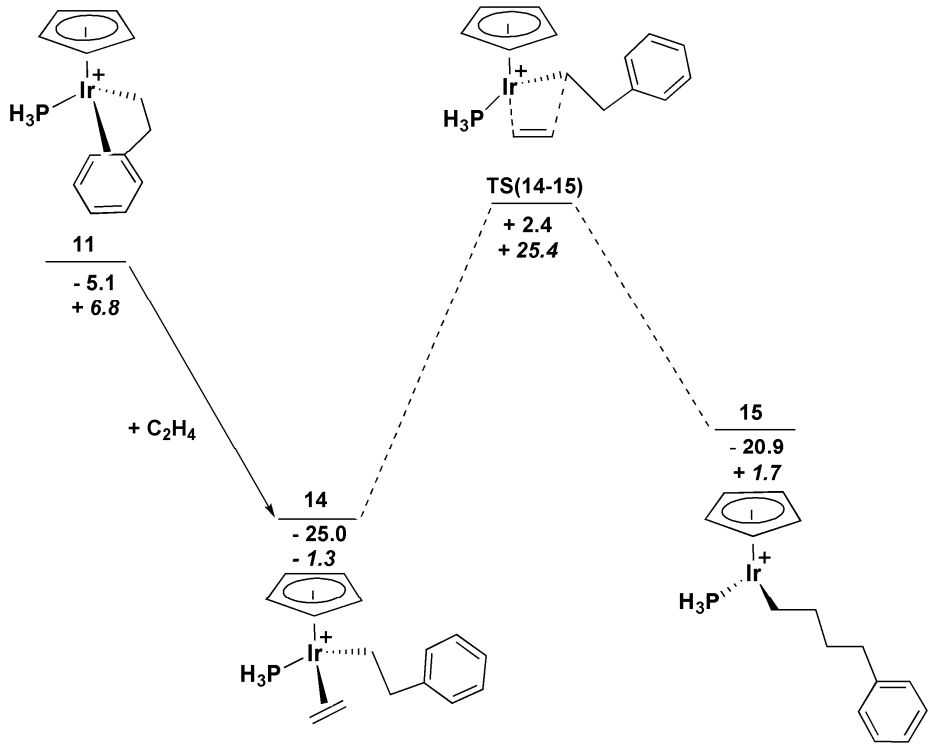

Figure 4.19 – Energy profile (kcal/mol) of the double insertion of ethene to **11**. Gibbs free energy in italics.

II. Protonolysis by ethene

This reaction involves hydrogen transfer from ethene to the 2-phenylethyl ligand and this was shown to involve an oxidative addition/reductive elimination mechanism. Characterisation of this process showed the initial reactant to be an η^2-C-H complex of ethene, **16** (E = -1.8 kcal/mol). Coordination via the C−H bond is much less favourable than via the C=C double bond as in **14** (E = -25.0 kcal/mol). Therefore complex **14** would initially have to reorganize to give complex **16**, although a transition state for this process was not considered. The formation of **16** is, however, only slightly endothermic relative to **11** (ΔE = +3.3 kcal/mol, see Figure 4.20). The following oxidative addition

forms the Ir(V) hydride complex **17** with an activation energy of 3.8 kcal/mol. Complex **17** is 3.3 kcal/mol less stable than **16**. The reductive elimination then requires an activation energy of 2.4 kcal/mol and leads to the vinyl complex **18** in which ethylbenzene is still loosely coordinated (E = -7.0 kcal/mol). The final dissociation of ethylbenzene is unfavourable by 7.5 kcal/mol. Overall protonolysis of **11** by ethene is endothermic by +5.6 kcal/mol and involves an overall barrier of +9.0 kcal/mol. The inclusion of the entropy does not significantly affect the overall energy of the reaction (ΔG = +2.3 kcal/mol) but does result in a larger value of $\Delta G^{\ddagger}$ = +19.6 kcal/mol.

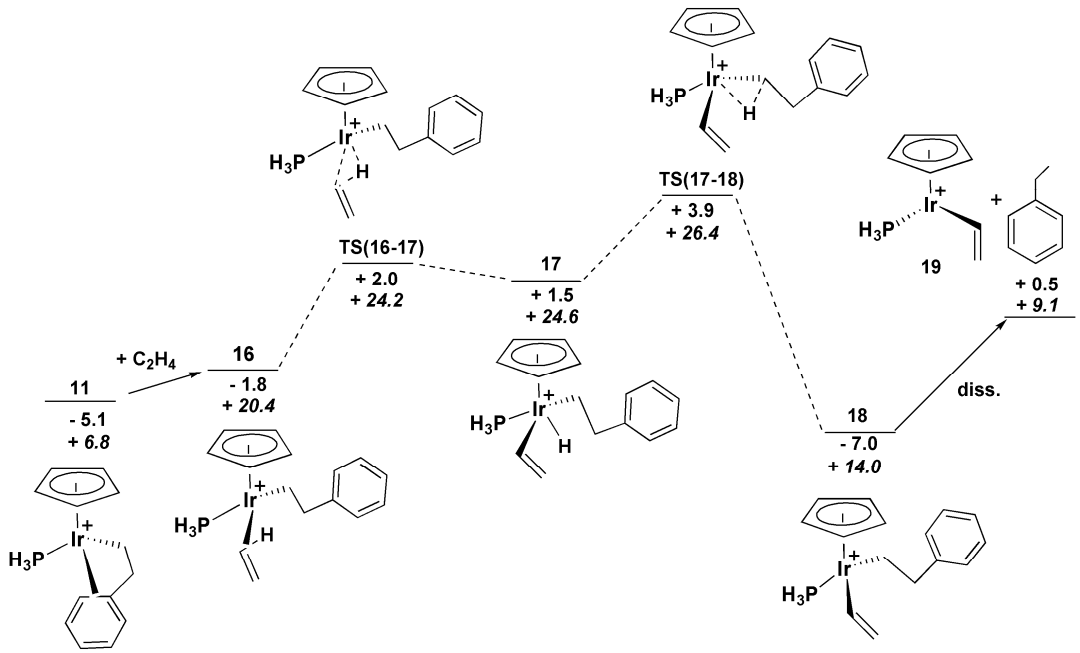

Figure 4.20 – Energy profile (kcal/mol) for protonolysis of **11** by ethene. Gibbs free energy in italics.

III. Protonolysis by benzene

Figure 4.21 shows the reaction profile for the protonolysis of **11** by benzene. As with ethene, this process involves oxidative addition and reductive elimination to release ethylbenzene with the formation of, in this case, an Ir−Ph complex, **23**. Benzene addition is endothermic by +5.5 kcal/mol and yields **20** from which oxidative addition to form the Ir(V) hydride **21** (E = +6.6 kcal/mol) occurs with a barrier of $\Delta E^{\ddagger}$ = +7.3 kcal/mol. The following reductive elimination has a barrier of only 1.7 kcal/mol to form the alkyl complex **22** (E = -1.3 kcal/mol). The final dissociation of ethylbenzene is uphill by 3.7 kcal/mol and gives the hydride complex **23**. Overall, protonolysis by

benzene is endothermic (ΔE = +7.5 kcal/mol) and involves an overall barrier of +13.4 kcal/mol. The equivalent free energy changes are ΔG = +3.7 kcal/mol and $\Delta G^{\ddagger}$ = 24.0 kcal/mol, with the much higher free energy of activation reflecting the addition of benzene in the initial step of the process.

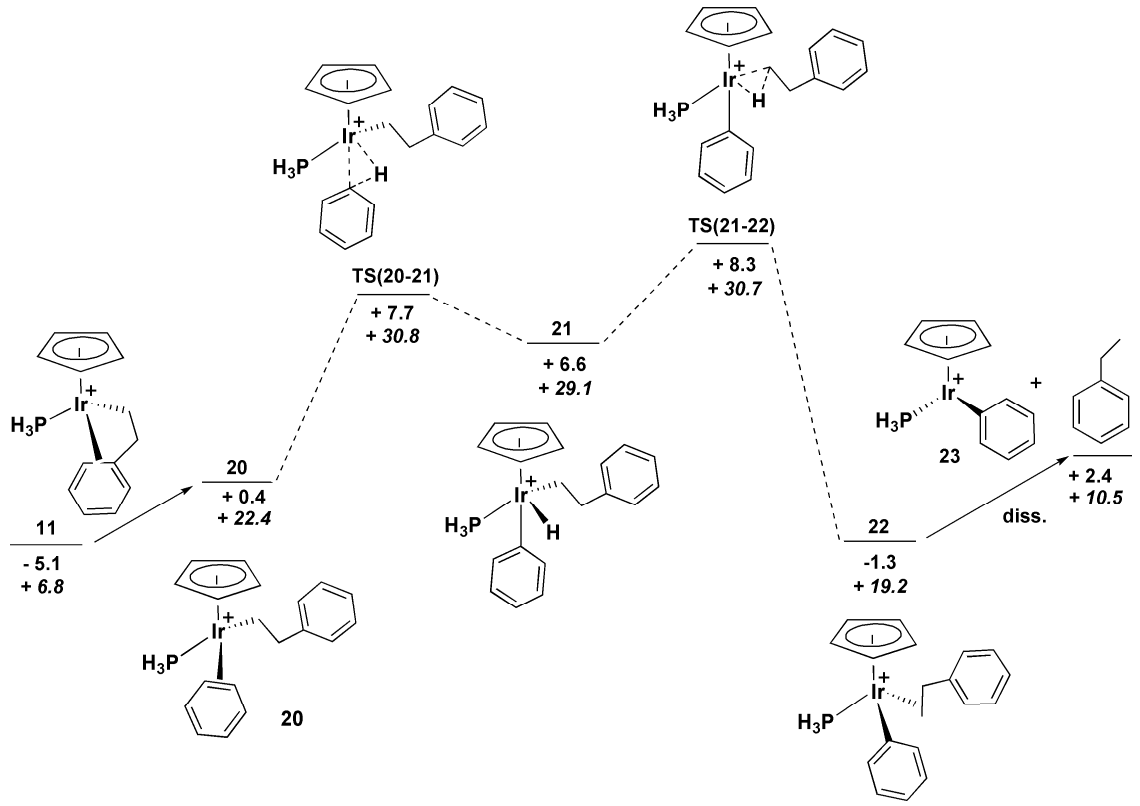

Figure 4.21 - Energy profile (kcal/mol) for protonolysis of **11** by benzene. Gibbs free energy in italics.

IV. β−H elimination

Figure 4.22 shows the reaction profile for the β-H elimination of styrene from **11**. In this case the transition state for β-H transfer, **TS(24-25)**, is unusual because there is no short contact between the Ir centre and either of the β-hydrogens (see Figure 4.23). Instead the key feature of **TS(24-25)** is the rotation around the Ir-C1 bond which forces the η^2-aryl moiety to move away from the metal centre. This makes a vacant site available at the metal centre which then allows β-H transfer to occur. Characterization of **TS(24-25)** led to an isomer of **11** with a different orientation of the aryl moiety (**24**, see Figure 4.23) From **24** the activation barrier for β-H transfer is +12.0 kcal/mol and generates the Ir hydrido-alkene complex, **25** (E = -16.9 kcal/mol). Overall β-H transfer

is relatively accessible with $\Delta E^{\ddagger}$ = +11.1 kcal/mol and the formation of **25** being favourable (ΔE = -11.8 kcal/mol). From **25** , however, the dissociation of the styrene is extremely difficult, being uphill by +45.6 kcal/mol. While the inclusion of entropy does not affect the β-H transfer it does promote the dissociation of styrene, although this is still highly endergonic (ΔG = 26.6 kcal/mol) and so would be unlikely to occur.

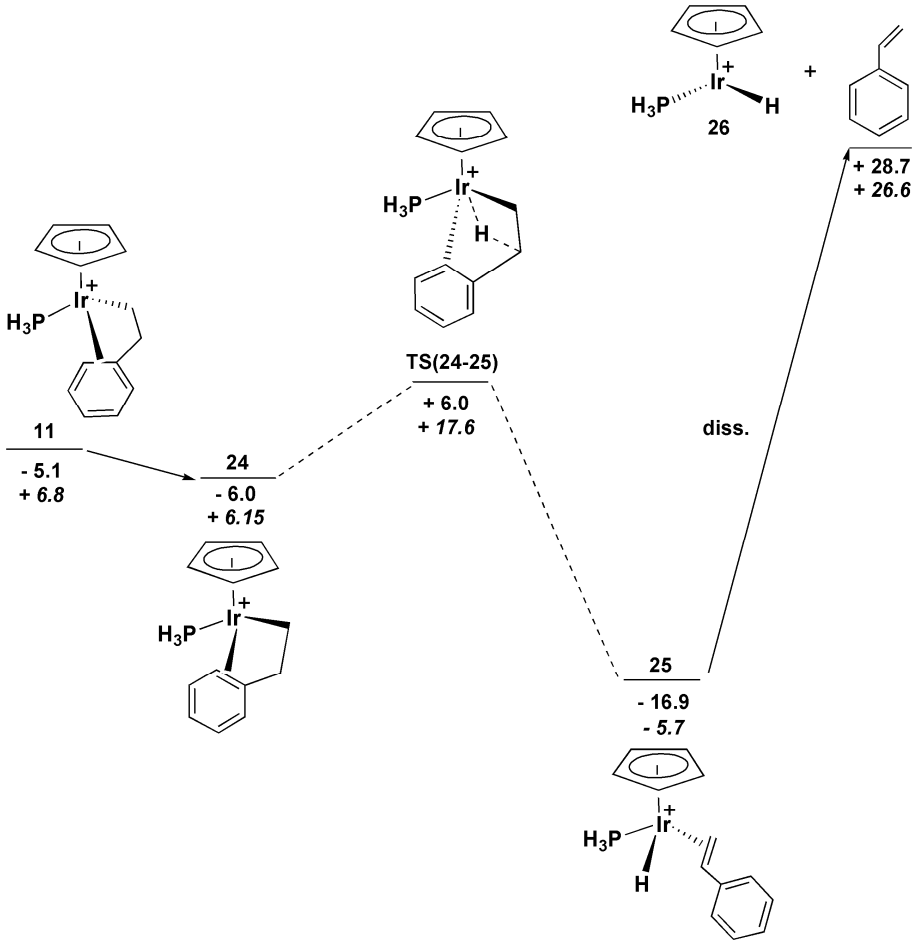

Figure 4.22 – Energy profile (kcal/mol) for the β-H elimination from **11**. Gibbs free energy in italics.

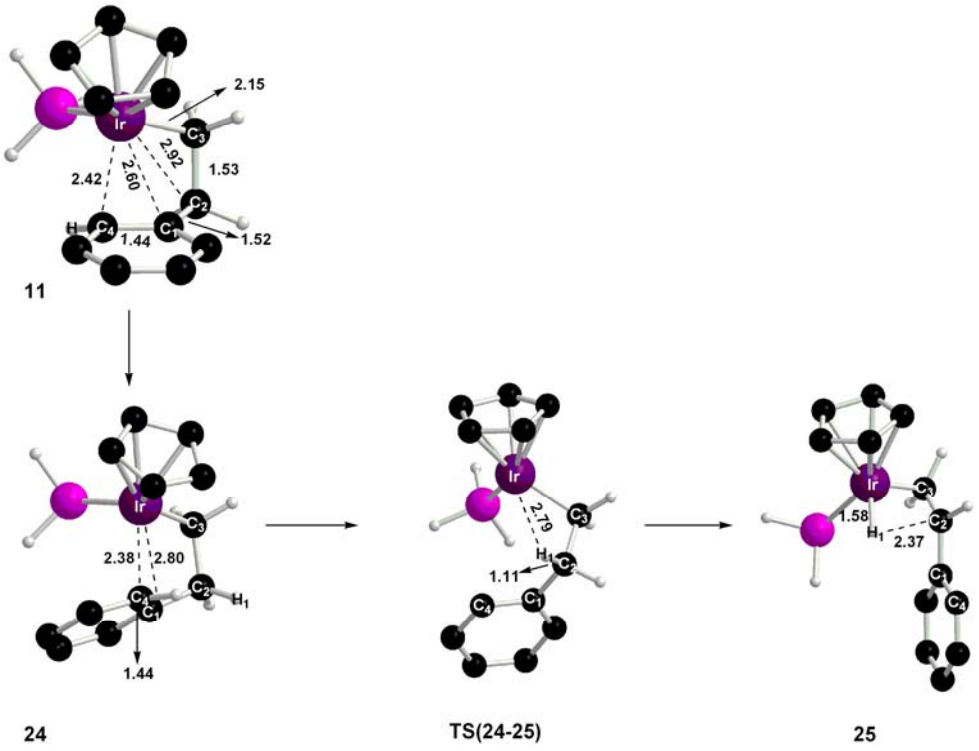

Figure 4.23 – Computed stationary points for the β−H elimination reaction of 11 to form 25.

V. Summary

A summary of the energetics for each of the intermolecular reactions of intermediate **11** considered here is shown in Figure 4.24. The addition of acetic acid is highlighted in green as it is the step that would close the proposed catalytic cycle. A number of these processes involve the initial addition of a ligand to **11** and this is most favourable for ethene (**14,** E = -25.0 kcal/mol) and acetic acid (**12**, E = -18.5 kcal/mol). The addition of ethene in a C-H binding mode (**16**) or benzene (**20**) are much less likely (E = -1.8 kcal/mol and +0.4 kcal/mol respectively). These trends are unaffected by the inclusion of entropy.

The lowest energy transition state for the subsequent protonolysis reactions was computed with acetic acid (**TS(12-13)**, E = -4.0 kcal/mol) and this is at least 6.4 kcal/mol lower than the other protonolysis transition states. This is also trend unaffected by including entropy effects. Overall, therefore although ethene will compete effectively with acetic acid to bind at the Ir metal centre in **11** the most accessible protonolysis process is still the targeted reaction with acetic acid via **TS(12-13)**.

Finally, although the transition state for β-H transfer is significant higher than **TS(12-13)**, E = +6.0 kcal/mol) the intramolecular nature of this reaction makes this competitive in terms of the Gibbs free energy (**TS(12-13)** $\Delta G^{\ddagger}$ = +19.2 kcal/mol; **TS(24-25)** $\Delta G^{\ddagger}$ = 17.9 kcal/mol). β-H transfer is therefore a likely competing pathway to the overall hydroarylation reaction.

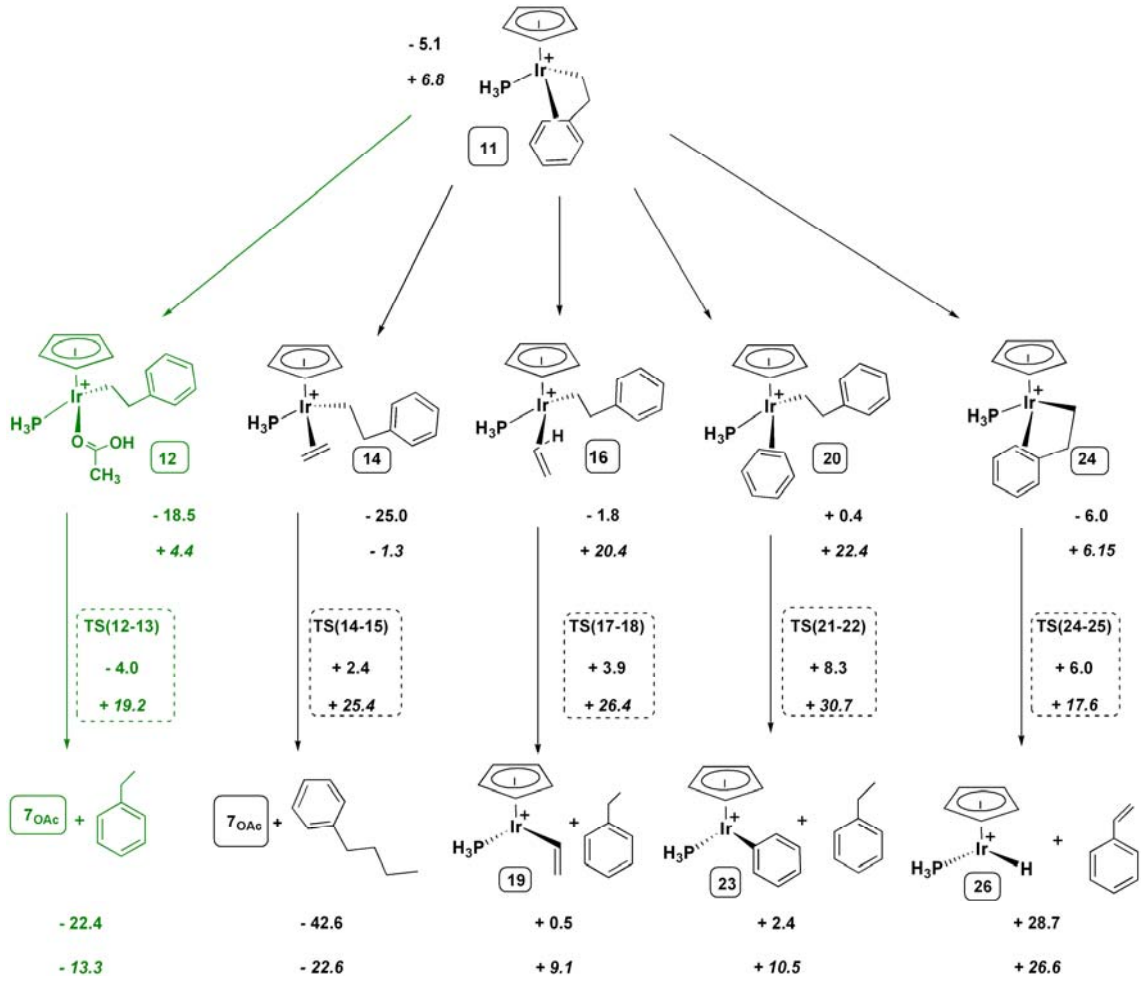

Figure 4.24 – Energetics (kcal/mol) for the addition reaction of acetic acid, benzene and ethene to complex **11**. The β−H transfer reaction is also considered.

4.5. Conclusions

Figure 4.25 shows the reaction profile for the hydroarylation of ethene in the presence of $[Ir(\eta\text{-}Cp)(PH_3)(\kappa^2\text{-}OAc)]^+$ (**7_{OAc}**) as catalyst. The two key steps of the process are the displacement of one arm of the base and approach of the benzene ring (**TS(7-8)$_{OAc}$,** E = 15.9 kcal/mol) and the alkene insertion (**TS(13-14)$_{OAc}$** E = +16.7 kcal/mol), the latter being the limiting step of the process. Goddard *et al.*[8] also identified these two processes as controlling the hydroarylation of ethene in their studies of this process at

the $\{Ir(\eta\text{-}Tp)CO\}^+$ and $\{Ru(\eta\text{-}Tp)CO\}^+$ fragments. With $\{Ir(\eta\text{-}Tp)CO\}^+$ the transition state energies for C−H activation and ethene insertion were +17.0 and +20.6 kcal/mol, respectively while with $\{Ru(\eta\text{-}Tp)CO\}^+$ these values were +19.7 kcal/mol and +24.9 kcal/mol. In our study, the use of $\mathbf{7_{OAc}}$ gives a lower barrier for alkene insertion, while the C−H activation step has a slightly more accessible barrier. The model catalyst $\mathbf{7_{OAc}}$ therefore appears to be a very promising target for catalysis. It is important to remember that the modelling of the full system $\mathbf{7^*_{OAc}}$ increases the C−H activation step, therefore our suggestion for the synthesis and use of this catalyst would be decrease the steric bulk of the co-ligands.

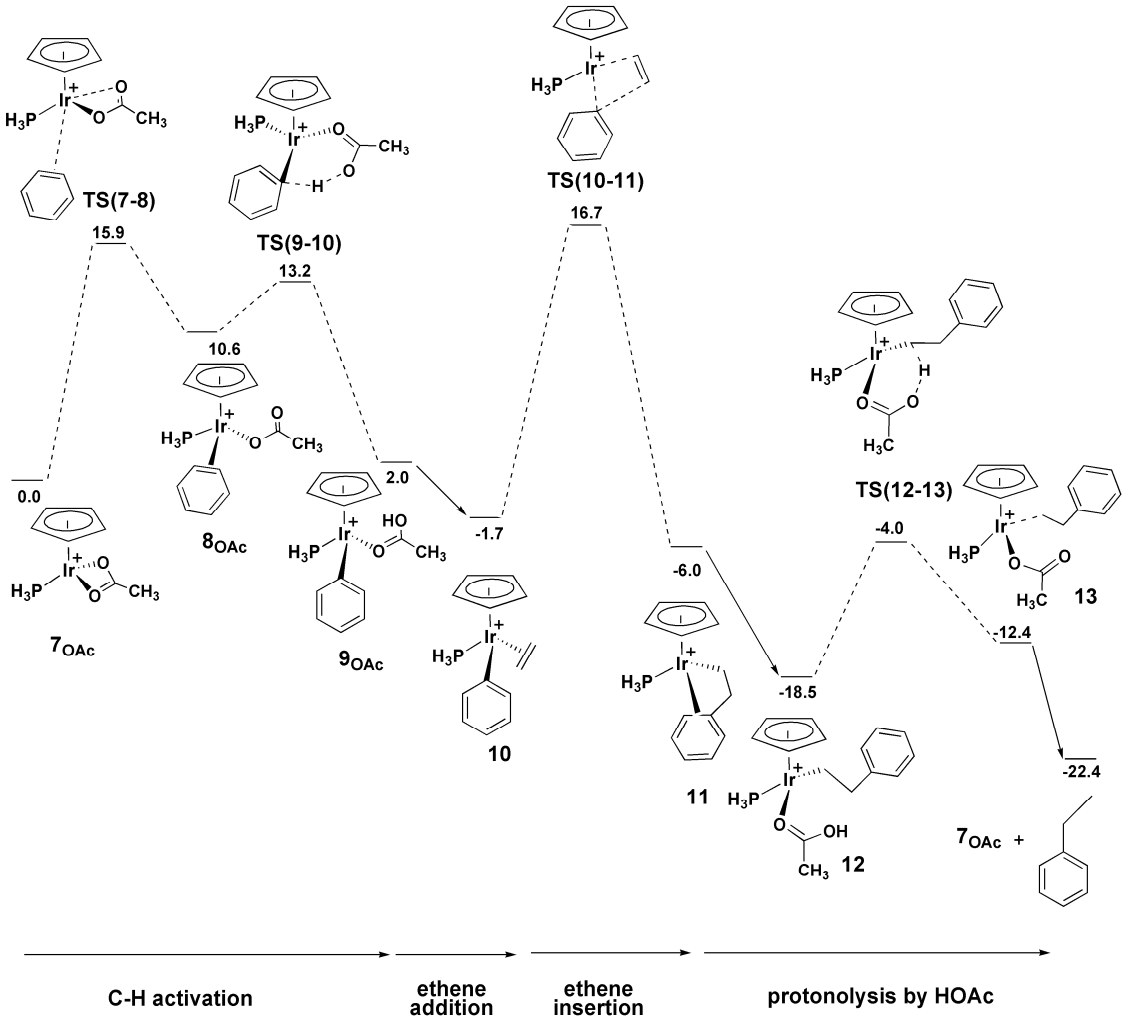

Figure 4.25 – Computed reaction mechanism profile (kcal/mol) for the catalytic cycle of the hydroarylation of ethene in presence of $\mathbf{7_{OAc}}$ as a catalyst.

4.6. References

1. J. Oxgaard, R. P. Muller, W. A. Goddard and R. A. Periana, *J. Am. Chem. Soc.*, 2004, **126**, 352-363; G. Bhalla, J. Oxgaard, W. A. Goddard and R. A. Periana, *Organometallics*, 2005, **24**, 5499-5502; G. Bhalla, X. Y. Liu, J. Oxgaard, W. A. Goddard and R. A. Periana, *J. Am. Chem. Soc.*, 2005, **127**, 11372-11389.
2. S. Q. Niu and M. B. Hall, *J. Am. Chem. Soc.*, 1998, **120**, 6169-6170.
3. W. J. Tenn, K. J. H. Young, G. Bhalla, J. Oxgaard, W. A. Goddard and R. A. Periana, *J. Am. Chem. Soc.*, 2005, **127**, 14172-14173.
4. J. Cook, J. E. Hamlin, A. Nutton and P. M. Maitlis, *J. Chem. Soc.-Dalton Trans.*, 1981, 2342-2352.
5. J.-F. Riehl, Y. Jean, O. Eisenstein and M. Pélissier, *Organometallics*, 1992, **11**, 792-737.
6. P. Burger and R. G. Bergman, *J. Am. Chem. Soc.*, 1993, **115**, 10462-10463.
7. D. L. Davies, S. M. A. Donald, O. Al-Duaij, S. A. Macgregor and M. Poelleth, *J. Am. Chem. Soc.*, 2006, **128**, 4210-4211.
8. J. Oxgaard, R. A. Periana and W. A. Goddard, *J. Am. Chem. Soc.*, 2004, **126**, 11658-11665.

5. Computational background

5.1. Introduction

This chapter will review some fundamental aspects of density functional theory (DFT), the computational method used in this thesis. The discussion will begin with some basic quantum mechanics and continue with an overview of the Hartree-Fock approximation. This will be followed by key concepts in the development of DFT.

5.2. Basic ideas of quantum chemistry

The main purpose of quantum chemical approaches is to solve, as far as possible, the time-independent non-relativistic Schrödinger equation: [1]

$$H\Psi_i = E_i\Psi_i \qquad (5-1)$$

where Ψ_i is the wave function which contains all the information about the system under study and H the Hamiltonian operator. This Hamiltonian operator acts on the wave function to produce an eigenvalue, E, which is the energy of the system.

H is a differential operator representing the total energy of a molecular system consisting of M nuclei and N electrons in the absence of magnetic or electric fields:

$$H = -\frac{1}{2}\sum_{i=1}^{N}\nabla_i^2 - \frac{1}{2}\sum_{A=1}^{M}\frac{1}{M_A}\nabla_A^2 - \sum_{i=1}^{N}\sum_{A=1}^{M}\frac{Z_A}{r_{iA}} + \sum_{i=1}^{N}\sum_{j>i}^{N}\frac{1}{r_{ij}} + \sum_{A=1}^{M}\sum_{B>A}^{M}\frac{Z_A Z_B}{R_{AB}} \qquad (5-2)$$

The first two terms represent the kinetic energy of the electrons and nuclei respectively while ∇_q^2 is the Laplacian operator which is defined as a sum of differential operators, where *x*, *y* and *z* are Cartesian coordinates, as shown in (5-3).

$$\nabla_q^2 = \frac{\partial^2}{\partial x_q^2} + \frac{\partial^2}{\partial y_q^2} + \frac{\partial^2}{\partial z_q^2} \qquad (5-3)$$

The remaining three terms define the components of the potential energy, which includes the attractive electrostatic interaction between the nuclei and the electrons, as well as the repulsive potentials due to the electron-electron and nucleus-nucleus interactions. Therefore, the total Hamiltonian operator can be expressed in terms of kinetic and potential energies of the nuclei and electrons, as shown in (5-4).

$$\mathrm{H_{tot}} = \mathrm{T_e} + \mathrm{T_N} + \mathrm{V_{Ne}} + \mathrm{V_{ee}} + \mathrm{V_{NN}} \qquad (5-4)$$

There are several approximations which can be made to simplify the solution of the Schrödinger equation, some of which are outlined in the following sections.

5.3. The Born-Oppenheimer approximation

The principle that the mass of an electron is extremely light in comparison with the nuclei is the basis of the Born-Oppenheimer approximation.[2] The smallest possible nucleus, a proton, is more than 1800 times heavier than an electron, therefore the nuclei will move considerably more slowly than the electron. This implies nuclei can therefore be considered as fixed in space, so their kinetic energy, T_N in (5-4), is zero and the potential energy due to the nucleus-nucleus repulsion, V_{NN}, is a constant. The Hamiltonian operator in equation (5-4) becomes:

$$\mathrm{H_{elec}} = \mathrm{T_e} + \mathrm{V_{Ne}} + \mathrm{V_{ee}} \qquad (5-5)$$

5.4. The variational principle

The variational principle states that all energies calculated from a trial wave function will always be higher, or at best equal, to the actual ground state energy E_0. This is shown in equation (5-6).

$$\mathrm{E_0} \leq \min_{\Psi} \mathrm{E}[\Psi] \qquad (5-6)$$

Thus, it is possible to assess the quality of trial wave functions, as the lower the energy, the better the trial wave function.

5.5. The Slater determinant

The wave function of a system must obey certain constraints, for example, Ψ must be finite, single-valued and continuous. Also, a suitable function must follow Pauli's exclusion principle which forbids two electrons from occupying the same state.

In 1929 Slater realised that a type of matrix called a determinant was a convenient way of expressing wave functions.[3] Equation (5-7) shows this, usually referred to as a Slater determinant, Φ_{SD}, of N electrons.

$$\Psi_0 \approx \Phi_{SD} = \frac{1}{\sqrt{N!}} \begin{vmatrix} \chi_1(x_1) & \chi_2(x_1) & \cdots & \chi_N(x_1) \\ \chi_1(x_2) & \chi_2(x_2) & & \chi_N(x_2) \\ \vdots & \vdots & & \vdots \\ \chi_1(x_N) & \chi_2(x_N) & \cdots & \chi_N(x_N) \end{vmatrix} \qquad (5-7)$$

The one-electron functions $\chi_i(x_i)$ are called spin orbitals, and are composed of the electron spatial position (x_i) and one of the two spin functions (α, spin up or β, spin down). A Slater determinant is antisymmetric with respect to the interchange of any two electrons. This means that swapping two rows will result in a change in the sign of Φ_{SD}. In addition, if two columns are the same, Φ_{SD} goes to zero, thus obeying the Pauli exclusion principle.

5.6. The Hartree-Fock approximation

The Hartree-Fock approximation is a common method used to attempt to solve the time-independent Schrödinger equation within the Born-Oppenheimer approximation. This approach assumes that the wave function of a chemical system can be defined by a single Slater determinant which is composed of spin orbitals, each representing one electron. Each electron is affected by the field created by the nuclei and the average repulsion from the other electrons present in the system.

In Hartree-Fock theory a self-consistent field (SCF) approach is adopted which works by generating an initial set of guess spin orbitals and improving them iteratively in each step. The energy of the guess orbitals is solved using the equation (5-8) and then compared to the input orbitals. The aim is to generate in each step an improved set of orbitals which will produce a lower energy.

$$f_i \chi_i = \varepsilon_i \chi_i \qquad (5-8)$$

The Fock operator, f_i, is defined as:

$$f_i = -\frac{1}{2}\nabla_i^2 - \sum_A^M \frac{Z_A}{r_{iA}} + V_{HF}(i) \qquad (5-9)$$

where the first term is the electron kinetic energy, the second term is the potential energy due to the electron-nucleus attraction and the third term is defined as the Hartree-Fock potential. This term, $V_{HF}(i)$, is defined as the average repulsive potential experienced by the i'th electron due to the remaining N-1 electrons present in the system. $V_{HF}(i)$ has two components, the Coulomb operator, J, and the exchange operator, K.

$$V_{HF}(i) = \sum_j^N \left(J_j(x_1) - K_j(x_1)\right) \qquad (5-10)$$

The Coulomb operator, $J_j(x_1)$, represents the potential that an electron at position x_1 experiences due to another electron in spin orbital χ_j at position x_2. This interaction is defined as

$$J_j(x_1) = \int \left|\chi_j(x_2)\right|^2 \frac{1}{r_{12}} dx_2 \qquad (5-11)$$

This Coulomb repulsion, corresponds to a particular distance between the reference electron at x_1 and another at position x_2, and is weighted by the probability that the other electron is at this point in space. Thus, an average potential is calculated by integration of this interaction over all space.

The second term, the exchange operator, $K_j(x_1)$, does not have a classical interpretation and can only be defined through its effect when operating on a spin orbital, as shown in (5-12).

$$K_j(x_1)\,\chi_1(x_1) = \int \chi_j^*(x_2)\frac{1}{r_{12}}\,\chi_i(x_2)\,dx_2\,\chi_j(x_1) \qquad (5-12)$$

As in the Coulomb repulsion, the value of $K_j(x_1)$ is inversely proportional to the distance between the two electron positions (x_1 and x_2), therefore it is also integrated over all possible positions of electron x_2. However, the exchange operator defined in (5-12) also depends on the exchange of the two electrons in two spin orbitals, χ_i and χ_j.

It is important to emphasize that this exchange term removes the artifact of 'self-interaction' in a one-electron system, which is a problem created by the Coulomb operator, $J_j(x_1)$. This means that if i = j, equation (5-11) would give a non-zero result, despite the fact that there is definitely no electron-electron repulsion in a one-electron system. The exchange operator, $K_j(x_1)$, takes perfect care of this as it produces an identical value to $J_j(x_1)$, therefore the subtraction shown in (5-10) is exactly zero.

5.7. Electron correlation

Importantly, Hartree-Fock theory does not include a treatment of electron correlation as it only considers that each electron experiences an average field from the other electrons. This is not accurate because in a real system two electrons close to each other will have a direct repulsion between them, therefore they will move in a way that is directly dependent on one another. The electron correlation energy, E_C^{HF}, can be defined as the error in energy between the Hartree-Fock energy and the true ground state energy, E_0, as shown in equation (5-13).[4]

$$E_C^{HF} = E_0 - E_{HF} \qquad (5-13)$$

In addition to the dynamic correlation defined above, another non-dynamical or static correlation contributes to E_c^{HF}. This second term arises under certain circumstances where a single Slater determinant is not sufficient to describe the system under study.

If we study this approximation by the Hartree-Fock theory in the typical example of a H_2 molecule, the Slater determinant will describe the wave-function as being made up by the following contributions: $(H^{\uparrow}.....H^{\downarrow}) + (H^{\downarrow}.....H^{\uparrow}) + (H^{-}{}^{\uparrow\downarrow}.....H^{+}) + (H^{+}.....H^{-}{}^{\uparrow\downarrow})$. The first two terms express the probability of each electron being distributed evenly over both nuclei, while the third and fourth terms represent the formation of a hydride and a proton. This description provides a reasonable approximation when the system is at its equilibrium geometry. However, when the bond distance increases the ionic contribution should tend to zero. Unfortunately this is not the case which results in errors in the computed dissociation energies. The solution to this static correlation will be the use of more than one Slater determinant for the description of the wave-function.

5.8. Density functional theory

Density functional theory (DFT) is focussed on an experimental observable, the electron density, ρ. Electron density is defined as the probability of finding an electron at a point in space and this probability tends to zero as the distance between the electron and the nucleus increases to infinity. DFT defines the electron distribution via 3 spatial variables regardless of the size of the system. This is an advantage compared to the wave function approach which takes into account 3N variables for an N-electron system, which this increases considerably the time of the calculation.

Hohenberg and Kohn[5] laid the foundations on which modern DFT is built. The first Hohenberg-Kohn theorem used the electron density to define the ground state energy of a system that can be expressed by:

$$E_0[\rho_0] = \int \rho_0(r) V_{Ne} dr + F_{HK}[\rho_0] \qquad (5-14)$$

This equation was divided into two parts. The first component depends on the specific system under study and is the nuclei-electron interaction (V_{Ne}). The second component is system independent and is made up of the sum of the kinetic energy ($T[\rho_0]$) and the electron-electron interaction ($E_{ee}[\rho_0]$), as described in (5-15).

$$F_{HK}[\rho_0] = T[\rho_0] + E_{ee}[\rho_0] \qquad (5-15)$$

$E_{ee}[\rho_0]$ can be divided into a classical Coulomb repulsion ($J[\rho_0]$) and a non-classical contribution ($E_{ncl}[\rho_0]$) (see Equation 5-16). From the latter, the electron-electron interaction can be extracted, containing all the effects of self-interaction, the exchange and correlation energies. This term is particularly difficult to calculate.

$$E_{ee}[\rho_0] = \frac{1}{2}\iint \frac{\rho(r_1)\rho(r_2)}{r_{12}} dr_1 dr_2 + E_{ncl}[\rho_0] = J[\rho_0] + E_{ncl}[\rho_0] \qquad (5-16)$$

The second Hohenberg-Kohn theorem is directly based on the variational principle. It identifies that the energy calculated from a specific density is always going to be overestimated compared to the energy of the true ground state density, $E_0[\rho_0]$.

Levy[6] was the first to look at minimization in DFT by using the variational principle to find the ground state energy of a system. The Levy constrained-search approach consists of a two step search. The first step is focussed on one specific density and it

searches through all the possible antisymmetric subsets of wave functions. The second step embraces all densities and generates the ground state energy. This approach is shown in equation (5-17) where the inner minimization corresponds to the first step.

$$E_0 = \min_{\rho \to N} \left(\min_{\Psi \to \rho} \langle \Psi | \mathrm{T} + \mathrm{V_{Ne}} + \mathrm{V_{ee}} | \Psi \rangle \right) \qquad (5-17)$$

This approach is good in theory although its practical use is not possible as it implies searching over all possible densities. Therefore, a further development was required in order to implement the ideas of DFT into a practical method.

5.9. The Kohn-Sham approach

Developments towards the application of DFT were made by Kohn and Sham in 1965.[7] They introduced the concept of a non-interacting reference system built from a set of orbitals (one electron functions) so that the major part of the kinetic energy can be exactly computed. The remainder of the kinetic energy is approximated along with the non-classical contributions to the electron-electron interaction. By this method only a small part of the total energy will be determined by an approximate functional. The non-interacting reference system is represented by a Slater determinant where φ represents a Kohn-Sham orbital.

$$\Theta_S = \frac{1}{\sqrt{N!}} \det\{\varphi_1(x_1)\ \varphi_2(x_2) \dots \varphi_N(x_N)\} \qquad (5-18)$$

The kinetic energy for the non-interacting electrons, $T_s[\rho]$, is expressed in the same way as in the Hartree-Fock approximation and the overall DFT energy can therefore be obtained from:

$$\mathrm{f^{KS}} \varphi_i = \varepsilon_i \varphi_i \qquad (5-19)$$

with the one-electron Kohn-Sham operator $\mathrm{f^{KS}}$ defined as:

$$\mathrm{f^{KS}} = -\frac{1}{2}\nabla^2 + \mathrm{V_{eff}}(r_1) \qquad (5-20)$$

The Kohn-Sham effective potential, $V_{eff}(r_1)$, and requires the three components of $J[\rho]$, E_{xc} and $E_{Ne}[\rho]$. Unfortunately, the exact $E_{xc}[\rho]$ functional needs to be approximated.

$$\mathrm{V_{eff}}(r_1) = \mathrm{T_S}[\rho] + \mathrm{E_{Ne}}[\rho] + \mathrm{J}[\rho] + \mathrm{E_{XC}}[\rho] \qquad (5-21)$$

5.10. The local density approximation

A common approach for the calculation of $E_{xc}[\rho]$ is to consider that the exchange and correlation energy for each particle can be approximated by the local value of electron density at that point. One system where this can be calculated accurately is the uniform electron gas, a model system where electrons of constant density move against a background of positive charges. This allows the calculation of both the exchange and correlation energies exactly or at least to very high accuracy. Central to this local density approximation (LDA) is the assumption that we can write E_{xc} as:

$$E_{XC}^{LDA}[\rho] = \int \rho(r)\varepsilon_{XC}\big(\rho(r)\big)\,dr \qquad (5-22)$$

where $\varepsilon_{XC}(\rho(r))$ is the exchange-correlation energy per particle of a uniform electron gas of density $\rho(r)$. This energy per particle is weighted with the probability, $\rho(r)$, that there is in fact an electron at this position in space. $\varepsilon_{XC}(\rho(r))$ can be divided in two terms for the exchange and correlation contributions:

$$\varepsilon_{XC}(\rho(r)) = \varepsilon_X\big(\rho(r)\big) + \varepsilon_C\big(\rho(r)\big) \qquad (5-23)$$

The exchange part, $\varepsilon_X(\rho(r))$, represents the exchange energy of an electron in a uniform electron gas of a particular density, an expression for which was defined by Slater:

$$\varepsilon_X(\rho) = -\frac{3}{4}\sqrt[3]{\frac{3\rho(r)}{\pi}} \qquad (5-24)$$

However there is no equation for the calculation of the correlation part, $\varepsilon_C(\rho(r))$, although it can be estimated very accurately.

5.11. The generalised gradient approximation

The previous LDA only has a moderate accuracy for real molecular systems as these do not have a uniform electron density. The suggestion of using not only the density $\rho(r)$ at a particular point r, but to supplement this with the information about the gradient of the charge density, $\nabla\rho(r)$, improved the LDA considerably. This expansion is called the generalised gradient approximation, GGA, and its functional can be expressed by:

$$E_{XC}^{GGA}[\rho_\alpha, \rho_\beta] = \int f\big(\rho_\alpha, \rho_\beta, \nabla\rho_\alpha, \nabla\rho_\beta\big)\,dr \qquad (5-25)$$

E_{XC}^{GGA} can be split into its exchange and correlation parts:

$$E_{XC}^{GGA} = E_X^{GGA} + E_C^{GGA} \qquad (5-26)$$

Approximations for the two terms are sought individually. Thus, the exchange part of E_{XC}^{GGA} can be rewritten as:

$$E_X^{GGA} = E_X^{LDA} - \sum_\sigma \int F(s_\sigma)\, \rho_\sigma^{4/3}(r)\, dr \qquad (5-27)$$

where s_σ is the reduced density gradient for spin σ and it is defined as a local inhomogenity parameter.

$$s_\sigma(r) = \frac{|\nabla \rho_\sigma(r)|}{\rho_\sigma^{4/3}(r)} \qquad (5-28)$$

s_σ assumes large values for large gradients and for regions with small densities. Of course, the homogeneous electron gas (LDA) will have $s_\sigma = 0$.

Of the many GGA exchange functionals, two are used especially widely. The first one was developed by Becke[8] and is abbreviated simply as B. It is defined by:

$$F^B = \frac{\beta s_\sigma^2}{1 + 6\beta s_\sigma \sinh^{-1} s_\sigma} \qquad (5-29)$$

β is an empirical parameter that was determined to reproduce the exactly known exchange energies of the noble gases from He through Rn. Functionals which are related to this approach are CAM and PW91.

The second class of GGA correlation functional was developed by Becke (B86)[9] and Perdew (P)[10, 11]and it does not contain any empirical parameters. Instead they use a rational function expansion of the reduced density gradient.

$$F^{P86} = \left(1 + 1.296\left(\frac{s_\sigma}{(24\pi^2)^{1/3}}\right)^2 + 14\left(\frac{s_\sigma}{(24\pi^2)^{1/3}}\right)^4 + 0.2\left(\frac{s_\sigma}{(24\pi^2)^{1/3}}\right)^6\right)^{1/15} \qquad (5-30)$$

Another popular functional is LYP, developed by Lee, Yang and Parr,[11] which is based on an expression for the correlation energy of the helium atom. This functional contains one empirical parameter.

5.12. Hybrid functionals

Becke developed the use of hybrid functionals in 1993. The idea was to calculate an exact value for E_x by the Hartree-Fock approximation, although the orbitals were calculated by the Kohn-Sham approximation. In addition, the exact exchange is combined with exchange and correlation contributions calculated using the local density approximation.

Becke proposed an approach that uses empirical parameters, chosen to reproduce experimental data, for each term.

$$E_{XC}^{B3} = E_{XC}^{LSD} + a\left(E_{XC}^{\lambda=0} - E_{XC}^{LSD}\right) + bE_X^B + cE_C^{PW91} \qquad (5-31)$$

Currently, the most popular hybrid functional is known as B3LYP as suggested by Stephens *et al.*[12] The correlation is now calculated by a LYP functional. Thus, the exchange-correlation energy expression is:

$$E_{XC}^{B3LYP} = (1-a)E_C^{LSD} + aE_{XC}^{\lambda=0} + bE_X^{B88} + cE_C^{LYP} + (1-c)E_C^{LSD} \qquad (5-32)$$

5.13. Basis sets

A basis set constitutes a number of predefined basis functions and these basis functions are used to describe the orbitals of an atom or molecule mathematically. It is possible to have an infinite number of basis functions within a basis set, although this would not be practical. Wave function based approaches are developed in such a way that the quality of the calculation increases with increasing basis set size. This trend is upheld for the Kohn-Sham approaches, although the basis set requirements are less strong, with the charge density being constructed by:

$$\rho(r) = \sum_i^N |\varphi_i(r)|^2 \qquad (5-33)$$

There are two main types of basis sets in common use: Slater-type orbitals (STO) and Gaussian-type orbitals (GTO). Mathematically, STOs are described as:

$$\eta^{STO} = Nr^{n-1}\exp[-\zeta r] \qquad (5-34)$$

where N is the normalization factor, n is the principal quantum number and ζ is the orbital exponent. STOs orbitals would be the ideal choice of function as they closely

model the true behaviour of atomic orbitals, however historically their use is very computationally demanding. To improve this, the Gaussian-type orbitals, GTOs, were developed. The general form for a GTO is:

$$\eta^{GTO} = N\, x^l\, y^m\, z^n\, \exp[-\propto r^2] \qquad (5-35)$$

where N is a normalization factor, α represents the orbital exponents which determines how compact or diffuse the resulting function is. L = l + m + n is used to classify the GTO as s-functions (L = 0), p-functions (L = 1), etc.

The choice of basis set is a balance between the accuracy that can be achieved and how time consuming the calculation will be. The minimal basis set only contains the number of basis functions required to accommodate all the electrons of the atom in the ground state. The simplest basis set is STO-3G[13, 14] which is defined by three primitive GTOs that are combined in order to obtain one STO. The next level of development involves double-zeta basis sets, which doubles the number of basis functions used to describe each atomic orbital. In this case, the simplest example is 3-21G,[15] where the core orbitals are represented by 3 GTOs while the valence are contracted from 2 GTOs and one GTO. This increases the flexibility of the basis set and therefore the accuracy of the calculation. One commonly used double-zeta basis set is 6-31G.

The addition of d-orbitals for heavy atoms and p-orbitals for hydrogen atoms add polarization and further increase the accuracy. This is indicated by one or two asterisks respectively next to the basis set, for example 6-31G**.

Finally, when the system contains atoms from the second row onwards, the use of effective core potentials (ECPs) are usually employed in order to reduce the time consume of the calculation. The more used are LANL[16] and SDD.[17]

5.14. Calculation details

All calculations in this thesis were performed using the GAUSSIAN 03 package.[18] The method used was the exchange functional of Becke[8] with the correlation functional of Perdew (BP86).[10] Iridium, rhodium, ruthenium, chlorine, phosphorus and sulfur atoms were represented by the relativistic core potential of the Stuttgart group[17] and the associated basis sets, with an added polarisation function on the chloride, phosphorus and sulfur atoms. [19] 6-31G** basis sets were used to represent the nitrogen, carbon, oxygen, fluorine and hydrogen atoms.[13, 20]

Transition states were located by first running a scan calculation based on an appropriate geometric parameter for the process under consideration. These produced an initial structure for a transition state optimisation and the stationary point located was characterised via a frequency calculation as having one imaginary frequency. Intrinsic reaction co-ordinate (IRC)[21] calculations were also run, which involve optimising a series of geometries in both directions from the transition state on the potential energy surface to find the adjacent local minima, (i.e. the reactant and product) from each transition state.

All energies reported in this thesis are enthalpies which include a zero-point energy correction. These values were obtained from frequency calculations performed on optimised stationary points. This also gives access to the Gibbs free energy which is quoted at 298.15 K and 1 atmosphere. In some cases the effect of solvation has been investigated using polarisable continuum model (PCM) calculations (radii=UFF).[22]

5.15. Comparison of different exchange-correlation functionals

In order to evaluate the behaviour of the functional used in this thesis (BP86), the energy profile which for the intramolecular cyclometallation reaction of dmba−H in the model $[Ir(\eta\text{-Cp})(dmba{-}H)(\kappa^2\text{-OAc})]^+$ (**1$_{Me}$**) via an AMLA-6 mechanism, described in Chapter 2, was re-computed. A comparison of the energetics computed with several different functionals is shown in Table 5.1, starting with BP86, which was the functional used in previous studies in the group.[23] The inclusion of B3 allowed us to compare with hybrid methods, therefore B3P86 and B3LYP were selected. In addition, pure DFT functionals, BLYP and BPW91 were also assessed. In all cases the same basis sets were used, namely SDD on iridium and 6-31G** on carbon, oxygen, nitrogen and hydrogen atoms.

	BP86	BLYP	BPW91	B3P86	B3LYP
$\mathbf{1_{Me}}$	0.0	0.0	0.0	0.0	0.0
$\mathbf{TS(1\text{-}2)_{Me}}$	+ 13.4	+ 12.1	+ 13.0	+ 14.4	+ 13.0
$\mathbf{2_{Me}}$	+ 8.6	+ 7.3	+ 8.8	+ 9.3	+ 7.9
$\mathbf{TS(2\text{-}3)_{Me}}$	+ 9.5	+ 10.3	+ 8.8	---	+ 11.7
$\mathbf{3_{Me}}$	- 5.6	- 2.3	- 5.7	- 6.6	- 3.8

Table 5. 1 – Energies (kcal/mol) for the cyclometallation reaction of $\mathbf{1_{Me}}$ via an AMLA-6 mechanism using different functionals.

In general, all functional gave very similar energy barriers. The major variation came in the energies of the products, where the use of the LYP correlation functional gave higher energies. The inclusion of the zero-point energy in BPW91 causes $\mathbf{TS(1\text{-}2)_{Me}}$ to fall below intermediate $\mathbf{2_{Me}}$ in energy, while B3P86 could not locate it. Despite these features, the overall energies are relatively similar. Therefore, BP86 appears to be a good choice for this process. Moreover, previous studies were already carried out with this functional.[23] Hence and in order to maintain the same methodology BP86 was chosen to continue this research.

5.16. References

1. E. Schrödinger, *Ann. Phys.*, 1926, 734; E. Schrödinger, *Phys. Rev.*, 1926, **28**, 1049.
2. M. Born and R. Oppenheimer, *Ann. Phys.*, 1927, **84**, 457.
3. J. C. Slater, *Phys. Rev.*, 1929, **34**, 1293.
4. D. R. Hartree, *Proc. Camb. Phil. Soc*, 1928, **24**, 89; V. Fock, *Z. Physical*, 1930, **61**, 126.
5. P. Hohenberg and W. Kohn, *Phys. Rev. B*, 1964, **136**, 864.
6. M. Levy, *Proc. Natl. Acad. Sci. USA*, 1979, **76**, 6062.
7. W. Kohn and L. J. Sham, *Phys. Rev.*, 1965, **140**, A1133.
8. A. D. Becke, *Phys. Rev. A*, 1988, **38**, 3098-3100.
9. A. D. Becke, *J. Chem. Phys.*, 1986, **84**, 4524-4529.
10. J. P. Perdew, *Phys. Rev. B*, 1986, **33**, 8822-8824.
11. C. Lee, W. Yang and R. G. Parr, *Phys. Rev. B*, 1988, **37**, 785.
12. P. J. Stephens, J. F. Devlin, C. F. Chabalowski and M. J. Frisch, *J. Phys. Chem.*, 1994, **98**, 11623.
13. W. J. Hehre, R. Ditchfield and J. A. Pople, *J. Chem. Phys.*, 1972, **56**, 2257-2261.
14. J. B. Collins, P. v. R. Schleyer, J. S. Binlkey and J. A. Pople, *J. Phys. Chem.*, 1976, **64**.
15. J. S. Binlkey, J. A. Pople and W. J. Hehre, *J. Am. Chem. Soc.*, 1980, **102**, 939; M. S. Gordon, J. S. Binlkey, J. A. Pople, W. J. Pietro and W. J. Hehre, *J. Am. Chem. Soc.*, 1982, **104**, 2797; W. J. Pietro, M. M. Francl, W. J. Hehre, D. J. Defrees, J. A. Pople and J. S. Binlkey, *J. Am. Chem. Soc.*, 1982, **104**, 5039; K. D. Dobbs and W. J. Hehre, *J. Comp. Chem.*, 1986, **7**, 359.
16. P. J. Hay and W. R. Wadt, *J. Chem. Phys.*, 1985, **82**, 270-283.
17. M. Dolg, *Theor. Comp. Chem.*, 2002, **11**, 793.
18. M. J. Frisch, G. W. Trucks, H. B. Schlegel, G. E. Scuseria, M. A. Robb, J. R. Cheeseman, J. A. Montgomery, Jr., T. Vreven, K. N. Kudin, J. C. Burant, J. M.

Millam, S. S. Iyengar, J. Tomasi, V. Barone, B. Mennucci, M. Cossi, G. Scalmani, N. Rega, G. A. Petersson, H. Nakatsuji, M. Hada, M. Ehara, K. Toyota, R. Fukuda, J. Hasegawa, M. Ishida, T. Nakajima, Y. Honda, O. Kitao, H. Nakai, M. Klene, X. Li, J. E. Knox, H. P. Hratchian, J. B. Cross, V. Bakken, C. Adamo, J. Jaramillo, R. Gomperts, R. E. Stratmann, O. Yazyev, A. J. Austin, R. Cammi, C. Pomelli, J. W. Ochterski, P. Y. Ayala, K. Morokuma, G. A. Voth, P. Salvador, J. J. Dannenberg, V. G. Zakrzewski, S. Dapprich, A. D. Daniels, M. C. Strain, O. Farkas, D. K. Malick, A. D. Rabuck, K. Raghavachari, J. B. Foresman, J. V. Ortiz, Q. Cui, A. G. Baboul, S. Clifford, J. Cioslowski, B. B. Stefanov, G. Liu, A. Liashenko, P. Piskorz, I. Komaromi, R. L. Martin, D. J. Fox, T. Keith, M. A. Al-Laham, C. Y. Peng, A. Nanayakkara, M. Challacombe, P. M. W. Gill, B. Johnson, W. Chen, M. W. Wong, C. Gonzalez and J. A. Pople, *Gaussian 03, Revision C.02*, Gaussian, Inc., Wallingford CT, 2004.

19. A. Hollwarth, M. Bohme, S. Dapprich, A. W. Ehlers, A. Gobbi, V. Jonas, K. Kohler, R. Stegman, A. Veldkamp and G. Frenking, *Chem. Phys. Lett.*, 1993, **208**, 237.

20. R. Ditchfield, W. J. Hehre and J. A. Pople, *J. Chem. Phys.*, 1971, **54**, 724-728; P. C. Hariharan and J. A. Pople, *Mol. Phys.*, 1974, **27**, 209; M. S. Gordon, *Chem. Phys. Lett.*, 1980, **76**, 163; P. C. Hariharan and J. A. Pople, *Theor. Chim. Acta*, 1973, **28**, 213-222; M. M. Francl, W. J. Pietro, W. J. Hehre, J. S. Binlkey, D. J. DeFrees, J. A. Pople and M. S. Gordon, *J. Chem. Phys.*, 1982, **77**, 3654; R. C. J. Binning and L. A. Curtiss, *J. Comp. Chem.*, 1990, **11**, 1206; V. Rassolov, J. A. Pople, M. A. Ratner and T. L. Windus, *J. Chem. Phys.*, 1998, **109**, 1223; V. A. Rassolov, M. A. Ratner, J. A. Pople, P. C. Redfren and L. A. Curtiss, *J. Comp. Chem.*, 2001, **22**, 976.

21. C. Gonzalez and H. B. Schlegel, *J. Chem. Phys.*, 1989, **90**, 2154-2161; C. Gonzalez and H. B. Schlegel, *J. Phys. Chem.*, 1990, **94**, 5523-5527.

22. S. Miertuš, E. Scrocco and J. Tomasi, *Chem. Phys.*, 1981, **55**, 117-129.

23. D. L. Davies, S. M. A. Donald, O. Al-Duaij, S. A. Macgregor and M. Poelleth, *J. Am. Chem. Soc.*, 2006, **128**, 4210-4211.

Alkyl dehydrogenation in a Rh(I) complex *via* an isolated agostic intermediate†

Adrian B. Chaplin,[a] Amalia I. Poblador-Bahamonde,[b] Hazel A. Sparkes,[c] Judith A. K. Howard,*[c] Stuart A. Macgregor*[b] and Andrew S. Weller*[a]

Received (in Cambridge, UK) 24th September 2008, Accepted 31st October 2008
First published as an Advance Article on the web 19th November 2008
DOI: 10.1039/b816739g

A well-characterised 14-electron rhodium phosphine complex, $[Rh(P^iPr_3)_3][BAr^F_4]$, which contains a β-CH agostic interaction, is observed to undergo spontaneous dehydrogenation to afford $[Rh(P^iPr_3)_2(P^iPr_2(C_3H_5))][BAr^F_4]$; calculations on a model system show that while C–H activation is equally accessible from the β-CH agostic species or an alternative γ-CH agostic isomer, subsequent β-H-transfer can only be achieved along pathways originating from the β-CH agostic form.

Transition metal-mediated alkane dehydrogenation is an important methodology for the selective transformation of alkanes.[1] The putative intermediates for such reactions are alkane sigma complexes, which then undergo successive C–H activation and β-H-elimination. For the intramolecular dehydrogenation of alkyl groups it is accepted that C–H activation is usually preceded by a M···HC agostic interaction (Scheme 1);[2] however, well-defined examples of such complexes that subsequently undergo alkyl dehydrogenation are, to the best of our knowledge, unknown. Indeed, as far as we are aware, there is only one example of a complex where an agostic interaction undergoes C–H activation for which both the agostic and C–H activated product have been crystallographically characterised,[3] and only a few examples where these tautomers are directly observed in solution.[4]

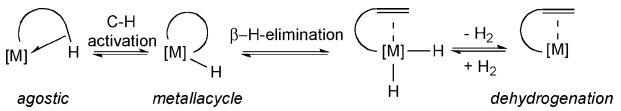

Scheme 1

We report here the isolation of a "T-shaped" 14-electron rhodium phosphine complex, $[Rh(P^iPr_3)_3][BAr^F_4]$ [**1**, Ar^F = 3,5-$C_6H_4(CF_3)_2$], that contains an unusual β-CH agostic interaction from the isopropyl phosphine ligand and undergoes intramolecular dehydrogenation. We also demonstrate, using computational methods, that the β-agostic interaction in **1** is important in defining the ultimate product of the reaction: dehydrogenation (C–H activation/β-elimination[5–7]) *versus* metallacyclobutane formation (C–H activation only[8,9]) which arises from an alternative γ-agostic interaction.

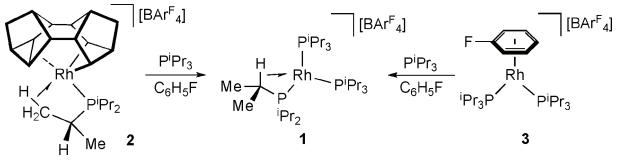

Scheme 2

Reaction of $[Rh(BINOR\text{-}S)(P^iPr_3)][BAr^F_4]$ (**2**)[10] with 2 equivalents of P^iPr_3 in C_6H_5F solution results in reductive elimination of BINOR-S and the formation of **1** in quantitative yield by NMR spectroscopy. Alternatively, **1** can be formed by the addition of P^iPr_3 to $[Rh(C_6H_5F)(P^iPr_3)_2][BAr^F_4]$ (**3**) in C_6H_5F (Scheme 2). Complex **1** is highly fluxional in solution at room temperature, displaying one phosphine environment by ^{31}P NMR spectroscopy which shows coupling to ^{103}Rh (δ 47.1, d, J_{RhP} = 173 Hz). This fluxional behaviour is not frozen out, even upon cooling to 200 K, where the $^{31}P\{^1H\}$ NMR spectrum shows a very broad signal. The ^1H NMR spectrum shows a featureless hydride region at all temperatures. In the solid state‡ (Fig. 1) the structure displays a distorted square planar geometry in which a β-CH agostic interaction from an isopropyl group occupies the fourth coordination site, showing a relatively short Rh1–C1a distance [2.494(12) Å, located Rh1–H1a 1.91(9) Å][11] and an acute Rh1–P1–C1a angle

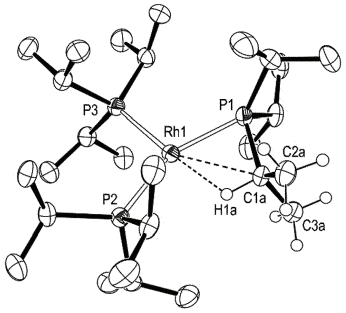

Fig. 1 Complex **1**; ellipsoids are depicted at the 50% probability level. The anion, most H atoms and minor component (**4**) are omitted for clarity. Key bond lengths (Å) and angles (°): Rh1–P1, 2.249(2); Rh1–P2, 2.395(2); Rh1–P3, 2.268(2); P1–Rh1–P2, 149.91(6); P1–Rh1–P3, 104.24(6); P2–Rh1–P3, 105.47(6); Rh1–C1a, 2.494(12); Rh1–H1a, 1.91(9); Rh1–P1–C1a, 73.8(4); C1a–C2a, 1.540(13); C1a–C3a, 1.540(13).

[a] *Department of Inorganic Chemistry, University of Oxford, UK OX1 3QR. E-mail: andrew.weller@chem.ox.ac.uk*
[b] *School of EPS – Chemistry, Heriot-Watt University, Edinburgh, UK EH14 4AS. E-mail: S.A.Macgregor@hw.ac.uk*
[c] *Department of Chemistry, University Science Laboratories, South Road, Durham, UK DH1 3LE. E-mail: j.a.k.howard@durham.ac.uk*

† Electronic supplementary information (ESI) available: Full experimental, characterisation and crystallographic details. Energies and Cartesian coordinates of all computed species; full reference for Gaussian 03. See DOI: 10.1039/b816739g/

[73.8(4)°]. The RhP_3 core is planar [sum of angles 359.6(1)°]. Complex **1** is a rare example of a formally 14-electron late-transition metal complex,[9–13] and is closely related to $[Rh(PPh_3)_3][ClO_4]$[13] and $Rh(^tBu_2PCH_2P^tBu_2)(CH_2Me_3)$.[12a]

Isopropyl phosphine groups have been shown to coordinate through γ-agostic interactions,[9,10,14] but as far as we are aware **1** is the first structurally characterised example of a β-agostic interaction with this ligand motif. Given the fluxional behaviour of **1**, even at 200 K, we have not been able to determine experimentally whether this interaction dominates in solution, or rapidly interconverting β- or γ-interactions are present. We did not observe a clear C–H stretch in the IR spectrum that could be assigned to the agostic C–H bond.

Complex **1** spontaneously,[6,16] but slowly ($t_{1/2} \sim 1.5$ h), undergoes dehydrogenation of one of the isopropyl substituents in solution at room temperature (C_6H_5F solvent). This results in the generation of an equilibrium mixture of $[Rh(P^iPr_3)_2(\eta^3\text{-}P^iPr_2(C_3H_5))][BAr^F_4]$ (**4**) and $[RhH_2(P^iPr_3)_3][BAr^F_4]$ (**5**)—see ESI† for full details including a solid-state structure—the latter of which arises from reaction of **1** with liberated H_2 (**1**:**4**:**5** = 1.0:0.95:0.35) (Scheme 3). **5** is closely related to previously reported $[IrH_2(P^iPr_2Ph)_3][BAr^F_4]$.[15] Due to this process and the structural similarity of **4**, isolation of **1** by crystallisation at low temperature occurs concomitant with small amounts of **4** (**1**:**4** ~ 4:1 on the basis of integrals in the ^1H NMR spectrum and X-ray diffraction). The dehydrogenation/hydrogenation equilibrium in solution is shifted towards **4** by successive removal of hydrogen through freeze–vacuum–thaw cycles, while addition of the hydrogen acceptor *t*-butylethene (*t*be) results in the clean formation of **4** (86% isolated yield). Addition of H_2 to **1** or **4** rapidly generates **5**, the latter presumably *via* **1**, showing that the dehydrogenation is reversible. In CH_2Cl_2 or THF dehydrogenation of **1** also occurs alongside decomposition to unidentified products.

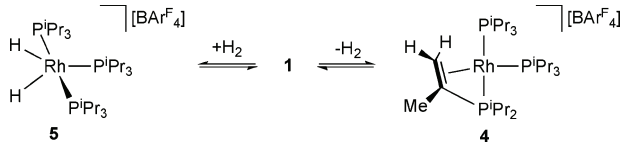

Scheme 3

The solid-state‡ structure of isolated **4** is shown in Fig. 2 and confirms dehydrogenation of one of the isopropyl groups to form an η^3-coordinated vinyl phosphine. The rhodium has an approximately square planar geometry, and the featureless high-field region of the ^1H NMR spectrum of **4** (200 K) supports the lack of a hydride ligand. The molecular geometry and structural metrics of the η^3-ligand are similar to those reported previously for vinyl phosphines.[6,7]

Mechanistically, phosphine dissociation during the dehydrogenation reaction is discounted as no inhibition is observed in the presence of excess phosphine (10 equivalents), while no dehydrogenation is observed for **3** in C_6H_5F. These observations suggest successive C–H activation and β-elimination in **1** followed by loss of dihydrogen (Scheme 1). Two questions thus arise: does C–H activation occur at the β or γ position, and how does this affect the ultimate outcome of the reaction (dehydrogenation *versus* cyclometallation)?

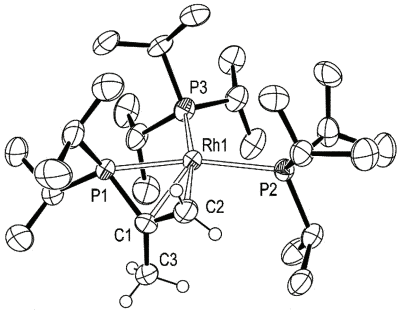

Fig. 2 Complex **4**; ellipsoids are depicted at the 50% probability level, the anion and most H atoms have been omitted for clarity. Key bond lengths (Å) and angles (°): Rh1–P1, 2.291(2); Rh1–P2, 2.395(2); Rh1–P3, 2.347(2); P1–Rh1–P2, 153.93(6); P1–Rh1–P3, 99.10(6); P2–Rh1–P3, 106.63(5); Rh1–C1, 2.183(6); Rh1–C2, 2.240(6); Rh1–P1–C1, 63.6(2); C1–C2, 1.399(8); C1–C3, 1.489(8).

To address these issues we have employed density functional theory calculations[17] to study the reactivity of the model cation, $[Rh(PH_2{}^iPr)(PH_3)_2]^+$, **1′**. Three forms of **1′** were located, **1′β** and **1′γ**, with β- and γ-CH agostic interactions, respectively (Fig. 3), as well as an anagostic form, **1′an**. For the simple model system **1′γ** is more stable than **1′β**, reflecting the lesser degree of strain associated with the five-membered Rh–P–C–C–H ring in this case. Although this is contrary to what is observed in the solid-state structure our model does not take into account the effects of ligand bulk which can play a significant role in determining the nature of an agostic interaction.[15] In addition solid-state packing effects may play a role in favouring one agostic form over the other. **1′β** and **1′γ** are linked *via* **1′an** (E = 2.9 kcal mol^{-1}), the highest point along this pathway being loss of the β-CH agostic *via* a TS at 5.9 kcal mol^{-1}. **1′an** corresponds to a very shallow minimum and forms **1′γ** with a negligible barrier (not shown in Fig. 3). The low overall activation energies for interconversion between **1′β** and **1′γ** are consistent with the highly fluxional behaviour observed in the NMR spectra of **1**.

C–H activation TS structures were located from both **1′β** and **1′γ** and the computed activation barriers of 11.9 kcal mol^{-1} and 11.5 kcal mol^{-1}, respectively, indicate that these processes are equally accessible. C–H activation is also endothermic and should be reversible. Importantly, the accessibility of the initial C–H activation does not depend significantly on the nature of the CH agostic bond present in the reactant.

In contrast, β-H-transfer in the C–H activated species **6′β** and **6′γ** depends markedly on which intermediate is involved.

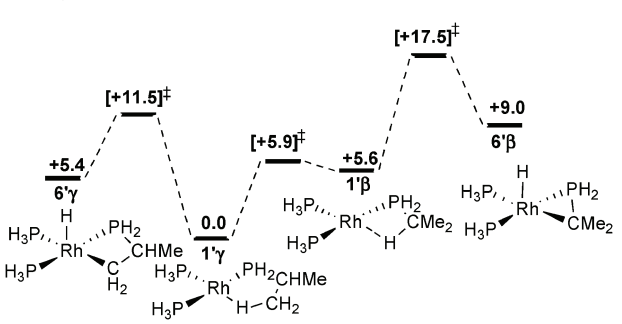

Fig. 3 Reaction profiles (kcal mol^{-1}) for C–H activation in **1′β** and **1′γ**.

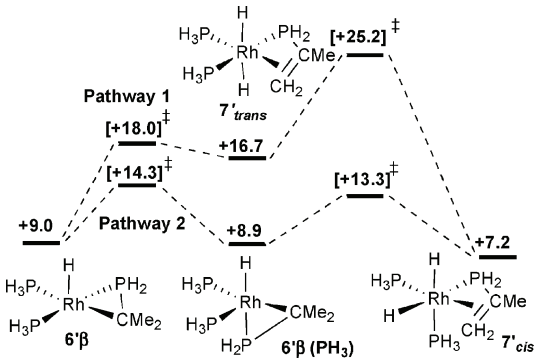

Fig. 4 Reaction profiles (kcal mol^{-1}) for β-H-transfer in **6′β**.

For metallacyclophosphabutane **6′γ**, we were unable to locate a TS for β-H-transfer to Rh. Scans based on the Rh-βH distance led to a steady increase in energy to over 30 kcal mol^{-1} above **6′γ**. TS structures were located but these were shown to be for a Rh-assisted 1,2 H shift resulting in isomerisation to **6′β** (E = +31.1 kcal mol^{-1}, see ESI†). For **6′β**, however, a number of low energy β-H-transfer pathways were characterised, two of which are shown in Fig. 4. In order to complete the dehydrogenation process a *cis*-dihydride must be formed upon β-H-transfer so that H_2 reductive elimination can be accessed. In Pathway 1 this is achieved by initial β-H-transfer from **6′β** to form *trans*-dihydride **7′*trans***, (E = +16.7 kcal mol^{-1}) followed by isomerisation to **7′*cis***. The *cis–trans* isomerisation TS is the highest point along Pathway 1 (E = +25.2 kcal mol^{-1}) and corresponds to a barrier of 19.6 kcal mol^{-1} relative to **1′β**. Alternatively, isomerisation of square-pyramidal **6′β** (where H is apical) occurs prior to β-H-transfer. The lowest energy mechanism of this type, Pathway 2, proceeds *via* a PH_3 apical isomer (**6′β(PH$_3$)**, E = +8.9 kcal mol^{-1}) from which β-H-transfer leads to **7′*cis***. The isomerisation TS is the highest point along Pathway 2 (E = +14.3 kcal mol^{-1}) equating to a barrier of only 8.7 kcal mol^{-1} relative to **1′β**. A second isomerisation/β-H-transfer route *via* isomer **6′β(PH$_3$)** (with {PH_2} apical) was also defined, Pathway 3. This was energetically intermediate with regard to Pathways 1 and 2 with an overall barrier of 13.4 kcal mol^{-1}, the highest TS being for β-H-transfer at +19.0 kcal mol^{-1}. Full details are given in the ESI†.

To complete the dehydrogenation, reductive elimination of H_2 from **7′*cis*** is required and a TS for this process was located at +15.1 kcal mol^{-1}. For Pathway 2 this is the highest point in the overall process, although for Pathways 1 and 3 this occurs earlier in the profile (either *cis–trans* isomerisation or β-H-transfer, respectively). The model products, **4′** + H_2, have a computed relative energy of +9.0 kcal mol^{-1}, although the entropy associated with H_2 dissociation means that the free energy of the products is only +2.9 kcal mol^{-1} above **1′β**, consistent with the reversibility of the dehydrogenation.

In conclusion we report a "14-electron" T-shaped Rh(I) complex with a supporting β-agostic interaction from an isopropyl phosphine that spontaneously undergoes dehydrogenation (C–H activation followed by β-H-transfer). Calculations show that while both γ- and β-agostic interactions can undergo reversible C–H activation to give metallacycle intermediates, subsequent H-transfer is only accessible when originating from the β-agostic form. Therefore only the product of C–H activation at the β-position can lead to productive dehydrogenation.

Notes and references

‡ *Crystallographic data*. **1**: $C_{59}H_{74.6}BF_{24}P_3Rh$, M = 1446.42, monoclinic, $P2_1/n$ (Z = 4), a = 13.1039(6) Å, b = 28.652(1) Å, c = 17.9634(8) Å, β = 106.228(1)°. V = 6475.6(5) Å^3, T = 120(2) K, 13 255 unique reflections [R(int) = 0.0395]. Final R_1 = 0.0455 [$I > 2\sigma(I)$]. **4**: $C_{59}H_{73}BF_{24}P_3Rh$, M = 1444.80, monoclinic, $P2_1$ (Z = 6), a = 19.3219(2) Å, b = 17.7292(2) Å, c = 29.0445(3) Å, β = 96.6182(4)°. V = 9883.2(2) Å^3, T = 150(2) K, 31 319 unique reflections [R(int) = 0.0396]. Final R_1 = 0.0506 [$I > 2\sigma(I)$].

1 (*a*) C. M. Jensen, *Chem. Commun*., 1999, 2443; (*b*) R. H. Crabtree, *J. Chem. Soc., Dalton Trans*., 2001, 2437; (*c*) A. S. Goldman, A. H. Roy, Z. Huang, R. Ahuja, W. Schinski and M. Brookhart, *Science*, 2006, **312**, 257.

2 (*a*) G. J. Kubas, *Metal Dihydrogen and σ-Bond Complexes*, Kluwer Academic/Plenum Publishers, New York, 2001; (*b*) M. Brookhart, M. L. H. Green and G. Parkin, *Proc. Natl. Acad. Sci. U. S. A*., 2007, **104**, 6908.

3 N. M. Scott, R. Dorta, E. D. Stevens, A. Correa, L. Cavallo and S. P. Nolan, *J. Am. Chem. Soc*., 2005, **127**, 3516.

4 (*a*) A. C. Albeniz, G. Schulte and R. H. Crabtree, *Organometallics*, 1992, **11**, 242; (*b*) B. Rybtchinski, L. Konstantinovsky, L. J. W. Shimon, A. Vigalok and D. Milstein, *Chem.–Eur. J*., 2000, **6**, 3287; (*c*) D. Buccella and G. Parkin, *J. Am. Chem. Soc*., 2006, **128**, 16358; (*d*) A. Toner, J. Matthes, S. Gruendemann, H. Limbach, B. Chaudret, E. Clot and S. Sabo-Etienne, *Proc. Natl. Acad. Sci. U. S. A*., 2007, **104**, 6945; (*e*) L. Mole, J. L. Spencer, N. Carr and A. G. Orpen, *Organometallics*, 1991, **10**, 49.

5 M. Baya, M. L. Buil, M. A. Esteruelas and E. Onate, *Organometallics*, 2004, **23**, 1416–1423.

6 P. B. Glaser and T. D. Tilley, *Organometallics*, 2004, **23**, 5799.

7 A. J. Edwards, M. A. Esteruelas, F. J. Lahoz, A. M. Lopez, E. Onate, L. A. Oro and J. I. Tolosa, *Organometallics*, 1997, **16**, 1316.

8 (*a*) D. L. Thorn, *Organometallics*, 1998, **17**, 348; (*b*) N. Thirupathi, D. Amoroso, A. Bell and J. D. Protasiewicz, *Organometallics*, 2005, **24**, 4099.

9 M. J. Ingleson, M. F. Mahon and A. S. Weller, *Chem. Commun*., 2004, 2398.

10 S. Brayshaw, J. Green, G. Kociok-Köhn, E. Sceats and A. S. Weller, *Angew. Chem., Int. Ed*., 2006, **45**, 452.

11 W. Baratta, C. Mealli, E. Herdtweck, A. Ienco, S. A. Mason and P. Rigo, *J. Am. Chem. Soc*., 2004, **126**, 5549.

12 (*a*) H. Urtel, C. Meier, F. Eisentrager, F. Rominger, J. P. Joschek and P. Hofmann, *Angew. Chem., Int. Ed*., 2001, **40**, 781; (*b*) P. H. M. Budzelaar, N. N. P. Moonen, R. de Gelder, J. M. M. Smits and A. W. Gal, *Eur. J. Inorg. Chem*., 2000, 753; (*c*) W. Baratta, S. Stoccoro, A. Doppiu, E. Herdtweck, A. Zucca and P. Rigo, *Angew. Chem., Int. Ed*., 2003, **42**, 105; (*d*) A. Y. Verat, M. Pink, H. Fan, J. Tomaszewski and K. G. Caulton, *Organometallics*, 2008, **27**, 166, and references therein.

13 Y. W. Yared, S. L. Miles, R. Bau and C. A. Reed, *J. Am. Chem. Soc*., 1977, **99**, 7076.

14 H. Aneetha, M. Jimenez-Tenorio, M. C. Puerta, P. Valerga, V. N. Sapunov, R. Schmid, K. Kirchner and K. Mereiter, *Organometallics*, 2002, **21**, 5334.

15 A. C. Cooper, E. Clot, J. C. Huffman, W. E. Streib, F. Maseras, O. Eisenstein and K. G. Caulton, *J. Am. Chem. Soc*., 1999, **121**, 97–106.

16 (*a*) T. M. Douglas and A. S. Weller, *New J. Chem*., 2008, **32**, 966; (*b*) T. M. Douglas, S. K. Brayshaw, R. Dallanegra, G. Kociok-Köhn, S. A. Macgregor, G. Moxham, A. S. Weller, T. Wondimagegn and P. Vadivelu, *Chem.–Eur. J*., 2008, **14**, 1004; (*c*) T. M. Douglas, H. Le Notre, S. K. Brayshaw, C. G. Frost and A. S. Weller, *Chem. Commun*., 2006, 3408.

17 Calculations employed Gaussian 03 with the BP86 functional. Rh and P centres were described with Stuttgart RECPs and basis sets with polarisation on P. 6-31G** basis sets were used for C and H atoms. All energies include a correction for zero-point energies. See ESI† for full details.

Mechanisms of C–H bond activation: rich synergy between computation and experiment

Youcef Boutadla,[a] David L. Davies,*[a] Stuart A. Macgregor*[b] and Amalia I. Poblador-Bahamonde[b]

Received 11th March 2009, Accepted 19th May 2009
First published as an Advance Article on the web 10th June 2009
DOI: 10.1039/b904967c

Recent computational studies of C–H bond activation at late transition metal systems are discussed and processes where lone pair assistance *via* heteroatom co-ligands or carboxylates are highlighted as a particularly promising means of cleaving C–H bonds. The term 'ambiphilic metal ligand activation' (AMLA) is introduced to describe such reactions.

1. Introduction

The activation and functionalisation of C–H bonds is one of the most active fields of current chemical research.[1,2] This work is motivated by the desire to make more efficient and effective use of cheap and abundant simple hydrocarbons as feedstocks for chemical synthesis. Central to this goal is the activation of the C–H bond itself. Such bonds can certainly no longer be considered 'inert' and a number of successful catalytic schemes based on intramolecular C–H bond activation have now been realised.[3] Successful catalysis based on intermolecular functionalisation of C–H bonds has also been demonstrated but progress in this area remains a considerable challenge.[4,5a] A thorough understanding of the means by which cleavage of a C–H bond can be achieved remains a key consideration and computational modelling is set to play a central role in providing insight into this process.

From the 1980s, experimental observations of intermolecular C–H activation have been quickly followed by seminal insights from computation and the state of play was summarised in some key reviews in 2000.[6] Over this period, improvements in methodology, in particular the advent of density functional theory (DFT),[7] coupled with improvements in computer power, have resulted in a dramatic expansion in both the range of systems that can be studied and the nature of the problems that can be addressed computationally. Above all, the ability of DFT to routinely define the structures and energies of reactive intermediates and transition states has been particularly important. Such information is, in most cases, very difficult to obtain from experiment. Increasingly, therefore, computational studies are being performed in parallel with experiment, bringing to bear a powerful synergy of complementary techniques to the intricate problem of understanding reaction mechanisms.

In the mid-1990s, mechanisms of C–H activation by organometallic complexes were generally considered to fall into one of three general categories: (i) oxidative addition (OA) at electron-rich low-valent transition metal centres (ii) σ-bond metathesis (SBM) at electrophilic early transition metal (and lanthanide) centres and (iii) electrophilic activation (EA) at electron-deficient late transition metal centres. More recently, the ability to categorise a C–H activation mechanism on the basis of the anticipated behaviour of a given metal centre has become increasingly problematic. One illustrative mechanistic quandary arose with the low-temperature activation of alkanes at $[Cp^*Ir(PMe_3)(CH_3)(OTf)]$.[8] As a late transition metal OA might

[a]*Department of Chemistry, University of Leicester, Leicester, UK LE1 7RH. E-mail: dld03@le.ac.uk; Fax: +44 (0)116 252 3789; Tel: +44 (0)116 252 2092*
[b]*School of Engineering & Physical Sciences, Heriot-Watt University, Edinburgh, UK EH14 4AS. E-mail: s.a.macgregor@hw.ac.uk; Fax: +44 (0)131 451 3180, +44 (0)131 451 8031*

Youcef Boutadla

Youcef Boutadla was born in Paris, France. He completed his undergraduate and Masters in Chemistry at the Université Pierre et Marie Curie in Paris. He started his PhD in the group of David Davies at the University of Leicester in 2006. His research involves mechanistic studies of acetate assisted C–H activation.

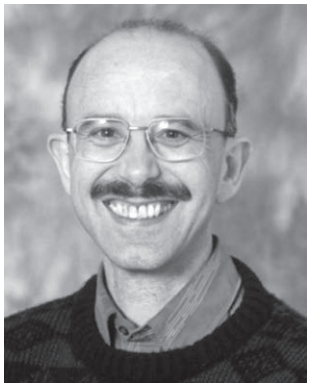

David L. Davies

David Davies did his BSc and PhD at Bristol University working with Prof. S. A. R. Knox and was then a NATO postdoctoral fellow at Caltech with Prof. J. E. Bercaw. He was appointed a lectureship at the University of Leicester in 1985, was promoted to senior lecturer in 1999 and to Reader in 2007. His research interests are quite broad encompassing organometallic chemistry and catalysis, with an emphasis on understanding mechanisms.

be anticipated at Ir, but in this case it must be coupled to rapid reductive elimination (RE) as no intermediate was observed. Given the electron-deficient nature of these cationic Ir^{III} species SBM was also considered a possibility (Fig. 1). Calculations ultimately defined an OA/RE pathway in these systems[9,10] and experimental support for this was subsequently gained from the direct observation of Ir^{III}/Ir^{V} C–H bond activation cycles.[11] At the same time, however, calculations on analogous Rh species were consistent with a one step process where the transition state takes on oxidative character normally associated with an OA intermediate (centre, Fig. 1).[12] Further examples of these one-step 'oxidative' reaction steps followed[13] and now it is apparent that SBM is possible at both early and late TM centres. In the following, we shall use the term SBM as a general label for these processes, although, as discussed below, several terms have been proposed by different groups. A further particularly promising development involves the design of well-defined systems with heteroatom-based groups to act as intramolecular H-acceptors. The widening array of systems capable of C–H activation have sparked debate on the mechanisms of this process, an issue computational chemistry is ideally placed to address.

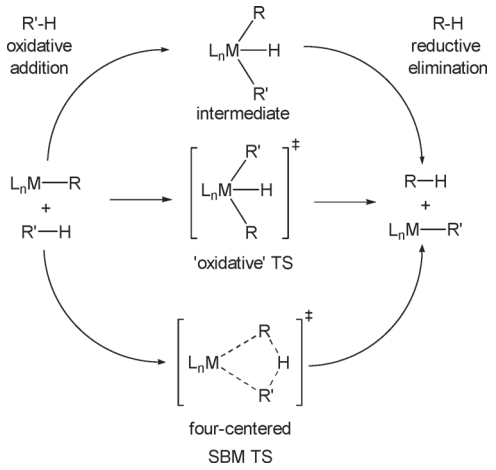

Fig. 1 General mechanisms of C–H activation at L_nM–R species. Adapted from ref. 14.

This perspective will discuss recent mechanistic insights into C–H bond activation arising from computational studies. We will only consider activations involving even electron processes where the metal is directly involved and thus exclude other types of C–H activation such as P450-based or radical processes.[15] Three broad systems, involving middle-late transition metals with d^n ($n \geq 4$), will be considered: (i) SBM processes at L_nM–R Bonds (R = C or B) (ii) systems where a heteroatom-based group bearing lone pairs acts as the H-acceptor (formal 1,2-addition) and (iii) "electrophilic activation" of C–H bonds which involve carboxylate or carbonate as base. In general no mention of the specific methodologies will be given; unless otherwise stated results are based on DFT and the original papers should be consulted for full details.

2. SBM reactions at L_nM–R bonds (R = C or B)

2.1. SBM at L_nM–R bonds (R = alkyl or aryl)

General aspects of this topic have been reviewed recently by Lin[14] who has emphasized the role of occupied metal d-orbitals in stabilizing the transferring hydrogen. As a result, computed transition states often feature short M ··· H contacts that are consistent with the presence of a M–H bond and Lin has called these 'oxidatively-added transition states' (OATS). The nature of the metal centre can therefore dramatically affect the C–H activation. In their study of C(sp^3)-H bond activation at $\{TpM(PH_3)(CH_3)\}$ fragments (M = Fe, Ru, Os; Tp = tris(pyrazolyl)borate) Lin, Lau and Eisenstein showed computed activation barriers increase in the order Os < Ru < Fe (see Fig. 2).[16] Even more striking was the changing nature of the C–H activation process. With M = Os 'normal' 3-centred oxidative addition was characterised, but with the Ru and Fe analogues 4-centred transition states were seen. For M = Ru a very shallow Ru^{IV}–H intermediate was located, while for M = Fe C–H activation was clearly a one-step process *via* a transition state featuring a short Fe ··· H distance of only 1.53 Å.

A lot of detailed computational work has been carried out on C–H activation at d^6 $\{Ir(acac')_2(R)\}$ and $\{TpRu(L)(R)\}$

Stuart A. Macgregor

Stuart Macgregor received a PhD from Edinburgh University in 1992. After a NATO Western European Fellowship at the Université de Paris-Sud working with Odile Eisenstein and two years at the Australian National University, Canberra, he returned to Scotland in 1997 to take up a lectureship in Inorganic Chemistry at Heriot-Watt University. He was promoted to Reader in 2005 and to Professor in 2008. His research interests lie in the use of computational chemistry to understand the structure and reactivity of transition metal systems, particularly in organometallic chemistry.

Amalia I. Poblador-Bahamonde

Amalia Poblador-Bahamonde was born in Madrid, Spain. After gaining her BSc from the University San Pablo CEU and her MPhil from the University Complutense of Madrid, she started her PhD in the group of Stuart A. Macgregor at Heriot-Watt University, Edinburgh. Her research involves computational studies of C–H activation by half-sandwich complexes.

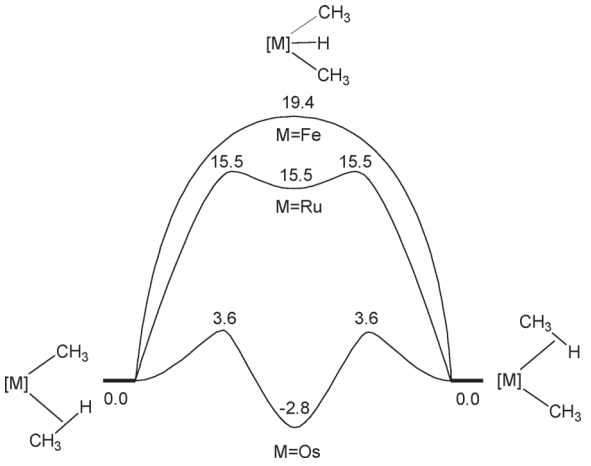

Fig. 2 Computed C–H activation energy profiles (kcal mol^{-1}) for {[M](CH_3)(CH_4)} species ([M] = TpM(PH_3), M = Fe, Ru, Os). Adapted from ref. 16.

fragments, inspired by the role these species play in catalytic alkene hydroarylation (see below). Typical is *cis*-[Ir(acac′)$_2$(CH_2CH_2Ph)(C_6H_6)], **1**, in which C–H activation occurs *via* SBM ($\Delta G^{\ddagger}$ = 14.1 kcal mol^{-1}) with an Ir···H distance of only 1.58 Å in the transition state (see Scheme 1). This implies an oxidation of the metal centre, prompting Goddard and Periana to adopt the term 'oxidative hydrogen migration' (OHM) for this type of process.[17] Interestingly, Periana had previously speculated that C–H activation in **1** might proceed *via* an OA pathway,[18] by analogy to Bergman's [Cp*Ir(PMe_3)(CH_3)(OTf)] system (see Introduction). The fact that a SBM pathway is computed for **1** may reflect an increase in steric crowding and a more electron deficient metal centre, both factors that mitigate against a 7-coordinate Ir(v) intermediate. Certainly distinguishing between these possibilities would have been difficult without computational input.

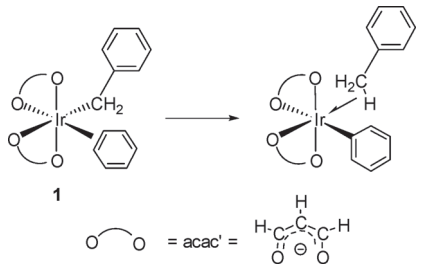

Scheme 1

Further studies by Periana and Goddard suggest that barriers to these SBM processes can be modulated by the ligand environment. Thus replacing the acac′ ligands in **1** with tropolonate reduces the activation barrier by 2.3 kcal mol^{-1}, a result thought to be related to the more electron-releasing character of the latter.[19] Similarly, although a lower C–H activation barrier was computed for the Ir^{III} complex **1** compared to [TpRu^{II}(CO)(CH_2CH_2Ph)(C_6H_6)][20] this trend was reversed by exchanging the ligand sets (*i.e.* [Ru^{II}(acac′)$_2$(CO)(CH_2CH_2Ph)(C_6H_6)]$^-$ has a lower barrier than [TpIr^{III}(CO)(CH_2CH_2Ph)(C_6H_6)]$^+$).[21] Predicting relative barriers on the basis of metal oxidation state alone is therefore difficult. Further work on isoelectronic d^6 analogues of these complexes yielded a wide range of C–H activation barriers, the lowest being only 0.7 kcal mol^{-1} for [Os^{II}(acac′)$_2$(CO)(CH_2CH_2Ph)(C_6H_6)]$^-$. In this case, (as was seen for the [TpOs(PH_3)(CH_3)(CH_4)] system above), C–H activation actually proceeds by an OA pathway.

A more complicated picture of co-ligand effects emerges from work by Gunnoe and Cundari on [TpRu(L)(R)(C_6H_6)] species. For R = CH_3 a lower computed barrier to C–H activation is found when L = PMe_3 ($\Delta G^{\ddagger}$ = 10.9 kcal mol^{-1}) compared to L = CO ($\Delta G^{\ddagger}$ = 14.9 kcal mol^{-1}). This is apparently consistent with the ability of the more electron-releasing PMe_3 ligand to stabilize 'oxidative character' in the transition state.[22,23] However, steric effects can dominate in these systems in particular, the combination of ligands present is important. Thus when L = CO computed barriers are relatively insensitive to changes in the accepting group, R (R = Ph: $\Delta G^{\ddagger}$ = 15.5 kcal mol^{-1} R = CH_2CH_2Ph: $\Delta G^{\ddagger}$ = 13.5 kcal mol^{-1}), but activation barriers increase significantly in the more sterically encumbered PMe_3 analogues (R = Ph: $\Delta G^{\ddagger}$ = 17.1 kcal mol^{-1}; R = CH_2CH_2Ph: $\Delta G^{\ddagger}$ = 20.0 kcal mol^{-1}).[24]

These results are all significant in the context of catalytic alkene hydroarylation, which has been demonstrated by both Periana[18] and Gunnoe[25] (Fig. 3). Currently, however, activities are still too low for practical use and one major difficulty in improving performance is the competitive C–H activation of ethene at the 2-phenylethyl intermediate, **2** (see Fig. 4). This releases ethylbenzene (the desired product) but stops catalysis through the formation of a M-vinyl that subsequently inserts another molecule of ethene to form stable η^3-allyl species (**3** in Fig. 4).[26,27] The much stronger binding of ethene results in increased barriers to

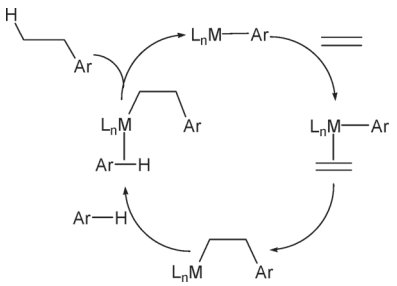

Fig. 3 General catalytic cycle for alkene hydroarylation.

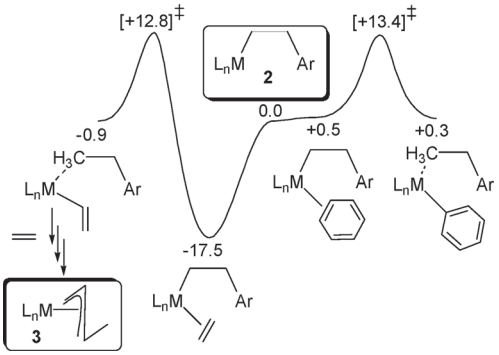

Fig. 4 Calculated free energy profiles (kcal mol^{-1}) for competing C–H activation at intermediate **2** with (right) benzene and (left) ethene. L_nM = Ir(acac')$_2$. Data taken from ref. 17.

C–H activation. For example C–H activation in *cis*-[Ir(acac′)$_2$-(CH_2CH_2Ph)(C_2H_4)] has a barrier of 30.3 kcal mol^{-1},[17] 17.4 kcal mol^{-1} higher than that for the benzene analogue, but overall the two C–H activation transition states are at very similar energies (Fig. 4). Goddard has highlighted the potentially intrinsic problems in the design of alkene hydroarylation catalysts of this type, in that a more electron rich metal centre that is thought to promote C–H activation would tend to retard the prior alkene insertion step by forming a strongly-bound alkene adduct.[20,21] Ironically, although much attention is focused on the C–H activation it is often the less glamorous components of a catalytic cycle that hamper progress, for example the displacement of ligands to create a vacant site for substrate activation or the 'mundane'[27] alkene insertion step.

Important insight into these SBM processes has been gained by varying the nature of the substrate. Thus, computed barriers for C–H activation in [(Tp)Ru(L)(Me)(*p*-C_6H_5X)] species, yield linear Hammett plots with $\rho = 2.6$ (L = CO) and 2.3 (L = PMe_3).[23] Electron withdrawing *para*-substituents therefore stabilize the C–H activation transition states, which is opposite to what is expected for classical electrophilic aromatic substitution. These Ru^{II} systems also appear more sensitive to substituent effects than the classic Cp^*_2Sc-Me system studied by Bercaw.[28] Ru···H distances in these [(Tp)Ru(L)(Me)(*p*-C_6H_5X)] transition states fall in the range 1.592 Å to 1.677 Å with the shortest bond being computed with the most electron withdrawing substituents. Even longer Ru···H distances of *ca.* 1.75 Å had been calculated in earlier studies of C–H activation of the 2-position of THF and thiophene at {(Tab)Ru(CO)Me} (where Tab is the [HB{–N=NH}$_3$]$^-$ model ligand).[29]

In general, more acidic C–H bonds appear easier to activate. Thus activation of a β-C–H bond in Et_2O by {TpRu(PH_3)(H)} showed a reduced barrier compared to CH_4 (relative in each case to their respective σ-adduct precursors).[30] Recent work by Gunnoe and Cundari supports this idea with computed C–H activation barriers at a {TpRu(PH_3)(CH_3)} fragment following the trend CH_3NO_2 < CH_3CN < $(CH_3)_2CO$ < THF < *c*-C_6H_{12}. Moreover a less basic acceptor group (CH_2CN in place of CH_3) increases the barrier. All these observations are consistent with a degree of heterolytic character in the transition states associated with these late transition metal SBM processes, with C–H activation resembling an intramolecular proton transfer.[31]

2.2. SBM at L_nM–boryl bonds

The success of the catalytic alkane hydroborylation[4] has prompted a number of computational studies on the mechanism of this process.[14] The C–H activation step has been studied by Hall for [CpFe(CO){$B(OMe)_2$}(CH_4)] and [$CpW(CO)_2${$B(OMe)_2$}-(CH_4)].[32] Both systems proceed by what Hall calls a "metal-assisted-SBM" with rather short M···H contacts of 1.50 Å (Fe) and 1.75 Å (W). A localised orbital analysis, however, has been interpreted in terms of very little oxidative character in the transition state. Instead the transferring H is protonic in nature and the reaction is assisted by the electron pair of the M-B bond. A Mulliken charge analysis suggests that this process is itself supported by back donation from the metal into the vacant p-orbital on boron, **4**. Similar conclusions were found for methane activation step at {CpRh(H)(BO_2R)} R = $–CH_2CH_2–$.[33]

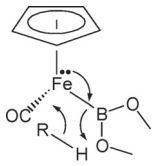

4

2.3. SBM at L_nM=CR_2 and L_nM≡CR bonds

Hall has stressed the isolability of the {L_nM–BR_2} and {L_nM=CR_2} moieties[33] and has studied C–H activation in [CpW(NO)(CH_2)(CH_4)] and [CpW(CO)(CH_2)(CH_4)]$^-$ species. Intriguingly, pathways corresponding to both a one-step SBM and a two-step OA/RE mechanism can be characterized for these systems (Fig. 5). For the nitrosyl species, SBM is slightly more accessible, while OA/RE is preferred with the anionic CO analogue.[34] The major geometric differences between the SBM transition state and OA/RE intermediate are in the C–W–C angles (40–50° wider in the OA intermediate) and W···H distances (*ca.* 0.1 Å shorter in the OA intermediate). More recently, activation of sp^2 and sp^3 C–H bonds by 1,2-addition across a titanium alkylidyne (M≡C) has been reported. DFT calculations suggested a SBM-like transition state.[35] More detailed calculations showed that there was a degree of polarisation in the transition state and the process corresponds to a heterolytic splitting of the C–H bond.[36] The behaviour of this M≡CR species is similar to that seen with M–OR/NR_2 systems (see below) and may reflect the presence of occupied orbitals on the accepting ligands in each case. For the M≡C systems this takes the form of occupied π-bonds, whereas the heteroatomic species have lone pairs available. By analogy, M=CR_2 species should show similar behaviour.

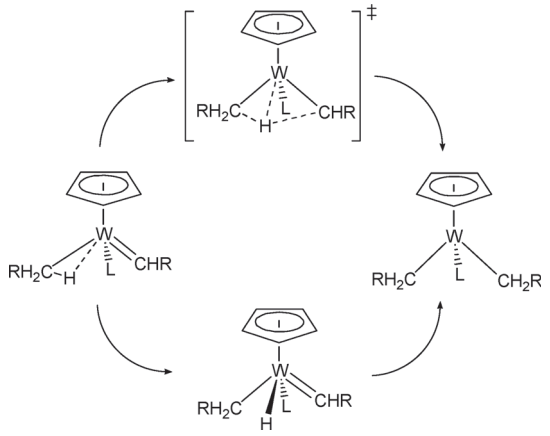

Fig. 5 Two step OA/RE (bottom) and one-step SBM (top) computed for H-transfer in [CpW(L)(CH_2)(CH_4)] systems (L = CO^-, NO).

2.4. Overview

The above discussion highlights the range of late transition metal L_nM–C/B systems where computation shows SBM to occur. Several of the research groups active in this field have

proposed mechanistic interpretations of these processes and the area is now awash with acronyms. Computational studies have focused on the nature of the transition state, thus OATS (Lin), OHM (Goddard) and MASBM (Hall). In addition, Perutz and Sabo-Etienne have proposed the σ-CAM (σ-complex-assisted metathesis) mechanism, based on the experimental observation of reactant and product E–H σ-complexes. E is most commonly H, SiR_3 or BR_2, but in principal this idea extends to C–H σ-complexes.[37] Hall has used the atoms-in-molecules (AIM) approach[38] to characterise different transition states in terms of the varying patterns of bond critical points (BCP) and ring critical points (RCP) (see Fig. 6).[39] Hall assigned these to transition states for (from left to right) SBM (computed for $[Cp_2Sc(CH_3)(CH_4)]$ and $[Pt(acac')_2(Ph)(C_6H_6)]^+$), MASBM ($[Pt(acac')_2(CH_3)(CH_4)]^+$), OATS/σ-CAM ($[Ir(acac')_2(C_2H_4Ph)(C_6H_6)]$, OA/RE ($[Cp^*Ir(PMe_3)(CH_3)(CH_4)]^+$) and OHM ($[Ir(acac')_2(CH_3)(CH_4)]$). This last pattern is also seen for an intermediate formed *via* OA (*e.g.* $([Cp^*Ir(PMe_3)(CH_3)H(CH_3)]^+$).

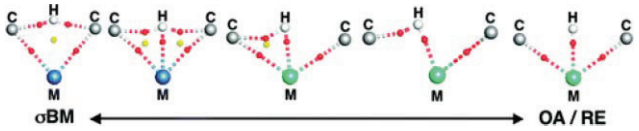

Fig. 6 Spectrum of mechanisms for metal-mediated C–H activation processes showing BCPs (red) and RCPs (yellow). Reproduced with permission from ref. 39. Copyright 2007, American Chemical Society.

Despite this elegant outcome, it seems likely that a continuum of transition state structures will be formed as more computational data become available on SBM processes. Indeed Hall refers to a 'spectrum of mechanisms for metal-mediated hydrogen transfer' and other workers have emphasized this in their work.[16,23] This continuum is already apparent in the range of Ru···H distances reported by Gunnoe and Cundari. In addition, a common feature of these SBM processes is that C–H activation involves a degree of heterolytic character and therefore proton transfer. Subtly 'different' mechanisms can therefore correspond to a different source of stabilization for this proton (electrons from the metal centre or from the acceptor M–ligand bond) or the degree of substrate acidity/acceptor group basicity. In this context, it is interesting to note that recent calculations on the SBM reactions of CH_4 with $[Cp_2M–Me]$ species (M = Sc, Y, La, Ce, Sm, Ho, Yb and Lu) are characterised by polar transition states with near-linear $\{Me^{\delta-}\cdots H^{\delta+}\cdots Me^{\delta-}\}$ moieties that suggest a proton transfer process.[40] As with late transition metal systems, C–H activation is computed to become more accessible when a more acidic hydrogen is transferred.[41]

A final issue concerns the relative accessibility of OA/RE *vs.* SBM in late transition metal systems. In several cases discussed above SBM appears to become 'necessary' only when the metal centre is not sufficiently electron rich to achieve an OA process, or perhaps when steric factors render a more highly coordinated intermediate inaccessible. However, there are now several cases where both SBM and OA have been characterised for the same system.[34,42] As more instances of this emerge the patterns that favour one process over another will become clearer. In the meantime, computational work must be careful to consider all possible pathways before deciding that the lowest energy route has been defined.

3. C–H activation at $L_nM–X$ bonds (X = O, N) (1,2-addition)

As discussed above, recent computational studies of SBM at M–C bonds suggest that these reactions can often be viewed as a proton transfer between a polarised C–H bond and a polarised M–C bond. Consistent with this idea the more polarised the starting M–C bond the faster the proton transfer. One might predict therefore that the related process in which a proton is transferred from a C–H bond to a more strongly polarised M–X bond (X = O, N) would be more facile (this process is also referred to as 1,2-addition). Another interesting question in these reactions is whether the lone pair on the acceptor atom (O, N) facilitates transfer of the hydrogen as a proton.

The earliest experimental examples of net 1,2-addition of C–H bonds to early transition metal M=X (X = O, N) double bonds were provided by the groups of Bergman[43] and Wolczanski.[44] Some of these complexes will even activate methane and computational studies of these reactions have also been reported[44b,c] (see also the discussion of the activation of sp^2 and sp^3 C–H bonds by 1,2-addition across a titanium alkylidyne (M≡C) in Section 2.3 above).

The reactions of late transition metal amides with C–H bonds has been known for some time.[45] However most early examples of this type of reactivity involve outer sphere acid–base type chemistry in which the metal plays a spectator role and the reactivity is rather similar to an alkali metal amide.[45,46] Such reactions initially lead to ion pairs; substitution of the amine by the anion may subsequently take place. To achieve the net 1,2-addition of a C–H bond to an M–X (X = O, N) bond requires a vacant site on the metal. This positions a Lewis acidic/electron deficient metal adjacent to a nucleophilic/basic heteroatom providing ambiphilic reactivity, ideal for a heterolytic splitting of a substrate bond. This process is related to the heterolytic splitting of H_2 across an M–X bond which is well established[47] and indeed plays a key role in many hydrogenation catalysts.[48,49]

The first examples of net 1,2-addition of a non-acidic C–H bond to an M–X (X = O, N) single bond were observed experimentally in 2005 by the groups of Gunnoe and Periana.[50,51] Gunnoe *et al.* first reported the C–H activation of benzene with $[TpRu(PMe_3)_2(OH)]$.[50] This complex undergoes H/D exchange with C_6D_6 at the hydroxide ligand and will catalyse H/D exchange between C_6D_6 and H_2O at 100 °C. Detailed kinetic experiments showed that the dissociation of PMe_3 was occurring prior to H/D exchange and the selectivity for H/D exchange at the *meta* and *para* positions of toluene is consistent with a metal-mediated process. DFT calculations on a model system showed that the reaction (Scheme 2) is substantially endergonic (ΔG = +18.4 kcal mol^{-1}) consistent with the final phenyl complex not being observed experimentally. Similarly, the formation of $[(Tab)Ru(PH_3)_2(Ph)]$ and water was calculated to be endergonic (ΔG = +9.1 kcal mol^{-1}).

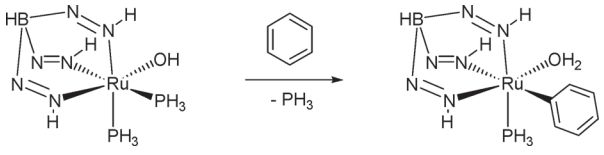

Scheme 2

Location of the transition state gave a free energy barrier to C–H activation of +17.6 kcal mol^{-1} relative to an η^2-benzene complex intermediate. The corresponding barrier for activation of benzene by {(Tab)Ru(CO)(Me)} was calculated to be +21.2 kcal mol^{-1}.

Subsequently, Gunnoe *et al.* extended this C–H activation chemistry to [TpRu(PMe_3)$_2$(X)] (X = OPh, NHPh, NH_2, SH, Cl, OTf).[52] Of these the NHPh complex showed H/D exchange of the NH group with C_6D_6, however the complexes X = NH_2, SH, Cl, OTf did not undergo C–H activation (note the NH_2 complex decomposed under the reaction conditions).[52] They suggested that the ease of C–H activation is related to the basicity of the group receiving the hydrogen and that C–H activations at non-dative, heteroatom-based ligands coordinated to low oxidation state late transition metals would entail inherently lower activation barriers than similar reactions with metal–alkyl or aryl bonds.

In an attempt to understand more about the various factors affecting the energetics of 1,2-additions Cundari and Gunnoe carried out a more extended computational study of C–H activation by the series of complexes [(Tab)M(PH_3)$_2$X]^q (X = OH or NH_2; M = Tc or Re, $q = -1$; M = Ru, $q = 0$; M = Co or Ir, $q = +1$; M = Ni or Pt, $q = +2$).[53] The first step in the C–H activation was loss of phosphine to provide a formally 16-electron five-coordinate species which may be stabilised by π-donation by X. In this study η^2-benzene adducts were only observed for the dicationic Ni or Pt complexes (X = OH, NH_2) and the monocationic [Ir–OH] complex. The increased interaction between the metal and benzene correlated well with the metal acidity as judged by the computed charge on the metal, although the authors emphasise that their calculations ignored solvation effects hence charge effects may dominate. Electron deficiency at the metal may be compensated by coordination of benzene or π-donation from the amide. The hydroxo complexes have more acidic metal centres than the amido ones (NH_2 is a stronger base than OH based on gas phase proton affinities) hence there are more stable benzene adducts in the hydroxo series.

The transition states for benzene activation have a 4-centred geometry with an obtuse angle at the hydrogen being transferred and relatively short M–H distances (Fig. 7). However, the M-H distances are longer on average (8% for OH and 12% for NH_2) than the estimated M–H covalent bond lengths and AIM[38] analyses on representative structures were consistent with no M-H bond being present in the transition state. In addition, for activation of benzene by [(Tab)Ru(PH_3)X] (X = Me, NH_2, OH) there is a substantial difference in the transition states between X = Me and X = NH_2/OH with a much shorter M–H distance in the transition state for X = Me (Fig. 7). They ascribe this difference to the presence of the lone pair on NH_2/OH, thus the directed sp^3 hybrid on Me less effectively bridges the transferring hydrogen and the metal. This is similar to the selectivity for transfer of H over alkyl in SBM observed by Bercaw *et al.* in 1987,[28] and similar conclusions have been reached in computational studies.[14,54a]

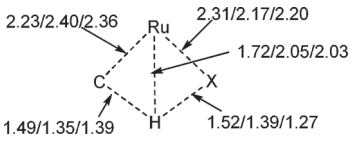

Fig. 7 Calculated metric data for C–H activation of benzene by [(Tab)Ru(PH_3)(X)] where X = Me, NH_2, OH.[53]

Cundari and Gunnoe conclude that this type of C–H bond activation is inherently more facile when the receiving atom is anionic and heteroatomic than hydrocarbyl and the mechanism should be viewed as an internal proton transfer. They also note that the complexes with more electrophilic metals give earlier transition states (shorter C–H distances, longer X–H distances). Similarly, earlier transition states are computed when an NH_2 is the accepting ligand compared to OH, as might be expected from the higher basicity of the former. The M–X distances in the transition states are closer to the products than to the active 16-electron species which they ascribe to a more significant contribution to the C–H activation from the ligand than from the metal. It is interesting to note that if the metal is made more electrophilic, by oxidation, the nature of the C–H activation chemistry can be radically altered. Thus, oxidation of [TpRu(PMe_3)$_2$(OH)] by AgOTf gives [TpRu(PMe_3)$_2$(OH)]OTf, which can abstract hydrogen atoms from relatively weak C–H bonds *e.g.* forms benzene from 1,4 cyclohexadiene.[55]

Periana *et al.* showed that [Ir(acac′)$_2$(OMe)(L)] (L = MeOH, pyridine) reacts with benzene at 160 °C to produce an Ir–Ph complex and that use of C_6D_6 led to formation of CH_3OD.[51] The reaction is insensitive to added oxygen and CH activation of toluene only occurs in the *meta* and *para* positions consistent with a non-radical process. Calculations were interpreted in terms of a reaction proceeding *via* a SBM-type process rather than oxidative addition. The complexes also catalyse H/D exchange between D_2O and C_6H_6 presumably *via* an Ir–OH species and this was subsequently verified experimentally.[56] Experiments in the presence of added pyridine, and comparison of the kinetic isotope effect (KIE) for reaction of [Ir(acac′)$_2$(OH)(Py)] with a mixture of C_6H_6 and C_6D_6 ($k_H/k_D = 1.07 \pm 0.24$) with that for 1,3,5-trideuteriobenzene ($k_H/k_D = 2.65 \pm 0.56$), are consistent with rate determining coordination of benzene followed by faster C–H activation. Calculations accurately model the KIE and show that the reaction is energetically favourable ($\Delta G = -6.8$ kcal mol^{-1}) and that the transition state for C–H cleavage is only 6.7 kcal mol^{-1} higher than the benzene adduct.

More recently, Oxgaard *et al.* carried out a detailed orbital analysis of the mechanism of the C–H activation step in the reaction of [Ir(acac′)$_2$(OMe)(Py)] with benzene and concluded that the forming O–H bond is not based on the same orbital as the breaking O–Ir bond.[57] The transition state is similar to that for [(Tab)Ru(PH_3)(OH)] (Fig. 7) with a C···H distance of 1.29 Å slightly shorter than that, 1.39 Å, for the Ru^{II} complex, consistent with an earlier transition state for the more electrophilic Ir^{III}. The analysis is not consistent with a traditional SBM mechanism but rather with an activation of the C–H bond by an electrophilic metal generating a positively charged hydrogen, which is then transferred to the metal-bound hydroxide *i.e.* to an internal base. Hence, they used the term internal electrophilic substitution (IES) to describe the mechanism. They note the similarities with heterolytic activation of dihydrogen[47] and with an asymmetric sigmatropic rearrangement. Interestingly, changing the nature of X in [Ir(acac′)$_2$(X)(C_6H_6)] (X = OMe, OCF_3, NH_2) has very little effect on the activation energy barriers (less than 2 kcal mol^{-1}).[57] In contrast, for the model system [(Tab)Ir(PH_3)X(C_6H_6)] the difference in $\Delta G^{\ddagger}$ is 11.3 kcal mol^{-1} between X = OH and NH_2 with the barrier being lower for OH.[53]

Whilst there is no doubt that the electrophilicity of the metal is playing an important role in the C–H activation, the term IES does not perhaps convey the extent to which the heteroatom lone pair plays a role in the activation of the C–H bond. Indeed, as suggested by Gunnoe and Cundari[53] the C–H activation is easier in the case of X = OH than X = Me; they also emphasise the significant contribution to C–H bond scission from the ligand.

In conclusion, the net 1,2-addition of C–H bonds to an M–X bond (X = O, N) occurs *via* a 4-centre transition state. However, there is no M–H bonding interaction and the forming X–H bond is not based on the same orbital as the breaking M–X bond. Thus, these processes are fundamentally different to conventional SBM and involve a concerted ambiphilic electron-deficient metal and basic ligand acting together to cause a heterolytic scission of the C–H bond. For further discussion see below.

4. "Electrophilic" C–H activation at late transition metals mediated by carboxylate or carbonate bases

Theoretical calculations have also offered insights into "electrophilic" type C–H activations. So-called Shilov chemistry has been known since 1969 and has been reviewed.[2,58] Such chemistry has been the subject of a number of computational studies and the C–H activation step has been modelled as oxidative addition or an electrophilic or SBM mechanism, aided by inter- or intramolecular base.[59–61] In this section we will concentrate on the more recently studied systems of "electrophilic activation" of C–H bonds which involve carboxylate or carbonate as base. Parallels with Shilov type chemistry will be made where appropriate.

4.1. Intramolecular C–H activation

Cyclometalated complexes of the platinum metals were first reported in 1965.[62] The facile cyclometalation by palladium acetate, particularly of N-donor ligands had been well studied experimentally in the 1980s and 1990s. Ryabov had proposed that cyclopalladation of dimethylbenzylamine occurred by an electrophilic substitution *via* a Wheland intermediate with subsequent intramolecular deprotonation by coordinated acetate *via* a 6-membered transition state (Fig. 8, **5**).[63] Detailed mechanistic studies, including volume of activation measurements, suggested a highly ordered transition state. Similar studies on cyclopalladation of imines led Gomez to propose a related mechanism but with a highly ordered 4-membered transition state for intramolecular deprotonation (Fig. 8, **6**).[64] Such a process would be closely related to the 1,2 additions discussed in Section 3. Distinguishing between these two possibilities by experiment is virtually impossible, however DFT calculations can shed light on the dilemma.

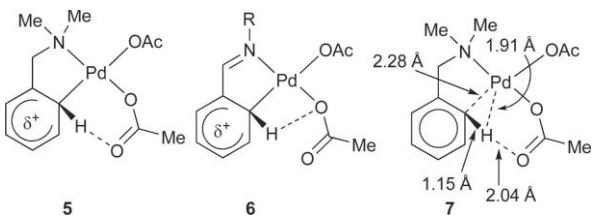

Fig. 8 Proposed transition states (**5**, **6**).[63,64a] and calculated agostic intermediate (**7**) in cyclometalation of dimethylbenzylamine by $[Pd(OAc)_2]$.[65]

Davies and Macgregor published the first computational study of these processes in 2005.[65] The calculations on $[Pd(DMBA\text{-}H)(OAc)_2]$ (DMBA-H = dimethylbenzylamine) located an intermediate in which an acetate arm has been displaced by one *ortho*-C–H bond of DMBA-H. The interaction between the electrophilic Pd^{II} centre and the C–H bond was more consistent with an agostic structure, rather than a Wheland intermediate formed by electrophilic attack on the π-system (Fig. 8, **7**). In addition, the agostic interaction, although rather weak (Pd ··· C and Pd ··· H distances of 2.28 and 1.91 Å, respectively), is sufficient to polarize the C–H bond and allow acetate to form an intramolecular hydrogen bond to the transferring hydrogen. Thus, the process is best viewed as an ambiphilic activation, by an electrophilic metal centre and an intramolecular base. The rate-determining step is computed to be formation of the agostic intermediate *via* the κ^2–κ^1displacement of acetate. Subsequent intramolecular deprotonation occurs with a minimal energy barrier (<1 kcal mol^{-1}). C–H activation *via* the 6-membered transition state was shown to be more favourable than the type of 4-membered transition state suggested by Gomez, although both these processes were considerably more favourable than an alternative oxidative addition of the C–H bond followed by reductive elimination of acetic acid. Interestingly, the central role of an agostic intermediate suggests that C–H activation in such systems may not be limited to aryl C–H bonds and this has proved to be the case (see below).

Subsequently, Davies and Macgregor showed that cyclometalation of DMBA-H with $[Cp^*_2IrCl_2]_2$ in the presence of sodium acetate occurred by a very similar mechanism. Calculations on the model intermediate, $[CpIr(DMBA\text{-}H)(\kappa^2\text{-}OAc)]^+$, (Fig. 9, **8a**) showed the 6-membered transition state to give **9a** was favoured over a 4-membered process *via* **8b** to **9b** or oxidative addition to an Ir^V species, **9c**.[66] In this case, unlike palladium, no intermediate agostic complex was observed on the calculated reaction path. The main activation energy barrier again seems to be related to converting a κ^2-acetate to κ^1 and once this is done there is essentially no barrier to C–H activation. The importance of the intramolecular hydrogen bonding in the activation was further

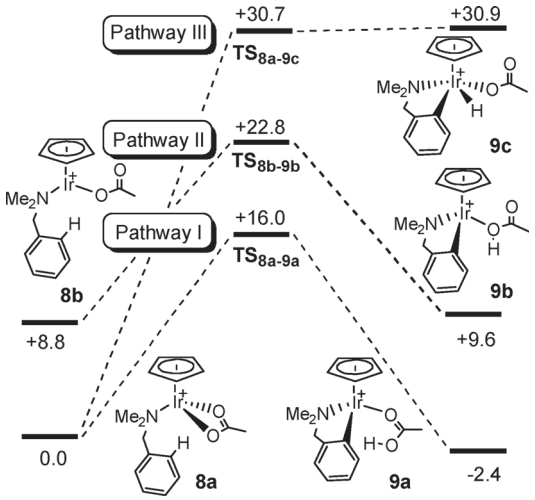

Fig. 9 Computed reaction profiles (kcal mol^{-1}) for C–H activation in $[Ir(DMBA\text{-}H)(OAc)Cp]^+$. **8**. Pathway I is *via* a 6-membered transition state, Pathway II *via* 4-membered transition state and Pathway III by oxidative addition.[66]

demonstrated in the preference for N-H activation over C–H activation in cyclometallation of a pyrrole imine.[67]

Related base-assisted cyclometallation reactions have also been incorporated into schemes for Pd-catalysed intramolecular arylation. These reactions typically involve initial oxidative addition of an aryl C–Br bond with cyclometallation occurring at a pendant substituent of the resultant M–aryl ligand. Echavarren, Maseras and co-workers reported an early combined experimental and theoretical study of such a process, where **10** reacted to give either **11** or **12**, depending on the substituents, R (Scheme 3).[68] Their experimental studies suggest the key step to be a C–H activation in which the hydrogen from the phenyl is transferred as a proton, rather than *via* an electrophilic aromatic substitution mechanism.

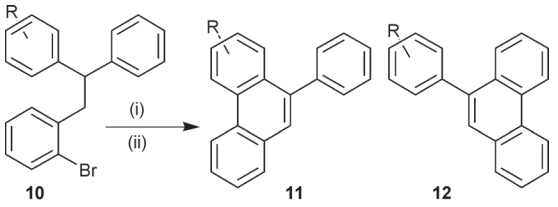

(i) $Pd(OAc)_2$, L, K_2CO_3, DMA, 135 °C (ii) DDQ

Scheme 3

Originally, the authors favoured an initial exchange of bromide (generated by C–Br oxidative addition), by bicarbonate. This then allowed the C–H cleavage to occur through a 6-membered transition state with strong hydrogen bonding between the proton being transferred and the bicarbonate (Fig. 10 **TS 10C**) with a calculated energy barrier of 23.5 kcal mol^{-1}. An alternative 4-membered transition state with bromide as the acceptor (**TS 10A**) (*c.f.* intramolecular transfer to chloride in Shilov chemistry)[59] had a rather higher energy barrier of 43.3 kcal mol^{-1}. In their later full paper[69] the authors gave further consideration to a mechanism in which the bicarbonate is not bound to the palladium but still assists the C–H cleavage step by intermolecular hydrogen bonding (**TS 10B**) (*c.f.* intermolecular transfer to chloride in Shilov chemistry).[60] The calculated energy difference between an inter- and intra-molecular proton abstraction was at most 6 kcal mol^{-1}, but which was the favoured pathway depended on the substituents on the ring being activated. The calculations accurately reproduce the trends in reactivity, *i.e.* electron-acceptor substituents in the ring being activated favour the reaction to give **11**, while electron-donating substituents drive the reaction to the unsubstituted ring (*i.e.* formation of **12**, Scheme 3). In a further study[70] these workers showed that bidentate phosphines are excellent ligands for this process and concluded that at least in this case the reaction proceeds by an intermolecular base-assisted proton abstraction mechanism.

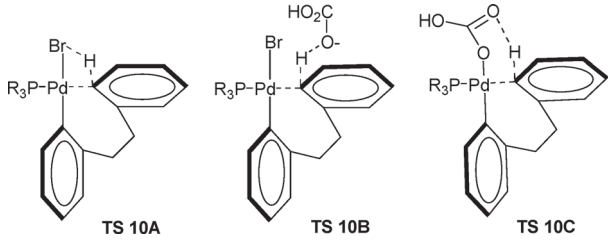

Fig. 10 Schematic transition states for aryl C–H bond activation, modelling intramolecular arylation of **10**.[68]

Similar strategies have allowed the activation of sp^3 C–H bonds to be exploited in synthesis. Fagnou *et al.* investigated the reactions of substrates such as **13** (Scheme 4) and calculations again show concerted palladation/intramolecular proton abstraction *via* 6-membered transition states. The computed results also correctly reproduce the observed selectivity *i.e.* formation of a 6-membered palladacycle by activation of a primary C–H bond (**TS 13A** $\Delta G^{\ddagger} =$ 27 kcal mol^{-1}) is favoured over formation of 6-membered palladacycle by secondary C–H activation (**TS 13B** $\Delta G^{\ddagger} = 32.5$ kcal mol^{-1}) or formation of a 7-membered palladacycle by activation of a methyl (**TS 13C** $\Delta G^{\ddagger} = 33.1$ kcal mol^{-1}), respectively.[71] The transition states all feature an agostic interaction between the activating C–H bond and palladium in combination with hydrogen bonding to the acetate.

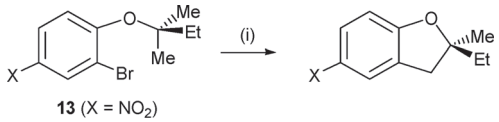

(i) $Pd(OAc)_2$, PCy_3-HBF_4, Cs_2CO_3, pivalic acid mesitylene, 135 °C

Scheme 4

Baudoin, Clot *et al.* also studied sp^3 C–H activation in the formation of benzocyclobutenes (Scheme 5).[72] Even in this case with formation of a strained 4-membered ring C–H activation is still the rate limiting step as confirmed by a KIE of 5.8. Surprisingly, the computed product of initial C–Br oxidative addition (Fig. 12, **14**) has phenyl *trans* to phosphine and bromine *trans* to the vacant site whereas in [Pd(Ph)(Br)(P^tBu_3)] characterised crystallographically by Hartwig *et al.*[73] Br is *trans* to phosphine with aryl opposite

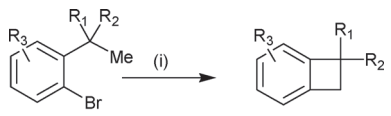

(i) $Pd(OAc)_2$, P^tBu_3, K_2CO_3, DMF, 140 °C

Scheme 5

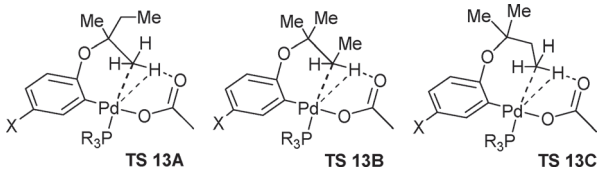

Fig. 11 Schematic transition states for sp^3 C–H activation in intramolecular cyclisation of **13** (X = H).[71]

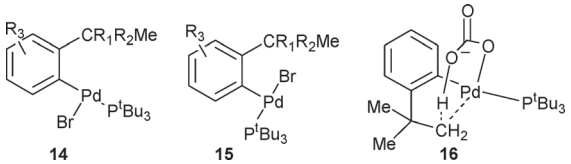

Fig. 12 Proposed oxidative addition products and subsequent transition state for sp^3 C–H activation in intramolecular cyclisation to form benzocyclobutenes (see Scheme 5).[72]

the vacant site (Fig. 12, **15**). Calculations confirm that the X-ray isomer (**15**) is more stable by 6.5 kcal mol^{-1}.

Calculations of the substitution of Br in **15** by various bases yielded (κ^2-O_2CX)Pd complexes (X = Me, OH, O^-) which give rise to transition states for C–H activation analogous to those found by Fagnou[71] (Fig. 11); however the activation energy barriers ($\Delta E^{\ddagger}$) are rather higher (33–45 kcal mol^{-1} compared with 27.0 kcal mol^{-1}) and C–H activation is computed to be strongly endothermic. The trends in computed $\Delta E^{\ddagger}$ (acetate lowest, carbonate highest) are also completely opposite to those found experimentally. Computation of C–H activation from the other isomer (**14**) proceeds *via* (κ^1-O_2CX)Pd complexes, which, in contrast with the bromo complex **15**, have a clear agostic interaction with one C–H bond on the ^{t}Bu group on the aromatic ring. Proton transfer from C(sp^3) now occurs in a plane perpendicular to the P–Pd–Ph axis (Fig. 12, **16**). The $\Delta E^{\ddagger}$ values are much lower (27.5–29.2 kcal mol^{-1}), the reaction is computed to be exothermic and the greater reactivity of carbonate is now correctly modelled. Thus, these calculations demonstrate that the carboxylate/carbonate does not need to be located *cis* to the site being activated in the square plane.

Computational studies of such direct arylation reactions are not limited to palladium. Maseras, Dixneuf and co-workers studied ruthenium-catalysed arylation of 2-phenyl pyridine.[74] They concluded that the most likely mechanism involves proton abstraction by coordinated bicarbonate, however in this case the proton is transferred to the metal bound oxygen *via* a 4-centre transition state.

4.2 Intermolecular C–H activation

The Pd(II) catalysed coupling of benzene with an alkene *via* a C–H activation was demonstrated experimentally by Fujiwara as long ago as 1967.[75] This reaction and others have traditionally been thought to proceed by an electrophilic aromatic substitution. In 2000 Sakaki carried out a theoretical study at the MP4(SDQ) level on the activation of benzene and methane by [M(η^2-$O_2CH)_2$] (M = Pd, Pt) and [M($PH_3)_2$].[76] He concluded that [M($PH_3)_2$] cannot easily achieve C–H activation but that [M(η^2-$O_2CH)_2$] can because the formate ligand assists the C–H bond activation through formation of a strong O–H bond. Key geometric parameters for the computed intermediate (**17**) and transition state (**18**) for benzene activation with [Pd(η^2-$O_2CH)_2$] are shown in Fig. 13. The reactions go *via* intermediates in which a C–H bond displaces one arm of a bidentate acetate and the C–H bond that is broken lengthens significantly in the transition state. An electron distribution analysis showed that in the C–H activation the atomic population of M significantly increases while that of H remarkably decreases. These data are consistent with an heterolytic fission of the C–H bond in which electrophilic attack of M to benzene or methane occurs concomitantly with the proton abstraction by the carboxylate ligand. These transition states are very similar to those computed for formate assisted heterolytic activation of dihydrogen by a ruthenium catalyst.[77]

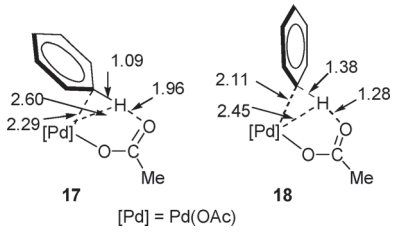

Fig. 13 Calculated metric data for the intermediate and transition state computed for the activation of benzene by [Pd($OAc)_2$].[76] Distances in Å.

In 2006 Fagnou *et al.* reported[78] the catalytic direct arylation of perfluorobenzenes.[79] Experimentally they showed that the reaction was favoured for electron deficient arenes *i.e.* a complete reversal of selectivity in comparison with electrophilic aromatic substitution. Computational studies showed that the reaction proceeds *via* a concerted arene metalation and C–H bond cleaving process which depends directly on the acidity of the C–H bond being cleaved. The lowest energy pathway was computed to be transfer of the proton to Pd-bound bicarbonate *via* a 6-membered transition state (*c.f.* **TS 10C** in Fig. 10). As seen in Maseras' work, transfer to coordinated bromide (*c.f.* **TS 10A**, Fig. 10) was a higher energy alternative. Fagnou used the term concerted metalation deprotonation (CMD), which also emphasises the dual role of metal and (intramolecular) base. In this case a pathway involving intermolecular deprotonation by external bicarbonate could not be located. Later, Fagnou *et al.* showed the experimental benefit of adding pivalic acid, and calculations suggested pivalate had a slightly lower (1.3 kcal mol^{-1}) transition state energy than bicarbonate.[80] We have shown that for intramolecular deprotonation variation in the pK_a of the base has only a rather small effect on activation energy barriers since the base strength is somewhat reduced by coordination to the metal.[81]

Interestingly, in a more wide-ranging study of direct arylation reactions across a broad range of aromatic substrates Gorelsky and Fagnou[82] were unable to find any evidence for Wheland-type intermediates but instead found the lowest energy route to involve 6-membered transition states in which very little charge builds up on the aromatic ring. This is a very similar pattern to that found in cyclometallation reactions.[65] This pathway correctly predicts the regioselectivity for all the arenes studied regardless of their electronic properties. An activation-strain analysis showed that π-electron rich aromatics have the most favourable interaction with the metal (most negative E_{int}) values but that these are offset by the highest energetic cost of distorting the catalyst and arene from the ground state to the transition state geometries. Electron deficient arenes have less favourable E_{int} but a more facile arene distortion so the transition state remains accessible. Benzene is not favoured by either value and has the highest $\Delta E^{\ddagger}$ of the arenes evaluated. Overall they concluded that this type of mechanism may be more widespread than previously thought in direct arylation reactions and may apply even to electron rich aromatics previously assumed to go *via* electrophilic aromatic substitution.

Periana *et al.* have recently compared C–H activation by K[Pt(pic)($TFA)_2$] (pic = picolinate) **19** and Pt(bpym)($TFA)_2$ (bpym = 2,2′-bipyrimidyl) **20** and considered the effect of the charge on the complex on the overall C–H activation process.[83] The calculated $\Delta H^{\ddagger}$ for C–H activation of benzene by complex **19** was 21 kcal mol^{-1} (experimental activation barrier for H/D exchange between C_6H_6 and CF_3CO_2D was 23 kcal mol^{-1}), significantly lower than the value for the bpym complex **20** of 27 kcal mol^{-1}. The C–H activation occurs in two steps, κ^2–κ^1 displacement of one TFA and coordination of the arene and then activation of the C–H bond. For complex **20**, the ΔH for the first step is 14 kcal mol^{-1} with the subsequent C–H cleavage step having an activation

barrier, $\Delta H^{\ddagger}$, of 13 kcal mol^{-1}. For complex **19**, the ΔH for the first step, displacement of an anionic TFA from the anionic complex, is much easier than from the neutral one at ~5.0 kcal mol^{-1} and the $\Delta H^{\ddagger}$ for C–H cleavage shows only a slight increase to ~16 kcal mol^{-1}. Thus the main difference in overall rates of H/D exchange for these complexes (TOF for complex **19** is about 300 times that for **20**) is due to more favourable coordination of benzene, with the overall C–H cleavage step being relatively unaffected by the overall increase in negative charge of the complex.

In a recent study, Ess *et al.* have carried out a transition state energy decomposition study of C–H activation of benzene and methane by [Ir(acac′)$_2$(X)] (X = OAc and OH).[84] Hydroxide can only act as an intramolecular base with a 4-membered transition state (see Fig. 14, **21**; this process is termed ES by this group) but acetate can have a 4-membered or 6-membered transition state (Fig. 14, **22** and **23**, respectively). As found previously,[65,66] C–H activation *via* 6-membered **23** is favoured over **22**, for both benzene and methane activation by about 20 kcal mol^{-1}, it is also favoured by about 15 kcal mol^{-1} over **21**. The authors conclude the most significant contribution to the energy difference between **23** and **22** is the energy required to deform the reactants into their transition state geometries. For activation of benzene in **22** the C–O bond lengths of the acetate are rather different at 1.35 and 1.21 Å, changing these to 1.25 and 1.28 Å, respectively, (as found in the 6-membered transition state) lowers the fragment distortion energy by ~13 kcal mol^{-1}. The authors also point out that the transition states for the hydroxide and 4-membered acetate are very similar, indeed we feel these should be considered as the same process (see below).

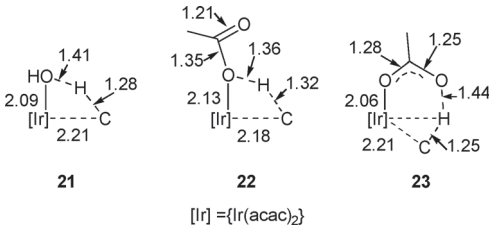

Fig. 14 Comparison of key metric data in transition states for the activation of benzene with {Ir(acac′)$_2$(X)}. Distances in Å.[84]

5. Overview of heteroatom-assisted C–H activation

Since 2000, several computational studies have shown that the combination of an electrophilic metal and a lone pair on an internal base, either metal-bound (4-membered) or pendant (6-membered) can lead to the concerted ambiphilic activation of C–H bonds. Davies and Macgregor also commented on the possible synergic effect of the two components.[67] Thus, interaction of the C–H bond with the electrophilic metal makes the C–H bond more acidic which in turn facilitates hydrogen bonding from the heteroatom lone pair. It is now easy to rationalise the great success of carboxylates, as well as bicarbonate and carbonate (and possibly phosphate) in palladium catalysed reactions involving a C–H activation step as being in large part due to their ability to act as an intramolecular base.[65] In some cases, however, it is possible that such bases act in an intermolecular fashion.[69,74] In passing, it is worth noting the resemblance between the 6-membered ring transition states discussed here and those associated with Noyori's transfer hydrogenation catalysts.[85] This also involve metal–ligand bifunctional cooperativity,[48,86] and calculations[87] have shown that transfer of the hydrogen from the alcohol to the catalyst occurs *via* a cyclic 6-membered transition state.

As pointed out in Section 3, C–H activation at M-X bonds (X = O, N) involves little, if any, M–H bonding interaction. Moreover, the forming X–H bond is not based on the same orbital as the breaking M–X bond. Thus, these processes are fundamentally different to conventional SBM at M–H, M–C and M–B bonds. In this regard C–H activation reactions at M–X bonds can then be considered as another variant of a concerted ambiphilic activation, where an electron-deficient metal and a basic ligand cause the heterolytic scission of a C–H bond.

The term internal electrophilic substitution (IES) has been suggested for C–H activation of benzene at an Ir–OH bond (see **21**, Fig. 14). However, in our opinion this does not convey the extent to which the heteroatom lone pair plays a role in the activation of the C–H bond. It is the concerted dual activation that make these processes different from a conventional electrophilic process and why their selectivity is different to conventional electrophilic aromatic substitution. The term concerted metalation deprotonation (CMD) has been used by Fagnou and this certainly emphasises the dual nature of the process. However, given that recent studies on SBM suggest these also have polarised transition states and can therefore be thought of as involving deprotonation, we feel it would be useful to distinguish concerted ambiphilic activations from SBM. Hence we propose that such processes should be termed ambiphilic metal ligand activations (AMLA), essentially showing that there must be an available "lone pair" on the ligand, with the number of atoms involved in the transition state, where known, listed in parentheses. Thus, in Fig. 14, **21** and **22** correspond to AMLA(4) processes and **23** is an AMLA(6).

6. Conclusions

The last decade has seen great progress in the information that computational chemistry can provide about reaction mechanisms, information that would otherwise be extremely difficult, if not impossible, to obtain by experiment. In particular, mechanistic subtleties abound in the field of C–H activation. SBM processes are now recognized to be accessible in a much wider range of metal complexes than previously, but delineation from OA reactions can only be routinely achieved computationally. Close collaboration between experiment and computation has provided a much better understanding of C–H activations at M–X bonds (X = O, N) and those mediated by carboxylate or carbonate bases. This powerful synergy has facilitated the discovery of new catalysts where C–H activation can be exploited in synthesis. Heteroatom-assisted C–H activations are particularly prominent in these developments and the common features of such processes appear to be the simultaneous ambiphilic activation by a Lewis acidic metal centre and an intramolecular base. We therefore suggest use of the acronym AMLA (ambiphilic metal ligand activation) for such reactions.

Acknowledgements

We thank the EPSRC for financial support (YB, AIP-B).

References

1 (*a*) R. G. Bergman, *Nature*, 2007, **446**, 391; (*b*) R. H. Crabtree, *J. Chem. Soc., Dalton Trans.*, 2001, 2437; (*c*) R. H. Crabtree, *J. Organomet. Chem.*, 2004, **689**, 4083; (*d*) J. A. Labinger and J. E. Bercaw, *Nature*, 2002, **417**, 507; (*e*) *Activation and Functionalization of C–H Bonds*, ed. A. S. Goldman and K. I. Goldberg, ACS Symposium Series 885, Washington DC, 2004.
2 A. E. Shilov and G. B. Shul'pin, *Chem. Rev.*, 1997, **97**, 2879.
3 (*a*) R. B. Bedford, *Chem. Commun.*, 2003, 1787; (*b*) F. Kakiuchi and S. Murai, *Acc. Chem. Res.*, 2002, **35**, 826; (*c*) V. Ritleng, C. Sirlin and M. Pfeffer, *Chem. Rev.*, 2002, **102**, 1731; (*d*) A. R. Dick and M. S. Sanford, *Tetrahedron*, 2006, **62**, 2439; (*e*) C. H. Jun, C. W. Moon and D. Y. Lee, *Chem.–Eur. J.*, 2002, **8**, 2423; (*f*) J. C. Lewis, R. G. Bergman and J. A. Ellman, *Acc. Chem. Res.*, 2008, **41**, 1013.
4 H. Y. Chen, S. Schlecht, T. C. Semple and J. F. Hartwig, *Science*, 2000, **287**, 1995.
5 (*a*) B. L. Conley, W. J. Tenn, K. J. H. Young, S. K. Ganesh, S. K. Meier, V. R. Ziatdinov, O. Mironov, J. Oxgaard, J. Gonzales, W. A. Goddard and R. A. Periana, *J. Mol. Catal. A: Chem.*, 2006, **251**, 8; (*b*) L. C. Campeau and K. Fagnou, *Chem. Commun.*, 2006, 1253; (*c*) D. Alberico, M. E. Scott and M. Lautens, *Chem. Rev.*, 2007, **107**, 174.
6 (*a*) A. Dedieu, *Chem. Rev.*, 2000, **100**, 543; (*b*) G. Frenking and N. Frohlich, *Chem. Rev.*, 2000, **100**, 717; (*c*) S. Niu and M. B. Hall, *Chem. Rev.*, 2000, **100**, 353.
7 W. Koch and M. C. Holthausen, *A Chemist's Guide to Density Functional Theory*, Wiley-VCH, 2001.
8 P. Burger and R. G. Bergman, *J. Am. Chem. Soc.*, 1993, **115**, 10462.
9 D. L. Strout, S. Zaric, S. Q. Niu and M. B. Hall, *J. Am. Chem. Soc.*, 1996, **118**, 6068.
10 S. Q. Niu and M. B. Hall, *J. Am. Chem. Soc.*, 1998, **120**, 6169.
11 (*a*) S. R. Klei, T. D. Tilley and R. G. Bergman, *J. Am. Chem. Soc.*, 2000, **122**, 1816; (*b*) S. R. Klei, J. T. Golden, P. Burger and R. G. Bergman, *J. Mol. Catal. A: Chem.*, 2002, **189**, 79.
12 M. D. Su and S. Y. Chu, *J. Am. Chem. Soc.*, 1997, **119**, 5373.
13 A. J. Toner, S. Grundemann, E. Clot, H. H. Limbach, B. Donnadieu, S. Sabo-Etienne and B. Chaudret, *J. Am. Chem. Soc.*, 2000, **122**, 6777.
14 Z. Y. Lin, *Coord. Chem. Rev.*, 2007, **251**, 2280.
15 These processes are referred to as the "Coordination Chemistry Approach" in ref. 1b.
16 W. H. Lam, G. C. Jia, Z. Y. Lin, C. P. Lau and O. Eisenstein, *Chem.–Eur. J.*, 2003, **9**, 2775.
17 J. Oxgaard, R. P. Muller, W. A. Goddard and R. A. Periana, *J. Am. Chem. Soc.*, 2004, **126**, 352.
18 R. A. Periana, X. Y. Liu and G. Bhalla, *Chem. Commun.*, 2002, 3000.
19 G. Bhalla, J. Oxgaard, W. A. Goddard and R. A. Periana, *Organometallics*, 2005, **24**, 3229.
20 J. Oxgaard and W. A. Goddard, *J. Am. Chem. Soc.*, 2004, **126**, 442.
21 J. Oxgaard, R. A. Periana and W. A. Goddard, *J. Am. Chem. Soc.*, 2004, **126**, 11658.
22 N. A. Foley, M. Lail, T. B. Gunnoe, T. R. Cundari, P. D. Boyle and J. L. Petersen, *Organometallics*, 2007, **26**, 5507.
23 N. J. DeYonker, N. A. Foley, T. R. Cundari, T. B. Gunnoe and J. L. Petersen, *Organometallics*, 2007, **26**, 6604.
24 N. A. Foley, M. Lail, J. P. Lee, T. B. Gunnoe, T. R. Cundari and J. L. Petersen, *J. Am. Chem. Soc.*, 2007, **129**, 6765.
25 M. Lail, B. N. Arrowood and T. B. Gunnoe, *J. Am. Chem. Soc.*, 2003, **125**, 7506.
26 G. Bhalla, J. Oxgaard, W. A. Goddard and R. A. Periana, *Organometallics*, 2005, **24**, 5499.
27 N. A. Foley, Z. Ke, T. B. Gunnoe, T. R. Cundari and J. L. Petersen, *Organometallics*, 2008, **27**, 3007.
28 M. E. Thompson, S. M. Baxter, A. R. Bulls, B. J. Burger, M. C. Nolan, B. D. Santarsiero, W. P. Schaefer and J. E. Bercaw, *J. Am. Chem. Soc.*, 1987, **109**, 203.
29 K. A. Pittard, J. P. Lee, T. R. Cundari, T. B. Gunnoe and J. L. Petersen, *Organometallics*, 2004, **23**, 5514.
30 S. M. Ng, W. H. Lam, C. C. Mak, C. W. Tsang, G. C. Jia, Z. Y. Lin and C. P. Lau, *Organometallics*, 2003, **22**, 641.
31 N. A. Foley, T. B. Gunnoe, T. R. Cundari, P. D. Boyle and J. L. Petersen, *Angew. Chem., Int. Ed.*, 2008, **47**, 726.
32 C. E. Webster, Y. B. Fan, M. B. Hall, D. Kunz and J. F. Hartwig, *J. Am. Chem. Soc.*, 2003, **125**, 858.
33 J. F. Hartwig, K. S. Cook, M. Hapke, C. D. Incarvito, Y. B. Fan, C. E. Webster and M. B. Hall, *J. Am. Chem. Soc.*, 2005, **127**, 2538.
34 Y. Fan and M. B. Hall, *J. Chem. Soc., Dalton Trans.*, 2002, 713.
35 B. C. Bailey, H. Fan, E. W. Baum, J. C. Huffman, M.-H. Baik and D. J. Mindiola, *J. Am. Chem. Soc.*, 2005, **127**, 16016.
36 B. C. Bailey, H. Fan, J. C. Huffman, M.-H. Baik and D. J. Mindiola, *J. Am. Chem. Soc.*, 2007, **129**, 8781.
37 R. N. Perutz and S. Sabo-Etienne, *Angew. Chem., Int. Ed.*, 2007, **46**, 2578.
38 R. F. W. Bader, *Atoms in Molecules: A Quantum Theory*, Oxford University Press, 1990.
39 (*a*) B. A. Vastine and M. B. Hall, *J. Am. Chem. Soc.*, 2007, **129**, 12068; (*b*) B. A. Vastine and M. B. Hall, *Coord. Chem. Rev.*, 2009, **253**, 1202.
40 N. Barros, O. Eisenstein and L. Maron, *Dalton Trans.*, 2006, 3052.
41 E. L. Werkema, E. Messines, L. Perrin, L. Maron, O. Eisenstein and R. A. Andersen, *J. Am. Chem. Soc.*, 2005, **127**, 7781.
42 J. M. Gonzales, J. Oxgaard, R. A. Periana and W. A. Goddard, *Organometallics*, 2007, **26**, 1505.
43 P. J. Walsh, F. J. Hollander and R. G. Bergman, *J. Am. Chem. Soc.*, 1988, **110**, 8729.
44 (*a*) C. C. Cummins, S. M. Baxter and P. T. Wolczanski, *J. Am. Chem. Soc.*, 1988, **110**, 8731; (*b*) T. R. Cundari, T. R. Klinckman and P. T. Wolczanski, *J. Am. Chem. Soc.*, 2002, **124**, 1481; (*c*) L. M. Slaughter, P. T. Wolczanski, T. R. Klinckman and T. R. Cundari, *J. Am. Chem. Soc.*, 2000, **122**, 7953.
45 J. R. Fulton, A. W. Holland, D. J. Fox and R. G. Bergman, *Acc. Chem. Res.*, 2002, **35**, 44.
46 K. Murata, H. Konishi, M. Ito and T. Ikariya, *Organometallics*, 2002, **21**, 253.
47 M. D. Fryzuk, C. D. Montgomery and S. J. Rettig, *Organometallics*, 1991, **10**, 467.
48 K. Muniz, *Angew. Chem., Int. Ed.*, 2005, **44**, 6622.
49 R. Noyori, M. Kitamura and T. Ohkuma, *Proc. Natl. Acad. Sci. U. S. A.*, 2004, **101**, 5356; G. J. Kubas, *Catal. Lett.*, 2005, **104**, 79.
50 Y. Feng, M. Lail, K. A. Barakat, T. R. Cundari, T. B. Gunnoe and J. L. Petersen, *J. Am. Chem. Soc.*, 2005, **127**, 14174.
51 W. J. Tenn, K. J. H. Young, G. Bhalla, J. Oxgaard, W. A. Goddard and R. A. Periana, *J. Am. Chem. Soc.*, 2005, **127**, 14172.
52 Y. Feng, M. Lail, N. A. Foley, T. B. Gunnoe, K. A. Barakat, T. R. Cundari and J. L. Petersen, *J. Am. Chem. Soc.*, 2006, **128**, 7982.
53 T. R. Cundari, T. V. Grimes and T. B. Gunnoe, *J. Am. Chem. Soc.*, 2007, **129**, 13172.
54 (*a*) L. Maron, L. Perrin and O. Eisenstein, *J. Chem. Soc., Dalton Trans.*, 2002, 534; (*b*) L. Perrin, L. Maron and O. Eisenstein, *Inorg. Chem.*, 2002, **41**, 4355.
55 Y. Feng, T. B. Gunnoe, T. V. Grimes and T. R. Cundari, *Organometallics*, 2006, **25**, 5456.
56 W. J. Tenn, K. J. H. Young, J. Oxgaard, R. J. Nielsen, W. A. Goddard and R. A. Periana, *Organometallics*, 2006, **25**, 5173.
57 J. Oxgaard, W. J. Tenn, R. J. Nielsen, R. A. Periana and W. A. Goddard, *Organometallics*, 2007, **26**, 1565.
58 A. E. Shilov, *Activation of Saturated Hydrocarbons by Transition Metal Complexes*, D. Riedel, 1984.
59 (*a*) P. E. M. Siegbahn and R. H. Crabtree, *J. Am. Chem. Soc.*, 1996, **118**, 4442; (*b*) T. M. Gilbert, I. Hristov and T. Ziegler, *Organometallics*, 2001, **20**, 1183.
60 J. Kua, X. Xu, R. A. Periana and W. A. Goddard, *Organometallics*, 2002, **21**, 511.
61 (*a*) A. Paul and C. B. Musgrave, *Organometallics*, 2007, **26**, 793; (*b*) X. Xu, J. Kua, R. A. Periana and W. A. Goddard, *Organometallics*, 2003, **22**, 2057.
62 A. C. Cope and R. W. Siekman, *J. Am. Chem. Soc.*, 1965, **87**, 3272.
63 (*a*) A. D. Ryabov, *Chem. Rev.*, 1990, **90**, 403; (*b*) A. D. Ryabov, I. K. Sakodinskaya and A. K. Yatsimirsky, *J. Chem. Soc., Dalton Trans.*, 1985, 2629.
64 (*a*) M. Gomez, J. Granell and J. Martinez, *J. Chem. Soc., Dalton Trans.*, 1998, 37; (*b*) M. Gomez, J. Granell and M. Martinez, *Organometallics*, 1997, **16**, 2539.
65 D. L. Davies, S. M. A. Donald and S. A. Macgregor, *J. Am. Chem. Soc.*, 2005, **127**, 13754.
66 D. L. Davies, S. M. A. Donald, O. Al-Duaij, S. A. Macgregor and M. Polleth, *J. Am. Chem. Soc.*, 2006, **128**, 4210.
67 D. L. Davies, S. M. A. Donald, O. Al-Duaij, J. Fawcett, C. Little and S. A. Macgregor, *Organometallics*, 2006, **25**, 5976.
68 D. Garcia-Cuadrado, A. A. C. Braga, F. Maseras and A. M. Echavarren, *J. Am. Chem. Soc.*, 2006, **128**, 1066.

69 D. Garcia-Cuadrado, P. de Mendoza, A. A. C. Braga, F. Maseras and A. M. Echavarren, *J. Am. Chem. Soc.*, 2007, **129**, 6880.
70 S. Pascual, P. de Mendoza, A. A. C. Braga, F. Maseras and A. M. Echavarren, *Tetrahedron*, 2008, **64**, 6021.
71 M. Lafrance, S. I. Gorelsky and K. Fagnou, *J. Am. Chem. Soc.*, 2007, **129**, 14570.
72 M. Chaumontet, R. Piccardi, N. Audic, J. Hitce, J.-L. Peglion, E. Clot and O. Baudoin, *J. Am. Chem. Soc.*, 2008, **130**, 15157.
73 J. P. Stambuli, C. D. Incarvito, M. Buhl and J. F. Hartwig, *J. Am. Chem. Soc.*, 2004, **126**, 1184.
74 I. Ozdemir, S. Demir, B. Cetinkaya, C. Gourlaouen, F. Maseras, C. Bruneau and P. H. Dixneuf, *J. Am. Chem. Soc.*, 2008, **130**, 1156.
75 I. Moritani and Y. Fujiwara, *Tetrahedron Lett.*, 1967, **8**, 1119.
76 B. Biswas, M. Sugimoto and S. Sakaki, *Organometallics*, 2000, **19**, 3895.
77 Y. Musashi and S. Sakaki, *J. Am. Chem. Soc.*, 2000, **122**, 3867.
78 M. Lafrance, C. N. Rowley, T. K. Woo and K. Fagnou, *J. Am. Chem. Soc.*, 2006, **128**, 8754.
79 For reviews of direct arylation of simple arenes see ref. 5b and ref. 5c.
80 M. Lafrance and K. Fagnou, *J. Am. Chem. Soc.*, 2006, **128**, 16496.
81 See the other paper in this issue by: Y. Boutadla, D. L. Davies, A. I. Poblador-Bahamonde and S. A. Macgregor, *Dalton Trans.*, 2009, DOI: 10.1039/b905469c.
82 S. I. Gorelsky, D. Lapointe and K. Fagnou, *J. Am. Chem. Soc.*, 2008, **130**, 10848.
83 V. R. Ziatdinov, J. Oxgaard, O. A. Mironov, K. J. H. Young, W. A. Goddard and R. A. Periana, *J. Am. Chem. Soc.*, 2006, **128**, 7404.
84 D. H. Ess, S. M. Bischof, J. Oxgaard, R. A. Periana and W. A. Goddard, *Organometallics*, 2008, **27**, 6440.
85 R. Noyori, M. Yamakawa and S. Hashiguchi, *J. Org. Chem.*, 2001, **66**, 7931.
86 T. Ikariya, K. Murata and R. Noyori, *Org. Biomol. Chem.*, 2006, **4**, 393.
87 (*a*) M. Yamakawa, H. Ito and R. Noyori, *J. Am. Chem. Soc.*, 2000, **122**, 1466; (*b*) C. Hedberg, K. Kallstrom, P. I. Arvidsson, P. Brandt and P. G. Andersson, *J. Am. Chem. Soc.*, 2005, **127**, 15083.

Computational and synthetic studies on the cyclometallation reaction of dimethylbenzylamine with $[IrCl_2Cp^*]_2$: role of the chelating base†

Youcef Boutadla,[a] David L. Davies,*[a] Stuart A. Macgregor*[b] and Amalia I. Poblador-Bahamonde[b]

Received 18th March 2009, Accepted 22nd May 2009
First published as an Advance Article on the web 24th June 2009
DOI: 10.1039/b905469c

The results of a joint computational and experimental study of the cyclometallation reactions of dimethylbenzylamine (DMBA-H) with $[IrCl_2Cp^*]_2$ and a range of chelating bases are presented. With acetate, density functional theory calculations on the key intermediate, $[Ir(DMBA\text{-}H)(\kappa^2\text{-}OAc)Cp]^+$, define a two-step C–H activation process involving initial κ^2–κ^1 displacement of base to give an intermediate that is stabilized by internal H-bonding. Facile C–H bond cleavage then occurs *via* 'ambiphilic metal ligand activation' (AMLA). A similar pattern is computed for other carboxylates and bicarbonate, and in each case the ease of C–H activation is governed by the accessibility of the κ^2–κ^1 base displacement step; thus, more weakly coordinating bases promote C–H activation. For triflate, $[Ir(DMBA\text{-}H)(\kappa^1\text{-}CF_3SO_3)Cp]^+$ is more stable than its κ^2-isomer and C–H activation proceeds with a barrier of only 3.8 kcal mol^{-1}. Experimental studies confirm that a range of carboxylates and triflate can effect cyclometallation; however, reactivity patterns are not consistent with the computed C–H activation barriers. Instead, the role of base in opening the $[IrCl_2Cp^*]_2$ dimer and subsequent formation of the $[Ir(DMBA\text{-}H)(base)Cp^*]^+$ intermediates appears crucial. Calculations indicate these processes are far more favourable for acetate than for triflate.

Introduction

Cyclometallation reactions are of current interest for the insight they bring to the general topic of C–H activation.[1] Moreover, cyclometallation is now being exploited in catalytic schemes leading to C–H bond functionalisation,[2] in particular intramolecular arylation processes.[3,4] Much of the progress in this area has been based on Pd systems and we[5] have provided a computational analysis using density functional theory (DFT) of the classic cyclometallation reaction of $[Pd(OAc)_2]$ with DMBA-H[6] (DMBA-H = dimethylbenzylamine). A number of related computational studies have considered C–H activation in the context of Pd-catalysed arylation reactions and have shown that the base plays a key role in this process.[3,4b,d,7] Experimentally, the nature and amount of the base employed is often crucial.[4c]

In 2003, one of us reported the cyclometallation reaction of DMBA-H with $[IrCl_2Cp^*]_2$.[8,9] Subsequently we used DFT calculations to characterise three different pathways for intramolecular C–H activation in the model intermediate $[Ir(DMBA\text{-}H)(\kappa^2\text{-}OAc)Cp]^+$.[10] Of these, the most accessible, Pathway I ($\Delta E^{\ddagger}$ = +16.0 kcal mol^{-1}, see Scheme 1), corresponded to a one-step process involving a 6-membered transition state, where dissociation of one acetate arm is coupled to proton transfer from DMBA-H to the now free arm of acetate. This transition state exhibits a C–H · · · M agostic interaction and an intramolecular C–H · · · O H-bond and both features were found to be important in facilitating C–H activation.[11] Thus the agostic interaction polarises the C–H bond and so enhances the acidity of the hydrogen which is then readily transferred to acetate. Similarly, strong H-bonding creates a more electron rich C–H bond which in turn facilitates an agostic interaction. These two components act synergically to facilitate C–H bond cleavage *via* an ambiphilic metal ligand activation process (AMLA).[12]

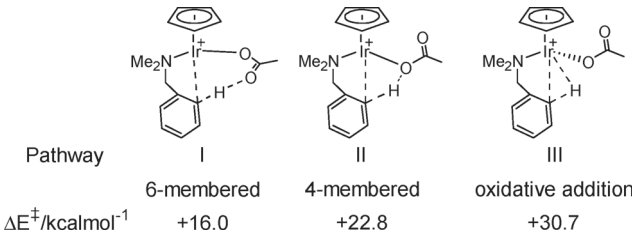

Scheme 1

The two higher energy routes for intramolecular C–H activation, Pathways II and III, both involve initial κ^2–κ^1 displacement of acetate such that the free arm is remote from the reacting C–H bond. This resulted in the formation of an intermediate species from which C–H activation can either occur *via* a 4-membered transition state with H-transfer to the Ir-bound oxygen (Pathway II, $\Delta E^{\ddagger}$ = +22.8 kcal mol^{-1}), or *via* an oxidative addition process (Pathway III, $\Delta E^{\ddagger}$= +30.7 kcal mol^{-1}).

In this paper, we focus on the role played by the chelating base in promoting intramolecular C–H activation and have studied a series of $[Ir(DMBA\text{-}H)(\kappa^2\text{-}RCO_2)Cp]^+$ carboxylate complexes, where R = Me, Ph, CF_3 and CCl_3, as well as the bicarbonate (R = OH) and triflate analogues. During this work, we characterized new variants of the reaction profiles described above for $[Ir(DMBA\text{-}H)(\kappa^2\text{-}OAc)Cp]^+$. These feature a slightly

[a]*Department of Chemistry, University of Leicester, Leicester, UK LE1 7RH. E-mail: dld03@le.ac.uk; Fax: +44 (0)116 252 3789; Tel: +44 (0)116 252 2092*
[b]*School of Engineering & Physical Sciences, Heriot-Watt University, Edinburgh, UK EH14 4AS. E-mail: s.a.macgregor@hw.ac.uk; Fax: +44 (0)131 451 3180; Tel: +44 (0)131 451 8031*
† Electronic supplementary information (ESI) available: Computed structures and energies for all species. See DOI: 10.1039/b905469c

different conformation of the DMBA-H ligand which leads to a stabilization of all stationary points along the three computed pathways. Pathway I *via* a 6-membered transition state remains the most favoured mechanism, but a useful new feature is that C–H activation *via* Pathway I can be a two step process. Crucially, the rate limiting step corresponds to the initial displacement of one arm of the acetate ligand by the aryl moiety and the subsequent C–H bond cleavage proceeds with a minimal barrier. The identification of two distinct steps has allowed us to gain better insight into the factors that control these C–H activation reactions. In the following we first present details of these new pathways for the [Ir(DMBA-H)(κ²-OAc)Cp]⁺ system before moving on to assess the effects of changing the chelating base ligand on the reaction energetics.

Results and discussion

[Ir(DMBA-H)(κ²-OAc)Cp]⁺

The reaction profile computed for C–H activation in [Ir(DMBA-H)(κ²-OAc)Cp]⁺, $\mathbf{1}_{Me}$, *via* Pathway I is shown in Fig. 1. The structure of $\mathbf{1}_{Me}$ is the same as that computed previously,[10] however in the present study a new transition state corresponding to displacement of the proximal (Ir–O1) acetate arm was located ($\mathbf{TS(1–2)}_{Me}$, E = +13.4 kcal mol⁻¹). This reflects a different angle

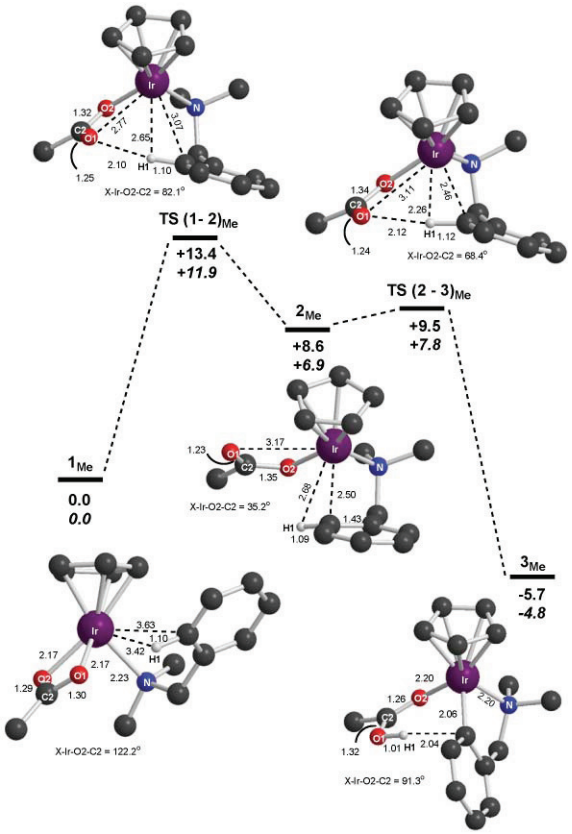

Fig. 1 Computed reaction profile (kcal mol⁻¹) for C–H activation in [Ir(DMBA-H)(κ²-OAc)Cp]⁺, $\mathbf{1}_{Me}$, with selected geometrical parameters (Å and °). X is the centroid of the Cp ring and non-participating H atoms are omitted for clarity. Energies corrected for solvent effects (CH_2Cl_2, PCM method) are given in italics.

of approach of the aryl moiety toward acetate which results in both an increase of the Ir–O1 distance (from 2.17 Å in $\mathbf{1}_{Me}$ to 2.77 Å in $\mathbf{TS(1–2)}_{Me}$) and rotation about the Ir–O2 bond (X–Ir–O2–C2 = 122.2° in $\mathbf{1}_{Me}$ *cf.* 82.1° in $\mathbf{TS(1–2)}_{Me}$, where X = the Cp ring centroid). Proton transfer does not occur at this point, but instead $\mathbf{TS(1–2)}_{Me}$ links to a new intermediate, $\mathbf{2}_{Me}$ (E = +8.6 kcal mol⁻¹), where further rotation about Ir–O2 has occurred (X–Ir–O2–C2 = 35.2°). O1 is therefore remote from both Ir and the target C1–H1 bond (Ir···O1 = 3.17 Å; H1···O1 = 3.16 Å) and H1 is in fact much closer to the Ir-bound oxygen (H1···O2 = 2.27 Å). As a result, $\mathbf{2}_{Me}$ appears ideally set up for proton transfer to O2 *via* a 4-membered transition state, although we will show below that this is a high energy process and that proton transfer to O1 *via* a 6-membered transition state is still preferred. The acetate ligand itself exhibits very different C–O bond lengths (C2–O2 = 1.35 Å, C2–O1 = 1.23 Å compared to *ca.* 1.30 Å in $\mathbf{1}_{Me}$) indicative of enhanced single and double bond character, respectively. The shortest contacts between Ir and the aryl moiety involve the C_{ipso}–C1 bond (Ir···C_{ipso} = 2.70 Å; Ir···C1 = 2.50 Å) and an elongation of the C_{ipso}–C1 distance, from 1.41 Å in **1** to 1.43 Å, suggests a degree of η²-interaction in $\mathbf{2}_{Me}$ (other C–C bonds are in the range 1.40–1.42 Å).

To effect C–H activation in $\mathbf{2}_{Me}$ the free acetate arm must approach the C1–H1 bond by rotation about Ir–O2 and in the resultant transition state ($\mathbf{TS(2–3)}_{Me}$, E = +9.5 kcal mol⁻¹) the X–Ir–O2–C2 torsion angle increases to 68.4°. The approach of the aryl moiety toward the Ir centre also results in a weak agostic interaction (Ir···H = 2.26 Å; Ir···C1 = 2.46 Å; C1···H1 = 1.12 Å) that in turn promotes a C1–H1···O1 H bonding interaction (H1···O1 = 2.12 Å). $\mathbf{TS(2–3)}_{Me}$ therefore exhibits both characteristic features of ambiphilic metal ligand activation and leads to the C–H activated species, $\mathbf{3}_{Me}$ (E = –5.7 kcal mol⁻¹).

Fig. 1 illustrates the two-step nature of C–H activation in $\mathbf{1}_{Me}$ and shows that the overall rate determining step for this process in $\mathbf{1}_{Me}$ will correspond to the initial displacement of acetate to form $\mathbf{2}_{Me}$. This occurs with a computed activation barrier of only 13.4 kcal mol⁻¹. Remarkably, cleavage of the C–H bond in $\mathbf{2}_{Me}$ proceeds with a barrier of less than 1 kcal mol⁻¹, despite the absence of any apparent pre-activation in this species. Thus, breaking of the C–H bond is not the difficult step in these intramolecular C–H activation processes. Instead, it is establishing the correct framework for CH cleavage, *i.e.* making available an intramolecular base and allowing the substrate to approach the metal centre, which incurs the major activation barrier.

Fig. 1 also gives relative energies with inclusion of the effects of solvent polarity (CH_2Cl_2, PCM method, data in italics) and these indicate a reduction in the barrier *via* $\mathbf{TS(1–2)}_{Me}$ of 1.5 kcal mol⁻¹. In contrast, the final product $\mathbf{3}_{Me}$ is destabilized by 1 kcal mol⁻¹, although C–H activation remains exothermic.

Compared to our previous study,[10] the new Pathway I provides a slightly more accessible route for C–H activation ($\Delta E^{\ddagger}$ = +13.4 kcal mol⁻¹ *cf.* +16.0 kcal mol⁻¹) and leads to a more stable initial product (ΔE = –5.7 kcal mol⁻¹ *cf.* –2.4 kcal mol⁻¹). These changes arise from an alternative orientation of the DMBA-H ligand due to different degrees of rotation about the Ir–N and C_{ipso}–C_{benzyl} bonds.[13] A similar stabilization of the highest lying transition state along Pathway II was also found ($\mathbf{TS(2'–3')}_{Me}$, E = +19.8 kcal mol⁻¹ *cf.* 22.8 kcal mol⁻¹, see Fig. 2). Location of an analogous oxidative addition transition state with the new

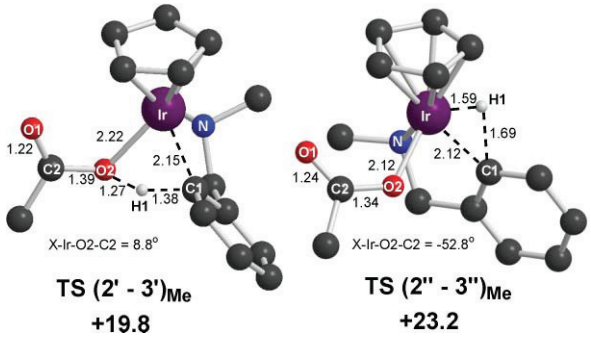

Fig. 2 Computed C–H activation transition states along Pathway II (4-membered, $\mathbf{TS(2'–3')}_{Me}$) and Pathway III (oxidative addition, $\mathbf{TS(2''–3'')}_{Me}$). Energies (kcal mol^{-1} *cf.* $\mathbf{1}_{Me}$) and selected distances (Å) are given, and non-participating H atoms are omitted for clarity.

orientation of the DMBA-H ligand failed, as this placed the C1–H1 bond too close to O2 to avoid converging on $\mathbf{TS(2'–3')}_{Me}$. Instead a new oxidative addition step was defined where the Ir–H bond develops *trans* to the acetate moiety *via* $\mathbf{TS(2''–3'')}_{Me}$ (E = +23.2 kcal mol^{-1}, Fig. 2). This is over 7 kcal mol^{-1} more stable than the previous result (Scheme 1), however, $\mathbf{TS(2''–3'')}_{Me}$ remains significantly higher in energy than either $\mathbf{TS(2–3)}_{Me}$ or $\mathbf{TS(2'–3')}_{Me}$. Full details of the other stationary points along Pathways II and III are given in the ESI.†

The major new feature in the present study is the location of κ^1-intermediate $\mathbf{2}_{Me}$, which appears to be ideally set up for proton transfer onto the Ir-bound oxygen. Moreover, computed natural atomic charges show that O2 actually carries the larger negative charge: –0.70 compared to –0.61 on O1. This larger charge is consistent with O2 being formally anionic compared to the neutral carbonyl character of O1 (as suggested by the C2–O1/2 distances noted above) and so may explain why H1 lies closer to O2 rather than O1 in $\mathbf{2}_{Me}$. Despite these features, the 4-membered transition state $\mathbf{TS(2'–3')}_{Me}$ remains more than 11 kcal mol^{-1} above $\mathbf{2}_{Me}$ while the barrier to C–H activation *via* the 6-membered transition state $\mathbf{TS(2–3)}_{Me}$ is only 0.9 kcal mol^{-1}. One factor that may promote Pathway I over Pathway II is the more flexible 6-membered structure in $\mathbf{TS(1–2)}_{Me}$ compared to the rather constrained 4-membered process in $\mathbf{TS(2'–3')}_{Me}$ and computed energy profiles for rotation about the Ir–O2 bond certainly indicate this is very facile. Recent studies by Ess and co-workers have also highlighted the greater deformation required of the acetate ligand to reach 4-membered transition states for the intermolecular C–H activation of benzene and methane.[14] Although this can also seen here (the C2–O1 and C2–O2 are, respectively, shorter and longer in $\mathbf{TS(2'–3')}_{Me}$ than in $\mathbf{TS(2–3)}_{Me}$) this effect it is not so marked, possibly due to the intramolecular nature of the C–H activation process under consideration.

Variation of the chelating base ligand

C–H activation reaction profiles were computed for [Ir(DMBA-H)(κ^2-RCO$_2$)Cp]$^+$ species, $\mathbf{1}_R$, where R = CCl$_3$, Ph, CF$_3$ and OH. Computation of Pathways I, II and III showed that Pathway I remains the most accessible route in each case and so only the results for this process will be presented. For each system, the rate-determining step for C–H activation along Pathway I corresponds to the κ^2–κ^1 displacement of the chelating base *via* $\mathbf{TS(1–2)}_R$. The global picture is therefore similar to that already described for the acetate system, however, for each base subtle variations in behaviour were seen and these will be described in turn below. Key geometrical parameters and energies for $\mathbf{TS(1–2)}_R$, $\mathbf{2}_R$ and $\mathbf{TS(2–3)}_R$ are shown in Fig. 3, where only the six atoms directly participating in C–H activation are highlighted. These positions encompass the greatest variation in geometry and so the complete structures, which otherwise closely resemble their acetate analogues, are reserved for the ESI,† along with details of the various reactant ($\mathbf{1}_R$) and product ($\mathbf{3}_R$) species.

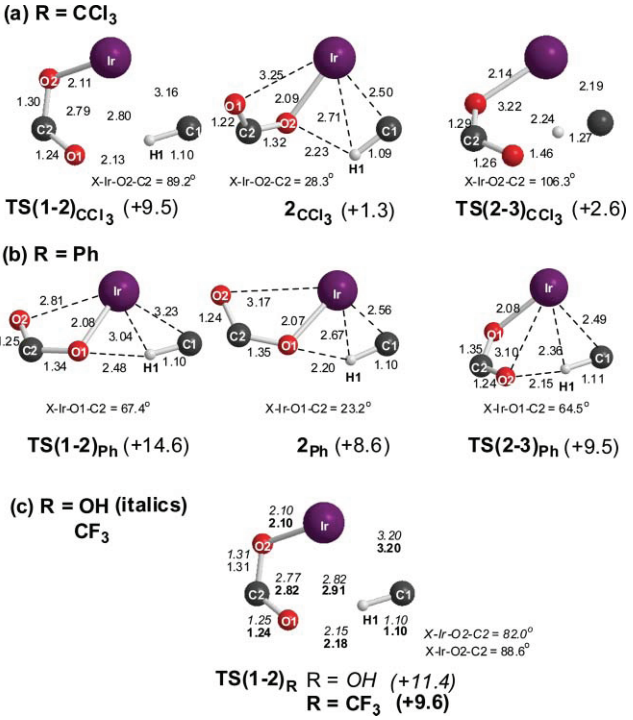

Fig. 3 Computed geometrical parameters (Å and °) for C–H activation in [Ir(DMBA-H)(κ^2-RCO$_2$)Cp]$^+$ (R = CCl$_3$, Ph, CF$_3$ and OH) highlighting the six atoms directly involved. X is the Cp ring centroid and energies (kcal mol^{-1}) are quoted relative to the appropriate reactant in each case.

Of the four [Ir(DMBA-H)(κ^2-RCO$_2$)Cp]$^+$ systems that with R = CCl$_3$ adheres most closely to the behaviour seen above with acetate. Thus, displacement of the Ir–O1 bond occurs with a similar movement of the carboxylate moiety and rotation about the Ir–O2 bond (X–Ir–O2–C2 = 89.2° in $\mathbf{TS(1–2)}_{CCl3}$ and 28.3° in $\mathbf{2}_{CCl3}$). When R = Ph an unexpected result was obtained as the approach of the aryl moiety toward the Ir centre resulted in the displacement of the distal Ir–O2 bond (Fig. 3b). All attempts to find a transition state corresponding to Ir–O1 bond elongation led instead to the C–H activation transition state $\mathbf{TS(2–3)}_{Ph}$. The movement of the benzoate moiety is therefore best quantified by the X–Ir–O1–C2 torsion which decreases from 120.3° in $\mathbf{1}_{Ph}$ through 67.4° in $\mathbf{TS(1–2)}_{Ph}$ to 23.2° in $\mathbf{2}_{Ph}$. For R = Ph and CCl$_3$ the κ^1-OC$_2$R intermediates both closely resemble $\mathbf{2}_{Me}$, with H1 being closer to the Ir-bound oxygen ($\mathbf{2}_{CCl3}$: H1···O2 = 2.23 Å; $\mathbf{2}_{Ph}$: H1···O1 = 2.20 Å). There is still only minimal Ir···C1–H1 agostic bonding at this point and the structures differ primarily in the orientation of the carboxylate moiety. When R = Ph significant rotation about the Ir–O1 bond is required to access the C–H bond

cleavage transition state. However, as mentioned above, this is a low energy process and ultimately the structure of $\mathbf{TS(2–3)_{Ph}}$ is essentially the same as $\mathbf{TS(2–3)_{Me}}$ and proton transfer proceeds with a barrier of less than 1 kcal mol^{-1}. $\mathbf{TS(2–3)_{CCl3}}$ exhibits a later transition state geometry with a longer C1 $\cdots$ H1 distance of 1.27 Å and a shorter O1 $\cdots$ H1 distance of 1.46 Å, although the barrier to proton transfer is still minimal (1.3 kcal mol^{-1}).

The remaining two systems also react *via* rate-limiting κ^2–κ^1 displacement of the chelating base and the structures of $\mathbf{TS(1–2)_{OH}}$ and $\mathbf{TS(1–2)_{CF3}}$ are very similar to $\mathbf{TS(1–2)_{Me}}$ (see Fig. 3c). Characterization of these transition states did lead to intermediate structures analogous to $\mathbf{2_{Me}}$. However, in these cases, inclusion of the zero-point energy correction caused the enthalpies of these intermediates to lie above those of the subsequent proton transfer transition states. Thus the very small barriers for proton transfer seen for R = Me, CCl_3 and Ph in fact disappear all together for R = CF_3 and OH. We therefore consider that $\mathbf{TS(1–2)_{OH}}$ and $\mathbf{TS(1–2)_{CF3}}$ lead directly to the C–H activation products and so have only shown these stationary points in Fig. 3c.

The energetics of C–H activation computed for all five [Ir(DMBA-H)(κ^2-RCO_2)Cp]$^+$ species are summarized in Table 1. Barriers to κ^2–κ^1 displacement are highest for $MeCO_2^-$ and $PhCO_2^-$ and lowest for $CCl_3CO_2^-$ and $CF_3CO_2^-$ and this reflects the relative coordinating abilities of the various ligands. An approximate correlation between barrier height and the proton accepting ability of the free base is also seen, where the latter is expressed as the negative of the pK_a of the conjugate acids (final column, Table 1). The relative energies of the intermediates $\mathbf{2_R}$ also reflect the coordinating ability of the chelating base, with κ^2–κ^1 displacement being much easier for $CCl_3CO_2^-$ ($\Delta E_{\mathbf{1}\rightarrow\mathbf{2}} = +1.3$ kcal mol^{-1}) than for $PhCO_2^-$ ($\Delta E_{\mathbf{1}\rightarrow\mathbf{2}} = +10.1$ kcal mol^{-1}) or $CH_3CO_2^-$ ($\Delta E_{\mathbf{1}\rightarrow\mathbf{2}} = +8.6$ kcal mol^{-1}).

As explained above, distinct barriers to C–H bond cleavage were only found when R = Me, Ph or CCl_3, although even here these are minimal (< 1.5 kcal mol^{-1}). No correlation with the nature of the chelating base is apparent, despite a variation of over 5 orders of magnitude in the proton accepting ability of the free anions. To investigate this we have compared the properties of the κ^1-base moieties in $\mathbf{2_{Me}}$, $\mathbf{2_{CCl3}}$ and $\mathbf{2_{Ph}}$ with the free anions (see Fig. 4). In the $\mathbf{2_R}$ species, the pendant C–O bond is approximately 0.03 Å shorter than the equivalent bonds in the anions, suggestive of enhanced carbonyl character and decreased basicity. Moreover, computed natural atomic charges show a reduction in negative charge associated with the pendant oxygen, $q(O_1)$, in $\mathbf{2_R}$ compared to the free anions, $q(O_A)$. For the free anions $q(O_A)$ follows the trend R = CH_3 > Ph >> CCl_3, consistent with the $-pK_a$ values and the expected donor capacities of the R groups. The difference

Table 1 Computed energetics (kcal mol^{-1}) for C–H activation in [Ir(DMBA-H)(κ^2-RCO_2)Cp]$^+$ species, relative to the appropriate reactant set to zero in each case. $-pK_a$ values for the conjugate carboxylic acids are also indicated.[15]

RCO_2^-	$\mathbf{TS(1–2)_R}$	$\mathbf{2_R}$	$\mathbf{TS(2–3)_R}$	$\mathbf{3_R}$	$-pK_a$
$CH_3CO_2^-$	13.4	8.6	9.5	–5.7	–4.76
$PhCO_2^-$	14.6	10.1	11.0	–5.7	–4.31
$HOCO_2^-$	11.4	—	—	–5.9	–3.83
$CCl_3CO_2^-$	9.5	1.3	2.6	–4.3	–0.65
$CF_3CO_2^-$	9.6	—	—	–4.3	+0.23

	C-O_A	q(O_A)	C-O_1	q(O_1)
R = Me	1.27	-0.76	1.23	-0.61
R = Ph	1.27	-0.73	1.24	-0.62
R = CCl_3	1.24	-0.64	1.22	-0.57

Fig. 4 Computed C–O distances (Å) and natural atomic charges on oxygen for intermediates $\mathbf{2_R}$ and for the equivalent free anions (average values are given for the latter).

in computed natural atomic charge on O1 between the free anions and $\mathbf{2_R}$ is much greater for R = Me ($\Delta q = 0.15$) and Ph ($\Delta q = 0.11$) than for R = CCl_3 ($\Delta q = 0.07$) and as a result the total range of 0.12 computed for $q(O_A)$ in the free anions reduces to only 0.05 for $q(O_1)$ in $\mathbf{2_R}$. The effect of the R group on the basicity of the accepting oxygen atom in $\mathbf{2_R}$ is therefore much less significant than in the free anions and this accounts for the similar behaviour computed for what initially appears to be a wide range of chelating bases. We noted above that the weakest base of the three, $CCl_3CO_2^-$, produces a later transition state structure for the C–H activation step with a greater C–H $\cdots$ Ir agostic interaction and a higher activation barrier. While this is consistent with the trend in $q(O_1)$ (R = Me ≈ Ph > CCl_3) the differences in the barrier are rather small ($\Delta E^{\ddagger} = 0.9$ kcal mol^{-1} for R = Me or Ph *cf.* 1.3 kcal mol^{-1} for R = CCl_3).

In contrast to the barriers for C–H bond cleavage, the energy change associated with this step ($\Delta E_{\mathbf{2}\rightarrow\mathbf{3}}$) does correlate with $-pK_a$, and is most exothermic for $CH_3CO_2^-$ and $PhCO_2^-$ ($\Delta E_{\mathbf{2}\rightarrow\mathbf{3}} = -14.3$ kcal mol^{-1} and -15.8 kcal mol^{-1}, respectively) than for $CCl_3CO_2^-$ ($\Delta E_{\mathbf{2}\rightarrow\mathbf{3}} = -5.6$ kcal mol^{-1}). Thus, a more favorable (in a thermodynamic sense) C–H bond cleavage (**2** → **3**) is associated with a less accessible κ^2–κ^1 displacement (**1** → **2**), and *vice versa*. The cancellation of these two effects accounts for the remarkable lack of variation in the overall energetics of C–H activation in $\mathbf{1_R}$ to give $\mathbf{3_R}$ across the whole range of bases studied ($\Delta E = -5.1 \pm 0.8$ kcal mol^{-1}).

Overall, C–H activation in these [Ir(DMBA-H)(κ^2-RCO_2)Cp]$^+$ species is characterised by a low energy barrier corresponding to κ^2–κ^1 displacement of the chelating base and follows the trend R = CF_3 ≈ CCl_3 < OH < CH_3 < Ph. The reaction is slightly exothermic in all cases and shows minimal variation in this regard with respect to the chelating base involved. Including solvent polarity effects *via* PCM calculations did not affect these trends significantly with all the systems behaving in a similar way to that described for acetate above.

[Ir(DMBA-H)(κ^2-CF_3SO_3)Cp]$^+$, 4

The identification of κ^2–κ^1 displacement of base as the rate determining step for C–H activation, along with the realization that the proton accepting ligand may not need to be strongly basic, led us to target triflate as a co-ligand in intramolecular C–H activation (Fig. 5). As anticipated with such a weakly coordinating species, the κ^2–κ^1 displacement step is very facile and has the smallest barrier computed so far ($\Delta E^{\ddagger} = 7.0$ kcal mol^{-1}). Moreover, the intermediate formed, [Ir(DMBA-H)(κ^1-CF_3SO_3)Cp]$^+$, **5**, is actually 3.0 kcal mol^{-1} more stable than κ^2-**4**. The geometry of **5**

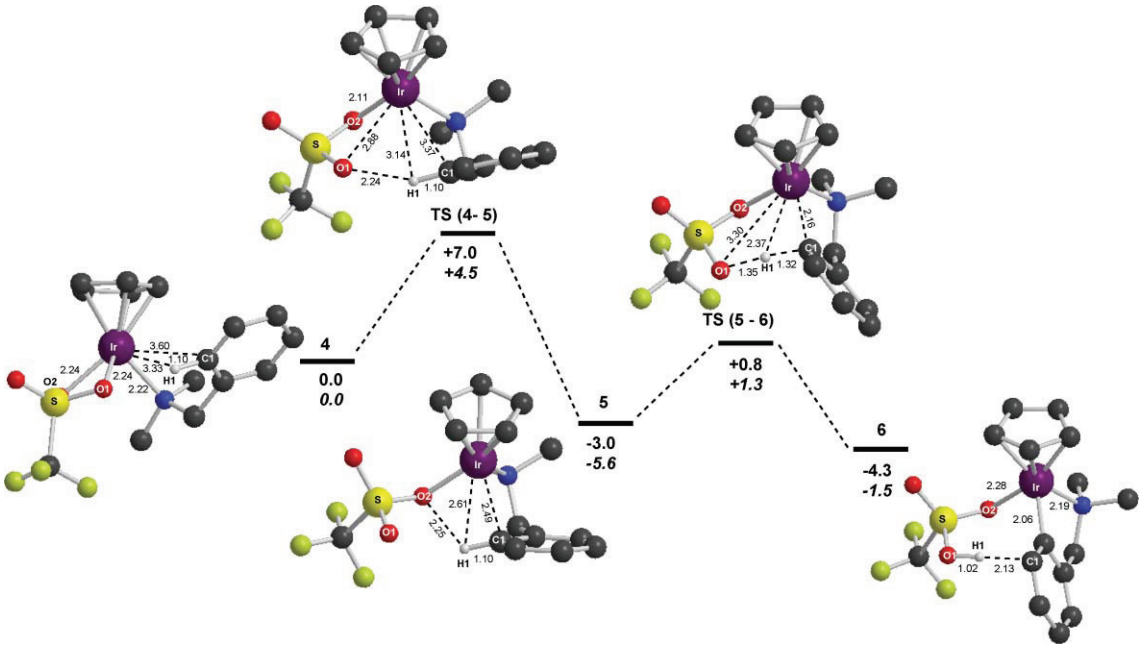

Fig. 5 Computed reaction profile (kcal mol^{-1}) for C–H activation in [Ir(DMBA-H)(κ^2-CF_3SO_3)Cp]$^+$, **4**, with selected geometrical parameters (Å and °). Energies corrected for solvent effects (CH_2Cl_2, PCM method) are given in italics, and non-participating H atoms are omitted for clarity.

resembles those of $\mathbf{2}_{Me}$, $\mathbf{2}_{Ph}$ and $\mathbf{2}_{CCl3}$, in having a short contact to the Ir-bound oxygen (H1 $\cdots$ O2 = 2.25 Å) and no significant agostic lengthening of the C1–H1 bond. The weakly basic nature of triflate means the subsequent C–H activation has a relatively high barrier of 3.8 kcal mol^{-1}, albeit still small in an absolute sense. As seen with the $Cl_3CCO_2^-$ system a higher barrier corresponds to a later transition state geometry and **TS(5–6)** features both the longest C1 $\cdots$ H1 distance (1.32 Å) and the shortest O1 $\cdots$ H1 distance (1.35 Å) of any of the C–H activation transition states computed so far. Despite this, **TS(5–6)** is over 6 kcal mol^{-1} more stable than **TS(4–5)** and in this sense the triflate system behaves in an analogous fashion to the carboxylate and bicarbonate analogues.

Unlike these analogues, however, in this case the κ^1-isomer, **5**, would be expected to be the dominant form in solution. As such, the C–H activation step becomes rate-determining with $\Delta E^{\ddagger}$ = 3.8 kcal mol^{-1}, the smallest value for the overall barrier found so far. PCM solvent corrections (italics, Fig. 5) do increase $\Delta E^{\ddagger}$ to 6.9 kcal mol^{-1}; moreover the formation of **6** from **5**, exothermic by 1.5 kcal mol^{-1} in the gas-phase, becomes endothermic by 4.1 kcal mol^{-1} in solution. Despite this, the triflate system remains a promising target for experiment as the barrier to C–H activation is still small and the endothermicity of this process should be overcome by displacement of CF_3SO_3H by Cl^- in the final step of the cyclometallation reaction (see below). We therefore turned our attention to the experimental investigation of this reaction.

Experimental studies.

Cyclometallation reactions were carried out through the room temperature reaction of $[IrCl_2Cp^*]_2$ with 1.25 equivalents (per iridium) of both dimethylbenzylamine and the relevant sodium carboxylate, sodium triflate or sodium bicarbonate in dichloromethane.[16] Reactions were run for 17 h and then filtered through celite to remove excess salts, and rotary evaporated to dryness. The solid was redissolved in $CDCl_3$ and mesitylene was added as an internal NMR standard and the yield of the product, [Ir(DMBA)(Cl)Cp*], was estimated by integration. The highest yield was for acetate (65%) then trifluoroacetate (55%) with trichloroacetate (28%) and benzoate (29%) approximately the same. Sodium triflate gave very little conversion after 17 h, however if left longer a reasonable yield of 50% was produced after 4 d. Sodium bicarbonate gave no product even after several days.

The overall rate of formation of the cyclometallated products does not follow a simple relationship with the activation energies computed above for C–H activation in [Ir(DMBA-H)(κ^2-RCO_2)Cp]$^+$ ($\mathbf{2}_R$) and [Ir(DMBA-H)(κ^1-CF_3SO_3)Cp]$^+$ (**5**). In particular, the reaction with acetate, which has the second highest computed barrier to C–H activation, is actually most efficient, while that with triflate, predicted to have the lowest barrier, is very slow. This indicates that C–H activation is not the rate determining step of the overall reaction. Additional steps that need to be considered are the initial opening of the $[IrCl_2Cp^*]_2$ dimer and the introduction of DMBA-H and the chelating base to the metal centre. We have previously shown that DMBA-H does not react with the $[IrCl_2Cp^*]_2$ dimer in absence of acetate;[8] moreover for the cyclometallation of 2-substituted pyridines, reaction of the $[IrCl_2Cp^*]_2$ dimer with acetate occurs prior to coordination of the pyridine.[17] The base therefore plays a dual role in these reactions, inducing dimer opening and acting as an intramolecular base for C–H activation.

In order to assess these additional steps we computed energies for [$IrCl_2$(κ^1-base)Cp]$^-$ and [IrCl(κ^2-base)Cp] for the extreme cases where the base is either $CH_3CO_2^-$ or $CF_3SO_3^-$. These complexes represent the likely initial product of dimer opening and one possible intermediate on the pathway to formation of $\mathbf{2}_{Me}$/**5**, respectively. Combining these results with those for C–H activation in Fig. 1 and 5, and the computed energy of the experimentally-observed cyclometallation product, [IrCl(DMBA)Cp], allowed us

to construct reaction profiles for both systems (see Fig. 6). The involvement of free anionic bases and Cl^- makes the inclusion of CH_2Cl_2 solvation *via* the PCM method essential and so only the solvent-corrected data are presented.

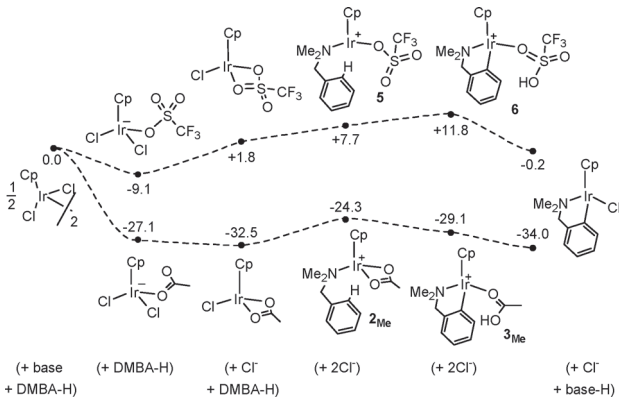

Fig. 6 Computed energies (kcal mol^{-1}) for key intermediates in the cyclometallation of DMBA-H by $[IrCl_2Cp]_2$ in the presence of $MeCO_2^-$ (bottom) or $CF_3SO_3^-$ (top). All energies include a correction for solvation effects (CH_2Cl_2, PCM method). See Fig. 1 and 5 for full details of the C–H activation steps.

Fig. 6 shows that initial dimer opening is significantly more favourable for acetate ($\Delta E = -27.1$ kcal mol^{-1}) than for triflate ($\Delta E = -9.1$ kcal mol^{-1}). For the acetate system, formation of $\mathbf{2_{Me}}$ is then slightly uphill ($E = -24.3$ kcal mol^{-1}) but is followed by exothermic C–H activation and displacement of HOAc by Cl^- that make the overall process very favourable ($\Delta E = -34.0$ kcal mol^{-1}). In contrast, with triflate the formation of **5** and C–H activation are uphill events such that **6** lies 11.8 kcal mol^{-1} above the reactants. The final displacement of CF_3SO_3H by Cl^- is thermodynamically favourable, but the overall reaction remains approximately thermo-neutral ($\Delta E = -0.2$ kcal mol^{-1}). The approximations inherent in the PCM approach mean the absolute energies in Fig. 6 should be treated with caution, especially for small anions where specific solvation will be particularly important. However, the computed trends should be more secure and on this basis the results are consistent with the much more efficient reaction seen experimentally with acetate rather than with triflate.[18] Analogous calculations on the remaining carboxylates and bicarbonate showed behaviour intermediate to that computed with acetate and triflate (see ESI).† The failure to observe cyclometallation with bicarbonate therefore appears anomalous. However, a further complicating factor is that these reactions are heterogeneous, in that not all the sodium salts dissolve in dichloromethane. Indeed, the reaction with bicarbonate is the only case in which unreacted $[IrCl_2Cp^*]_2$ is the sole {Cp*Ir} species observed by ^1H NMR spectroscopy.

Conclusions

Density functional theory calculations have been employed to study the role of chelating base, RCO_2^- (R = Me, CCl_3, CF_3, OH, Ph), in the cyclometallation reactions of DMBA-H with $[IrCl_2Cp^*]_2$. Calculations on C–H activation in $[Ir(DMBA\text{-}H)(\kappa^2\text{-}MeCO_2)Cp]^+$ define a two-step process involving initial κ^2–κ^1 displacement of acetate followed by facile C–H bond cleavage. Further calculations show that C–H activation is controlled by the ease of base displacement and so higher activation barriers are computed with more strongly coordinating bases (R = Me, Ph). For R = CF_3 and OH, C–H bond cleavage occurs without a barrier upon base displacement. In cases where an $[Ir(DMBA\text{-}H)(\kappa^1\text{-}RCO_2)Cp]^+$ intermediate was located (R = Me, Ph, CCl_3) the basicity of the free base is shown to be significantly attenuated by binding to the metal centre. For the analogous triflate system $[Ir(DMBA\text{-}H)(\kappa^1\text{-}CF_3SO_3)Cp]^+$, **5**, was computed to be more stable than its κ^2-isomer and C–H activation proceeds with a barrier of only 3.8 kcal mol^{-1}. The counter-directing effects of coordination strength and basicity mean that the overall energy associated with C–H activation in these species is remarkably insensitive to the intramolecular base employed.

Parallel synthetic studies confirm the ability of a range of chelating bases, including triflate, to effect cyclometallation. However, no simple correlation between reactivity and the computed C–H activation barriers is seen, suggesting that this process is not rate determining in these systems. Instead PCM calculations suggest that opening the $[IrCl_2Cp^*]_2$ dimer and the subsequent formation of $[Ir(DMBA\text{-}H)(base)Cp^*]^+$ intermediates control reactivity; these steps are much more favourable for acetate compared to triflate.

The C–H activation reactions computed for the $[Ir(DMBA\text{-}H)(base)Cp]^+$ systems are prime examples of ambiphilic metal ligand assistance (AMLA),[11] where the electrophilic metal centre acts in a concerted fashion with an intramolecular base to effect C–H bond cleavage. The fact that such weak bases as triflate can promote this reaction underlines the powerful synergy the metal and ligand bring to bear on this process.

Computational details

All geometries were optimised without constraints using Gaussian 03, revision C.02[19] employing the BP86 functional.[20] The SDD relativistic ECPs and associated basis sets were used for Ir,[21] while 6–31G** basis sets were employed for all other atoms.[22] Stationary points were confirmed as either minima or transition states through analytical frequency calculations and characterised through IRC calculations and subsequent geometry optimisation. Solvent effects were assessed through polarised continuum model (PCM) calculations and employed UFF radii.

Acknowledgements

We thank the EPSRC for funding (AIPB, YB) and Heriot-Watt University and the University of Leicester for support.

Notes and references

1 (*a*) R. G. Bergman, *Nature*, 2007, **446**, 391; (*b*) R. H. Crabtree, *J. Chem. Soc., Dalton Trans.*, 2001, 2437; (*c*) R. H. Crabtree, *J. Organomet. Chem.*, 2004, **689**, 4083; (*d*) J. A. Labinger and J. E. Bercaw, *Nature*, 2002, **417**, 507; (*e*) A. S. Goldman and K. I. Goldberg, in *Activation and Functionalization of C–H Bonds*, Washington DC, 2004; (*f*) A. E. Shilov and G. B. Shul'pin, *Chem. Rev.*, 1997, **97**, 2879.

2 (*a*) R. B. Bedford, *Chem. Commun.*, 2003, 1787; (*b*) F. Kakiuchi and S. Murai, *Acc. Chem. Res.*, 2002, **35**, 826; (*c*) V. Ritleng, C. Sirlin and M. Pfeffer, *Chem. Rev.*, 2002, **102**, 1731; (*d*) A. R. Dick and M. S. Sanford, *Tetrahedron*, 2006, **62**, 2439; (*e*) C. H. Jun, C. W. Moon and D. Y. Lee, *Chem.–Eur. J.*, 2002, **8**, 2423.

3 (*a*) D. Garcia-Cuadrado, A. A. C. Braga, F. Maseras and A. M. Echavarren, *J. Am. Chem. Soc.*, 2006, **128**, 1066; (*b*) D. Garcia-Cuadrado, P. de Mendoza, A. A. C. Braga, F. Maseras and A. M. Echavarren, *J. Am. Chem. Soc.*, 2007, **129**, 6880; (*c*) S. Pascual, P. de Mendoza, A. A. C. Braga, F. Maseras and A. M. Echavarren, *Tetrahedron*, 2008, **64**, 6021; (*d*) M. Lafrance, S. I. Gorelsky and K. Fagnou, *J. Am. Chem. Soc.*, 2007, **129**, 14570; (*e*) M. Chaumontet, R. Piccardi, N. Audic, J. Hitce, J.-L. Peglion, E. Clot and O. Baudoin, *J. Am. Chem. Soc.*, 2008, **130**, 15157; (*f*) I. Ozdemir, S. Demir, B. Cetinkaya, C. Gourlaouen, F. Maseras, C. Bruneau and P. H. Dixneuf, *J. Am. Chem. Soc.*, 2008, **130**, 1156; (*g*) L. Ackermann, R. Vicente and A. Althammer, *Org. Lett.*, 2008, **10**, 2299; (*h*) L. Ackermann and A. Althammer, *Angew. Chem., Int. Ed.*, 2007, **46**, 1627; (*i*) F. Yang, Y. Wu, Z. Zhu, J. Zhang and Y. Li, *Tetrahedron*, 2008, **64**, 6782.

4 Direct arylation reactions which do not require cyclometallation are a also known, see: (*a*) I. Moritani and Y. Fujiwara, *Tetrahedron Lett.*, 1967, **8**, 1119; (*b*) M. Lafrance, C. N. Rowley, T. K. Woo and K. Fagnou, *J. Am. Chem. Soc.*, 2006, **128**, 8754; (*c*) M. Lafrance and K. Fagnou, *J. Am. Chem. Soc.*, 2006, **128**, 16496; (*d*) S. I. Gorelsky, D. Lapointe and K. Fagnou, *J. Am. Chem. Soc.*, 2008, **130**, 10848; (*e*) J. C. Lewis and R. G. Bergman, *Acc. Chem. Res.*, 2008, **41**, 1013.

5 D. L. Davies, S. M. A. Donald O Al-Duaij, S. A. Macgregor and M. Pölleth, *J. Am. Chem. Soc.*, 2005, **127**, 13754.

6 A. D. Ryabov, *Chem. Rev.*, 1990, **90**, 403; A. D. Ryabov, I. K. Sakodinskaya and A. K. Yatsimirsky, *J. Chem. Soc., Dalton Trans.*, 1985, 2629.

7 B. Biswas, M. Sugimoto and S. Sakaki, *Organometallics*, 2000, **19**, 3895.

8 D. L. Davies, O. Al-Duaij, J. Fawcett, M. Giardiello, S. T. Hilton and D. R. Russell, *Dalton Trans.*, 2003, 4132.

9 In this paper, the term 'cyclometallation' will be used for the overall reaction starting from $[IrCl_2Cp^*]_2$ and DMBA-H to form $[Ir(DMBA)(Cl)Cp]^+$. 'C–H activation' refers to the transformation of intermediates of the form $[Ir(DMBA\text{-}H)(base)Cp]^+$ to give $[Ir(DMBA)(H\text{-}Base)Cp]^+$, while 'C–H bond cleavage' refers to a one step C–H bond breaking event.

10 D. L. Davies, S. M. A. Donald and S. A. Macgregor, *J. Am. Chem. Soc.*, 2006, **128**, 4210.

11 D. L. Davies, S. M. A. Donald, O. Al-Duaij, J. Fawcett, C. Little and S. A. Macgregor, *Organometallics*, 2006, **25**, 5976.

12 Y. Boutadla, D. L. Davies, S. A. Macgregor and A. I. Poblador-Bahamonde, *Dalton Trans.*, 2009, DOI: 10.1039/b904967c.

13 For example in $\mathbf{TS(1–2)_{Me}}$ C_{benzyl}–N–Ir–X = 139.7° and C1–C_{ipso}–C_{benzyl}–N = 77.2°; the equivalent values computed previously are 66.4° and 0.3°, respectively[9].

14 D. H. Ess, S. M. Bischof, J. Oxgaard, R. A. Periana and W. A. Goddard, *Organometallics*, 2008, **27**, 6440.

15 J. F. J. Dippy, S. R. C. Hughes and A. Rozanski, *J. Chem. Soc.*, 1959, 2492.

16 In a typical run, a mixture of $[IrCl_2Cp^*]_2$ (20 mg, 0.025 mmol), DMBA-H (8.5 mg, 0.063 mmol) and NaOAc (5.2 mg, 0.063 mmol) in dichloromethane (10 mL) was stirred for 18 h. After this time, the mixture was filtered through Celite and evaporated to dryness. The sample was dissolved in 0.5 mL of a $CDCl_3$ solution containing mesitylene (0.05 mmol L^{-1}) and the amount of product was determined by integration of the ^1H NMR spectrum. The yield was 65%.

17 Y. Boutadla, O. Al-Duaij, D. L. Davies, G. A. Griffith and K. Singh, *Organometallics*, 2009, **28**, 443.

18 In the case of triflate, the ^1H NMR spectrum after 17 h reaction shows almost complete consumption of $[IrCl_2Cp^*]_2$ The calculations are consistent with this, in that while dimer opening appears feasible, the subsequent reaction to the cyclometallated product is then unfavourable.

19 M. J. Frisch, G. W. Trucks, H. B. Schlegel, G. E. Scuseria, M. A. Robb, J. R. Cheeseman, J. A. Montgomery, Jr., T. Vreven, K. N. Kudin, J. C. Burant, J. M. Millam, S. S. Iyengar, J. Tomasi, V. Barone, B. Mennucci, M. Cossi, G. Scalmani, N. Rega, G. A. Petersson, H. Nakatsuji, M. Hada, M. Ehara, K. Toyota, R. Fukuda, J. Hasegawa, M. Ishida, T. Nakajima, Y. Honda, O. Kitao, H. Nakai, M. Klene, X. Li, J. E. Knox, H. P. Hratchian, J. B. Cross, V. Bakken, C. Adamo, J. Jaramillo, R. Gomperts, R. E. Stratmann, O. Yazyev, A. J. Austin, R. Cammi, C. Pomelli, J. Ochterski, P. Y. Ayala, K. Morokuma, G. A. Voth, P. Salvador, J. J. Dannenberg, V. G. Zakrzewski, S. Dapprich, A. D. Daniels, M. C. Strain, O. Farkas, D. K. Malick, A. D. Rabuck, K. Raghavachari, J. B. Foresman, J. V. Ortiz, Q. Cui, A. G. Baboul, S. Clifford, J. Cioslowski, B. B. Stefanov, G. Liu, A. Liashenko, P. Piskorz, I. Komaromi, R. L. Martin, D. J. Fox, T. Keith, M. A. Al-Laham, C. Y. Peng, A. Nanayakkara, M. Challacombe, P. M. W. Gill, B. G. Johnson, W. Chen, M. W. Wong, C. Gonzalez and J. A. Pople, *GAUSSIAN 03 (Revision C.02)*, Gaussian, Inc., Wallingford, CT, 2004.

20 (*a*) H. L. Schmider and A. D. Becke, *J. Chem. Phys.*, 1998, **108**, 9624; (*b*) J. P. Perdew, *Phys. Rev. B: Condens. Matter Mater. Phys.*, 1986, **33**, 8822.

21 (*a*) A. Bergner, M. Dolg, H. Kuechle, H. Stoll and H. Preuss, *Mol. Phys.*, 1993, **80**, 1431; (*b*) M. Kaupp, P. v. R. Schleyer, H. Stoll and H. Preuss, *J. Chem. Phys.*, 1991, **94**, 1360; (*c*) M. Dolg, H. Stoll, H. Preuss and R. M. Pitzer, *J. Phys. Chem.*, 1993, **97**, 5852.

22 (*a*) W. J. Hehre, R. Ditchfield and J. A. Pople, *J. Chem. Phys.*, 1972, **56**, 2257; (*b*) P. Hariharan and J. A. Pople, *Theor. Chim. Acta*, 1973, **28**, 213.